Reactive Aromatic Molecules on Metal Surfaces: Syntheses, Reactions and Structures

Dissertation

zur Erlangung des
Doktorgrades der Naturwissenschaften
(Dr. rer. nat.)

dem
Fachbereich Chemie
der
Philipps-Universität Marburg

vorgelegt von
Malte Sikko Albrecht Zugermeier
M.Sc.

aus
Oldenburg (Oldb)

Marburg, 2018

Tag der Einreichung: 08.06.2018

Vom Fachbereich Chemie der Philipps-Universität Marburg (Hochschulkennziffer: 1180) als Dissertation angenommen am: 26.07.2018

Tag der Disputation: 06.08.2018

Erstgutachter:
Prof. Dr. J. Michael Gottfried – Philipps-Universität Marburg, Fachbereich Chemie

Zweitgutachter:
Prof. Dr. Gerhard Hilt – Carl von Ossietzky Universität Oldenburg, Institut für Chemie

Meinen Eltern, meiner Schwester und Jessika

Contents

Selbstständigkeitserklärung

gemäß § 10 Abs. 1 der Promotionsordnung der Mathematisch-Naturwissenschaftlichen Fachbereiche und des Medizinischen Fachbereichs für seine mathematisch-naturwissenschaftlichen Fächer der Philipps-Universität Marburg vom 15.07.2009.

Ich erkläre, dass eine Promotion noch an keiner anderen Hochschule als der Philipps-Universität Marburg, Fachbereich Chemie, versucht wurde.
Ich versichere, dass ich meine vorgelegte Dissertation mit dem Titel

Reactive Aromatic Molecules on Metal Surfaces:
Syntheses, Reactions and Structures

selbstständig und ohne fremde Hilfe verfasst, nicht andere als die angegebenen Quellen oder Hilfsmittel benutzt, alle vollständig oder sinngemäß übernommenen Zitate als solche gekennzeichnet sowie die Dissertation in der vorliegenden oder einer ähnlichen Form noch bei keiner anderen in- oder ausländischen Hochschule anlässlich eines Promotionsgesuchs oder zu anderen Prüfungszwecken eingereicht habe.

Marburg, _____ _____

Malte Zugermeier

Abstract

The interaction of organic molecules with metal contacts and the reactivity of those molecules are of high technological interest, especially in the field of organic electronics and surface-assisted catalysis. Surface chemistry addresses the arising fundamental questions. The presented work comprises the investigation of several reactive aromatic compounds on coinage metal surfaces. Although all systems raise their own scientific questions, all discussions concern either the on-surface synthesis, possible reactions or the formation of two-dimensional structures. In the studies, the methods of scanning tunneling microscopy (STM), X-ray and ultraviolet photoelectron spectroscopy (XPS, UPS) as well as near-edge X-ray absorption fine structure (NEXAFS) spectroscopy were employed. The experimental results are substantiated with insights from density functional theory (DFT) calculations.

The first experimental topic is focused on the structures and reactions of tetrapyrrole macrocycles on diverse surfaces. Corroles exhibit a slightly different chemical structure than porphyrins. In the investigations of hexaethyldimethylcorrole (3H-HEDMC) monolayers on Ag(111), an enhanced surface reactivity was observed. Already below room temperature, one of the three pyrrolic nitrogen atoms is deprotonated. Furthermore, superstructures of 2H-HEDMC are formed. The periodic structure is based on a double-S motif, which is composed of the ethyl substituents of the corrole macrocycle. The metalation of 3H-HEDMC with iron, cobalt and nickel was studied on Ag(111). The resulting organometallic complexes were investigated regarding the electronic state of the metal center. By combination of different experimental methods probing occupied and unoccupied molecular states, differences in the electronic structure of the metalated hexaethyldimethylcorrole and octaethylporphyrin as reference object were revealed. While multilayer experiments suggest the presence of an oxidation state of $+\,\mathrm{III}$ in the metalated corrole and $+\mathrm{II}$ in the corresponding porphyrin, the electronic properties in the monolayers cannot be assigned to formal oxidation states due to a substantial interaction with the metal substrate. The investigation of tetraphenylporphyrin with co-adsorbed lead revealed a possible metalation and a transmetalation at increased temperatures. A bromine substituted nickel-tetraphenylporphyrin was studied concerning its reactive coupling and thus a resulting formation of covalent $\mathrm{C}-\mathrm{C}$ bonds due to an Ullmann coupling. The organometallic intermediate was observed in large, highly ordered domains.

The investigations on aromatic dicarbonitriles are dedicated to the influence of functional groups in reactively formed or self-assembled structures. An annulated naphthalenedicarbonitrile serves as precursor for the synthesis of an extended iron-naphthalocyanine. The precursor molecules self-assemble in locally ordered phases, which will be explained concerning the intermolecular interactions. The tetramerization was observed after post-deposition of iron onto a monolayer of the corresponding precursor and a subsequent annealing. The naphthalocyanine molecules are arranged in ordered islands. Beside the tetrameric products also oligomers are formed in the metal-mediated reaction. While dicarbonitriles can be reactively linked in this fashion, the functional groups are also responsible for self-assembled nanostructures. The nitrile moities can form hydrogen bonds with the phenyl groups of adjacent molecules. The

experimental results provide insight into the interaction of molecules on surfaces. These interactions can either be utilized to form expanded structures or in the on-surface synthesis of large organic molecules which are otherwise not accessible for surface science studies.

Large acenes are promising novel organic semiconductors, which provide small HOMO-LUMO gaps, high charge carrier mobilities and further beneficial properties. These properties scale with increasing length of the annulated aromatic backbone. However, large acenes exhibit also increasing reactivity. The accessibility is therefore limited. The reason for this unfavorable trend is explained by the low number of Clar π-sextets resulting in a loss of aromatic character and a decreased stability. If the conjugation is interrupted, the corresponding compound is more stable due to the formation of a second π-sextet. A diketone-bridged precursor was used in a surface-assisted synthesis of heptacene. The transition is achieved by thermal didecarbonylation, which was observed in a photoemission spectroscopic heating series. The precursor and heptacene molecules were investigated by means of STM. Low-temperature images revealed the generation of individually resolved heptacene molecules. The images show a substantial influence of the surface on the molecules. These interactions are explained by complementary experimental and theoretical results. The results are consistent with the preliminary considerations of the aromatic π-sextets.

Kurzzusammenfassung

Die Wechselwirkungen von organischen Molekülen mit Metallkontakten und die Reaktivität dieser Moleküle sind von großem technologischen Interesse, besonders im Bereich der organischen Elektronik und der oberflächengestützen Katalyse. Die hier präsentierte Dissertation umfasst die Untersuchung von diversen reaktiven aromatischen Verbindungen auf Münzmetalloberflächen. Obwohl alle untersuchten Systeme ihre eigenen wissenschaftlichen Fragestellungen aufwerfen, beziehen sich die Diskussionen entweder auf die Synthese auf Oberflächen, mögliche Reaktionen oder die Bildung zweidimensionaler Strukturen. Die Studien wurden anhand der Methoden der Rastertunnelmikroskopie (STM), der Röntgen- und Ultraviolettphotoelektronenspektroskopie (XPS, UPS) sowie der Röntgen-Nahkanten-Absorptionsspektroskopie (NEXAFS) durchgeführt. Die experimentellen Ergebnisse wurden darüber hinaus durch Erkenntnisse aus Rechnungen der Dichtefunktionaltheorie (DFT) untermauert.

Das erste experimentelle Thema ist ausgerichtet auf die Strukturen und Reaktionen von Tetrapyrrolmakrozyklen auf unterschiedlichen Oberflächen. Corrole weisen eine leicht abweichende chemische Struktur von derjenigen der Porphyrine auf. In den Untersuchungen an Monolagen von Hexaethyldimethylcorrol (3H-HEDMC) auf Ag(111) wurde eine erhöhte Oberflächenreaktivität beobachtet. Bereits unterhalb von Raumtemperatur wird eines der drei pyrrolischen Stickstoffatome deprotoniert. Außerdem formiert sich bei dieser Temperatur eine bemerkenswerte Überstruktur. Diese periodische Struktur basiert auf einem Doppel-S-Motiv, welches aus den Ethylsubstituenten des Corrolmakrozyklus gebildet wird. Die Metallierung von 3H-HEDMC mit Eisen, Cobalt und Nickel wurde auf der Ag(111)-Oberfläche untersucht. Die resultierenden organometallischen Komplexe wurden bezüglich des elektronischen Zustandes des Metallzentrums untersucht. Durch die Kombination verschiedener experimenteller Methoden, die die besetzten und unbesetzten molekularen Zustände erforschen, wurden Unterschiede in der elektronischen Struktur des metallierten Hexaethyldimethylcorrols und eines Octaethylporphyrins als Vergleichsverbindung aufgedeckt. Während Multilagenexperimente auf einen Oxidationszustand von $+\,\mathrm{III}$ im Falle des metallierten Corroles und von $+\,\mathrm{II}$ beim entsprechenden Porphyrin hinweisen, können die elektronischen Eigenschaften in den Monolagen nicht einem formalen Oxidationszustand zugeordnet werden, da das Metallsubstrat eine erhebliche Wechselwirkung mit den Molekülen eingeht. Die Untersuchung von Tetraphenylporphyrin mit co-adsorbiertem Blei offenbarte eine mögliche Metallierungsreaktion. Außerdem kann eine Transmetallierung bei erhöhten Temperaturen beobachtet werden. Die reaktive Verknüpfung eines Brom-substituierten Nickeltetraphenylporphyrins und eine anschließende Bildung von kovalenten C–C-Bindungen durch eine Ullmann-Reaktion wurde untersucht. Das organometallische Intermediat tritt in großen, hochgradig geordneten Domänen auf.

Die Untersuchungen von aromatischen Dicarbonitrilen beziehen sich auf den Einfluss funktioneller Gruppe in Strukturen, die durch chemische Reaktionen gebildet wurden oder selbstorganisiert sind. Ein anneliertes Naphthalindicarbonitril dient als Edukt in der Synthese eines erweiterten Eisennaphthalocyanins. Die Eduktmoleküle fügen sich in lokal geordneten Phasen zusammen, die bezüglich der intermolekularen Wechselwirkungen erklärt werden. Die Tetra-

merisierung wurde nach dem zusätzlichen Aufbringen von Eisen auf die Monolage der reaktiven Vorstufe beobachtet. Die Naphthalocyaninmoleküle befinden sich dabei in geordneten Inseln. Neben den Tetramerprodukten bilden sich auch Oligomere bei der Metall-induzierten Reaktion. Während die Dicarbonitrile reaktiv verknüpft werden können, sind die funktionellen Gruppen auch für die Selbstanordnung von Nanostrukturen verantwortlich. Die Nitrilgruppen können Wasserstoffbrückenbindungen mit den Phenylgruppen benachbarter Moleküle ausbilden. Die experimentellen Ergebnisse liefern Einsicht in die Wechselwirkungen von Molekülen auf Oberflächen. Diese Wechselwirkungen können entweder für ausgedehnte Strukturen oder in der oberflächengestützten Synthese von großen organischen Molekülen, die auf anderem Wege für die Oberflächenforschung nicht zugänglich sind, genutzt werden.

Lange Acene sind vielversprechende neuartige organische Halbleiter, die eine kleine HOMO-LUMO-Lücke, hohe Ladungsträgermobilitäten und weitere nutzbringende Eigenschaften aufweisen. Diese Eigenschaften skalieren mit der zunehmenden Länge des annelierten aromatischen Systems. Lange Acene besitzen jedoch auch eine erhöhte Reaktivität. Aus diesem Grund ist die synthetische Zugänglichkeit der Verbindungen eingeschränkt. Der Grund für diesen widrigen Trend kann durch die geringe Anzahl an π-Sextetten nach Clar erklärt werden, durch die der aromatische Charakter des Moleküls verloren geht und die Stabilität abnimmt. Eine Unterbrechung der Konjugation führt zu einem zweiten π-Sextett und einer stabileren Verbindung. Eine Diketon-überbrückte Vorstufe wurde in der oberflächengestützten Synthese des Heptacens verwendet. Die Umwandlung erfolgt durch thermische Didecarbonylierung, deren Erfolg in einer Heizserie mittels Photoemissionsspektroskopie untersucht wurde. Die Edukte und Heptacenmoleküle wurden des Weiteren mittels STM untersucht. Tieftemperaturaufnahmen zeigen die gebildeten Heptacenmoleküle, die einzeln sichtbar sind. Darüber hinaus zeigt sich ein deutlicher Einfluss der Oberfläche auf die Moleküle. Diese Wechselwirkungen werden anhand komplementärer experimenteller und theoretischer Methoden erläutert. Die Ergebnisse sind konsistent mit den Vorüberlegungen zu den aromatischen π-Sextetten.

Abbreviations

General Acronyms

2D-MOCN	2D metal-organic coordination network
AEY	Auger electron yield
AFM	Atomic force microscopy
DFT	Density functional theory
ESCA	Electron spectroscopy for chemical analysis
ESI	Electrospray ionization
fcc	Face-centered cubic
hcp	Hexagonal close-packed
HOMO	Highest occupied molecular orbital
LEED	Low-energy electron diffraction
LT	Low temperature
LUMO	Lowest unoccupied molecular orbital
nc-AFM	Non-contact atomic force microscopy
NEXAFS	Near-edge X-ray absorption fine structure
NMR	Nuclear magnetic resonance
PDOS	Partial density of states
PES	Photoelectron spectroscopy
PEY	Partial electron yield
QCM	Quartz-crystal microbalance
RT	Room temperature (300 K)
SEM	Scanning electron microscopy
SOMO	Singly occupied molecular orbital
SPM	Scanning probe microscopy
STM	Scanning tunneling microscopy
STS	Scanning tunneling spectroscopy
TEY	Total electron yield
ToF-SIMS	Time-of-flight secondary ion mass spectrometry
TPD	Temperature-programmed desorption
UHV	Ultra-high vacuum
UPS	Ultraviolet photoelectron spectroscopy
VT	Variable temperature
XANES	X-ray absorption near-edge structure
XAS	X-ray absorption spectroscopy
XPS	X-ray photoelectron spectroscopy

Chemical Nomenclature

NDN*	1′,1′,4′,4′-Tetramethyl-1′,2′,3′,4′-tetrahydroanthracene-6,7-dicarbonitrile
2HOEP	2,3,7,8,12,13,17,18-Octaethylporphyrin
2HTPP	5,10,15,20-Tetraphenylporphyrin
2HTPyP	5,10,15,20-Tetra(4-pyridyl)porphyrin
3H-HEDMC	2,3,8,12,17,18-Hexaethyl-7,13-dimethylcorrole
CoOEP	Cobalt(II)-2,3,7,8,12,13,17,18-octaethylporphyrin
DEH	7,16-Dihydro-7,16-ethanoheptacene-19,20-dione
GNR	Graphene nanoribbon
HOPG	Highly oriented pyrolytic graphite
m-3PDN	1,1′:3′,1″-Terphenyl-4,4″-dicarbonitrile
m-4PDN	1,1′:3′,1″:4″,1‴-Quaterphenyl-4,4‴-dicarbonitrile
Nc	Naphthalocyanine
NiOEP	Nickel(II)-2,3,7,8,12,13,17,18-octaethylporphyrin
NiTBrPP	Nickel(II)-5,10,15,20-tetrakis(4-bromophenyl)porphyrin
Pc	Phthalocyanine

Constants

Ag L_α	X-ray line	2984.3 eV
Al K_α	X-ray line	1486.7 eV
e	Elementary charge	$1.602\,176 \cdot 10^{-19}$ C
h	Planck constant	$6.626\,08 \cdot 10^{-34}$ J s
$\hbar$	Reduced Planck constant $\hbar = \frac{h}{2\pi}$	$1.054\,57 \cdot 10^{-34}$ J s
k	Boltzmann constant	$1.380\,65 \cdot 10^{-23}$ J K^{-1}
m_e	Electron rest mass	$9.109\,38 \cdot 10^{-31}$ kg
R	Gas constant	8.314 47 J mol^{-1} K^{-1}

Variables

A	Area	m^2
α	Absorption coefficient	cm^{-1}
E	Energy	J = eV/$(1.602\,176 \cdot 10^{-19})$
I	Current	A
I	Intensity	*arbitrary units*
l	Path length	m
λ	Inelastic mean free path length	m
λ	Wavelength	m

M	Molar mass	$\mathrm{g\,mol^{-1}}$
$\dot{m}$	Effusion rate (mass per unit time)	$\mathrm{kg\,s^{-1}}$
ν	Frequency	Hz
ν	Frequency factor	$\mathrm{s^{-1}}$
P	Degree of polarization	
p	Pressure	Pa
Φ	Work function	eV
σ	Photoionization cross section	$\mathrm{b} = 10^{-28}\,\mathrm{m^2}$
T	Temperature	K
T	Transmission function	*arbitrary units*
Θ	Coverage	ML, $\mathrm{ML_{ads}}$, $\mathrm{ML_{substr}}$
V	Voltage, electric potential difference	V
v	Velocity	$\mathrm{m\,s^{-1}}$

Indices

0	Initial value
A	Activation
ads	Adsorbate
B	Binding
F	Related to the Fermi level
f	Final state
i	Initial state
kin	Kinetic
O	Orifice
pass	Pass
r	Relaxation
s	Sample
sp	Spectrometer
substr	Substrate
vac	Related to the vacuum level

1 Introduction

In recent years, the number of highly specialized materials for technical and medicinal questions has increased rapidly. Simultaneously, sustainable production and usage gained in importance. Since these developments include novel classes of compounds and take advantage of the interplay of diverse materials, the necessity of fundamental knowledge about the properties and reactivity of suitable chemical compounds emerges. This demand includes studies in the relatively young field of surface chemistry, which deviates in many aspects from the commonly exploited and well-approved procedures as well as the reaction mechanisms in solution phase or solid state chemistry. Surface chemistry does not only allow a tunable surface functionalization by sophisticated choice of chemical components but also by surface patterning due to molecular self-assembly. To contribute to these investigations, this work comprises the reactivity of organic, aromatic molecules on noble metal surfaces with regard to their surface coordination chemistry, the on-surface synthesis and the formation of supramolecular structures.

Predominantly, the investigations reported in this work were conducted on two classes of organic molecules, corroles and porphyrins as cyclic tetrapyrroles and acenes as linearly fused aromatic hydrocarbons. The choice and range of molecules and the variety of experiments are not supposed to satisfy the claim that they contribute to specific technological developments, but general relevance arises for the various fields of catalysis, organic electronics, and the treatment of serious diseases. The main focus in the studies is on the role of organic macrocycles and metal cations in their inner core – in the case of coordination compounds – as well as the interaction of organic molecules with metal surfaces.

The surface interaction of porphyrins and their metalation – either as direct metalation with post- and pre-deposited metal atoms or as self-metalation with surface adatoms or atoms extracted from the top-most layer – has been widely studied.[1–5] The corroles, however, have rarely been subject to investigation. The question arises whether the conclusions from the porphyrin studies are also valid for those related macrocycles or whether the structural differences induce their own characteristics. Acenes are the most widely studied molecular organic semiconductors and model systems for organic electronics.[6–8] Here, the accessibility of a highly reactive, elongated molecule and the metal/organic interface are in the center of interest. In the multilayer systems of organic electronics, the inter-layer interaction is an essential property.[9–14] Multilayers are very much affected by the first layer, since it acts as a structural template for the growth of further layers and electronically couples to the substrate. For this reason, monolayers of relevant compounds are regarded here. Two-dimensional structures can either be produced by intermolecular reaction and covalent bond formation or by intermolecular forces. The experiments will be discussed depending on the coverage in the submonolayer to monolayer regime, the orientation of involved molecules and the resulting intermolecular forces. Additionally, dicarbonitriles are used as precursors in on-surface reactions establishing a synthetic route for even larger molecules which are otherwise not accessible for surface science.

1.1 Organic Macrocycles

Living organisms possess fascinating and manifold chemical reactions in their metabolic pathways, in which especially organic macrocycles and their organometallic derivatives are of high significance. The redoxactivity of the metal ion in the central pocket of those complexes is the crucial part in the functional capability of the active centers in enzymes, which are essential for life in general. As ligands, the organic macrocycles play an integral role in the reactivity as they provide a stable environment for the metal ions.

Members of the tetrapyrrole family are the prevalent form of organic macrocycles in nature. Prominent examples for the natural occurance of those macrocycles are the aromatic porphine ring in heme B (Fig. 1.1 (a)) and the non-aromatic corrin ring in vitamin B_{12} or cobalamin (Fig. 1.1 (b)) including Fe(II) and Co(III), respectively, in the main form of the compounds. The relevance of the metal center can be illustrated by the oxygen transport. Heme B is the active binding site in hemoglobin, which serves as oxygen-transport protein in red blood cells and thus allows aerobic respiration. Oxygen binds to the iron center as superoxide increasing the oxidation state to Fe(III). The loaded form, oxyhemoglobin exhibits a red color, while the unloaded form, deoxyhemoglobin, is blue. Due to this color change induced by a high concentration of deoxyhemoglobin, hypoxia leads to a bluish skin color, the cyanosis.

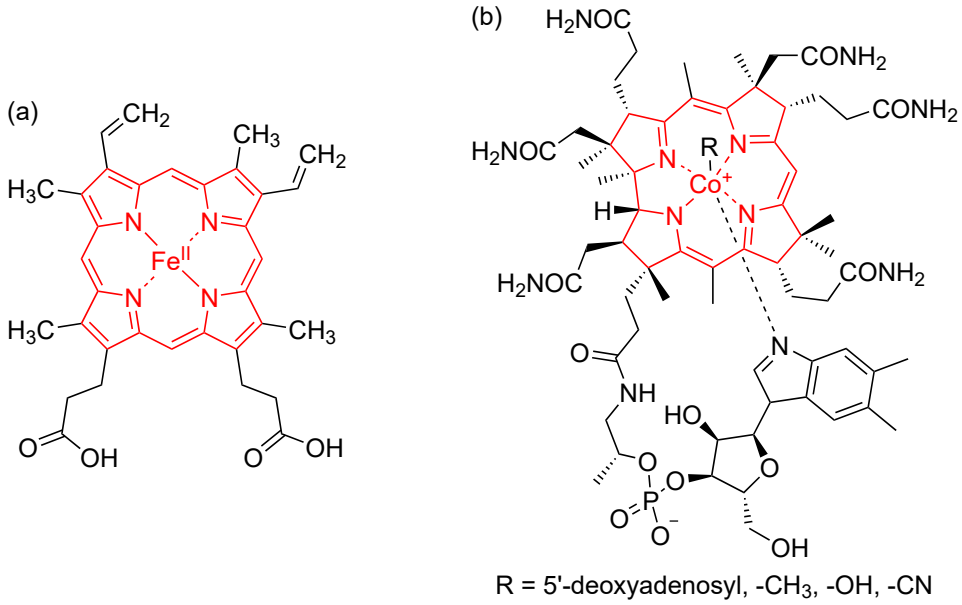

Figure 1.1: Organic macrocycles and their occurrence in nature, *e.g.*, as (a) porphine ring in heme B or as (b) corrin ring in vitamin B_{12}.

1.1.1 Porphyrinoid Tetrapyrroles and Their Metal Complexes

Technical and medicinal applications in a huge variety were developed using aromatic, cyclic tetrapyrroles derived from the natural porphyrins as well as employing closely related, synthetic macrocycles, corroles, phthalocyanines and naphthalocyanines.

Porphine (Fig. 1.2 (a)) is the parent macrocycle of the porphyrins, which are named after the greek word "πορφύρα" (*porphyra*, purple) indicating their color. When a slight modification

of the porphine macrocycle is conceptually performed, it is transformed into the corrole (Fig. 1.2 (b)), which is – in its alkyl-substituted form (2,3,8,12,17,18-hexaethyl-7,13-dimethylcorrole (3H-HEDMC), Fig. 1.2 (c)) – one of the objects of investigations in this thesis. While the four pyrrole units in porphine are linked by methine bridges, one of those bridges is absent in the corrole macrocycle resulting in a tighter coordination environment and a tribasic acid form.[15] Furthermore, corrole is the aromatic and partially dehydrogenated derivative of the corrin macrocycle and also referred to as octadehydrocorrin.

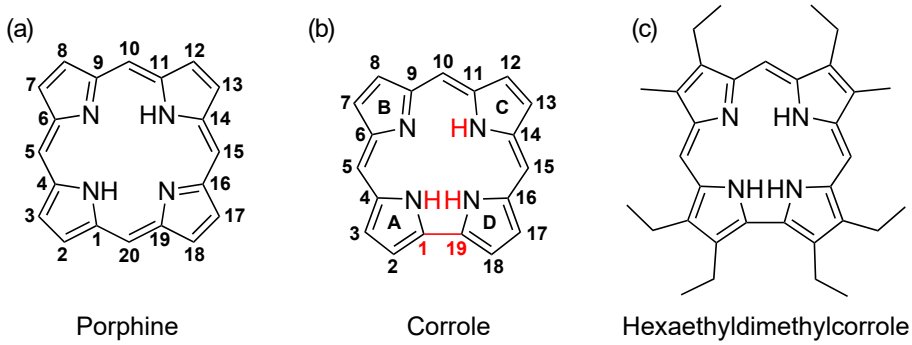

Figure 1.2: The family of porphyrinoid tetrapyrroles. (a) The parent organic, aromatic macrocycle of all porphyrins is the unsubstituted porphine. Porphine possesses two iminic (–N=) and two pyrrolic (–NH–) nitrogen atoms in its center. (b) The corrole resembles the porphine with the exceptions (highlighted in red) of one missing methine bridge and a tribasic acid character due to an additional pyrrolic nitrogen. Furthermore, corrole is derived from the biologically relevant non-aromatic corrin macrocycle. (c) The alkyl-substituted 2,3,8,12,17,18-hexaethyl-7,13-dimethylcorrole (3H-HEDMC) was reactant in the here reported on-surface and coordination reactions.

Porphyrins

The relevance of porphyrins in scientific studies investigating manifold reactions and applications can already be estimated by the large extent of the famous book series "Porphyrin Handbook" and "Handbook of Porphyrin Science". Metalloporphyrins are of high interest because they act as a model system for the interaction of organic ligands with metal ions. The key aspect is the oxidation state of the metal as mentioned above for the natural purpose of those organometallic compounds but also for potential homogeneous and heterogeneous catalysis. Coordination reactions were studied on metal and semiconductor surfaces[2,3,5] and interphase systems.[16]

Low-temperature nuclear magnetic resonance (NMR) studies on deuterated species of porphyrins revealed the presence of two tautomers, in which the hydrogen atoms of the pyrrolic (–NH–) nitrogens changed the place in a concerted two-step, two-proton shift and the former iminic (–N=) nitrogen atoms become hydrogenated.[17,18] Since Erich HÜCKEL's rule for aromaticity ($4n+2$ conjugated π-electrons in a planar, cyclic system) cannot be used to describe polycyclic compounds, the aromacity of porphyrins is usually interpreted by the 18π main conjugation pathway as reported by Franz SONDHEIMER *et al.* for [18]annulene.[19–22]

A huge variety of studies was conducted on substituted porphyrins. The chemistry and especially the intermolecular behavior of those porphyrins shown in Figure 1.3 often depends on the nature of the peripheral substituents. In this work, phenyl- and pyridyl-substituted por-

phyrins, 5,10,15,20-tetraphenylporphyrin (2HTPP) and 5,10,15,20-tetra(4-pyridyl)porphyrin (2HTPyP), were subject to metalation with a large metal cation. The alkyl-substituted porphyrin, 2,3,7,8,12,13,17,18-octaethylporphyrin (2HOEP), was the reference molecule for the investigation of the likewise alkyl-substituted corrole.

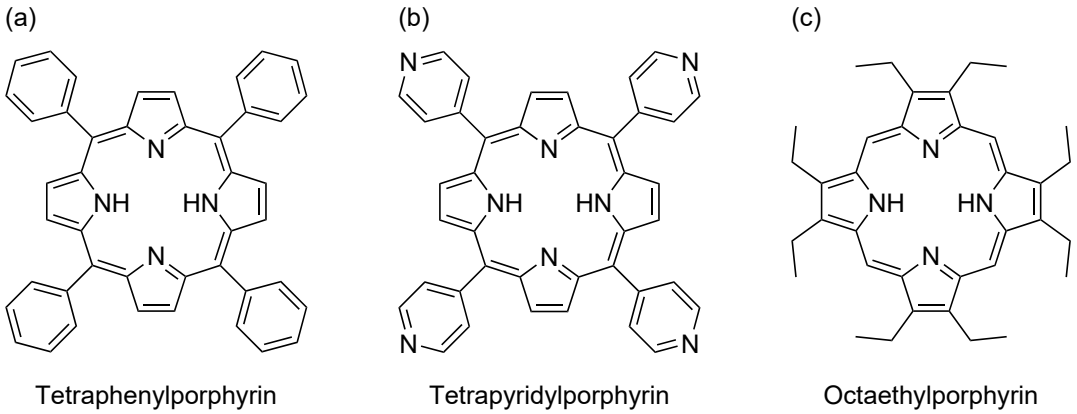

Figure 1.3: Prominent representatives of the porphyrines. The substituted macrocycles, (a) 5,10,15,20-tetraphenylporphyrin (2HTPP), (b) 5,10,15,20-tetra(4-pyridyl)porphyrin (2HTPyP) and (c) 2, 3,7,8,12,13,17,18-octaethylporphyrin (2HOEP), were studied in this work.

A recently published review discusses the application of metalloporphyrins for the detection of explosives, neurotoxic and biological agents and even radioactive material.[23] The detection mechanisms include either the reactivity of metalloporphyrins toward decomposition products of the relevant weapons or the incorporation of actinoid cations in sandwich complexes.

Corroles

While the synthesis of porphyrins can start with pyrrole derivatives as reactants, the crucial step in the synthesis of corroles is to achieve the direct link of two pyrrole units. Therefore, a reaction of four symmetric parts is not suitable and the synthesis becomes more difficult.[15,24] A common pathway is the oxidative ring closure of linear precursor molecules.[25] In this fashion, the here examined 3H-HEDMC was synthesized from 1,19-didesoxy-2,3,8,12,17,18-hexaethyl-9, 13-dimethylbiladiene dihydrobromide.[26,27]

Corroles are studied with regard to various possible applications. Medicinal applications use corrole-based catalytic antioxidants in diabetes treatment[28] or cytotoxicity toward human breast cancer cells by specific binding of proteins conjugated with Ga-corroles to the respective receptors on the cell surface.[29–31] Technical applications benefit from the metal center in catalytic reduction of CO_2, reversible O_2 binding or the sensing of CO gas by Co(III)-corroles.[29] The close relation to the porphyrins also induces relevance in other catalytical aspects.[32,33] Corrole-based pH sensors are imaginable due to the dependency of the three protonation states of the pyrrolic nitrogens in the core of macrocycle ($[H_4(\text{corrole})]^+$, $[H_3(\text{corrole})]$, $[H_2(\text{corrole})]^-$) on aqueous pH values.

Min Chen performed preliminary investigations on 3H-HEDMC regarding the metalation with Co atoms[34], which were continued here and extended by reactions with further metals and substantiated with microscopic studies. The tribasic acid character and the constricted

core of the macrocycle suggest the stabilization of high-valent metal cations with smaller radii as it was observed in solution phase experiments.

1.1.2 Phthalocyanines and Naphthalocyanines

A comparison of the synthetic phthalocyanines with porphine as the fundamental skeleton unveils the relation to the porpyhrins (Fig. 1.4), obvious also in the alternative name tetrabenzotetraazaporphyrin. Phthalocyanines are composed of benzopyrroles linked *via* iminic bridges (Fig. 1.4 (b)). Annulation of the pyrrole rings with naphthalene instead of benzene units leads to naphthalocyanine molecules (Fig. 1.4 (c)).

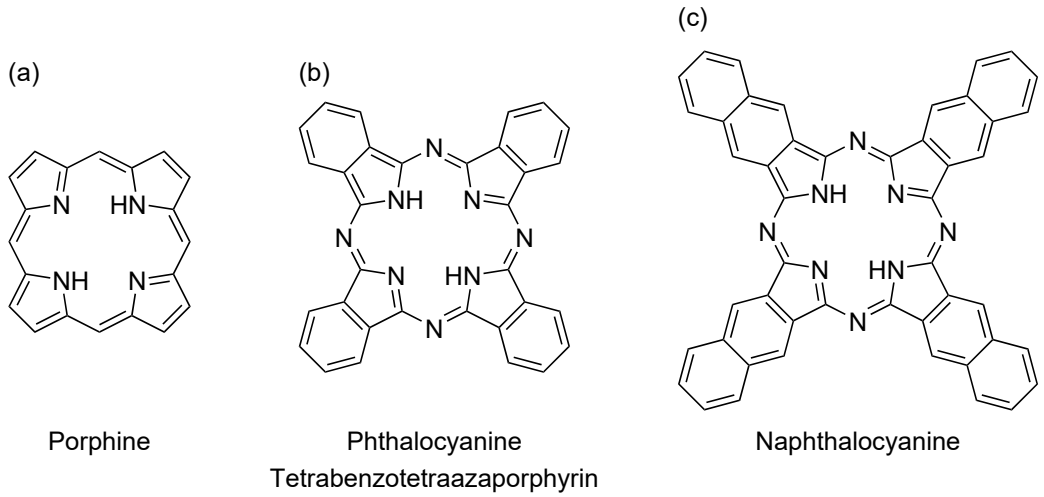

Figure 1.4: From (a) porphine to synthetic macrocycles. (b) Phthalocyanine (Pc) can be referred to as tetrabenzotetraazaporphyrin illustrating their close relationship, while naphthalocyanine (Nc) is an extended phthalocyanine.

Copper-phthalocyanine as well as other complexes are important pigments, but phthalocyanines are also commonly used as catalysts and organic semiconductors.[2,35] Naphthalocyanine compounds were studied in the context of photodynamic cancer therapy.[36] The hydrogen tautomerism in a naphthalocyanine molecule on a NaCl bilayer on Cu(111) was switched by tunneling current and investigated as a prototype for a single-molecule logic switch at the IBM Zurich Research Laboratory.[37] Another approach for molecular switching are tip-induced, conformational transformations concerning the metal center as reported for tin-phthalocyanine.[38–40] Phthalocyanines can be generated by reactive building blocks even in a two-dimensionally confined environment in a simple manner.[41,42] The on-surface synthesis of an extended naphthalocyanine will be discussed later in this work.

1.2 Large Acenes

Due to their interesting and promising properties for organic electronics and molecular spintronics, acenes play an important role in the development of novel organic semiconductors and in basic research. Acenes are polycyclic aromatic hydrocarbons (Fig. 1.5) which are composed of linearly fused aromatic rings. They can be regarded as building blocks of carbon nanotubes

or graphene and can be referred to as narrowest graphene nanoribbons with zigzag edge (Fig. 1.6).[43] While the smaller homologues, benzene, naphthalene and anthracene, are naturally available, the access to larger acenes is only possible on the synthetic way. However, the accessibility is limited due to a high reactivity toward oxygen, poor solubility and an increased light sensitivity.[44] Alongside this unfavorable trend, also other properties scale with an increased number of annulated rings, *e.g.*, a smaller HOMO-LUMO gap, reduced reorganization energy, reduced electron-phonon coupling, and a higher charge carrier mobility in the solid state.[45–48] These properties can be tuned by introducing heteroatoms or substituents at the periphery.[47,49,50] Such derivatives are attractive for devices like organic field-effect transistors, organic light-emitting diodes or organic photovoltaics, which require extraordinary properties for a high performance and a controlled fabrication of organic films.[51,52]

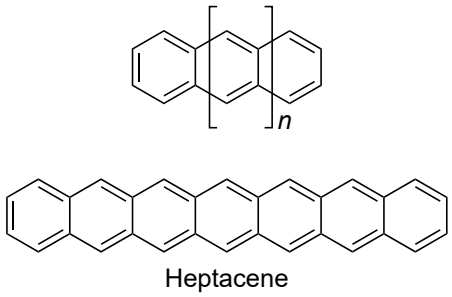

Figure 1.5: General structural formula of acenes (top) and structural formula of heptacene (bottom) generated in this work by on-surface synthesis.

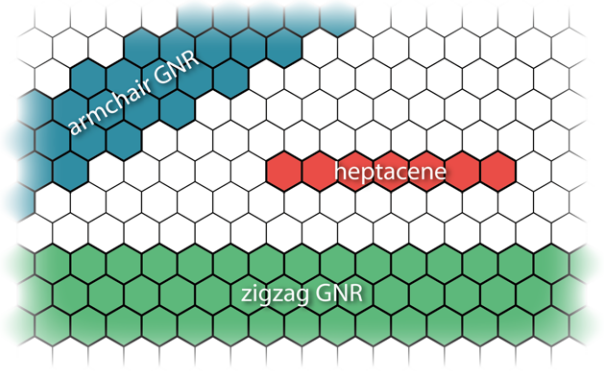

Figure 1.6: Sections of the graphene lattice. Acenes represent the narrowest form of a graphene nanoribbon (GNR) with zigzag edge.

In 1972, Erich Clar wrote his famous book "The Aromatic Sextet", in which he introduced a facile system to estimate properties and especially the stability of polycyclic aromatic hydrocarbons.[53] The fundamental idea of his rules is to find the largest number of π-sextets, benzene-like moieties, in the resonance structures of an aromatic system (Fig. 1.7).[54] These π-sextets are drawn as a circle in the Clar structure. According to the concept, molecules with a higher number of π-sextets are chemically more stable. Acenes share only one π-sextet among all the rings in their conjugated chains.[43] Since the π-sextet is quasi-migrating, all rings exhibit similar aromaticity (Fig. 1.8). The low number in π-sextets and thus a loss in overall aromaticity results in a high reactivity of the acenes, although this finding is contra-

dictory to the usual increase in stability with expansion of a conjugated system.[55] Therefore, larger acenes have an increased tendency toward dimerization and reactions at the central rings. This 1,4-interaction goes along with the formation of an extra π-sextet and thus results in a higher stability.[54] Furthermore, open-shell ground states with biradical character are more stable for higher acenes than the closed-shell states.[54,56]

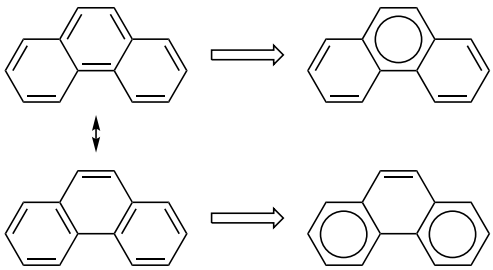

Figure 1.7: According to Clar's rules, only the structure with the largest number of π-sextets is called Clar structure, although π-sextets vizualized by circles can be drawn into two possible resonance structures of phenanthrene.

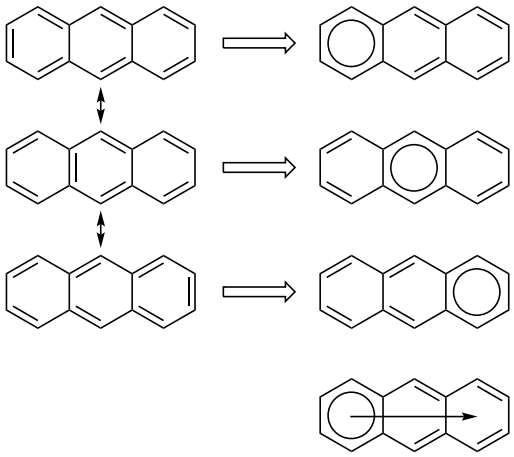

Figure 1.8: By the example of anthracene, a small representative of the acene family, it becomes obvious that every aromatic ring can embody the Clar π-sextet. This property is termed as migration of the π-sextet and depicted with an arrow.

The synthesis of acenes, especially of those with larger size, has been discussed for more than half a century. After his report on the synthesis of hexacene[57], it was Clar[58] to claim the first synthesis of heptacene in 1942[59], albeit the report had to be withdrawn shortly afterwards, when Ch. Marschalk failed to reproduce the synthesis[60]. The previously observed UV-Vis absorption bands were reassigned to benzo[*a*]hexacene.[61] The subsequent synthesis report by William J. Bailey and Chien-Wei Liao was likewise disproved.[62,63] Several further attempts resulted in the formation of heptacene dimers.[64] In 2005, the first syntheses of various substituted heptacenes were reported by Marcia M. Payne.[65] The crucial factor in the synthesis of pure heptacene is the prevention from the formation of dimers or even oligomers.[66,67]

J. Strating and B. Zwanenburg studied the expulsion of bis-CO from bridged π-diketones. They discovered that thermal decarbonylation of dibenzobicyclo[2.2.2]octadiene-2,3-dione results in charring of the organic compound, whereas photolysis yields in a quantitative

amount of anthracene under release of CO. In 2006, Rajib Mondal *et al.* succeeded in synthesizing pure heptacene in a Strating-Zwanenburg photodidecarbonylation[68] of 7,16-dihydro-7,16-ethanoheptacene-19,20-dione (DEH) (Fig. 1.9) in a poly(methyl methacrylate) matrix. The stability of heptacene over 4 h at room temperature (RT) was confirmed by mass spectrometry.[69–71] The immobilization in a solid matrix prevents photodimerization.[72] The precursor was formed in a 4-step synthesis from 2,3-dibromonaphthalene and bicyclo[2.2.2]oct-2,3,5,6,7-pentaene. Holger F. Bettinger *et al.* realized the synthesis of heptacene from the same bridged α-diketone precursor, and analogously the synthesis of even larger acenes, octacene and nonacene, from the corresponding reactants in an argon inert gas matrix.[66,73] The photoreactivity and mechanism of the didecarbonylation was studied in detail.[44,66,67,72,74–76] The stability of the aromatic hydrocarbon parts of the molecule plays a decisive role, since photodecarbonylations of diones are otherwise unusual. Furthermore, a synthesis of heptacene in solution cannot be performed in the same photochemical way, since the product is highly sensitive toward oxygen and reacts as a Diels-Alder diene in the presence of oxygen.[69] Recently, Ralf Einholz *et al.* showed that bulk heptacene can be produced by thermal cycloreversion of diheptacenes, which are formed by reduction of 7,16-heptacenequinone.[77] The solid-state heptacene is stable for several weeks at RT.

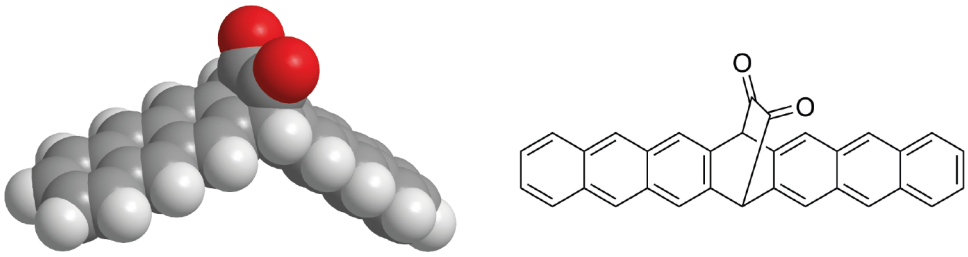

Figure 1.9: Space-filling model and Kekulé structure of 7,16-dihydro-7,16-ethanoheptacene-19,20-dione.

Surface-related studies of larger acenes are, however, rarely performed due to stability reasons and challenging accessibility, while smaller acenes like anthracene and pentacene are extensively studied.[78–84] Justus Krüger and co-workers reported the first on-surface synthesis of tetracene[85] and hexacene[86] by tip-induced reductions and thermally induced deoxygenation of mono- and oligoepoxy precursors on Cu(111) and Au(111) (Fig. 1.10 (a), (d)). Decacene was generated in the same fashion on Au(111).[87] Epoxyacenes preferably form trimers on Au(111) due to intermolecular hydrogen bonds. Upon annealing, oxygen adducts stabilize these trimers.[88] Supramolecular structures of both epoxytetracene and tetracene assemble in Kagome lattices. Rafal Zuzak *et al.* have chosen a different approach and used an air-stable, partially saturated hydroacene as precursor. Dehydrogenation of 6,10,17,21-tetrahydrononacene on Au(111) lead to the formation of nonacene by annealing or by tip-induced cleavage of the C_{sp^3}–H bonds (Fig. 1.10 (b), (e)).[89] Furthermore, acenes are model systems in the study of graphene and the on-surface synthesis of nanographenes. Peripentacene features zig-zag as well as armchair edges and was formed upon thermally induced cyclodehydrogenation of 6,6′-bipentacene on Au(111).[90] José I. Urgel *et al.* dehalogenated a dibromo-substituted α-diketone precursor and investigated the resulting organometallic complexes (Fig. 1.10 (c), (f)).[91] The complexes were subsequently converted into organometallic

chains of 2 to 9 heptacene units by tip-induced or thermal cleavage of the diketone groups. The aforementioned surface studies on nonacene, decacene and the organometallic heptacene complexes were performed parallel to the herein reported work.

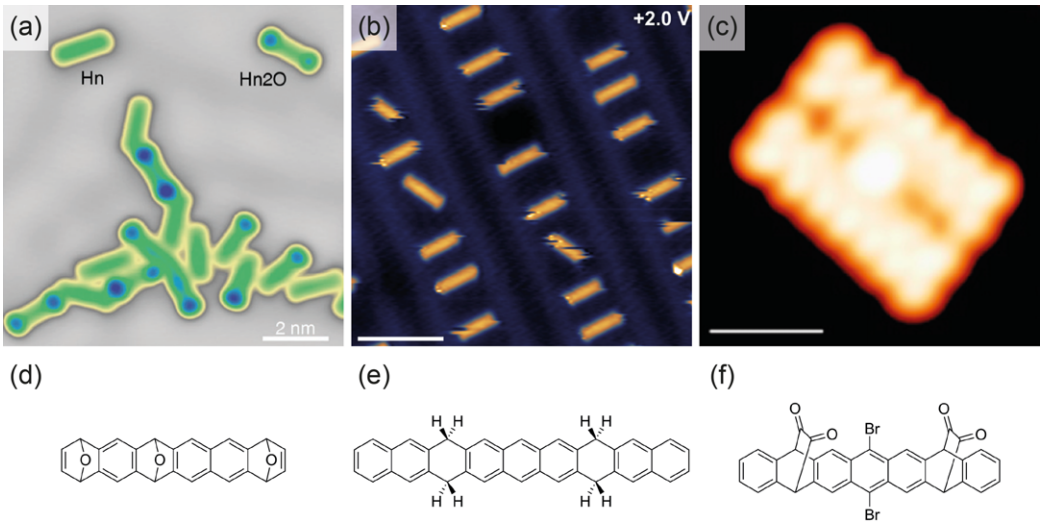

Figure 1.10: Surface studies of larger acenes. (a) Hexacene formed by deoxygenation of triepoxyhexacene[86], (b) nonacene formed by dehydrogenation of tetrahydrononacene[89], (c) heptacene-Au-heptacene organometallic complex formed by dehalogenation of a dibromo-substituted α-diketone precursor[91]. Figures (d), (e), (f) show the structural formulas of the corresponding precursors. ((a) Reproduced in part from Ref. [86] with permission of The Royal Society of Chemistry. (b) Reprinted with permission from Ref. [89]. Copyright 2017 American Chemical Society. (c) Reprinted with permission from Ref. [91]. Copyright 2017 American Chemical Society.)

Relating to the matrix stabilized synthesis of heptacene, the question arises whether a surface can act as a two-dimensional matrix and whether the formation of heptacene from an unsubstituted α-diketone precursor is possible on a surface-assisted route. The experimental work was supplemented with calculations. The results will be discussed in Chapter 6.

2 Preceding and Current Developments in Surface Science

Early work in surface science goes back to Irving Langmuir. He reported on the adsorption characteristics of gases on metal filaments as well as the surface energies of liquid films.[92] This work can be regarded as a milestone in an upcoming, new field of physics and chemistry. With the establishment of ultra-high vacuum (UHV) systems and electron spectroscopic methods in the 1960s, modern surface science began to rise.[93] This chapter will summarize preceding and recent trends in modern surface science which are relevant for the experiments in this work.

2.1 Surface Coordination Chemistry

Alfred Werner was the first to resolve the chemical binding properties in coordination compounds, for which he was awarded the Nobel Prize in 1913.[94] With this new understanding, coordination chemistry emerged from its beginnings. At almost the same time, the study of surfaces became more important as stated above. These two developments were the foundation for modern surface science. Beside investigations of adsorption characteristics and reactions of gases on surfaces[95], which was a main focus in surface science for a long time, the new field of coordination chemistry including various organic molecules on metal surfaces was studied by many means of spectroscopic and microscopic methods in the past decades.[2,96–98] While the study of chemical reactions on surfaces is fascinating for itself and of a groundbreaking importance, ideas for future applications and transfer to existing technologies are widespread. It includes heterogeneous catalysis[99], surface modifications[12], (opto-)electronic devices[6,51,100], molecular machines[101] and medical applications[29]. These application cases have in common that a certain degree of control over the electronic or magnetic properties of a organic molecule and/or a metal incorporated or involved in chemical reactions as well as over their interaction with surfaces is needed.

Relevant processes in the non-covalent interaction of molecules on surfaces are the adsorption, the mobility on the surface including 2D rotational motion and thermal migration as well as the lateral interactions. Functional groups can interact *via* van der Waals forces, hydrogen bonding, electrostatic attraction between ions or in metal-ligand interactions.[96] Involved metal atoms can originate from a dedicated deposition source or from the substrate, *i.e.*, in the form of adatoms[102], from atomic step edges on the substrate or extracted from the topmost layer of the defect-free surface. In the present work mainly the interaction between post-deposited transition metals (Fe, Co, Ni) or main group metals (Pb) and (aromatic) organic ligands will be addressed but also the single-crystalline noble metal substrates play a crucial role.

The formation of metal-organic networks, which are already known from supramolecular chemistry as metal-organic frameworks or coordination polymers, is one of the aims in surface coordination chemistry. Due to their 2D confinement, these networks are also referred to as 2D metal-organic coordination networks (2D-MOCN). For example, Sylvain Clair *et al.* observed

the formation of 2D Co-terephthalate nanostructures.[103] After deposition of Co onto Au(111), Co bilayer islands were found at the elbow sites of the herringbone reconstruction of the gold surface. Exposition to terephthalic acid leads to *in situ* dissolution of the Co clusters and 2D coordination of single Co atoms with simultaneous deprotonation of the carboxyl groups. The yield of metal-organic structures could be increased by annealing slightly above room temperature. The appearance and properties of metal-organic networks can be steered by the choice of organic building blocks. In a work by Uta Schlickum *et al.*, dicarbonitrile-polyphenyl linkers, NC–Ph_n–CN with $n = 3, 4, 5$, were assembled on Ag(111) with Co atoms in stoichiometric amounts.[104] The thereby formed Co-carbonitrile network exhibits a threefold symmetry resulting in a honeycomb lattice. The size of the cavities in this network can be adjusted by the backbone length of the molecular linkers, namely by the choice of the precursor. The symmetry of the network is not induced by the substrate as a second study shows.[105] In this case, 4,4′-biphenol was assembled with iron on Cu(100). Although the substrate has a fourfold symmetry, the resulting network is composed of threefold Fe(biphenolate)$_3$ motifs. Furthermore, the exceptional result is that this symmetry is not known for iron phenolates in 3D phases. The 2D confinement forces the coordination network in its symmetry despite the mismatch with the Cu(100) lattice. However, the mismatch leads to different hexagons within the network and a limited periodicity compared to the situation on threefold Ag(111) surfaces. Angled dicarbonitrile-polyphenyl molecules and their surface structures will be studied in this work (Ch. 5.2). Other templating effects are introduced by reactive Cu(111) surfaces in the coordination of 2HTPyP with Cu.[106] Linear and triangular structures after annealing to 393 K were reported (Fig. 2.1). The coordination motifs are formed surface-inducedly from metal-ligand interactions between pyridylic N of the porphyrin molecules and copper adatoms. Again, twofold linear Cu coordination cannot be found in 3D chemistry.

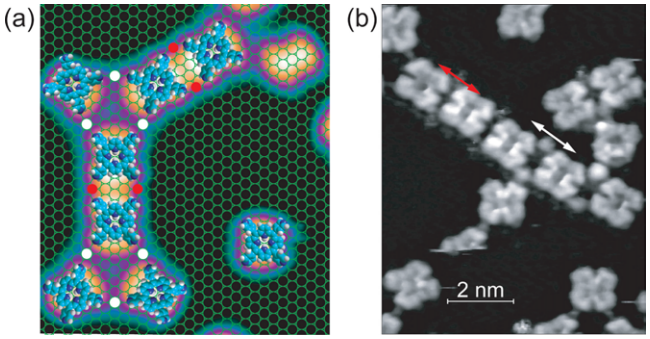

Figure 2.1: Coordination of Cu adatoms with pyridyl groups to tetrapyridylporphyrins at 393 K. (a) Model of triangular and linear coordination motifs. (b) STM image of linearly linked TPyP molecules with Cu adatoms.[106] (Reprinted from Ref. [106], with the permission of AIP Publishing.)

Beside coordination networks, the formation of metal-organic complexes, *e.g.*, the *in vacuo* metalation of tetrapyrrole molecules on surfaces, is subject to various studies with spectroscopic, microscopic and theoretical methodology.[1–3,5,107] The metalation can follow different protocols. The most common method is the physical vapor deposition of metal atoms prior or subsequent to the deposition of the tetrapyrroles. By using reactive substrates and annealing steps, the macrocycles can also be metalated in a self-metalation reaction by surface atoms. Metalloporphyrins and metallophthalocyanines can act as model systems for the interaction

of metal ions with surfaces and are therefore studied frequently. The elements introduced into the macrocycles range from light main group metals over heavy transition metals to even lanthanoides and actinoides, and also non-metals were incorporated, thus covering almost the entire periodic table. Naturally occurring metal centers are Mg and d-block metals in the fourth period from V to Zn.[108] The direct or *in situ* metalation offers a facile way to study metalloporphyrins which are not possible to synthesize in solution or are not suitable for deposition in UHV, *e.g.*, FeTPP is extremely sensitive toward oxidation.[109] Early studies were done by J. Michael Gottfried *et al.*[110] The complexation of Co with pre-deposited 2HTPP as a tetradentate molecular ligand was monitored by means of X-ray photoelectron spectroscopy (XPS) (Fig. 2.2). The research was extended with density functional theory (DFT) calculations for gas-phase reactions of porphine with Fe, Co, Ni, Cu and Zn.[111] First, the initial complex, an unreduced 2H-metalloporphyrin, is formed in the metalation reaction. The subsequent steps describe the transfer of the pyrrolic hydrogen atoms to the metal atom, where H_2 is formed and released. The metalation with Zn exhibits an activation barrier of 32.6 kcal mol^{-1}. Experimentally, this activation energy was overcome by annealing, whereby a temperature of 300 K only leads to a partial metalation and a temperature of 550 K achieved a complete reaction of a 2HTPP monolayer. Influence of the order in the deposition protocol for the direct metalation on the reaction between Ni and 2HTPP was investigated with additional respect to the activation barrier.[112]

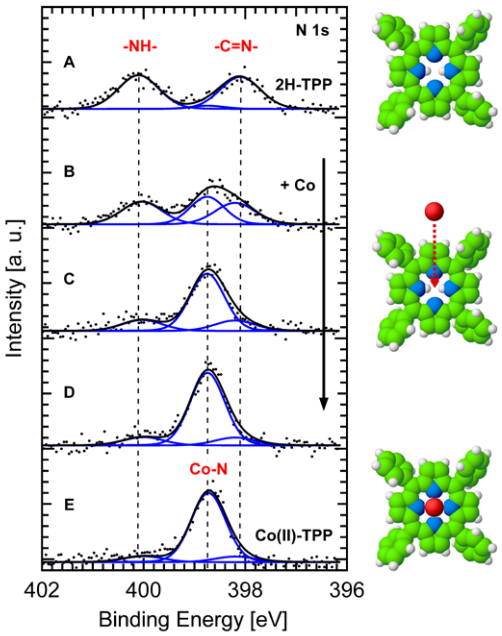

Figure 2.2: N 1s XP spectra of the direct metalation of 2HTPP with Co. (A) Pristine 2HTPP monolayer, after deposition of (B) 0.022 ML, (C) 0.036 ML, (D) 0.047 ML Co and (E) pre-synthezised CoTPP for comparison.[110] (Reprinted with permission from Ref. [110]. Copyright 2006 American Chemical Society.)

Rare-earth metals form sandwich-type complexes with porphyrins in solution due to their increased atomic diameter. However, on Ag(111), a novel CeTPP was discovered. In contrast to transition-metal-porphyrins, the metal center is not directly incorporated into the macrocycle but sits 1 Å above the porphyrin plane.[113] Electronically, the lanthanoide complex is

similar to the structure of CoTPP.[114] Certainly, also homoleptic double-decker, $Ce(TPP)_2$, and triple-decker, $Ce_2(TPP)_3$ sandwich complexes are possible on surfaces as found in solution phase, provided that a multilayer of 2HTPP is exposed to an atomic beam of Ce. In this case, a rotational motion of the upper porphyrin ligands can be induced by scanning tunneling microscopy (STM) manipulation as reported by David Écija.[115]

As stated above, adatoms play an interesting role in the interaction with organic molecules. At low temperature, $17 \pm 3\%$ of the 2HTPP molecules on Au(111) have a gold adatom underneath, which originate from step edges. In STM images a characteristic change in the electronic structures is visible and porphyrin molecules located on top of adatoms appear brighter than two observed saddle tautomers on the planar surface. The distance between one of the nitrogen atoms in the macrocycle and the gold adatom is 2.34 Å, while in the saddle state the gold-nitrogen distance is 3.7 Å. The coordination bond with the gold atom leads to an energy gain of 0.6 eV.[116] In this thesis, the reaction of a corrole with a silver surface will be studied (Ch. 4.1.1).

Additional axial ligands attached to metalloporphyrins influence the interactions between the metal ion and the surface. In investigations of nitrosyl complexes of metalloporphyrins ((NO)MTPP with M = Co, Fe) on Ag(111), a suppression of the bond to the surface was observed.[117,118] Specifically, the bond between the metal ion and the substrate is formed as a covalent two-orbital, two-electron bond between the M $3d_{z^2}$ in (NO)MTPP and the Ag 5s orbitals, whereas the Ag 5s is nonbonding in CoTPP and weakly bonding in FeTPP. The influence on the metal-surface interaction depends on the structural and kinetic lability of the ligands. In this case, the Ag(111) substrate represents the weaker ligand. Due to the similarity to the solution-chemistry concept of two competing ligands in *trans*-position of a metal ion, the concept of the surface *trans* effect was established. Another approach of controlling the electronic structure of the metal center will be introduced in Chapter 4.2.

Naturally, the metalation can also be observed for other macrocyclic compounds like the related class of the phthalocyanines. Partial metalation of a 2HPc monolayer with iron enables the observation of both metalated and unmetalated phthalocyanine species with bright protrusions in the center of the metallophthalocyanines.[119] Again, the metalation can be monitored by means of XPS resulting in N 1s XP spectra of iron(II)-phthalocyanine similar to those of the metalloporphyrins. Since no metal atoms could be detected between the macrocycles in the STM images, it was concluded that the metalation takes effect fast and that the Fe ions are preferably coordinated by the nitrogen atoms in the macrocyclic center. The degree of metalation (95%) is somewhat higher than for FeTPP (89%).[109,120] Single-molecule magnets like magnetic aluminum-phthalocyanine are potential candidates for the application in molecular spintronics, which allows the encoding of information in spin states and thus high-density information storage and quantum computing.[121,122] Since the organic macrocycle tends to form a $-$II state, metallotetrapyrroles with metal centers which prefer oxidation states different from $+$II are unstable in air. A formation of those molecules is, however, possible by direct metalation on surfaces. In a recent study by I-Po Hong *et al.*, 2HPc and Al were co-deposited on Au(111) under UHV conditions. The formed, air-unstable AlPc shows a paramagnetic behavior. The spin is distributed over the molecular plane according to DFT calculations.[123]

Another interesting application are molecular switches. STM sample voltages of $\leq -1.9\,\mathrm{V}$ allowed SnPc on Ag(111) to be irreversibly switched from a Sn-up to a Sn-down conformation. If a SnPc buffer layer is used, the top layer is decoupled from the metal surface enabling a reversible switching between the states.[38]

In this section, only coordination bonds, in coordination networks and in metal-organic complexes on surfaces, were discussed. The following pages will identify the advantages of covalent bonds in the synthesis of molecules and the formation of molecular networks on surfaces.

2.2 On-Surface Synthesis

In 1959, Richard P. Feynman gave his famous and inspirational talk "There's Plenty of Room at the Bottom" during the annual meeting of the American Physical Society at the California Institute of Technology.

> *"Ultimately, we can do chemical synthesis. A chemist comes to us and says, 'Look, I want a molecule that has the atoms arranged thus and so; make me that molecule.' The chemist does a mysterious thing when he wants to make a molecule. He sees that it has got that ring, so he mixes this and that [...] and, at the end of a difficult process, he usually does succeed in synthesizing what he wants. [...] But it is interesting that it would be, in principle, possible (I think) for a physicist to synthesize any chemical substance that the chemist writes down. Give the orders and the physicist synthesizes it. How? Put the atoms down where the chemist says, and so you make the substance."*[124]
>
> — Richard P. Feynman, 1959

Modern synthesis in surface science can be regarded as the realization of Feynman's vision. On the way to novel surface characteristics for catalytic or electronic applications, molecules and nanostructures are often fabricated *on-surface* by using physicochemist's or physicist's expertise in contrast to techniques established in solution chemistry. While on-surface synthesis uses a bottom-up approach, especially the development of silica-based semiconductors is often based on a top-down method by downsizing commonly used structures. *E.g.*, the Intel 4004 microprocessor from 1971 was using structures in the size of $10\,\mu\mathrm{m}$[125], whereas current Intel Core i processors were downsized to $14\,\mathrm{nm}$[126]. However, the downsizing approach of the silicon semiconductor industry already runs into physical limits, where even smaller devices are not accessible anymore. Against this background, modern surface science tries to fabricate nanosized structures from the bottom, which will later most likely influence industrial developments of (opto-)electronic or catalytical devices. In this context, on-surface synthesis develops methods for linkage of reactive organic building-blocks in the nanometer regime to build up larger structures and to translate reaction mechanisms known from solution phase chemistry into the world of surface science.[127–130]

The invention of the scanning tunneling microscopy in 1981 by Gerd Binnig and Heinrich Rohrer, for which they were awarded the Nobel Prize in Physics in 1986 together with

Ernst Ruska, was a requirement for this new field in surface science, since classical surface-analytical methods are not suitable in cases like reaction studies at very low coverages.[131] The later developed non-contact atomic force microscopy (nc-AFM) enabled access to high-resolution inter- and intramolecular details.[132–135]

The relatively new field of on-surface synthesis covers reactions in an unusual environment, specifically reactions of single molecules on surfaces. Therefore, the studied systems are often not compatible to solution chemistry, which induces that well-known reactions are not necessarily transferable. A very important advantage is that the UHV conditions and especially the used substrate can stabilize reaction products and also intermediates. This advantage allows studying systems which are not accessible with other reaction methods. In recent years, the Ullmann coupling was established as the most prominent reaction in surface science and it was performed in various ways.[136] Fritz Ullmann reported the coupling of aryl halides in the presence of copper already in 1904.[137] In this reaction an organocopper compound is formed, which further reacts with another aryl halide in a nucleophilic aromatic substitution to a biaryl. Saw-Wai Hla *et al.* conducted renowned real-space experiments of an on-surface Ullmann coupling in a tip-induced single molecule reaction of iodobenzene on Cu(111) in 2000 (Fig. 2.3).[138] By applying a voltage pulse with an STM tip on a single iodobenzene molecule, the carbon-iodine bond was cleaved. The reaction intermediates, phenyl radicals, were brought together by lateral manipulation and homocoupled resulting in biphenyl molecules. This experiment clearly shows the previously described advantages, since the highly reactive and under solution-phase conditions instable phenyl radicals could only be observed due to π-interactions with the Cu(111) surface and σ-interactions with copper atoms of the step edges. Preparatory work was provided by previous temperature programmed desorption (TPD) studies of X. L. Zhou and STM experiments of Paul S. Weiss *et al.*[139,140] Ming Xi and Brian E. Bent proposed the first bonding scheme for the formation of biphenyl from iodobenzene on Cu(111).[141]

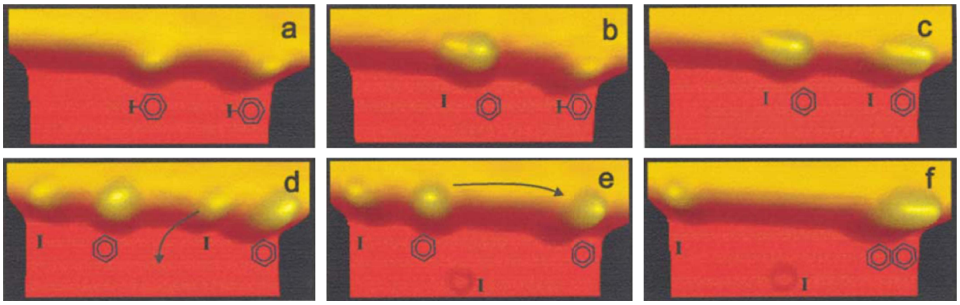

Figure 2.3: Tip-induced Ullmann homocoupling of iodobenzene on Cu(111).[138] Note that in Figure (f) the phenyl radical from the left side was moved close to the other phenyl radical by manipulation with the STM tip and that this representation should not imply the formation of a naphthalene molecule. (Reprinted with permission from Ref. [138]. Copyright 2000 by the American Physical Society.)

While the work of Saw-Wai Hla *et al.* covered single molecule reactions and is thus not suitable for a larger number of molecular units, the Ullmann coupling can also be used for polymerization and thereby for network formation. Leonhard Grill *et al.* used the thermal activation of the C–X (X = halogen) bond for a systematic covalent linkage of molecules.[142]

The building blocks in this study, brominated tetraphenylporphyrins, were assembled by either depositing the brominated molecules on a Au(111) surface with subsequent annealing or by deposition at higher evaporator temperatures with the result that the adsorbed molecules are already activated. Both methods then lead to covalently linked tetraphenylporphyrins on the surface. By using molecules with different substitution patterns of Br substituents, namely BrTPP, *trans*-Br_2TPP and Br_4TPP, the dimensionality of polymerization can be controlled achieving dimers, molecular chains or two-dimensional networks (Fig. 2.4). Another approach is hierarchical growth in the polymerization by sequential activation of the reactive sites due to different halogen substituents.[143] The prudent choice of halogenated molecules promoted the formation of even more complex nanostructures or large ordinarily instable molecules. A focus of recent studies was the synthesis of large cyclic organic molecules due to their relevance for organic electronics.[127] Brominated *meta*-linked oligophenyls like 4,4″-dibromo-*m*-terphenyl undergo intermolecular cyclizations. Therefore, large aromatic molecules in the form of honeycombs (also called honeycombene or hyperbenzene) could be synthesized on different noble metals. The yield of hyperbenzenes is highly depending on the type and crystallographic plane of the substrate, the substrate temperature and the deposition flux.[144–148] By using a Cu(110)-(2×1)O template, 2D confined syntheses were achieved.[149] Ullmann-type coupling reactions were also performed with non-aromatic compounds, alkyl halides (Wurtz reaction)[150], alkenyl halides[151] and alkynyl halides[152].

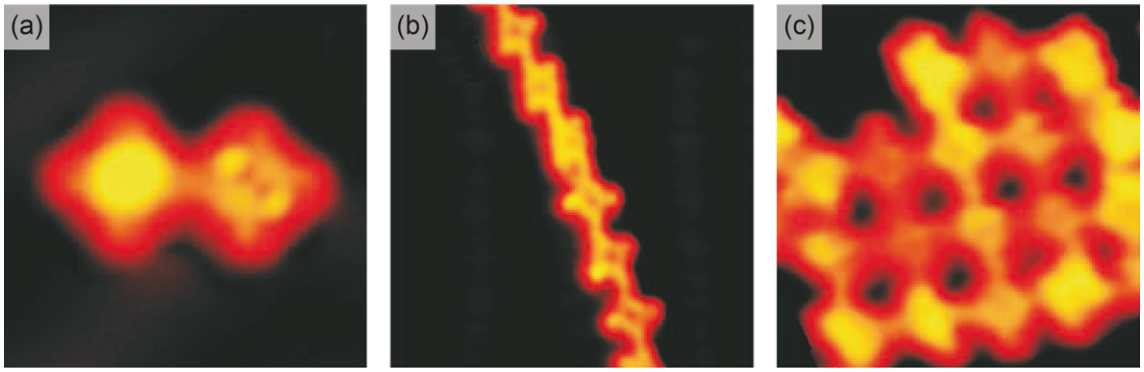

Figure 2.4: STM images of covalenty linked porphyrins in different dimensions. (a) Dimer, (b) chains (c) network on Au(111) formed from BrTPP, *trans*-Br_2TPP and Br_4TPP, respectively.[142] (Reprinted by permission from Springer Nature: Ref. [142], Copyright 2007.)

Alongside with already known reactions transferred to the surfaces, also totally new reaction mechanisms are possible. *E.g.*, Laurentiu E. Dinca *et al.* converted brominated anthrate-trathiophene on Ni(111) to a pentacene-like product by annealing to 200 °C and verified the reaction by means of STM and time-of-flight secondary ion mass spectrometry (ToF-SIMS).[153] The observation of fully hydrogenated pentacene in the *ex situ* mass spectrometry resulted from exposition to the atmosphere. The list of reaction steps, dehalogenation, ring-opening, desulfurization, partial dehydrogenation, intramolecular rebonding and intramolecular cyclization, shows the complexity of mechanisms in a 2D confinement, which would not be achieved in solution.

Other interesting examples for on-surface syntheses are the dehydrogenative C–C coupling in a Scholl reaction[90] or the Glaser coupling of aryl alkynes[154]. On-surface reactions

based on carbon types with different sp hybrid orbitals like carbenes, alkynyl, aryl and alkenyl carbons as well as alkyl halides and linear alkanes were reported.[155] Furthermore, multi-step reactions were performed, like a combined Ullmann coupling with subsequent Scholl reaction of 10,10′-dibromo-9,9′-bianthryl for the bottom-up fabrication of graphene nanoribbons.[156] Generally, the formation of graphene nanoribbons or graphene-like structures is the most famous goal in the on-surface synthesis community. Bruno Schuler *et al.* drew attention with their study of an intramolecular reversible Bergman cyclization by means of non-contact atomic force microscopy.[157] This method allowed high-resolution imaging of reactants, reaction intermediates and products. The reaction was triggered by atomic manipulation with voltage pulses. Already beforehand, the group achieved a discrimination of bond orders with a carbon monoxide functionalized AFM tip.[158] More difficult are multi-component reactions because molecules on the surface tend to form islands and are therefore less mixed with the result that the substrate has to support a sufficient mobility to bring the components together. Quite early in the development of surface reactions, imines were synthesized in a two-component condensation reaction of an aldehyde and an amine on Au(111).[159] While the metalation of tetrapyrroles was already discussed in the previous section, the synthesis of the macrocycles of metallophthalocyanines can be regarded starting from small precursor molecules. Mathieu Abel *et al.* synthesized phthalocyanine networks by deposition of 1,2,4,5-tetracyanobenzene and Fe in a ratio of 2 : 1 at RT on Ag(100).[160] The results are discussed later.

Compared to the previously described molecular self-assembly and surface coordination chemistry, the on-surface synthesis provides several significant benefits.[128] As a result of the formation of covalent bonds, the molecular networks and large molecules exhibit higher structural stability and better material properties, *e.g.*, for electron transport. The predominantly used scanning probe microsopies allow to track the reactions in real space. While solution chemistry often lacks to synthesize molecules which are too fragile or which have a low solubility, on-surface synthesis can access these molecules due to 2D confinement or surface-stabilization effects. In contrast, the non-reversibility of covalent bonds and the chemoselectivity are still a subject of recent studies.[130] While most studies are based on trial-and-error experiments, more knowledge and theoretical considerations on the relevant reaction mechanisms are needed to predict reaction products and structures.[129]

In this work, on-surface synthesis will be used to achieve large networks of porphyrins. On the other hand, this work covers molecules poorly accessible by solution chemistry and molecules which would undergo decomposition during UHV deposition. On-surface synthesis is a facile way to study these molecules. Specifically, tetrapyrroles formed from dicarbonitrile precursors (Ch. 5.1) and large instable acenes (Ch. 6) generated from diketone precursors were prepared on coinage metal substrates.

3 Experimental Methods

The studied reactive organic species in this thesis were examined using a multi-methodical experimental approach. By using different microscopic and spectroscopic techniques, the samples were subject to chemical, physical and structural characterization.

The predominant part of this work was focused on STM to visualize intermolecular coordinative and covalent structures that are formed either spontaneously or due to thermal activation, and to reveal intramolecular electronic changes due to metalation as well as dehydrogenation and decarbonylation reactions. LT-STM was performed in order to inhibit the mobility of weakly adsorbed molecules. Occupied electronic states of the core levels and the valence band were probed with XPS and ultraviolet photoelectron spectroscopy (UPS), respectively, to unveil the chemical environment. Temperature activated reactions were monitored in XPS heating series. The nature of chemical reactions can be explored by probing the corresponding orbitals. To complete the photoelectron spectroscopy (PES) measurements, information on the unoccupied molecular orbitals were gathered by means of near-edge X-ray absorption fine structure (NEXAFS) spectroscopy. Additionally, the orientation of molecules on the surfaces can be determined by this technique.

In the following sections, the theoretical background of the measurement techniques, the provided setups and the experimental details will be explained to provide insight into the experimental background for the subsequent discussion and evaluation of the projects and the results.

3.1 Scanning Tunneling Microscopy

> *"Art and science are both products of the creativity of man, and the beauty of nature is reflected in both."*[131]
>
> — Gerd Binnig and Heinrich Rohrer, 1987

Although spectroscopic and mass spectrometric methods can shed light on the nature of surfaces as well as adsorbed and desorbed species, they cannot provide information on the structures, which affect the properties of surfaces massively. Since diffraction techniques were readily available in the 20^{th} century, these methods became import tools in surface science. However, either they are not suitable to receive information on the surface only and not on the bulk phase or they are not restricted to local structures but average over the total measured area. Low-energy electron diffraction (LEED) is a commonly used tool for the determination of surface structures, but it is limited to periodic structures and does only provide geometric information.

Therefore, microscopy is needed to investigate locally constrained phenomena in real space and to reveal the content of unit cells. The resolution of light optical microscopes depends, however, on the wavelength of light and is consequently limited to $d \geq \lambda/2$ (Abbe limit). While electron microscopes use the interaction of an incident electron beam with the sample to overcome this resolution limit, scanning tunneling microscopy approaches the imaging of

subnanometer structures differently. The awarding of the NOBEL Prize in Physics to Ernst RUSKA "for his fundamental work in electron optics, and for the design of the first electron microscope" and to Gerd BINNIG and Heinrich ROHRER "for their design of the scanning tunneling microscope" in 1986 illustrates the high technical and scientific relevance of both techniques.

Belonging to the category of scanning probe techniques, scanning tunneling microscopy takes advantage of the interaction of a probe head, the STM tip, with the sample surface in a two-dimensional scan. While the images in scanning tunneling microscopy depend on the surface electron density, the later developed and also stylus-type atomic force microscopy evaluates the interaction forces between the probe and the sample.[132] The nature of the imaging process is the reason that the application area of both scanning probe techniques differs, since electrically conducting samples are needed for STM. In principle, scanning probe techniques resemble the stylus profilometry, which was already mentioned by E. J. ABBOTT and F. A. FIRESTONE in 1933 and described by J. B. P. WILLIAMSON in 1967.[161,162] The major and thus fundamental difference to the later technique is that profilometry uses mechanical contacts with the surface. On the other hand, the basic principle for STM is the quantum mechanics and especially the quantum tunneling, which was already known in 1927, when Friedrich Hermann HUND tried to calculate the ground state of the double-well potential.[163] Specifically, STM uses the tunneling of electrons through a small vacuum gap between a sharp metal tip and a conducting sample by applying a bias voltage and thus links the resulting tunneling current with the line scans. In 1972, Rusell YOUNG *et al.* presented the *Topografiner*, a field-emission microscope, which can be regarded as the predecessor of the scanning tunneling microscope.[164] Due to the high voltage and a large distance between emitter and sample (200 Å), this microscope was using field-emission currents instead of tunneling. The lateral resolution was limited to 4000 Å (30 Å vertical resolution) and it was therefore in the range of optical microscopy. However, YOUNG *et al.* already had the vision to apply metal-vacuum-metal tunneling on the examination of surfaces. Heinrich ROHRER and his colleague Gerd BINNIG at the Zürich Research Laboratory of the IBM Research Division had the idea to investigate "inhomogeneities on surfaces, especially those of thin oxide layers grown on metal surfaces" using tunneling spectroscopy, for which the foundation was laid with the NOBEL Prize in Physics awarded to Leo ESAKI and Ivar GIAEVER "for their experimental discoveries regarding tunneling phenomena in semiconductors and superconductors, respectively" in 1974.[131,165] The first successful observation of the exponential dependence of the tunneling current from the tip sample distance[166] using a primitive setup and the first STM images of atomic monosteps[167,168] were achieved in 1981. Additional publicity was gained, when Donald M. EIGLER and Erhard K. SCHWEIZER manipulated Xe atoms on a Ni(110) surface with an STM tip to form the lettering "IBM".[169,170]

What do the STM images represent? As above mentioned, a bias voltage is applied producing a small but yet measurable tunneling current. The tunneling efficiency depends on the electronic properties of the sample, in which the electronic states of surface objects are convoluted with the surface topography as it will be explained in the following. The quantum tunneling can be illustrated by an electron wave function and a barrier with an infinitely high potential V. Classical physics forbids the penetration of the barrier by electrons with

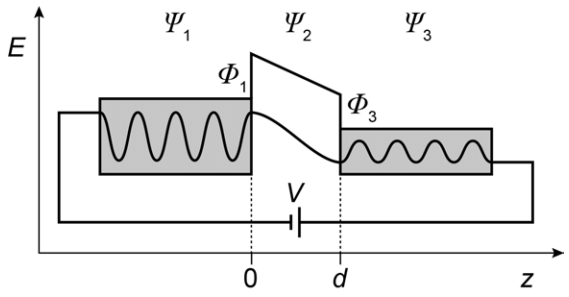

Figure 3.1: Overlapping of electron wave functions Ψ of two potential wells separated by a barrier of the distance d with applied potential difference V resulting in the one-dimensional tunneling of electrons.

$E < V$. Considering the probability distribution of the electrons, the wave function will not end abruptly but rather penetrate the potential barrier. Applied to the one-dimensional tunneling in the STM, three situations have to be regarded (Fig. 3.1): The incident electron wave before the barrier (in the tip), the barrier with thickness d (*e.g.*, the vacuum gap) and the electron wave function behind the barrier (in the sample). The HAMILTONians $\hat{H}$ of the SCHRÖDINGER equation can be written as Equations 3.1 and 3.2 for the cases outside and inside the barrier, respectively, considering the reduced PLANCK constant $\hbar$ and the electron rest mass m_e.[171,172]

$$\hat{H} = -\frac{\hbar}{2m_\mathrm{e}}\frac{\mathrm{d}^2}{\mathrm{d}z^2} \text{ for } z < 0 \text{ and } z > d \tag{3.1}$$

$$\hat{H} = -\frac{\hbar}{2m_\mathrm{e}}\frac{\mathrm{d}^2}{\mathrm{d}z^2} + V \text{ for } 0 < z < d \tag{3.2}$$

The electron wave functions Ψ can be written as given in Equations 3.3 and 3.4 for electrons outside and inside the barrier, respectively. The two pre-exponential factors before and after the barrier differ of course resulting in a second set of factors, F and G (Eq. 3.5). For Equation 3.4, two cases have to considered: Either inequation $E > V$ is valid, then electrons can overcome the barrier as allowed by the classical physics, or the energy is lower than the potential barrier ($E < V$) and quantum mechanics predicts a decent probability to meet an electron inside the barrier.

$$\Psi_1 = A\mathrm{e}^{\mathrm{i}k_1 z} + B\mathrm{e}^{-\mathrm{i}k_1 z} \text{ with } k_1 = \sqrt{\frac{2m_\mathrm{e}E}{\hbar^2}} \text{ for } z < 0 \tag{3.3}$$

$$\Psi_2 = C\mathrm{e}^{k_2 z} + D\mathrm{e}^{-k_2 z} \text{ with } k_2 = \sqrt{\frac{2m_\mathrm{e}(V-E)}{\hbar^2}} \text{ for } 0 < z < d \tag{3.4}$$

$$\Psi_3 = F\mathrm{e}^{\mathrm{i}k_1 z} + G\mathrm{e}^{-\mathrm{i}k_1 z} \text{ with } k_1 = \sqrt{\frac{2m_\mathrm{e}E}{\hbar^2}} \text{ for } d < z \tag{3.5}$$

Considering a sufficiently narrow gap between tip and sample and the application of a potential difference, electron wave functions overlap leading to the passage of electrons through the barrier, the so called tunneling. The measurable current is usually in the range of several pA to 1 nA. A simple approximation of the tunneling current is given in Equation 3.6. The

current depends exponentially on the distance d between tip and sample and the square root of the local work function Φ.

$$I \propto \mathrm{e}^{-2\kappa d} \text{ with } \kappa = \sqrt{\frac{2m_\mathrm{e}\Phi}{\hbar^2}} \tag{3.6}$$

Up to now, only a simple one-dimensional model of the STM was regarded. A real tip and sample relation, though, has to be treated three-dimensionally. Shortly after the invention of the STM, Jerry Tersoff and Donald R. Hamann suggested a "Theory of the scanning tunneling microscope".[173] A general expression for the tunneling current (Eq. 3.7) was derived taking into account the Fermi level E_F, the energy E_μ of the state Ψ_μ in absence of tunneling and the matrix element $M_{\mu,\nu}$ (Eq. 3.8) between states Ψ_μ of the probe tip and Ψ_ν of the sample. S is an arbitrary surface between tip and sample.

$$I = \frac{2\pi}{\hbar} e^2 V \sum_{\mu,\nu} |M_{\mu,\nu}|^2 \delta(E_\nu - E_\mathrm{F}) \delta(E_\mu - E_\mathrm{F}) \tag{3.7}$$

$$M_{\mu,\nu} = \frac{\hbar^2}{2m_\mathrm{e}} \int \mathrm{d}S (\Psi_\mu^* \nabla \Psi_\nu - \Psi_\nu \nabla \Psi_\mu^*) \tag{3.8}$$

Assuming a spherical tip, Equation 3.9 can be formed, in which $D_\mathrm{t}(E_\mathrm{F})$ is the density of states at the Fermi level per unit volume of the probe tip, R_t is the radius of the tip and $\vec{r}_0$ is the center of curvature of the tip.

$$I = 32\pi^3 \hbar^{-1} e^2 V \Phi_0^2 D_\mathrm{t}(E_\mathrm{F}) R_\mathrm{t}^2 \kappa^{-4} \mathrm{e}^{2\kappa R_\mathrm{t}} \sum |\Psi_\nu(\vec{r}_0)|^2 \delta(E_\nu - E_\mathrm{F}) \tag{3.9}$$

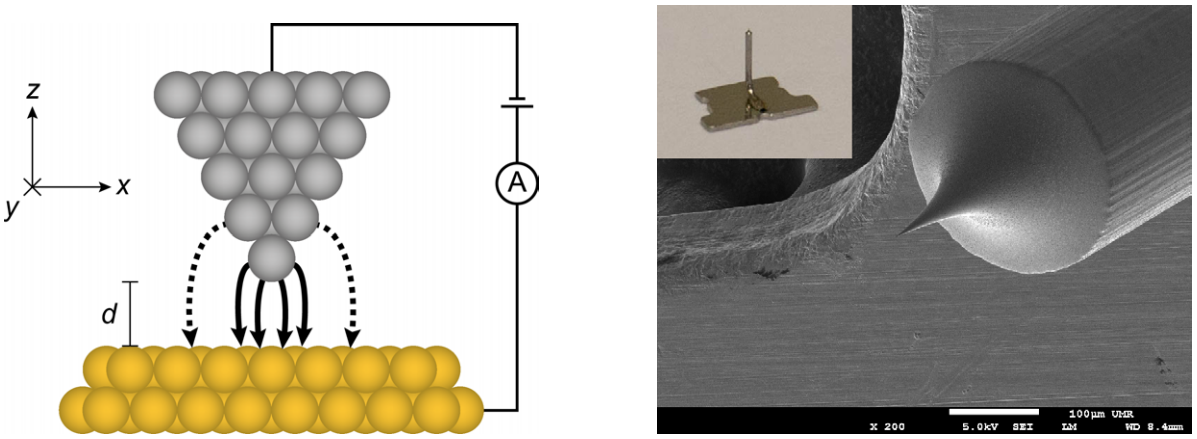

(a) (b)

Figure 3.2: (a) Sketch of the electron tunneling from an atomically sharp tip to a positively biased sample surface. The different degree of participation of the atoms at the apex of the tip in the tunneling process is represented by solid and dashed lines. (b) Scanning electron microscopy (SEM) image of an unused, etched W tip for the SPECS STM Aarhus 150. The inset shows a photograph of the tip and its holder.

These considerations point out that the STM image consists not only of a convolution of the real topography and the electronic states of the surface but also of the electronic states of the tip. Ideally, a sharp tip with a single atom on the apex is regarded (Fig. 3.2 (a)), of

which most tunneling electrons originate from the terminating atom and the contribution of the surrounding atoms is significantly smaller (exponential dependence of d). The etched W tip in Figure 3.2 (b) features an apex of approximately 30 nm (with an additional oxide layer). Although the tip will be sharpened further in its initial usage due to voltage pulsing, its geometry will have an important influence on the image resolution and quality. The tip is the main reason for artifacts in STM. A blunt tip will lead to an imaging of the tip itself by atomically sharp surface features. Furthermore, the presence of more than one apex in close proximity at the tip produces ghost images, the so-called double-tip effect. These obstacles have to be considered during the measurements and the interpretation of data. The conditioning of STM tips will be discussed later (Ch. 3.5.2).

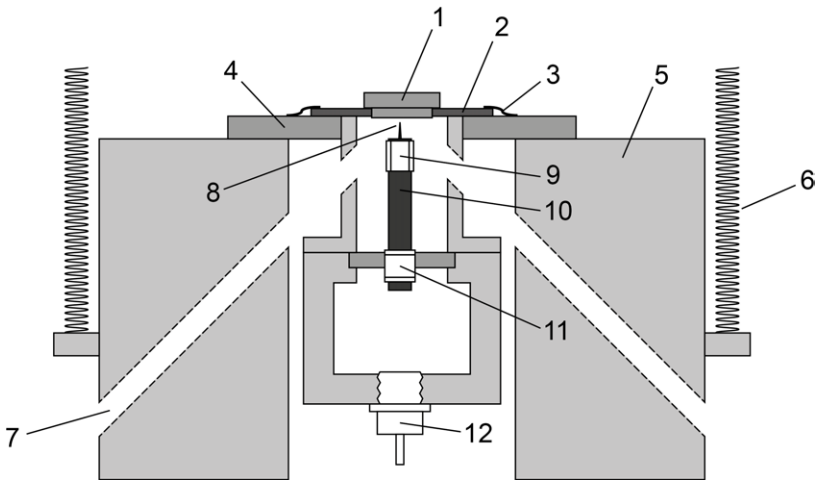

Figure 3.3: Cross-sectional sketch of the Aarhus STM design, produced by SPECS Surface Nano Analysis GmbH under license. (1) Sample, (2) sample holder, (3) sample holder clamps, (4) top stage, (5) gold coated copper block, (6) suspension springs, (7) access for *in situ* evaporation and light, (8) W tip, (9) scanner piezo tube for *x*-*y*-*z* motion, (10) approach motor rod, (11) inch-worm piezo tube, (12) Zener diode for counter-heating of the STM motor during cooling. (Adapted from Refs. [174–176].)

To reduce the vibration sensitivity during measurements and to realize atomic resolution under air, Flemmig Besenbacher, Erik Lægsgaard and Ivan Stensgaard from the Interdisciplinary Nanoscience Center at the Aarhus University, Denmark, designed a small ("thimble-sized"[177]) and robust STM in 1987 (Fig. 3.3).[178] The miniaturization of the STM increases the stability due to a rigid setup, which is insensitive to vibrations and acoustical noise.[177] In contrast to common designs, the compact approach motor of the Aarhus STM is located in a copper or – in the original design – in an aluminum block and the sample lying upside down is approached from the bottom. The linear coarse positioning is realized by an *inch-worm* motor, which is controlled fully electronically without mechanical parts. The inch-worm moves by means of a piezo tube consisting of three piezoelectric parts. Depending on the desired direction of movement, one side of piezo tube clamps the approach motor rod, while the other side is unclamped. Alternating expansion and contraction of the center part induces the movement of the approach motor. Further stabilization is gained by suspension springs and Viton dampers.

3.2 X-Ray Photoelectron Spectroscopy

Alongside the nanoscopic and microscopic structures, the chemical composition of surfaces determines their properties. Aim of this work was to study several organic molecules on surfaces in their structural arrangement but also to monitor reactions they undergo. As a surface-sensitive method, X-ray photoelectron spectroscopy provides the necessary insight into this question.

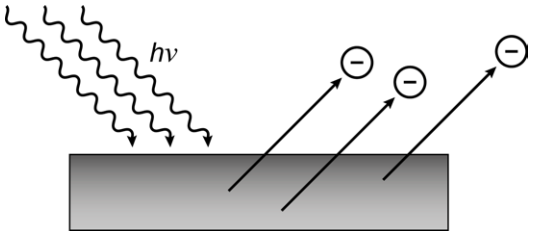

Figure 3.4: Schematic of the photoelectric effect: Photoelectrons are emitted from a material upon irradiation with short-wavelength light.

Fundamental principle for the photoelectron spectroscopy is the photoelectric effect.[179] In the 1880s, Heinrich Rudolf Hertz discovered that ultraviolet light influences the electrostatic discharge of Ni plated and brazen spheres by measuring the length of sparks.[180] His student, Wilhelm Ludwig Franz Hallwachs, reported the dependence of this effect on the electric charge of metal parts. By means of a gold-leaf electroscope, he was able to show that negatively charged zinc plates loose their charge upon irradiation with ultraviolet light, which could not be observed for positively charged plates.[181] The principle of this effect, the photoelectric effect, was later theoretically described by Albert Einstein[I].[182] In 1921, he was awarded with the Nobel Prize in Physics for the description of this effect ("for his services to Theoretical Physics, and especially for his discovery of the law of the photoelectric effect"). If a sample is irradiated with light, the photons can interact with the matter in different ways: Either the photon can pass the matter without interactions or the photon can interact with atomic orbital electrons leading to a partial or total transfer of its energy. The affected electron is emitted from the atom (*photoemission*) if the photon energy $h\nu$ exceeds the electron binding energy E_B (Fig. 3.4), which represents a threshold value characteristic for the electronic state in the material. The resulting kinetic energy E_kin of the so-called photoelectron arises from these two energy contributions as expressed in the Einstein equation (Eq. 3.10).

$$E_\mathrm{B} = h\nu - E_\mathrm{kin} \tag{3.10}$$

The kinetic energy is measured in a PES experiment and converted into the binding energy, since the photon energy is known. This approximation will be limited later. Kai Manne Börje Siegbahn, son of the Nobel Prize laureate Karl Manne Georg Siegbahn, discovered that the binding energy of core-shell electrons is dependent on the chemical environment and he developed the electron spectroscopy for chemical analysis (ESCA) – today known as XPS –

[I] Due to own interests, the author wants to emphasize that Albert Einstein liked to spend his free time on his sailing boat *Tümmler*, a *20er Jollenkreuzer*, which he received from his friends on the occasion of his 50$^{\mathrm{th}}$ birthday.

out of this knowledge. For this development, he was likewise awarded with the NOBEL Prize in Physics 1981. If an atom undergoes a chemical bonding in the form of covalent or ionic bonds, the binding energy is altered. As a result, the change in the binding energy ΔE_B is often referred to as the chemical shift. Furthermore, the binding energies of gases and adsorbed molecules of the same species differ, since the interaction with a surface leads to an additional energy contribution.

In the following, the influences on the binding energy will be discussed in more detail. Generally, the binding energy can be regarded as the energy difference between a $(n-1)$ electron final state and an initial state n of the corresponding photoion (Eq. 3.11). Therefore, the binding energy corresponds to the negative orbital energy ε as approximated in KOOPMANS'[II] theorem (Eq. 3.12) and can be calculated using HARTREE-FOCK methods.[183]

$$E_\mathrm{B} = E_\mathrm{f}(n-1) - E_\mathrm{i}(n) \tag{3.11}$$

$$E_\mathrm{B} \approx -\varepsilon \tag{3.12}$$

Neglected in this approximation is, however, that other electrons in the corresponding atom do not remain untouched. Inherent in the photoemission is the formation of a core hole which can be compensated by a rearranging of the remaining electrons, a final state effect, considered as the relaxation energy E_r. Additionally, the binding energy has to corrected for the differential correlation $\delta\varepsilon_\mathrm{corr}$ and relativistic effects $\delta\varepsilon_\mathrm{rel}$.

$$E_\mathrm{B} \approx -\varepsilon - E_\mathrm{r} - \delta\varepsilon_\mathrm{corr} - \delta\varepsilon_\mathrm{rel} \tag{3.13}$$

All changes of the ground state of an atom involved in the photoemission are initial state effects which will contribute to the chemical shift. As already mentioned, the most important influence is the chemical bonding. Increasing formal oxidation state leads to a rise in the binding energy. The same applies for electronegative functional groups. Strictly speaking, this assumption should only be used for ionic bonds, while for covalent bonds the attention should be drawn toward the charge of the atom. In contrast, final state effects arising from rearrangement of electrons (atomic relaxation in the corresponding atom and extra-atomic relaxation in adjacent atoms) lead to a decrease in the binding energy. As an example for the consequences of inital and final state effects, a discrepancy from the oxidation state ranking is known for Co and Cu, since the relaxation energies vary for the oxidation states. Furthermore, multiplet splitting was observed due to an interaction of the core hole and unpaired electrons, *e.g.*, for Co. With increasing layer thickness, another effect appears more pronounced. Since emitted electrons can interact with valence electrons resulting in their excitation, so-called shake-up satellites with a lower kinetic energy can be observed.[179]

X-ray photoelectron spectroscopy is a qualitative and semi-quantitative method. While the quantitative evaluation of XP spectra will be explained in Chapter 3.6.2, some requirements for the qualitative information should be mentioned here. Since small deviations in the binding

[II] Tjalling Charles KOOPMANS started his studies in mathematics, switched to theoretical physics and graduated with a PhD in mathematical economics.

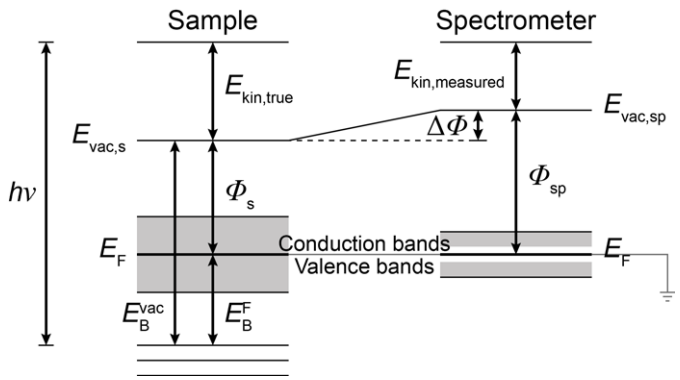

Figure 3.5: Energy level diagram of an XPS experiment with a conducting sample: The FERMI levels of the sample and the spectrometer are aligned to reference the binding energy. To determine the true kinetic energy of the photoelectrons, the work function of the spectrometer Φ_{sp} must be known, while the work function Φ_s of the sample is irrelevant.

energy can lead to different conclusions, the spectrometer has to be calibrated and referenced. The binding energy is referenced by aligning the FERMI levels of the sample and the spectrometer usually achieved by grounding both parts. In contrast to the EINSTEIN equation, the binding energy cannot directly be calculated from the photon energy and the kinetic energy of the photoelectrons as measured by the spectrometer (Fig. 3.5), since the work function, the energy difference between the FERMI level E_F and the vacuum level E_{vac} (Eq. 3.14), of the spectrometer has to be included. Therefore, the referenced binding energy results from Equation 3.15. Since the work function of the spectrometer Φ_{sp} is essential for the experiment – with conducting samples –, the spectrometer has to be calibrated using a standard sample. An easier way is to record the spectral range around E_F which is then used as reference point ($E_B = 0\,eV$). Furthermore, the work function of the sample Φ_s can be determined by measuring the full width of the spectrum between the FERMI edge and the secondary electron cutoff (Eq. 3.16).

$$\Phi = E_F - E_{vac} \tag{3.14}$$

$$E_B^F = h\nu - E_{kin,measured} - \Phi_{sp} \tag{3.15}$$

$$h\nu = (E_{kin}^{max} - E_{kin}^{min}) + \Phi_s \tag{3.16}$$

The setup of an XPS experiment includes a sample positioning system, an X-ray source, a lens system (or electron optics), an analyzer and a detector (Fig. 3.6). Usually, the X-ray source is monochromatized to select a single wavelength. Depending on the desired photon energy, the anode can be made of different materials, but also synchrotron sources are common. See Chapter 3.3 for information on synchrotron radiation. Emitted photoelectrons enter the lens system, where they are retarded. To split the electrons according to their kinetic energy, a hemispherical electrostatic analyzer or, alternatively, a time-of-flight analyzer is used. In a hemispherical analyzer, electrons with the correct pass energy E_{pass} reach the detector on a center line in the analyzer, while electrons not meeting the pass energy are diverted to

the concentric electrodes in the outer or inner hemisphere. Ordinary detectors are channel electron multipliers. Spatial resolution can be reached with 2D detectors including charge-coupled device cameras. Since X-ray radiation exhibits a relatively large penetration depth in matter, this limitation can be neglected in laboratory experiments. More important is the inelastic mean free path of the photoelectrons. The actual length depends on the energy of the photoelectrons and thus on the incident radiation, on the chemical elements in the sample and on the specific core level from which the photoelectron is excited.[184,185] With a minimum around 100 eV, the so called universal curve shows the energy dependence. By adjusting the photon energy, the origin of the majority of photoelectrons, *i.e.*, the surface- or bulk-sensitivity, can be chosen.

Although XPS can also probe the valence region close to the FERMI level, ultraviolet radiation is used as photon source to analyze valence electronic states, since the cross sections are low at the high photon energies used in XPS. UPS measurements can contribute to the interpretation of contrast mechanisms in STM experiments. As a radiation source, often He discharge lamps are used. By controlling the gas supply, either He I or He II discharge lines can be achieved. The choice of line depends on the energy region of interest and the presence of and the hindrance by radiation satellites in case of a unmonochromatized source. In the present study, He I_α at a photon energy of 21.22 eV was used.

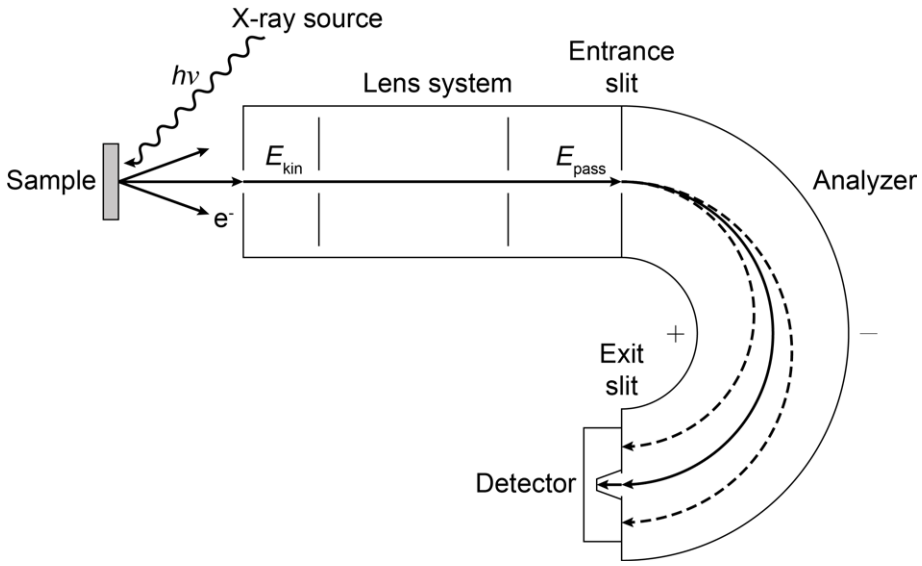

Figure 3.6: Schematic of the X-ray photoelectron spectroscopy: The incident X-ray photons interact with the sample resulting in the release of photoelectrons, which are retarded to the pass energy of the analyzer by electron optics. Electrons with the correct energy pass the hemispherical analyzer on the continuous center line until the detector, while other electrons are diverted.

3.3 Near Edge X-Ray Absorption Fine Structure

While XPS and UPS cover occupied core or valence electronic states, respectively, near-edge X-ray absorption fine structure spectroscopy can probe unoccupied levels. Aims of this method are the investigation of intra- and extramolecular interactions as well as molecular orientations. In contrast to PES, the energy of the incident photons is varied, which makes tunable syn-

chrotron light a requirement for this measurement technique. X-ray absorption spectroscopy (XAS) can be performed in different spectral regions, of which NEXAFS is limited to the region around the characteristic absorption edges of the elements in the sample material. The method was developed for the study of low Z molecules (referring to the atomic number Z) with the transition of electrons from the K-edge to unoccupied orbitals. Hence, the excitation radiation usually ranges between extreme ultraviolet radiation and *soft* X-rays (100-700 eV). Advantage over UPS is the lower influence of the background signals from metal substrates and the specific absorption in the desired elemental region. A synonym is X-ray absorption near-edge structure (XANES), though NEXAFS is more commonly used in the context of surface studies. NEXAFS spectroscopy is also the method of choice to determine the orientation of molecules on surfaces, since the excitation into the σ^* and π^* molecular orbitals with particular orientation is responsive to the incident angle of the polarized light. The analysis of NEXAFS experiments is performed in a relatively facile way, but separating the origins of the resonances is not often feasible without insight from theory and the method is not quantitative with respect to the sample stoichiometry.

The attenuation of intensity by absorption of photons is described by the Beer Lambert law (Eq. 3.17), which was originally discovered by Pierre Bouguer, attributed to Johann Heinrich Lambert and later extended by August Beer.[186,187] In this notation of the equation, the initial intensity I_0 undergoes an exponential decay considering an absorption coefficient α and the path length in the matter l.

$$I = I_0 \cdot \mathrm{e}^{-\alpha l} \tag{3.17}$$

While in XPS, core shell electrons from the sample material are excited into the vacuum level upon irradiation with X-rays exceeding the corresponding binding energy, NEXAFS uses lower photon energies to excite the electrons into the unoccupied valence band or molecular orbitals only. The empty core hole is subsequently filled by an electron from a higher level. The excess energy is either dissipated by the emission of a so called Auger electron[III] or the emission of a fluorescence photon. Auger electrons from the bulk can provoke the emission of secondary electrons in a cascading way.

As mentioned above, the sample is irradiated with X-ray photons and the energy of the photons has to be variable. With the development of synchrotron radiation facilities of the 3$^{\mathrm{rd}}$ generation, which were built for an increased brilliance of the X-ray radiation, NEXAFS instruments with a high resolution became more readily available, since the resolution of this method is not determined by the energy analyzer but by the radiation source and especially by the monochromator. Furthermore, the advantage of synchrotron radiation is a high intensity, a broad spectral range and a defined polarization.

Synchrotron radiation is emitted from relativistic particles if they experience an acceleration perpendicular to their velocity. The discovery of this radiation was described by Frank R.

[III] The physical phenomenon commonly referred to as Auger effect was first discovered and reported by Lise Meitner in 1922.[188] The attention of the scientific community, however, was only attracted, when Pierre Auger reported his independent discovery shortly after. To recognize the work of both scientists, the phenomenon should be called Meitner-Auger effect. Only for the sake of briefness and conventionality, this term is not used here.

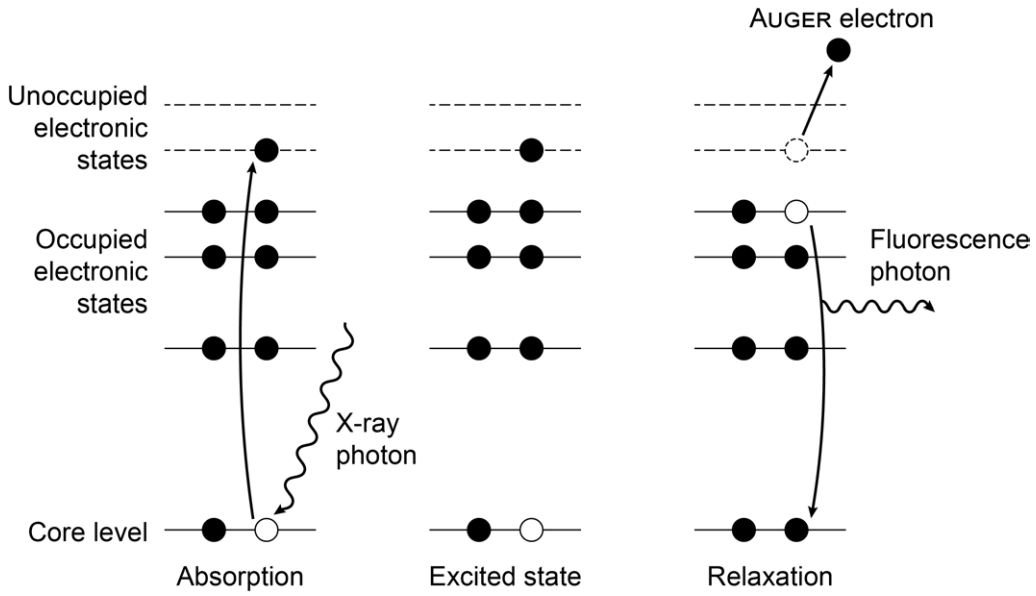

Figure 3.7: In the photoabsorption process during NEXAFS spectroscopy, a core level electron is excited into an unoccupied electronic state upon irradiation with an X-ray photon. The core hole is filled subsequently. Energy dissipation occurs radiatively or non-radiatively.

ELDER *et al.* in 1947.[189] The first usage was parasitic at accelerator facilities intended for the study of nuclear physics. In the present case, the particles are electrons which are generated by means of thermionic emission. The electrons are accelerated close to the speed of light in a cyclic synchrotron and directed into a storage ring, where they exhibit a lifetime of up to 10 h.[190] The electrons are held on a circular path using bending magnets. ELDER *et al.* discovered that the so called synchrotron light is emitted tangentially to the circular path. In synchrotron facilities, the radiation is generated at the insertion devices, which force the particles on a specific track. The choice of the insertion device depends on the purpose of operation. Simple, also referred to as 1st generation devices are dipole magnets, which ensure the circular path of the electrons and produce tangential radiation. To achieve higher intensities, new insertion devices were developed. They consist of a large number of periodically arranged dipole magnets (typically 30-100 periods), which influence the particle track to perform oscillations and thus induces the multiple emission of synchrotron radiation at each turning point. High brilliance light is usually either generated as a continuous spectrum by wigglers, insertion devices of the 2nd generation, or as a line spectrum by undulators, insertion devices of the 3rd generation. In this work, all synchrotron based measurements were performed at the HE-SGM (*high-energy spherical grating monochromator*) beamline of the BESSY II synchrotron using a dipole as insertion device. In the beamline, which directs the radiation to the experimental station, the light is monochromatized.

The X-ray absorption is detected using different approaches. The choice of the detection technique depends on the targeted scientific question. As illustrated in Figure 3.7, possible detection modes could be the measurement of fluorescence photons, AUGER electrons or secondary electrons. For low Z compounds, the fluorescence yield is, however, quite low compared to the AUGER electron yield.[191] The detection of secondary electrons can be performed in three different ways. Measuring all electrons which are emitted from the sample is referred

to as total electron yield (TEY) detection. In contrast, electrons from the bulk of the sample material with a lower kinetic energy can be suppressed by applying a retardation voltage at the opening of the detector. Since, the high surface sensitivity of NEXAFS is of relevance for many experiment, the measurement of selected electrons, namely the partial electron yield (PEY), is mostly the method of choice. While fluorescence yield and TEY cover large probe depths, PEY is used for the analysis of adsorbates and surfaces making NEXAFS an important experimental technique in surface science. Recording TEY and PEY is done in a facile way using retardation grids, a channel electron multiplier[192] and a simple collector (Fig. 3.8), while an energy analyzer is required for the detection of the AUGER electron yield (AEY). However, detection of only elastically scattered AUGER electrons is the most surface sensitive way.

The setup for a common NEXAFS experiment, furthermore, contains a Au grid to record the X-ray intensity and to calibrate the energy by determining the absorption edge of adsorbed carbon species. The sample can be moved in three spatial directions to set the spot of incidence and rotated for angle-resolved analysis.

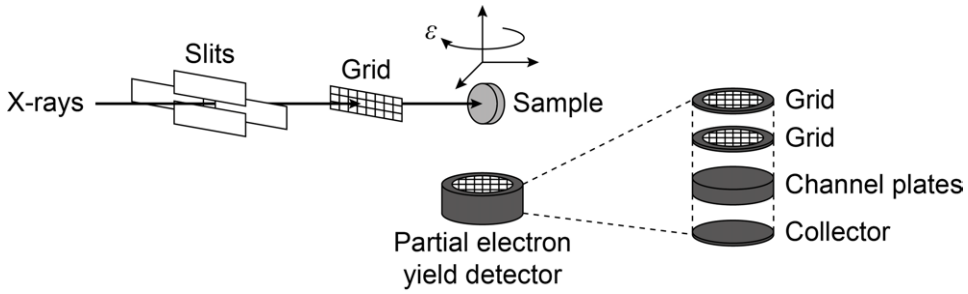

Figure 3.8: Sketch of a NEXAFS experiment with details of the detector setup.

The study of molecular orientations and the direction of chemical bonds benefits from the dependence of the absorption into different unoccupied orbitals on the linear polarization of the synchrotron radiation. Incident light is only absorbed if the direction of its electric field vector is parallel to the transition dipole moment. In the case of a simple molecule like benzene on Au(111) which adsorbs with its molecular plane parallel to the surface plane, the absorption into a π^* molecular orbital corresponds to a grazing incidence, while σ^* orbitals are addressed if the electric field vector is perpendicular to the surface normal (Fig. 3.9).[191,193] This X-ray dichroism is also called *search light effect*.

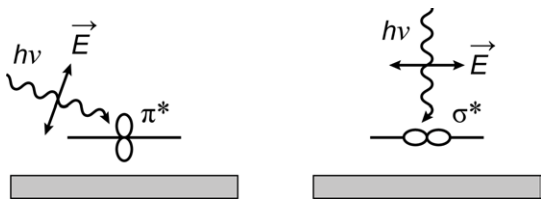

Figure 3.9: The search light effect explained in a sketch of a simple molecule like benzene which is oriented with the ring plane parallel to the Au(111) surface. The linear polarization of the incident light is used to address different unoccupied orbitals.

In this work, a quantitative angular analysis was performed. The intensity of an electronic dipole transition from an initial state to a final state can be described according to FERMI's

Golden Rule (Eq. 3.18). The transition probability, the intensity of the resonance, depends on the orientation of the electric field vector $\vec{E}$ relative to the transition dipole moment μ_{fi}, which is given by the matrix element of the dipole operator $\hat{\mu}$ and the involved initial and final state orbitals ϕ_i and ϕ_f, in the presence of the density of states $\rho(E_{fi})$.[194,195] For low Z molecules, measurements are performed by excitation from the K-edge as the initial state shell. The transition is successful, when the electric field vector of the incident light coincides with the direction of the largest amplitude of the p-component of the final state $\vec{T}$, the transition dipole. The intensity depends therefore on the angle δ between both vectors.

$$I \propto \frac{2\pi}{\hbar}|\vec{E}\cdot\mu_{fi}|^2\rho(E_{fi}) \propto \frac{2\pi}{\hbar}|\vec{E}\cdot\langle\phi_f|\hat{\mu}|\phi_i\rangle|^2\rho(E_{fi}) \propto |\vec{E}\cdot\vec{T}|^2 \propto \cos^2\delta \tag{3.18}$$

To simplify the geometric contemplation of the molecule on the surface during the analysis, two further angles are introduced (Fig. 3.10). The intensity of the π^* resonance corresponds to Equation 3.19 under consideration of the angle α between the surface normal and $\vec{T}$, the angle ε between the surface normal and $\vec{E}$, and the degree of polarization of the incident light P. The angle defined by Equation 3.20 is called magic angle and exhibits no dependence on the molecular orientation. This angle is therefore used to address both π^* and σ^* resonances in one measurement. For the HE-SGM beamline, the magic angle is 53° at a polarization degree of 0.91.

$$I_{\pi^*} \propto P\cos^2(\varepsilon)\left(\cos^2(\alpha) + \frac{1}{2P}\tan^2(\varepsilon)\sin^2(\alpha)\right) \tag{3.19}$$

$$\varepsilon = \arctan(\sqrt{2P}) \tag{3.20}$$

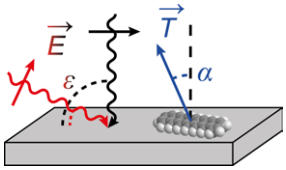

Figure 3.10: Visualization of the angles in a NEXAFS experiment to determine the orientation of molecules on a surface considering the angle of incidence. For representation reasons, the angle ε is shown as the angle between the incident light and the surface, which equals the angle between the surface normal and $\vec{E}$.

3.4 Experimental Setups

The samples in this thesis were investigated with microscopic (STM) and spectroscopic methods (XPS, UPS, NEXAFS) in three UHV systems. The predominant part of the experiments was performed in the laboratories of Prof. Dr. J. Michael Gottfried at the Philipps-Universität Marburg using a combined STM/PES setup. Wherever synchrotron radation was needed, the concerning experiments were carried out at the synchrotron radiation facility BESSY II. While the STM experiments in Marburg were performed at variable temperature (VT), an STM setup for low temperature (LT) experiments at the Christian-Albrechts-Universität zu Kiel was used in a project cooperation to study highly mobile molecules.

3.4.1 Combined Setup for Microscopy and Spectroscopy in Marburg

The combined STM/PES setup from SPECS Surface Nano Analysis GmbH is presented in Figure 3.11. The setup was installed at the beginning of the work on this thesis and it was extended with additional methods and functionalities over time. The UHV system is equipped with three chambers separated with gate valves. The chambers are dedicated to sample preparation, spectroscopic and microscopic analysis, respectively. The combination of the experimental methods in one setup allows the chemical and structural characterization of each individual sample.

The preparation chamber is evacuated by a turbomolecular pump and contains an argon ion source (SPECS IQE 11/35) for sample sputtering, the evaporators for organic molecules and metals depending on the running experiments and a quartz-crystal microbalance (QCM). The elongated chamber (analysis chamber) in the center of the system is used for photoelectron spectroscopy (PES). Two photon sources can be used to irradiate the sample either with X-ray or with UV photons. The X-ray source (SPECS XR 50 M) contains two anodes for Al K_α[196] and Ag L_α[197] radiation and is monochromatized with quartz crystals arranged in a Rowland circle (SPECS FOCUS 500) allowing the selection of both X-ray lines, while the UV source, a He gas discharge lamp, (SPECS UVS 10/35) is unmonochromatized. The sample is situated on a 3-axis rotational manipulator, which can be cooled with liquid nitrogen or liquid helium – the latter cryogenic refrigerant was not used for the experiments presented here. The sample itself can also be heated with an e-beam heating filament on this manipulator. Photoelectrons are focused in an electronic lens system orthogonal to the longitudinal axis of the chamber, separated in a hemispherical analyzer (SPECS PHOIBOS 150) and finally detected with a SPECS MCD-9 multi channeltron detector with nine channels. A three-grid LEED optics device (SPECS ErLEED 1000-A) allows the structural investigation of samples in reciprocal space. Reaction products and residual gas can be detected with a quadrupole mass spectrometer (Hiden HALO 201-RC).

The analysis chamber and the STM chamber are evacuated with turbomolecular pumps (base pressure $2 \cdot 10^{-10}$ mbar). To remove residual gas by chemisorption and ion implantation and thus lowering the base pressure to the 10^{-11} mbar regime, additionally an ion getter pump and two titanium sublimation pumps can be used. The pressures in all chambers are measured with hot-cathode ionization gauges. The substrates are mounted on transferable SPECS sample holders with a type-K thermocouple directly attached to the crystal.

The STM chamber is equipped with a SPECS STM Aarhus 150 instrument (Fig. 3.12). The SPECS STM Aarhus 150 is a VT-STM which allows to perform measurements in a temperature range of 90 to 400 K. To perform STM measurements at low temperatures, gaseous nitrogen (inlet pressure 0.5-1.5 bar) is liquefied in a cooling coil, which then flows through a cooling piston pressed against the backside of the STM metal block. Two Zener diodes allow controlling the temperature of the metal block, which is in contact with the sample. Most of the VT-STM measurements were conducted either at room temperature (RT, 300 K) or at an equilibrium temperature of 150 K, which allows a stable, low temperature over a long time using liquid nitrogen cooling and counter heating. A third Zener diode is used to keep the z-approach motor close to room temperature to ensure a proper functioning

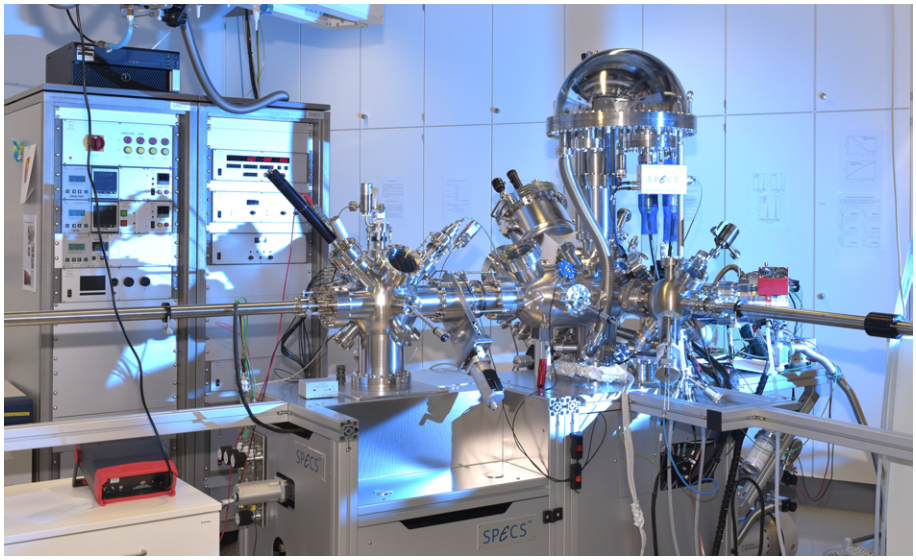

Figure 3.11: The SPECS STM/XPS setup in Marburg contains an STM chamber with a sample storage and Ar ion sources (left), an analysis chamber with a monochromator and a hemispherical analyzer for photoelectron spectroscopy (center) and a small preparation chamber (right).

during low-temperature measurements. Additionally, the STM chamber contains a sample storage with e-beam heater and two argon ion sources for sputtering of the sample or the tip in tip-sharpening procedures.

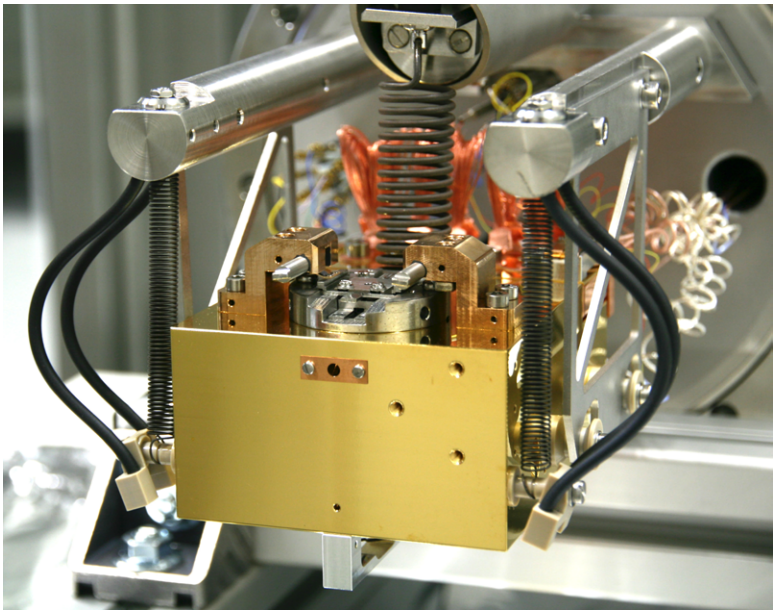

Figure 3.12: The SPECS STM Aarhus 150 is mounted on a CF 150 flange and is suspended with springs and damped with Viton bands. The sample stage and STM motor are inserted into a gold coated copper block.

Recently, the original preparation chamber was exchanged with a larger chamber including new features. Since only two final experiments were conducted with a preparation in this new chamber, the details will only be described shortly here. The new preparation chamber facilitates the sample preparation due to an increased number of ports which allows to mount more evaporators at the same time and thus increases the number of parallel running projects.

In comparison to the former chamber, an elaborate sample manipulator instead of a simple transfer rod extends the possibilities of control over the conditions during the preparation, *e.g.*, samples can be heated or cooled. Substrates can now be annealed directly in the preparation chamber during the cleaning procedures. The chamber is also equipped with a sample storage. Furthermore, two ports are pumped differentially to use chemical compounds which are sensitive to the temperatures reached during bake-out or which are mounted only temporarily.

3.4.2 Synchrotron-Based Setup in Berlin

To analyze unoccupied valence orbitals of the molecules and to determine their orientation on the surface with polarized light, NEXAFS measurements were performed. A fundamental requirement for this method is that the energy of the incident X-ray beam has to be varied continuously. Therefore, synchrotron radiation sources are used. To cover also occupied core levels in the same experiments in order to perform routine controls of the chemical environment and thus to monitor reactions, the measurement setup should also allow XPS. The endstation of the beamline HE-SGM (Fig. 3.13) at the synchrotron radiation facility BESSY II of the Helmholtz-Zentrum Berlin für Materialien und Energie fulfills these requirements.

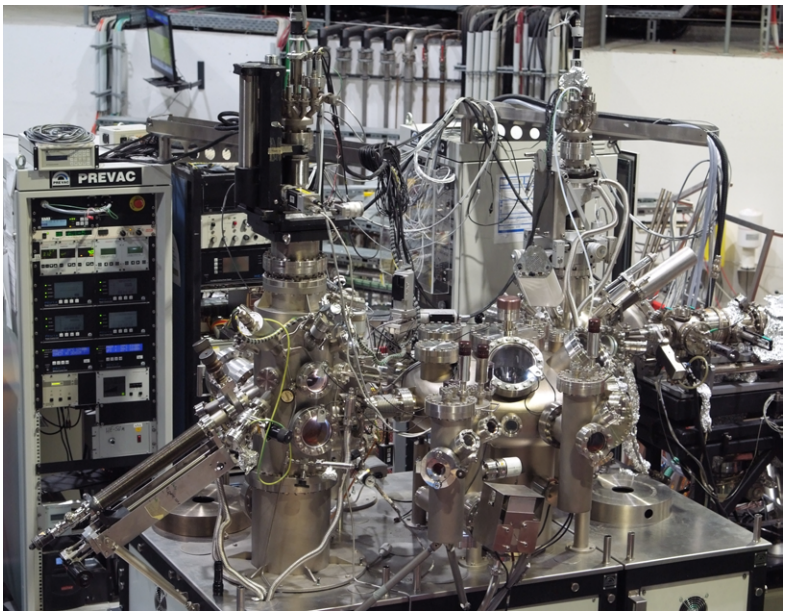

Figure 3.13: The endstation of the beamline HE-SGM at the synchrotron radiation facility BESSY II is used for NEXAFS and XPS experiments. The setup contains a preparation chamber (left), a transfer chamber with load lock and samples storages (center) and the analysis chamber (right). On the right side of the image, the connection to the beamline can be seen.

The PREVAC UHV system of this endstation mainly consists of three chambers, a preparation chamber, a spheroid-shaped transfer chamber and an analysis chamber, which is connected to the synchrotron beamline. The preparation chamber contains a manipulator including temperature control of the substrate during deposition or for annealing, an Ar^+ ion source for sample sputtering and the desired deposition sources at differentially pumped ports. The transfer chamber is equipped with a load lock and two sample storages. The measurements were carried out with a VG Scienta R3000 analyzer for XPS and a channel plate detector

for NEXAFS spectroscopy. The channel plate detector was operated in PEY mode with a retarding field of −150 V and a detector voltage of 2.2 keV. The HE-SGM beamline is a dipole beamline which exhibits an energy resolution of 300 meV at the carbon K-edge and provides linearly polarized radiation with a polarization degree of $P = 0.91$. The incident energy is selected with a temperature-stabilized single-crystal monochromator. The substrates are mounted on PREVAC sample holders which include e-beam or infrared heating sources and type-K thermocouples.

3.4.3 Low-Temperature Setup in Kiel

The LT-STM studies of the on-surface synthesis of heptacene (Ch. 6) were performed in cooperation with Dr. Manuel Gruber in the group of Prof. Dr. Richard Berndt at the Christian-Albrechts-Universität zu Kiel.

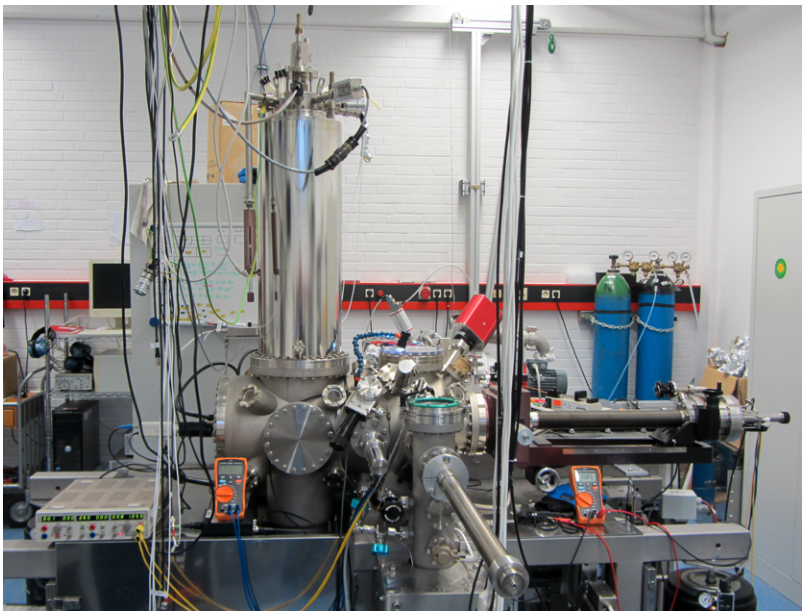

Figure 3.14: The low-temperature STM setup in Kiel is equipped with an STM chamber (left) containing the 4 K STM with a liquid helium cryostat (top), a preparation chamber (center) with sample manipulator (right) and a load lock (front).

The barrel-shaped main chamber of the CreaTec LT-STM setup (Fig. 3.14) is subdivided into two parts, a preparation chamber and an STM chamber with an integrated gate valve. The preparation chamber contains a sputter gun and two sample manipulators with a CreaTec transfer system. The base pressure is about $3 \cdot 10^{-10}$ mbar in the preparation chamber and $5 \cdot 10^{-11}$ mbar in the STM chamber. Additionally, the UHV system is equipped with a chamber for electrospray ionization (ESI) deposition of fragile molecules, which was not used in this work. Samples can be introduced into the UHV system via a small load lock. The temperature of the substrate is measured with a type-K thermocouple. The evaporator for organic molecules, a tantalum crucible, is also mounted on a CreaTec sample holder.

The low-temperature STM manufactured by CreaTec is operated at 4 K using a liquid helium cryostat with an outer liquid nitrogen reservoir. The STM itself is housed in a radiation shield to avoid heating due to IR radiation. The STM is controlled by a Nanonis SPM controller from

SPECS Zurich, which also allows the usage of an nc-AFM tip. Furthermore, the LT-conditions and the instrumental equipment allow scanning tunneling spectroscopy (STS).

3.5 Experimental Procedures

In the following section, the experimental procedures including their fundamental principles and the corresponding conditions will be described for the preparation of the substrates and the deposition of organic molecules and metals onto the surfaces. Furthermore, the sharpening of the STM tips will be regarded in relation to achieving high-resolution images.

3.5.1 Sample Preparation

The term *sample* refers to an individual object of investigation in the realized experiments. A sample is composed of a monocrystalline metal substrate and an adsorbed (sub-)monolayer or multilayer of organic compounds. The substrate has to be prepared with respect to cleanliness and surface quality, *e.g.*, concerning sufficiently low roughness and high area of interest, before the preparation of the organic layer. The sample molecules are then thermally deposited onto the substrate.

Substrates

Mono- and multilayers of the different organic substances were prepared on single crystalline noble metal substrates of the periodic table group 11, namely Cu, Ag, Au. The choice of the material was based on the desired interaction with the organic molecules. All three metals crystallize in an fcc crystal structure. The crystal plane determined by the MILLER indices (111) shows a densely packed plane of metal atoms in a hexagonal arrangement and thus a sixfold symmetry (Fig. 3.15). Due to the high density of surface atoms and their arrangement, the (111) surface plane is atomically flat and features a high number of adsorption sites for the molecules. Furthermore, the preparation and also the preservation of this surface is relatively simple. The interaction of surface and deposited molecules depends on the number of defects on a surface, the step edges as well as the crystal plane. In contrast to the (111) plane, other surface planes, *e.g.*, the (110) plane with a lower coordination of the surface atoms and thus a more open structure features an increased reactivity. However, the reactivity in the group of used metals decreases significantly. While Cu is a more reactive metal, Ag is less reactive and Au is almost entirely inert. The situations of the corresponding surfaces are similar but yet slightly different due to the distinct influence of overlapping orbitals on thin molecular films. Therefore, Au(111) was used as an inert surface, Ag(111) as a medium-reactive surface and the purpose of Cu(111) was a high interaction with the molecules. This reactivity can be reflected in the bonding distance, the distortion of molecules and the appearance of new hybrid orbitals of former molecular and substrate electronic states but also in the mobility of the molecules on the surface.[1,198] The specialty of the Au(111) surface is its characteristic $(22\times\sqrt{3})$ reconstruction, also referred to as *herringbone reconstruction*. In the top layer of the (111) terminated Au single crystal, the interatomic distances are contracted and therefore result in both fcc and hcp sites (Fig. 3.16).[199–201] Due to the surface reconstruction,

location dependent reactivities and preferred adsorption places can arise.[103,202] The other two substrates do not suffer from reconstruction effects. The Cu(111), Ag(111) and Au(111) single crystals were commercially acquired from MaTecK. The crystals were grown using the Czochralski process, cut under control with X-ray diffraction techniques and polished to decrease the surface roughness. They exhibit a purity of 99.999 % (Cu(111): 99.9999 %), a roughness of < 0.01 µm (Cu(111): < 0.03 µm) and an orientation accuracy of $< 0.1°$.

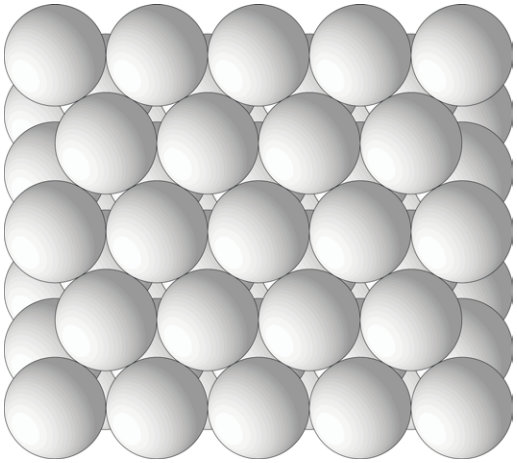

Figure 3.15: The (111)-surface of a face-centered cubic Bravais lattice exhibits a perfectly flat crystal plane. The figure was produced with the help of the Surface Explorer (Version 2) based on BALSAC (Copyright Klaus Hermann, Fritz-Haber-Institut, Berlin (Germany), 1991-2010).[203]

The described perfectly flat surface is the ideal case and some effort is needed to achieve large flat terraces, which are required in order to study large coordination networks and to reduce the risk of STM tip crashes. Surface irregularities can appear as step edges, islands, screw dislocations or surface defects in the form of adatoms or vacancies. The generation of atomically flat terraces is therefore a substantial part in the process of substrate cleaning for STM measurements. Initially, residual molecules and atoms are removed from the surfaces by Ar^+ ion bombardment. The ions are formed in an ion source, also known as sputter gun, by collision of electrons emitted from a filament with neutral Ar atoms. The Ar^+ ions are accelerated onto the sample surface. Contaminations are removed from the surface by collision with these ions. In the used setups, the substrate surface was brought into an orthogonal position with respect to the ion beam. Depending on the lattice plane terminating the substrate, also other geometries could be needed. Furthermore, the sputtering process introduces additional roughness.[204,205] These often crater-shaped irregularities have to be healed in the next step. High-temperature annealing decreases the surface roughness due to a diffusion of surface atoms. However, the annealing can lead to a recontamination of the surface due to diffusion of contaminants from the bulk phase to the surface. In addition, strongly cross-linked organic residues cannot always be removed in the initial sputtering process. Iterated cycles of Ar^+ ion sputtering and annealing are used to clean the substrates. Practically, the substrates were prepared by Ar^+ ion sputtering at an ion energy of 0.5 to 1 keV resulting in a sample current of approximately 10 to 15 µA for 30 min with a subsequent annealing at 800 to 850 K for 30 min.

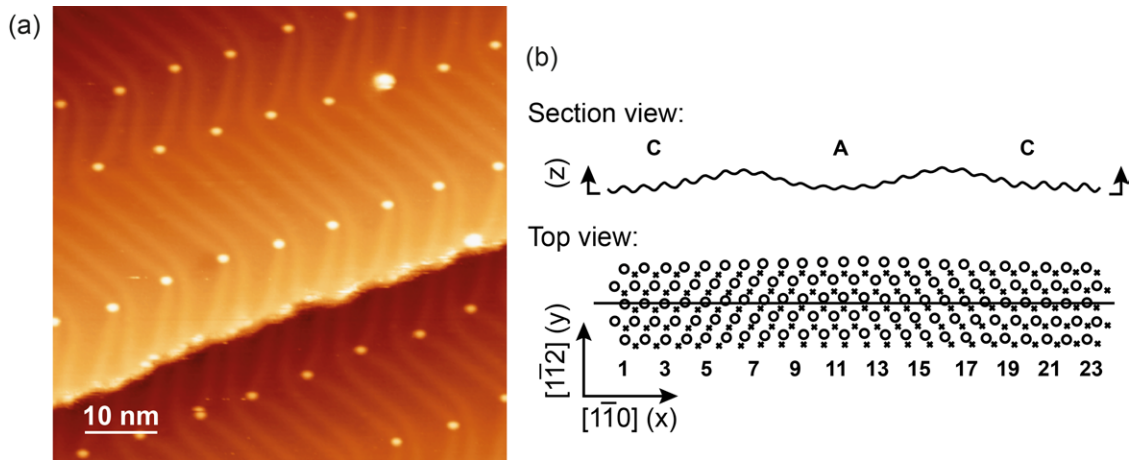

Figure 3.16: Due to a contraction in the top layer of Au(111), the surface is $(22\times\sqrt{3})$-reconstructed. (a) STM image of the Au(111)-$(22\times\sqrt{3})$ herringbone reconstruction. The variation in surface reactivity is depicted in the preferred adsorption of residual molecules at the ellbows of the herringbone pattern. Tunneling parameters: $-1.40\,\mathrm{V}$, $-0.27\,\mathrm{nA}$. (b) Model of the herringbone reconstruction. The circles represent the contracted first layer, while the crosses represent the second layer. The letters C and A refer to the layers in the ABC (fcc) and ABA (hcp) stacking scheme. The section view is represented by a hard-wall corrugation function. ((b) Reprinted with permission from Refs. [199, 206]. Copyright 1989, 1985 by the American Physical Society.)

Evaporation of Organic Molecules

The transfer of organic molecules, which are often fragile with respect to high temperatures, onto the substrate surface is the most critical step in the preparation of the samples. This step was achieved by physical vapor deposition in the UHV system. The deposition source is a home-built Knudsen cell evaporator. This cell named after the Danish physicist Martin Hans Christian Knudsen[IV] allows effusive evaporation. Inside the Knudsen cell, the solid and vapor phases are in an equilibrium state.[207–209] If the following three requirements for this kind of evaporation cells are fulfilled, the velocity distribution of the molecular beam matches the Maxwell-Boltzmann distribution and the effusion rate $\dot{m}$ can be defined as given in Equation 3.21. The cell should be heated isothermally, which is approximately given due to the small size of the evaporator. The mass loss into the vacuum has to be replaced instantly, which is given due to the large surface area of the substance to be evaporated. Furthermore, a random effusion is given due to the large mean free path of the gas molecules compared to the orifice.[210] The effusion rate depends on the vapor pressure p of the material within the cell, the gas constant R, the temperature T of the cell, the average velocity $\langle v\rangle$ of the particles, and the area A_O of the cell orifice. The velocity is determined by the Boltzmann constant k, the temperature, and the molar mass M of the material.

$$\dot{m} = \frac{1}{4}\frac{p}{RT}\langle v\rangle A_\mathrm{O} = \frac{1}{4}\frac{p}{RT}\sqrt{\frac{8kT}{\pi M}}A_\mathrm{O} \tag{3.21}$$

In this work, the evaporator consisted of a stainless steel crucible with a drill hole of 3-4 mm. The crucible is heated resistively *via* two electrical connections to the crucible material.

[IV] The Knudsen number Kn is defined as the ratio of the molecular mean free path of the gas particles to the characteristic length of the flow field, and estimates whether the fluid dynamics are in the range of viscous or molecular flow. Interestingly, Martin Knudsen was also known for his physical oceanography.

Once the desired temperature for the sublimation of the substance is reached, the evaporator behaved stable and was only adjusted by slightly varying the heating current. The molecular flow was determined by a QCM. Mostly, the flux was set in such a magnitude that a monolayer of the particular substance could be produced in a few minutes. This allows a fast preparation and it still sustains the possibility of depositing submonolayers in a controlled way. For the sample preparation in Kiel, a similar, also home-built design was used. In this case, a small Ta crucible was mounted on a transferable holder. Prior to deposition, the substances were degassed by heating the evaporator to the later used evaporation temperature for about 2 h.

The reactive coupling of tetraphenylporphyrins following the Ullmann mechanism (Ch. 4.4) was studied on a molecule with brominated phenyl substituents, nickel(II)-5,10,15,20-tetrakis(4-bromophenyl)porphyrin (NiTBrPP), which was commercially available from TriPorTech. The surface structures of corrole molecules (Ch. 4.1) and their metalation reactions (Ch. 4.2) were examined on 2,3,8,12,17,18-hexaethyl-7,13-dimethylcorrole (3H-HEDMC). The substance was provided by Prof. Dr. Martin Bröring from the Technische Universität Braunschweig. As reference molecules, 2,3,7,8,12,13,17,18-octaethylporphyrin (2HOEP) from Tokyo Chemical Industry (purity > 93 %), cobalt(II)-2,3,7,8,12,13,17,18-octaethylporphyrin (CoOEP) from PorphyChem and nickel(II)-2,3,7,8,12,13,17,18-octaethylporphyrin (NiOEP) from Porphyrin Systems (purity 98 %), were used. The metalation of porphyrins with a large ionic radius metal was studied on 5,10,15,20-tetraphenylporphyrin (2HTPP) (Ch. 4.3), which was purchased from Sigma-Aldrich (purity ≥ 99 %). Precursor for the formation of naphthalocyanine tetramers (Ch. 5.1) was 1′,1′,4′,4′-tetramethyl-1′,2′,3′,4′-tetrahydroanthracene-6,7-dicarbonitrile (NDN*). This compound was part of the PhD thesis of Dr. Martin B. Liebold[35] in the group of Prof. Dr. Jörg Sundermeyer (Philipps-Universität Marburg). The *meta*-linked dicarbonitriles, 1,1′:3′,1″-terphenyl-4,4″-dicarbonitrile (*m*-3PDN) and 1,1′:3′,1″:4″,1‴-quaterphenyl-4,4‴-dicarbonitrile (*m*-4PDN), of which the self-assembly was observed (Ch. 5.2), were synthesized by Dr. Julian R. Kuttner in his PhD work[211] under supervision of Prof. Dr. Gerhard Hilt (Philipps-Universität Marburg, now Carl von Ossietzky Universität Oldenburg). The α-diketone 7,16-dihydro-7,16-ethanoheptacene-19,20-dione (DEH) was already studied in the group of Prof. Dr. Holger Bettinger at the Eberhard Karls Universität Tübingen for a long time and was prepared for the herein presented experiments by Dr. Ralf Einholz (Ch. 6).

The evaporation conditions for the deposition of organic molecules are summarized in Table 3.1. The fluxes were measured with a QCM. A detailed reference to the relevant preparation conditions, the coverages and the temperatures for triggering the reactions is given in the discussion of each individual experimental project.

The coverages Θ are usually given in monolayers (ML_{ads}), which stands for a complete first layer of the corresponding adsorbate uniformly covering the substrate (adsorbate referenced). The term monolayer stands specifically for this layer. The definition of the unit, however, differs from the classical definition of ML as the number of objects (atoms or molecules) per surface atom (substrate referenced), which will be referred to as ML_{substr} in this work to avoid confusions. The units were selected in such a way that they are appropriate for the relevant discussion and that they enhance the understanding.

Table 3.1: Evaporation parameters for the studied organic substances.

Organic substance	Flux ($nm\,min^{-1}$)	Evaporation temperature[a] (K)	Substrate temperature (K)	Substrates
NiTBrPP	0.03 – 0.5	590 – 680	RT	Cu(111)
3H-HEDMC	0.08 – 0.4	465 – 475	100 – 180, RT	Ag(111)
2HOEP	0.07 – 0.28	520 – 545	RT	Ag(111)
CoOEP	0.08	545	RT	Ag(111)
NiOEP	0.05	475	RT	Ag(111)
2HTPP	0.12	580	RT	Au(111)
NDN* [b]	0.13 – 0.3	380 – 390	RT	Cu(111), Ag(111)
m-3PDN	1	420	RT	Ag(111)
m-4PDN	0.1	415	RT	Ag(111)
DEH	0.08 – 0.13	530 – 570	RT	Ag(111), Cu(111)

[a] Note that the evaporation temperatures which are measured at the crucible are given as averaged values. The temperature for a required flux can vary slightly due to different filling levels of the evaporator, thermal contact of the powder or recrystallization of the substance.

[b] Due to the low evaporation temperature of NDN*, the chamber could not be baked out but was pumped down over night before degassing the substance.

Evaporation of Metals

The evaporation of metals requires higher temperatures than for the previously mentioned organic compounds due to the low vapor pressures of the metal evaporants. Therefore, an electron beam evaporator was utilized (Fig. 3.17). The evaporation source can either be a metal rod, as it was in this work, or a crucible containing the evaporant. The heating of the source results from electron impacts. The electrons are emitted from a thoriated W filament and are targeted on the evaporant, on which a high potential, usually 990 V, is applied. In front of the evaporation source, which consists of the evaporant and the heating filament inside a copper cooling body, a flux monitor is placed. The *flux* correlates with the current of metal ions leaving the evaporator and is therefore given in nA. To avoid the formation of metal clusters, the lowest possible yet stable flux was chosen, which was 1.0-1.1 nA. The current is proportional to the ion flux. For the synchrotron-based measurements, a higher flux (3-4 nA) was required, since the distance of the metal evaporator to the substrate was distinctly larger.

For the deposition of lead, a different approach was developed. Pb exhibits a comparably low ductility and is therefore easily malleable even by hand. Due to this property, the evaporation from a rod source in the e-beam evaporator was not applicable. A Mo crucible could have been mounted inside this evaporator alternatively. However, since a temperature of only 580 K for a vapor pressure of approximately 10^{-9} mbar is needed, Pb can readily be evaporated from a KNUDSEN cell.[213] In this case, the KNUDSEN cell was built from a BN crucible, around which a Ta heating wire was wound (Fig. 3.18). To isolate and stabilize the wire, which additionally holds the crucible, the wire was led through ceramic tubes. A type-K thermocouple was attached to the bottom of the crucible with ceramic glue. Spilling of molten Pb was avoided with a Ta orifice.

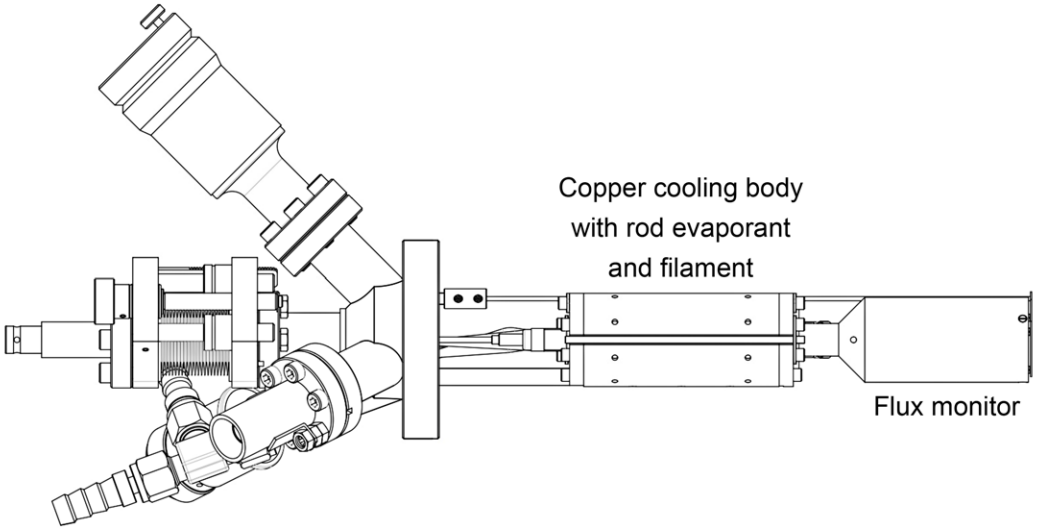

Figure 3.17: Post-deposition of Fe, Co and Ni was carried out with the electron beam evaporator FOCUS EFM 4 using 2 mm thick rod evaporants.[212] (Adapted from Ref. [212].)

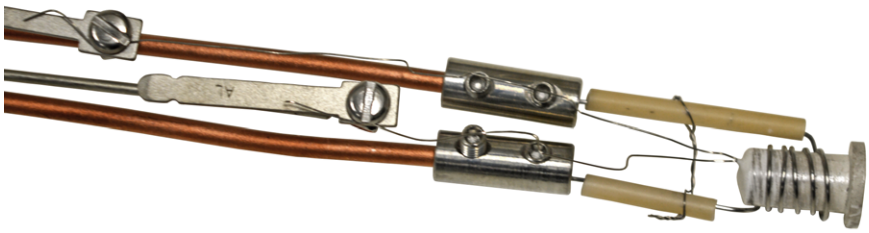

Figure 3.18: KNUDSEN cell evaporator for the deposition of Pb. The Ta wires, which serve as heating wires and simultaneously hold the BN crucible, are stabilized and isolated with ceramic tubes. The additional Ta shield at the orifice of the crucible is not shown in this photograph.

3.5.2 Tip Conditioning

As stated in Chapter 3.1, an atomically sharp tip is essential for high-resolution STM imaging. In contrast to the ideal case of a tip apex terminated with a single atom, real tips are often slightly blunt and have to be sharpened. To restore and maintain sharp tips, there is a large number of recipes depending on the tip material, the STM type and the imaging application. Common recipes include high-temperature annealing, treatment with hydrofluoric acid or ion bombardment. The STM tips are usually made from W or Pt/Ir wires, which are either electrochemically etched or pinched off. In the present case, the W tips were received as ready-for-use from SPECS. The tips were produced by etching.

Although the tips should be in a perfect state, some effort was necessary to maintain the tips sharp. After introducing the tips into the UHV, the oxide layer as visible in Figure 3.19, which builds up during the storage in air, had to be removed. The SPECS STM setup allows to sputter the tip installed on the STM motor. Before initial usage, the tips were sputtered with Ar^+ ions at 1.0-3.0 keV resulting in a sputtering current of 0.5-2.0 µA for 10-30 min. During the work for this thesis, various recipes were tried including applying counter potentials to

increase the electric field at the tip apex and thus deflect the ions from the sharpest part. However, the application of a counter potential was not sufficiently effective. It turned out that gentle sputtering at an ion energy of approximately 1.0 keV is enough to remove the oxide layer. Too high energies would lead to decapitation of the tip.[214] Further sharpening can be achieved by voltage pulses up to 8-10 V.

For the LT-STM, the W tips were likewise produced by electrochemical etching of a wire. The tips were further prepared by flash annealing in UHV. Conditioning of the tips was carried out by voltage pulsing and intentional indentations into the substrate.

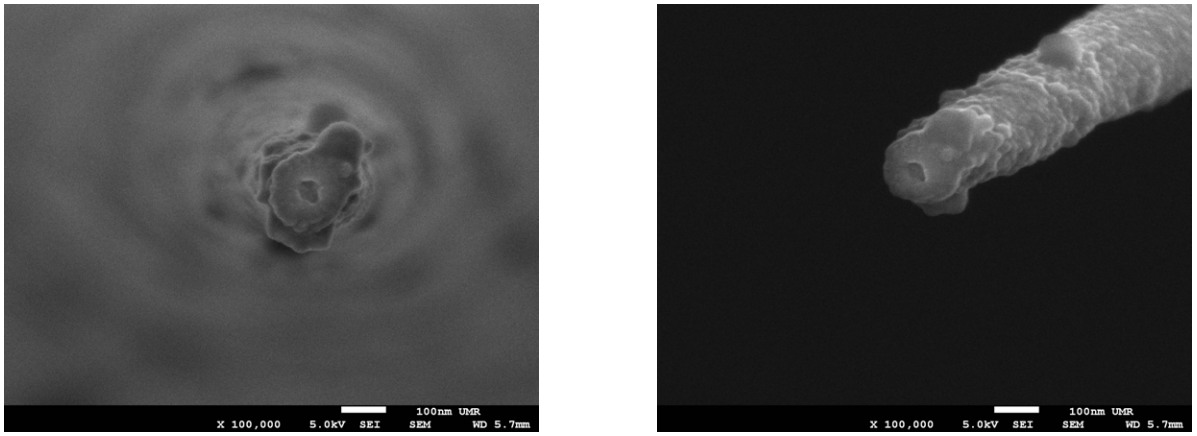

Figure 3.19: SEM images of oxide layers on an unused, etched W tip for STM (front and side view).

3.6 Data Treatment and Analysis

The results of the measurements were treated according to the following procedures. Deviations from these standard procedures are mentioned with the reported results. According to good analysis practice, the data treatment was carried out using standard procedures as known from literature and with respect to the data integrity, especially during the processing of STM images.

3.6.1 Imaging with Scanning Tunneling Microscopy

All STM measurements were performed in constant-current mode. The reported bias voltages are applied and refer to the sample (sample bias). Therefore, the tunneling direction is from occupied states of the tip to unoccupied states of the sample for positive sample bias voltages and *vice versa* for negative voltages.

For the processing of RT- and VT-STM images, WSxM v5.0 Develop 8.4 was used.[215] LT-STM images were processed by Manuel Gruber with Gwyddion 2.47.[216] The conducted treatment includes flattening and planing steps, scale adjustment and slightly filtering with a Gaussian filter. Some zoom-in images were subject to a further Gaussian smoothing with Adobe Photoshop to reduce the influences of the pixel interpolation in the magnification of image details. This step was only conducted for esthetic reasons and under prevention of losing detail information. In a few cases which will be mentioned specifically, images were dewarped

to correct the distortion due to a strong thermal drift during the measurement to enhance the qualitative impression of the results, and this image manipulation was by no means integrated in a quantitative evaluation.

The calibration of the length scale for STM was conducted using a standard sample of highly oriented pyrolytic graphite (HOPG). The sample was acquired from NT-MDT and exhibits a mosaic spread of 0.4-0.7°. The spots in STM images of HOPG originate from only three out of six adjacent carbon atoms in a graphene hexagon unit cell resulting from the asymmetry in the surface atom environment due to the two different sublattices of graphite. With a C–C bond length of 0.142 nm, the distance between two visible, nearest neighbors is 0.246 nm.

3.6.2 Photoelectron Spectroscopic Measurements

XPS and UPS measurements were analyzed with WaveMetrics Igor Pro 7.06 using the fit assistant X-ray Photoelectron Spectroscopy Tools developed by Dr. Martin Schmid.[217,218]

For the quantification of the concentration n_i of present elements i in XP spectra, the stoichiometry of the sample, and thus the comparison of peak intensities, several dependencies on physical properties of the sample and the analyzer have to be regarded. The intensity, more precisely the area of peak j of element i can be determined by Equation 3.22.[179] The transmission functions T were determined for the SPECS analyzer system and are given in Equations 3.23, 3.24 and 3.25 for an iris opening of 30 mm and the specified energy ratios. The angular symmetry factor L_{ij} for the orbitals cancels for the comparison of intensities originating from s orbitals and can even be neglected for solids. The atomic subshell photoionization cross sections σ_{ij} were taken from the publication of J. J. Yeh and I. Lindau.[219] The inelastic mean free path at the specified kinetic energy $\lambda(E_{\mathrm{kin}})$ can be neglected for monolayer samples. The angle θ is the take-off angle of the photoelectrons with respect to the surface normal. The measurements were performed at a sample orientation orthogonal to the lens system, *i.e.*, in normal emission geometry (0°). Therefore, the cosine function equals one. Practically, the peak integrals were corrected by means of dividing by the photoionization cross sections and the individual transmission function. After this procedure, the stoichiometry of the sample can directly be determined from the corrected peak integrals.

$$I_{ij} = T(E_{\mathrm{kin}}) L_{ij} \sigma_{ij} n_i \lambda(E_{\mathrm{kin}}) \cos\theta \tag{3.22}$$

$$T_{\mathrm{rel},1} = 13.4733837 \left(\frac{E_{\mathrm{pass}}}{E_{\mathrm{kin}}}\right)^{0.74269} \quad \text{for } 0.0021247 \leq \frac{E_{\mathrm{pass}}}{E_{\mathrm{kin}}} \leq 0.0258157 \tag{3.23}$$

$$T_{\mathrm{rel},2} = 1197249.71 \left(\frac{E_{\mathrm{pass}}}{E_{\mathrm{kin}}}\right)^{15.202+12.323\log(E_{\mathrm{pass}}/E_{\mathrm{kin}})+3.262\log^2(E_{\mathrm{pass}}/E_{\mathrm{kin}})} \quad \text{for } 0.0258157 \leq \frac{E_{\mathrm{pass}}}{E_{\mathrm{kin}}} \leq 0.0431644 \tag{3.24}$$

$$T_{\mathrm{rel},3} = 0.51263877 \left(\frac{E_{\mathrm{pass}}}{E_{\mathrm{kin}}}\right)^{-0.20653} \quad \text{for } 0.0431644 \leq \frac{E_{\mathrm{pass}}}{E_{\mathrm{kin}}} \leq 0.1026290 \tag{3.25}$$

3.6.3 Absorption Spectroscopic Measurements

As stated above, the NEXAFS measurements in this work were performed at the HE-SGM dipole beamline of the synchrotron radiation facility BESSY II (Helmholtz-Zentrum Berlin) using the partial electron-yield mode. The incident photon flux was monitored with a gold grid. The photon energy was calibrated by means of a carbon-related absorption on the grid.[220] The literature value for the observed π^* resonance is 285.09 eV.[221] Sebastian Reiss determined this energy by comparison with HOPG. The resonance in the calibration spectrum I_0 was fitted using a Gaussian function. The shift of the resonance relative to the literature value was used to correct the energy axis of the corresponding sample spectra. Deviating from this procedure for experiments at the carbon K-edge, the photon energy of spectra at the metal L-edges could not be corrected due to the lack of reference absorptions. NEXAFS spectra of the clean substrate, Ag(111), were recorded to reduce the background resonances by subtraction from the sample spectra. Depending on the origin of the background components, the correction can either be performed by division or by subtraction.[194] Since, in the herein reported experiments, the major background features originate from substrate excitations, a subtraction was used. A division would further correct for the monochromator transmission function and instabilities in the radiation source which were negligible. Sample and clean substrate spectra were normalized in the pre-edge region at 281 eV for carbon K-edge measurements, at 700 eV and 705 eV for multilayer and monolayer measurements of the iron L-edge, respectively, and at 778 eV for the cobalt L-edge. The substrate spectra were interpolated with a smoothing spline prior to subtraction from the sample spectra to reduce the noise. In a final step, the sample spectra of the carbon K-edge were normalized in the range behind the absorption edge, 310 eV. The quantitative analysis of the molecular orientation was performed using the relation between the intensity of the π^* resonance and the angle of incidence (*cf.* Equation 3.19 in Chapter 3.3). NEXAFS results were analyzed in WaveMetrics Igor Pro 7.06.

4 Structures and Reactions of Tetrapyrrole Macrocycles

4.1 Surface Reactivity and Self-Assembly of a Free-Base Corrole on Ag(111)

As aforementioned, corroles exhibit a slightly different structure than porphyrins due to the absence of one bridging methine group between the carbon atoms 1 and 19. A difference in the surface reactivity can be anticipated due to this substantial change in the chemical environment. While porphyrins are stable on inert metal surfaces at room temperature, the behavior of corroles in this respect will be regarded in this chapter. Furthermore, the study was broadened by the observation of highly ordered superstructures.

4.1.1 Surface-Assisted Dehydrogenation

To investigate the surface reactivity, multi- and monolayers of an alkyl-substituted corrole, 3H-HEDMC, were prepared on Ag(111) by vapor deposition. The substance was contributed by Martin Bröring. Standard procedures were conducted in the preparation and deposition. If not stated differently, the samples were annealed for a duration of 3 min at the specified temperature.

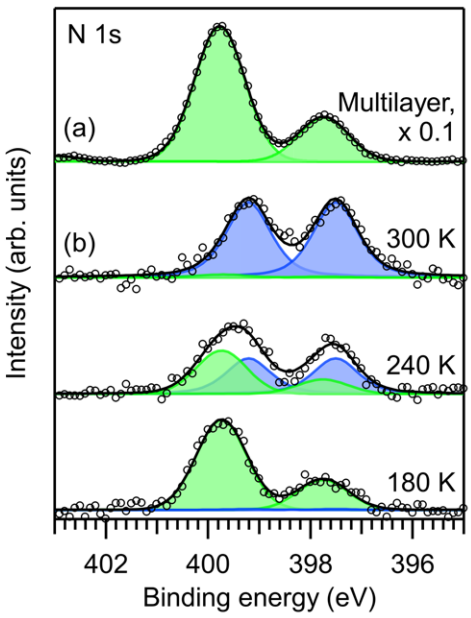

Figure 4.1: N 1s XP spectra of 3H-HEDMC (a) multi- and (b) monolayers on Ag(111). The expected intensity ratio of 3 : 1 representing the stoichiometry of the three pyrrolic (−NH−) and one iminic nitrogen atoms (−N=) in the macrocycle is present for the multilayer, while the monolayer shows a dehydrogenation indicated by the development of a 2 : 2 ratio.

Due to the structural characteristics of corrole compared to porphine, the macrocycle contains three pyrrolic (−NH−) and one iminic (−N=) nitrogen atom in the pyrrole units instead

of two of each binding situation. This different ratio should be reflected in the peak integrals of the N 1s species in an XP spectrum. Indeed, the ratio 3 : 1 is present in a multilayer experiment as shown in Figure 4.1 (a) indicating the intactness of the deposited 3H-HEDMC. The peaks at 399.8 eV and 397.8 eV are attributed to −NH− and −N=, respectively. A monolayer measured at room temperature exhibits two peaks with the same integral at 399.2 eV and 397.5 eV (Fig. 4.1 (b)). This finding suggests the dehydrogenation of one pyrrolic component resulting in a 2 : 2 ratio.[I] If the monolayer is produced at a temperature of 180 K, the original ratio can be observed. A coexistence between unreacted 3H-HEDMC and reacted 2H-HEDMC is found at 240 K. The different situations for the multilayer and monolayer samples indicate that the Ag(111) surface plays a crucial role in the dehydrogenation. While the monolayer shows a temperature-dependent reactivity, the multilayer is decoupled from the substrate and stable at room temperature.

A heating series from 180 K to 650 K (Fig. 4.2) reveals the dehydrogenation reaction. The spectral intensity evolution can roughly be described by a continuous transition of the peak integrals and a shift toward lower binding energies. To consider the contributions of both HEDMC species and to quantify the changes, the spectra were fitted with peak integrals for 3H-HEDMC (green) and for 2H-HEDMC (blue). The positions of the peaks were held constant. The surface reaction of 3H-HEDMC is suppressed by cooling of the sample to 180 K, since no contribution of the dehydrogenated species can be found. The peaks of the three pyrrolic and the one iminic nitrogen are located at 399.7 eV and 397.7 eV, respectively, and thus shifted by 0.1 eV to lower binding energies compared to the multilayer. The peaks are separated by 2.0 eV. Except for the peak height, the situation resembles previous observations reported for 2HOEP and 2HTPP on Ag(111) with a similar peak separation (2.0-2.1 eV in the multilayer and 2.0 eV in the monolayer).[222,223] The shift toward lower binding energy upon reduction of the coverage to one monolayer is assigned to an increased core hole screening by the metal substrate.[224,225] The evolution of 2H-HEDMC starts far below room temperature. Already at 240 K, the amounts of 3H-HEDMC and 2H-HEDMC in the mixed phase are almost equal with a even slightly higher contribution of 57% for 2H-HEDMC. The conversion of the corrole species is completed at RT with only an insignificantly small contribution of the former compound. In contrast to measurements of free-base porphyrins, where the N 1s peak intensities of the pyrrolic and iminic species slightly deviate from an ideal 2 : 2 ratio due to an overlapping of a satellite from the iminic species at lower binding energy with the pyrrolic peak at higher binding energy, the dehydrogenated HEDMC exhibits equal peak heights.[226] The peak position of −NH− is shifted by −0.6 eV in binding energy and the peak separation is reduced to 1.7 eV compared to the intact monolayer and the multilayer. The considerable shift indicates an increased substrate-molecule interaction. However, the C 1s spectrum is less affected with only a small shift by −0.2 eV (Fig. 4.3). This finding suggests a potential charge transfer from the surface to the macrocycle with a charge localization at the N atoms.

For further insight into the reaction process, the normalized, relative intensities of the N 1s peak integrals of both HEDMC species in the heating series were plotted *versus* the temper-

[I] To facilitate the comprehension of the intramolecular changes, the ratio is given as 2 : 2 instead of the mathematically common reduced fraction, 1 : 1.

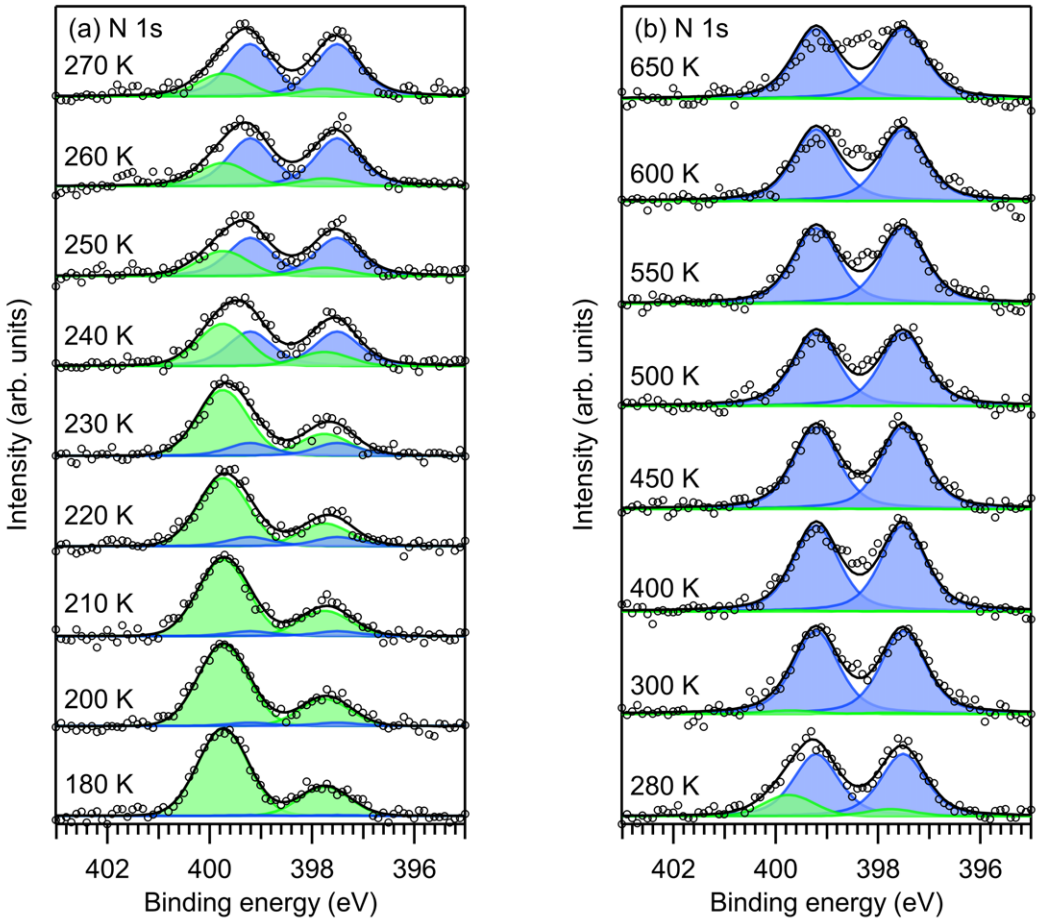

Figure 4.2: XPS temperature series of the N 1s region of a 3H-HEDMC monolayer on Ag(111) in a range of (a) 180-270 K and (b) 280-650 K. The dissociation of the N-H bond starts at 240 K as it can be seen by the decreasing intensity of the 3H-HEDMC N 1s species in favor of the 2H-HEDMC species with an equilibrium at 240 K. According to the spectra, 2H-HEDMC is stable until 450 K.

ature (Fig. 4.4). The development of the peak contributions features an inflection point at 240 K as already observed before. A completion of the dehydrogenation reaction is reached at 300 K, since the relative intensities converge toward a limit above this temperature. Further changes of the N-H bond do not occur until above 450 K. The pyrrolic groups are therefore stable in a temperature range of at least 150 K and do not undergo further dehydrogenation. Above 450 K, an unspecific reaction starts as can be seen by the collapse of the N 1s peaks as well as the shift and more symmetric shape of the C 1s peak. The reason for this behavior will be regarded later.

Since 3H-HEDMC is intact upon initial deposition on the cooled Ag(111) surface, the presence of an activation barrier which can be overcome by thermal treatment is assumed. Using the Arrhenius equation (Eq. 4.1), the energy E_A of this barrier can be calculated.

$$k = A \cdot \mathrm{e}^{-E_A/RT} \tag{4.1}$$

By transformation of the equation considering the experimentally derived, relative intensities I/I_0, Equation 4.2 is obtained. As mentioned above, the duration of the annealing process τ

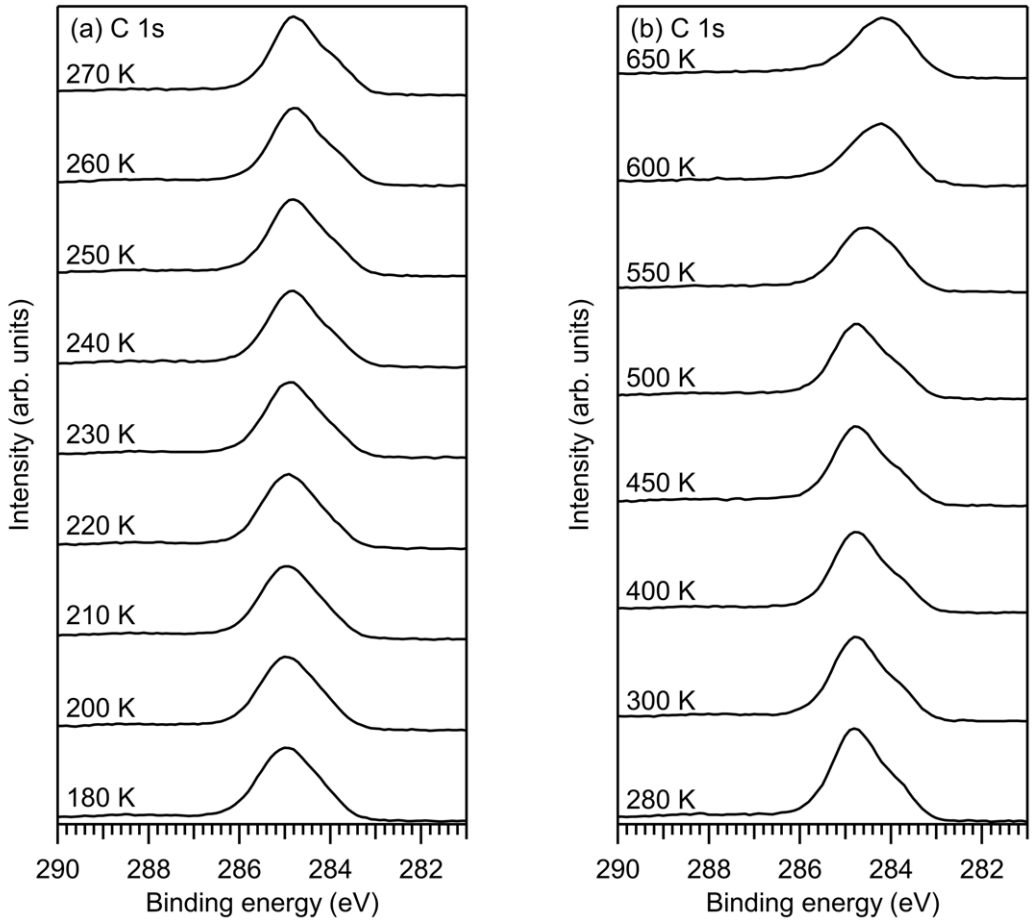

Figure 4.3: XPS temperature series of the C 1s region of a 3H-HEDMC monolayer on Ag(111) in a range of (a) 180-270 K and (b) 280-650 K.

was 180 s. The frequency factor ν was assumed to be of $1 \cdot 10^{13}$ s^{-1}. This value is commonly used for first-order gas phase reactions. Although a deviation from this ideal situation is obvious for the observed surface reaction, the assumption was necessary as the experimental results did not provide a more precise value. The activation energy was calculated for the temperatures 230 K, 240 K and 250 K (Tab. 4.1) and yields an averaged energy of 74 kJ mol^{-1}.

$$E_A = -RT \cdot \left(-\frac{1}{\tau\nu} \cdot \ln \frac{I}{I_0} \right) \tag{4.2}$$

Upon thermal treatment, one of the former three pyrrolic nitrogens of 3H-HEDMC is dehydrogenated. The loss of the hydrogen in the –NH– bond is indicated by the decreased ratio of the nitrogen species in XP spectra. Two chemically equivalent iminic as well as two pyrrolic nitrogen atoms are present in the center of the 2H-HEDMC macrocycle. In solution, the bond cleavage should occur as heterolytic dissociation of a proton. Only in a very special case, a homolytic bond cleavage was observed on trimesitylcorrole in solution yielding in a low amount of the radicalic product.[227] Due to the significantly higher acidity found for the first deprotonation of a corrole ($pK_a = 5.2$) compared to the equally substituted porphyrin ($pK_a = 32.8$)[228], the formation of the mono-deprotonated corrole is easily obtained. This

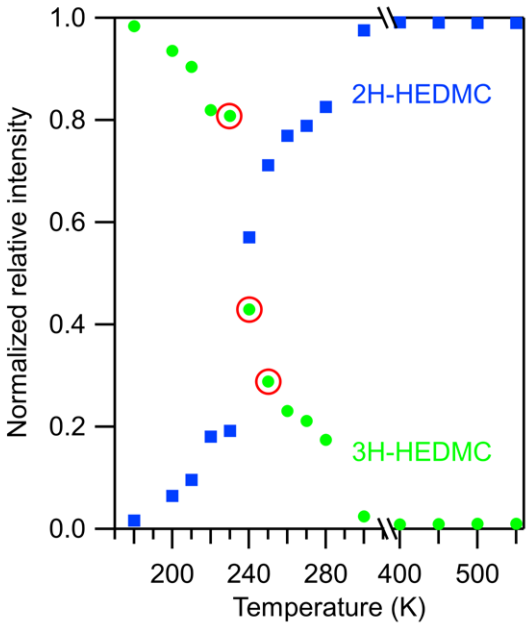

Figure 4.4: Relative intensities of the N 1s peak integrals of 3H-HEDMC compared to 2H-HEDMC. The resulting development clearly shows the dissociation of the N-H bond around 240 K. The red circles highlight the temperatures which were used for the calculation of the activation energy.

Table 4.1: Calculation of the activation energy for the dehydrogenation of 3H-HEDMC.

Temperature T **(K)**	**Intensity** I_0	**Intensity** I	**Activation barrier** E_A **(kJ mol^{-1})**
220	-	0.81967	-
230	0.81967	0.80795	75.28
240	0.80795	0.42968	71.01
250	0.42968	0.28857	74.93

could also explain why corroles readily react with surfaces, while porphyrins behave almost inert at room temperature. The high acidity can be explained by a steric effect on the proton attached to the third pyrrolic nitrogen due to repulsion between the –NH– groups. X-ray crystallography revealed that the corresponding third proton is twisted out of the pyrrole plane.[229] Studies of the direct metalation of deuterated tetrapyrroles on Cu(111) provided a mechanism for the dehydrogenation including the transfer of the hydrogen to the metal surface leading to adsorbed hydrogen atoms – or deuterium atoms in this comparative study.[230] A similar mechanism is expected for the removal of the third hydrogen from the pyrrole units in the corrole macrocycle. Stefano Tebi *et al.* reported the site-specific dehydrogenation of tris(pentafluoro-phenyl)-corrole on Ag(111) by annealing and revealed the presence of a radicalic species and thus a homolytic cleavage of the –NH– bond by investigating the surface Kondo effect providing evidence for unpaired electron spin density.[231] The resulting unpaired electron spin density is distributed over the dehydrogenated nitrogen and surrounding parts of the molecule. In the here presented XP spectra of 2H-HEDMC on Ag(111), no evidence for a spin-induced broadening of the N 1s signals was found. It can be assumed that the spin

is quenched by interaction with the substrate. Furthermore, the reported shift toward lower binding energy suggests a charge transfer from the metal substrate to the organic molecule. Jan Herritsch performed DFT calculations on unsubstituted 2H-porphine, 3H-corrole and 2H-corrole in the gas phase and adsorbed on Ag(111).[232] 2H-Corrole exhibits a closer distance to the surface and an increased interaction. It might be that a radical is formed initially. Due to interaction with the surface, electron density is transferred into the singly occupied molecular orbital (SOMO) of the corrole molecule. While the aromaticity of the macrocycle would have been lost upon formation of the delocalized radical, the electron transfer retains the aromatic 18 π-electron system on 17 atomic centers (Fig. 4.5). Jan-Niclas Luy examined the reaction of the free-base 3H-HEDMC with the Ag(111) surface employing DFT calculations and considered the energetics.[233] Upon adsorption, the most acidic hydrogen, which is the hydrogen attached to the pyrrolic nitrogen in ring D, points toward the surface, while the alkyl substituents are directed upward. Annealing induces the reaction and thus the transfer of the most acidic hydrogen to the surface. The activation barrier exhibits an energy of 102 kJ mol^{-1}, thus by 28 kJ mol^{-1} higher than the experimentally estimated barrier. The energy of the final state, an adsorbed 2H-HEDMC molecule and an adsorbed hydrogen atom, is 80.5 kJ mol^{-1}. The reaction is endothermic, since the product lies above the initial state.

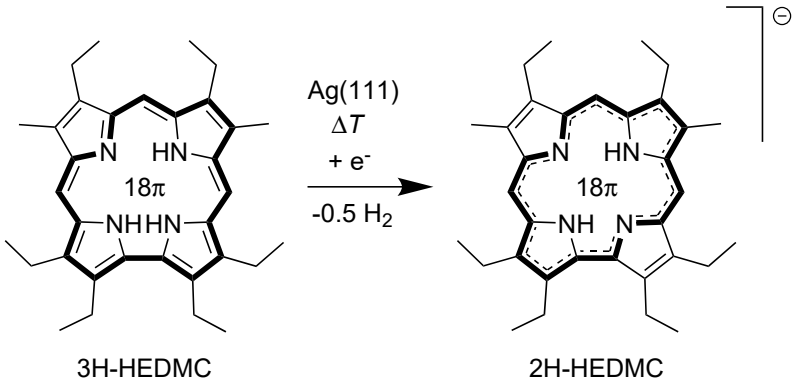

Figure 4.5: N-H bond dissociation and formation of a negatively charged 2H-HEDMC from 3H-HEDMC on Ag(111). The aromatic 18 π-electron system is retained and highlighted in bold.

If the studied monolayer samples in the following experiments are explicitly referred to as 3H-HEDMC, the adsorption of molecules was performed at temperatures below 180 K to avoid the surface-induced dehydrogenation.

4.1.2 Formation of 2H-HEDMC Superstructures

Porphyrins arrange in well-defined, periodic structures with a long-range order as reported in various studies.[234–237] A similar behavior can be observed in low-resolution STM images of 3H-HEDMC on Ag(111) at 150 K (Fig. 4.6 (a)). The molecules in the monolayer are laterally ordered in an oblique, near hexagonal pattern. The unit cell is defined by four molecules with a dimension of $(14.3 \pm 0.1) \times (13.0 \pm 0.2)$ Å^2 and an inner angle of $(108 \pm 2)°$. A high-resolution image reveals an apparent disorder (Fig. 4.6 (b)), in which certain structures reappear. To understand these structures, a closer look on the structural features of 3H-HEDMC is necessary. Due to steric repulsion of three hydrogen atoms in the smaller corrole ring, the macrocycle

is not perfectly planar on the surface in contrast to planarly adsorbed porphyrins. More prominent are the alkyl substituents, especially the six flexible ethyl groups. A detailed view of a high-resolution STM image (Fig. 4.6 (c)) reveals the ethyl groups as protrusions by superimposing with a molecular model featuring the ethyl groups as discs. The prominence was previously reported for the eight ethyl substituents of 2HOEP.[237,238]. The protrusions of the HEDMC molecule can be divided into two subsets, the four adjacent ethyl groups at the positions 2, 3 and 17, 18 on the short side of the macrocycle with the missing methine group and the two ethyl groups at the positions 8 and 12 on the opposite side, both separated by the methyl groups which are not visible. The size of the features can be attributed to the topography of the protruding ethyl groups pointing toward the vacuum and to the flexibility of the ethyl chains influencing the tunneling process. The raw image of the individual molecule shows a compression in the vertical direction, which is an intrinsic artifact commonly observed for VT-STM due to a thermal drift resulting from a temperature difference between the cooled sample and the STM tip held at room temperature. Scanning speed artifacts can contribute to this phenomenon as well.

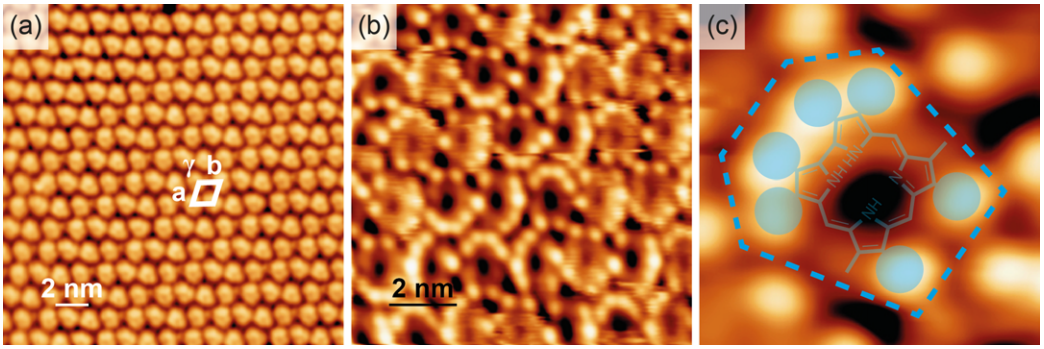

Figure 4.6: STM images of intact 3H-HEDMC on Ag(111) at 150 K. (a) Overview of a monolayer 3H-HEDMC with a superimposed unit cell ($(14.3 \pm 0.1) \times (13.0 \pm 0.2)$ Å^2, $(108 \pm 2)°$). (b) High-resolution STM image with submolecular details and an apparent rotational disorder of the molecules. (c) A close-up (dewarped to correct the thermal drift) shows the appearance of a single molecule (in this case 2H-HEDMC) with a depression of the vacant center of the macrocycle and the six protruding ethyl groups. Tunneling parameters: (a) −1.68 V, −1.22 nA; (b) −1.20 V, −1.76 nA; (c) −1.58 V, −0.99 nA.

With the knowledge of the image features, light can be shed on the assembly of 3H-HEDMC molecules in the monolayer. The molecules exhibit four preferential azimuthal orientations each determined by the group of the four neighboring ethyl groups on the short side of the macrocycle and rotated by multiples of 90° as highlighted in Figure 4.7 (a). While a long-range periodicity cannot be detected, the impression of an apparent rotational disorder of the molecules is weakened, when the molecules of neighboring (vertical) molecular rows are compared (Fig. 4.7 (b)). While the molecules marked in blue are oriented vertically, the molecules in green are oriented horizontally with respect to the plane of projection.

Annealing to 300 K leads to the formation of a striking superstructure in the 2H-HEDMC monolayer consisting of a double-S motif, which occurs in two enantiomeric forms as shown in Figure 4.8 (a). The unit cell of the superstructure expands over $(25.8 \pm 0.2) \times (33.1 \pm 0.2)$ Å^2 with an angle of $(90 \pm 2)°$. While the molecules showed no long-range order in the low-temperature phase, they exhibit an extraordinary regularity at room temperature. Again,

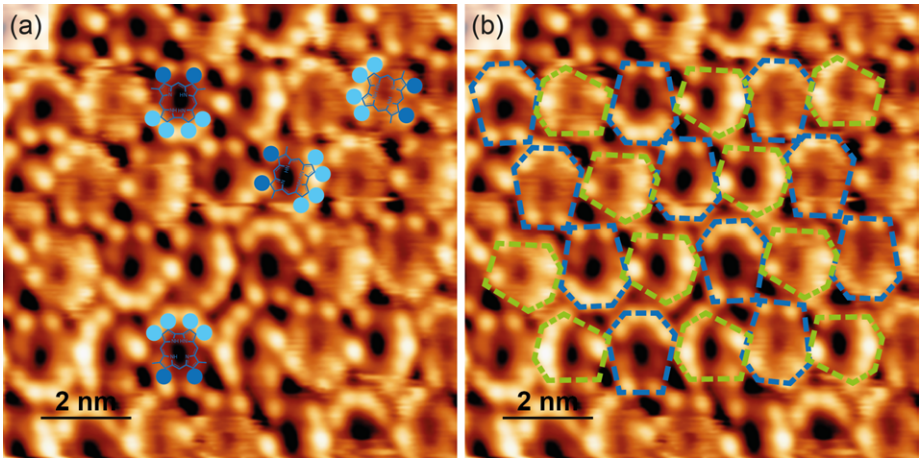

Figure 4.7: Orientation of 3H-HEDMC molecules on Ag(111) at 150 K. (a) The azimuthal orientations of the molecules can be determined by the group of four adjacent ethyl groups at the positions 2, 3, 17 and 18 (highlighted in light-blue). The molecules are rotated by multiples of 90°. The elongation of the molecules pointing upward in the image results from a thermal drift during the scanning process. (b) Within a row of molecules, the orientation is either horizontal (blue) or vertical (green) referring to the azimuthal orientation of the molecules determined by the position of the four adjacent ethyl groups. Tunneling parameters: −1.20 V, −1.76 nA.

the azimuthal orientation is determined by the position of the four ethyl substituents on the short side of the macrocycle (Fig. 4.8 (b)). In the following, the azimuthal orientation of the molecules will be given with respect to the image plane and denoted with arrows. The periodicity of the orientational appearance is down, up, right, left (or with arrowheads indicating the position: ↓, ↑, →, ←). The sequence in the subjacent row is shifted by one molecule. A detailed inspection of a double-S feature explains its composition (Fig. 4.9 (a)). The double-S contains contributions of four neighboring 2H-HEDMC molecules each rotated by multiples of 90°. Within a *single-S*, the tine which points toward the other *S* is composed of all adjacent ethyl groups 2, 3, 17, 18 on one molecule, while one ethyl substituent next to a methyl substituent of the adjacent molecule is at the end of the *single-S* (Fig. 4.9 (b)). The second *single-S* can be generated by a transformation on the basis of a C_2 rotational axis located in the center of the double-S.

The molecular density of 3H-HEDMC and 2H-HEDMC in the corresponding LT- and RT-phases on Ag(111) can be compared by consulting the areas covered by the unit cells. At 150 K, 3H-HEDMC arranges in a primitive unit cell size of 177 Å^2, which contains only one molecule (Fig. 4.6 (a)). The calculated area of the unit cell of 2H-HEDMC at 300 K yields 854 Å^2 with four molecules (Fig. 4.8 (a)). Since the ratio of the areas (4.8) is higher than the ratio of the numbers of observed molecules per unit cell (4), the room-temperature superstructure is spatially more demanding, although an increased order should result in a higher packing density. The reduced molecular density can be explained by considering the intermolecular interactions. Ethyl groups are terminating the molecules outwards. These substituents are flexible and can arrange in such a way that the intermolecular VAN DER WAALS forces are maximized. While this arrangement supports the stability of the supermolecular structure, it requires more space on the other hand.

The reported superstructure can easily be reproduced and covers very large areas of the

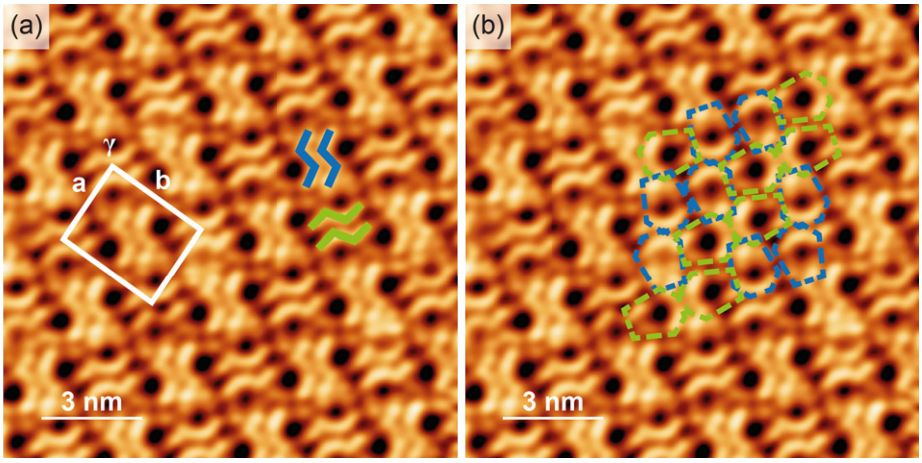

Figure 4.8: STM images of 2H-HEDMC on Ag(111) annealed to 300 K and its superstructure. (a) The two enantiomeric double-S motifs are highlighted in blue and green. The unit cell parameters are: $(25.8 \pm 0.2) \times (33.1 \pm 0.2)\,\text{Å}^2$, $(90 \pm 2)°$. (b) The molecules exhibit a rotational long-range order with a double-S motif. Within a row, the iterating azimuthal orientations are ↓, ↑ (blue) and →, ← (green) with the arrowheads indicating the position of the four adjacent ethyl groups. Tunneling parameters: −1.54 V, −0.89 nA, 160 K.

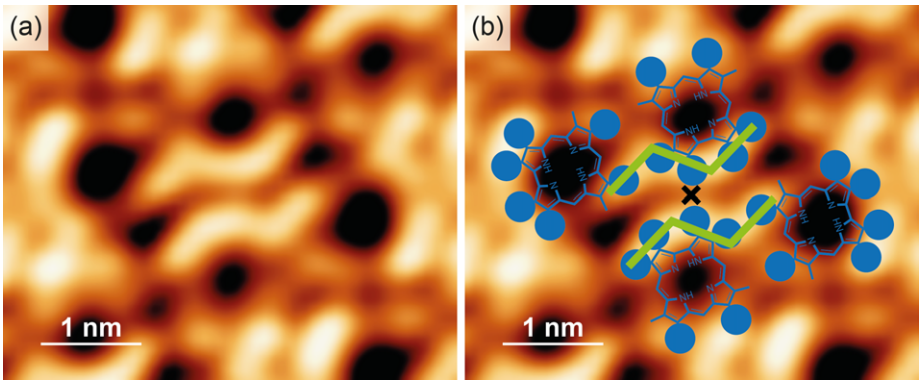

Figure 4.9: Detail image of 2H-HEDMC on Ag(111) annealed to 300 K. (a) STM image of the double-S motif. (b) The motif is formed by four 2H-HEDMC molecules rotated by multiples of 90° as indicated by the superimposed models. Each single-S contains the four adjacent ethyl groups of one molecule and one ethyl group on the opposite side of another molecule. The cross represents the position of the C_2 rotational axis. Tunneling parameters: −1.54 V, −0.89 nA, 160 K.

surface. Defects are rarely present. However, some domain bounderies were observed as illustrated in Figure 4.10 representing the polycristallinity of the organic monolayer. The boundaries are overlayed by a white semitransparent trapezoid. Laterally, the boundaries contain two molecules. The molecular rows are not interrupted cross-border and are also not misplaced, but the aforementioned order within a line is disturbed. While the molecules are arranged ↓, ↑, →, ← in a monocrystalline domain, the only azimuthal orientation in the boundary is ←, → and thus doubles the horizontally oriented subunit within a row (Fig. 4.10 (b)).

4.1.3 Dehydrocyclization of Alkyl Substituents

As seen in the XPS heating series, the C 1s peak shifts further to lower binding energies with a simultaneous transformation of the peak form at high temperatures above 500 K. This finding

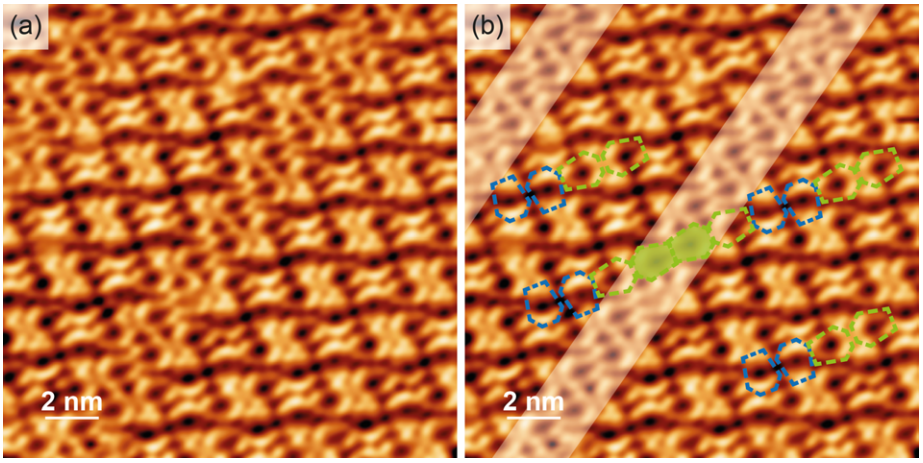

Figure 4.10: Domain boundaries in the double-S structure. The discontinuity of the repetitive units within a row (↓, ↑, →, ←) is illustrated by the filled frames in the domain boundary (marked in transparent white). Tunneling parameters: −1.54 V, −0.83 nA, 160 K.

indicates additional reactions of the molecule. STM images taken after annealing to 650 K show a significant change in the appearance of the 2H-HEDMC molecules (Fig. 4.11). The former prominent ethyl groups are not protruding anymore. Instead, the molecule appears mostly flat and the macrocycle is more pronounced. The edges of the molecule are laterally expanded. Together with the result of the XPS measurements, a reaction of the substituents can be proposed. Two cases of reacted molecules occur. Alongside some isolated molecules, many molecules seem to be interconnected, which suggests the incidence of intra- as well as intermolecular reactions. Christopher G. Williams *et al.* examined the dehydrocyclization of peripheral alkyl groups in 2HOEP on Ag(111) at 600 K and on Cu(100) at 500 K under the formation of tetrabenzoporphyrin.[239] Similar results were reported for 2HOEP on Au(111) at 530 K[238], Fe-OEP on Cu(111) already at 380 K[240] and octaethyl-tetraazaporphyrin on Au(111) at 573 K[241]. Concerning the different temperatures, a substantial influence of the substrate can be recognized. While Ag(111) and Au(111) are comparably inert, the Cu surfaces have a relatively high reactivity. The temperatures resemble conditions commonly used with solid Pt catalysts for alkane dehydrogenation to reduce the temperatures mandatory in gas phase reactions.[242,243] Octaethylporphyrins appear four-fold symmetric comparable to the structures in Figure 4.11. The mechanism of the peripheral reactions includes surface-catalytic dehydrogenation and subsequent cyclization, a 6 π pericyclic step, finalized by a dehydrogenative formation of the benzo group (Fig. 4.12). Tris(pentafluoro-phenyl)-corrole undergoes an on-surface cyclodefluorination, yet under influence on the corrole macrocycle and an associated planarization of the molecule.[231]

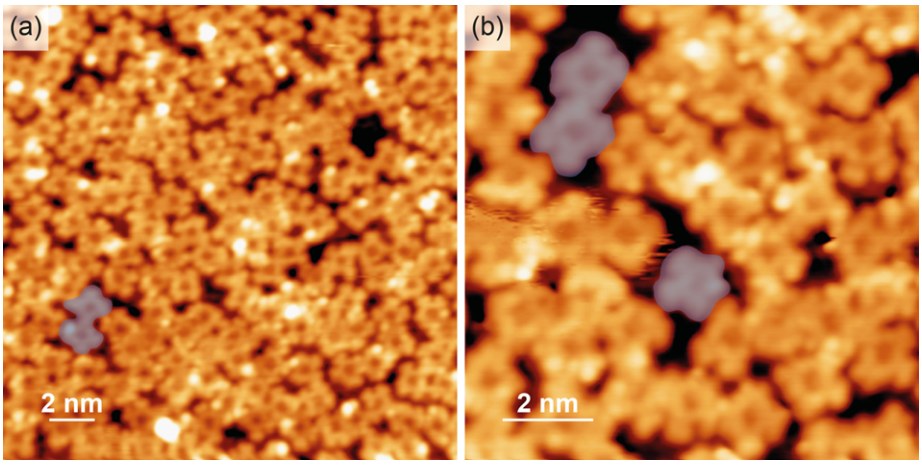

Figure 4.11: STM images of 2H-HEDMC annealed to 650 K. The protrusions of the ethyl groups disappeared due to dehydrogenation and cyclization of the alkyl substituents. Highlighted in blue are individual and interconnected molecules. Tunneling parameters: (a) −1.44 V, −0.49 nA, 155 K; (b) −1.40 V, −0.51 nA, 155 K.

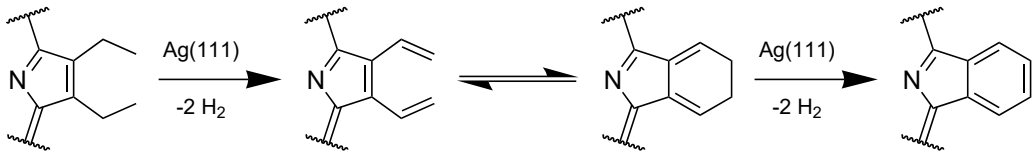

Figure 4.12: Reaction mechanism of the dehydrocyclization of ethyl substituents in the periphery of 2H-HEDMC.

4.2 Coordination Reactions of a Corrole on Ag(111)

In nature, tetrapyrroles often occur in their metalated form due to the relevance of the metal ion in the redox reactions of biological processes like the photosynthesis or the oxygen transport in the circulatory system. For the transferability on the application of metalated macrocycles in technical catalysis, the study of properties related to the metal center is of high interest. The role of corrole as a model system for a modified ligand is therefore focal point of the following projects. The metalation of 3H-HEDMC was studied by using the d-block elements Fe, Co and Ni.

4.2.1 Metalation of Corrole with Iron

Post-deposited Fe was used for direct metalation of 3H-HEDMC on Ag(111).[II] Since the corrole ligand contributes a tighter coordination environment as commonly used porphyrins, an octaethylporphyrin was object of comparison to study the consequences of the macrocyclic ligand on the metal center.

As in the previous study of the free-base corrole, multi- and monolayers were generated by vapor deposition. Since the monolayer experiments of HEDMC are only comparative, the corresponding samples were not necessarily prepared on cooled substrates and thus consist of the dehydrogenated 2H-HEDMC as aforementioned. Fe atoms were post-deposited using an electron beam evaporator at a flux of 0.01 ML_{substr}/min. For a higher reaction yield, the produced metal/organic layers were annealed to 400 K during or after the deposition. The post-annealing step was performed either as flash-annealing, for a duration of 3 min for the UPS measurement, or for 10 min in case of the co-deposition STM experiment. For spectroscopic measurements of monolayers, the amount of deposited Fe was limited to substoichiometric values to prevent the formation of Fe(0) clusters on the surface. To facilitate the preparation of the organic layers, 2HOEP was deposited as multilayers and the well-ordered, intact monolayers were generated by multilayer desorption at 515 K as approved in the literature.[3,5]

Since the binding energy depends on the oxidation state of the investigated species, the first idea was to examine the metalated HEDMC and OEP layers by means of XPS. In two separate experiments, multilayers of approximately 5.5 nm 2HOEP and approximately 8 nm 3H-HEDMC were deposited on Ag(111). 0.09 ML_{substr} Fe were vapor deposited onto the multilayers sufficiently to metalate three monolayers of the corresponding tetrapyrrole. A further increase in the amount of deposited Fe would not contribute to a metalation of deeper layers.[16] The reaction should readily happen at room temperature.[111,120,245] The multilayer 2HOEP exhibits two components in the N 1s XP spectra (Fig. 4.13 (a)). The peaks with their maxima at 400.4 eV and 398.3 eV are attributed to the –NH– and the –N= species. The multilayer 3H-HEDMC shows its N 1s peaks at 400.1 eV and 398.1 eV with its characteristic 3 : 1 ratio (Fig. 4.13 (b)) as reported above. Upon deposition of Fe, a third component evolves between the pyrrolic and iminic nitrogen features. This component is situated at 399.4 eV for the 2HOEP multilayer and at 399.3 eV for the 3H-HEDMC multilayer. According

[II] The results of this project were published in: M. Schmid, M. Zugermeier, J. Herritsch, B. P. Klein, C. K. Krug, L. Ruppenthal, P. Müller, M. Kothe, P. Schweyen, M. Bröring, J. M. Gottfried, *J. Phys. Chem. C* **2018**, *122*, 10392–10399, DOI 10.1021/acs.jpcc.8b00067 .

to Patrizia Borghetti *et al.*, the additional peak results from the reaction of the Fe atom with the 2HOEP macrocycle.[225] The reduction in height of both unreacted species suggests that both former pyrrolic and iminic species are included in the new fourfold coordination. Since the development of the N 1s species is similar for the HEDMC multilayer, the formation of FeHEDMC can be proposed. The involvement of all pyrrolic nitrogens suggests that the bonds between Fe and all nitrogen atoms are equivalent.

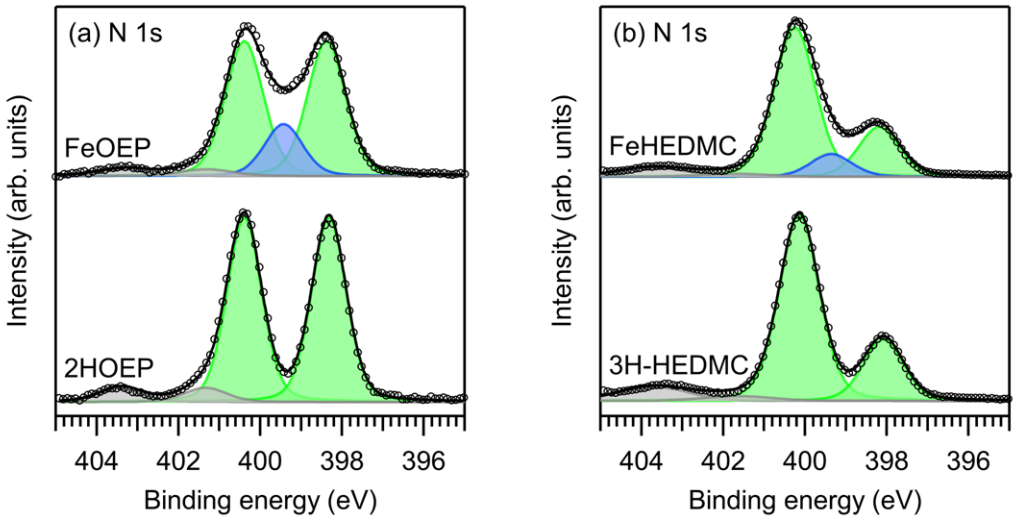

Figure 4.13: N 1s spectra of (a) OEP and (b) HEDMC multilayers on Ag(111) before (bottom) and after (top) partial metalation with Fe. Photon energy: $h\nu = 1486.7\,\text{eV}$.

Monolayers show the same behavior. The N 1s spectrum of a pristine 2HOEP monolayer contains the pyrrolic species at 400.4 eV and the iminic species at 398.7 eV (Fig. 4.14 (a)). The components appear at 400.0 eV (−NH−) and at 398.4 eV (−N=) for 2H-HEDMC in Figure 4.14 (b). The larger shift of the N 1s species of 2H-HEDMC compared to the multilayer corresponds again to the increased substrate-molecule interactions. Furthermore, the monolayer shows a surface-induced broadening due to a shorter lifetime of the core holes as observed before.[222] To prevent the presence of unreacted Fe(0) on the surface, only substoichiometric amounts of $35 - 40\%$ ($0.01\,\text{ML}_{\text{substr}}$) of the corresponding stoichiometric amounts were deposited. The metalation reaction was triggered by flash annealing to 400 K. Subsequent to the deposition of Fe onto the organic monolayers, a new N 1s peak emerges as seen for the multilayer study. The peak attributed to FeOEP lies at 399.2 eV. The comparison of unreacted and reacted species yields a degree of metalation of 40%. The −N−Fe− species of FeHEDMC is present at 399.1 eV. In contrast to the multilayers of the metalated tetrapyrroles, the newly formed species related to the metalation of the monolayers are shifted by −0.2 eV, which corresponds to the previous observations.

Further insight was obtained by considering the complementary Fe 2p core levels in the XP spectra in Figure 4.15. The Fe $2p_{3/2}$ signals of the undisturbed FeOEP and FeHEDMC multilayers are of comparable shape, but the FeHEDMC peak is shifted by +0.3 eV and its full width at half maximum is by 0.4 eV narrower (Fig. 4.15 (a)). The shift toward higher binding energy indicates a higher oxidation state of the iron ion in FeHEDMC.[246] Generally speaking, the broadening of the Fe $2p_{3/2}$ peaks of both iron tetrapyrroles results from a spin-spin coupling

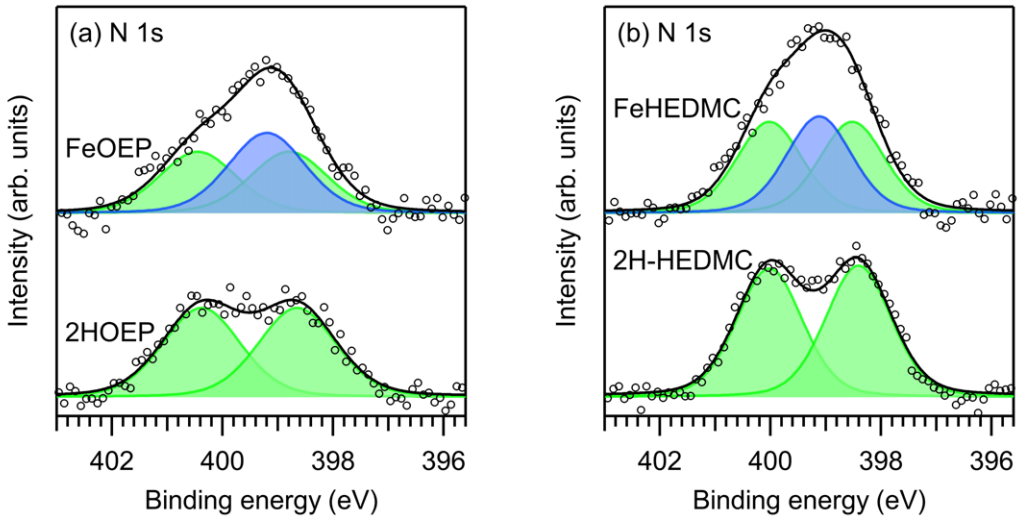

Figure 4.14: N 1s spectra of (a) OEP and (b) HEDMC monolayers on Ag(111) before (bottom) and after (top) partial metalation with Fe. Photon energy: $h\nu = 600\,\mathrm{eV}$.

of the core hole electron with unpaired spin in the d-subshell and gives a complex multiplet structure.[245] While the substrate signals are highly attenuated by the organic multilayers, the monolayer spectra suffer from a domination of the very broad Ag 3s peak (Fig. 4.15 (b)). Therefore, the spectrum of the clean Ag(111) substrate was fitted and the normalized fit function was subtracted from the relevant raw spectra revealing the actual form of the Fe 2p peak. Figure 4.15 (c) is restricted to the $2p_{3/2}$ peak for the sake of simplicity. Compared to the Fe(0) signal, the features of the organometallic complexes are broader and slightly shifted toward higher binding energy as it would be expected for a higher oxidation state. However, both complexes show a distinct Fe(0) contribution (FeOEP with a shoulder at the Fe(0) position), which indicates a charge transfer from the substrate to the metal ions as observed before.[2,107,118,247] Thus, an unambiguous differentiation between the oxidation states in FeOEP and FeHEDMC cannot be drawn from the Fe 2p spectra. Although the multilayer experiments reveal a difference, the question concerning the exact electronic state of the Fe ion in the center of the corrole macrocycle remains unanswered.

Unoccupied states of the metal center were probed by means of NEXAFS spectroscopy at an incident angle of 53°. Multilayers were produced as stated above as mixed layers of FeHEDMC and FeOEP, respectively, and the corresponding unmetalated compounds. FeOEP shows a prominent splitting of the Fe L_3-edge with peaks at 709.2 eV and 710.8 eV, while the Fe L_3-edge of FeHEDMC is broad and asymmetric (Fig. 4.16). The Fe L_2-edges allow no further conclusions. Additional deposition of excess Fe onto the FeHEDMC multilayer reduces the Fe L_3- and Fe L_2-edges to less broad but yet asymmetric peaks. To interprete the NEXAFS spectra, examples of similar metalorganic complexes are consulted. A similar double peak structure as for FeOEP can be found in NEXAFS experiments of Fe-phthalocyanine.[248] Since for both metalorganic complexes, an oxidation state of +II is expected, the congruence is not surprising. The situation of the metal center in FeHEDMC resembles an Fe ion coordinated by a TPP ligand with an additional axial ligand like in FeTPP-Cl, which leads to a +III state.[249] Also, isoelectronic Mn(II) in Mn-phthalocyanines exhibits similar broad resonances

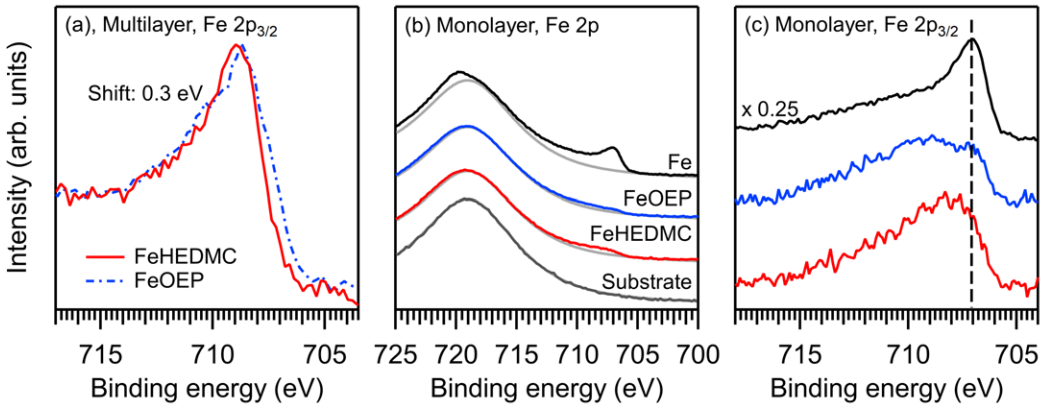

Figure 4.15: Fe 2p spectra of partially metalated FeOEP und FeHEDMC (a) multi- and (b, c) monolayers. (a) The Fe $2p_{3/2}$ peak of FeHEDMC is shifted by 0.3 eV toward higher binding energy compared to the corresponding FeOEP peak. (b) In monolayer experiments, the relevant binding energy region is dominated by the Ag 3s signal. Fe (black) and Ag(111) (dark grey) spectra are shown for reference. (c) The raw data were corrected by subtraction of the fitted substrate background (light grey). The difference between the FeOEP and the FeHEDMC signals is marginal. Photon energy: $h\nu = 1486.7$ eV.

at the Mn L_3-edge.[250] It can be concluded that the Fe ion in the center of FeHEDMC in multilayers possesses a +III oxidation state character as expected.

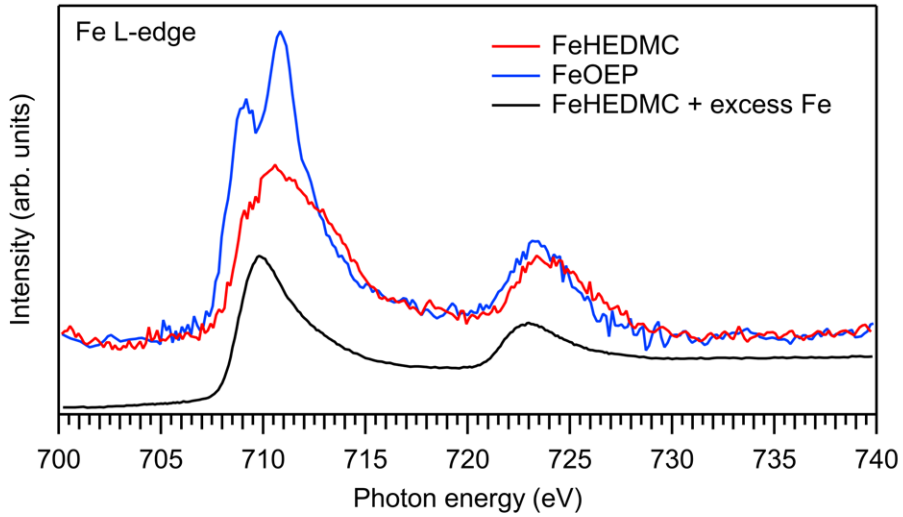

Figure 4.16: Fe L-edge NEXAFS spectra of FeOEP and FeHEDMC multilayers. The metallotetrapyrrole species were prepared by partial metalation with post-deposited Fe. The spectrum of an Fe-HEDMC multilayer with excess Fe is shown for comparison. The angle of the incident radiation was 53°.

Reducing the coverage to one monolayer yields in NEXAFS spectra strongly shaped by the background of the Ag(111) substrate (Fig. 4.17 (a)). However, a difference between the FeOEP and the FeHEDMC becomes obvious (*cf.* the inset in Figure 4.17 (a)). The spectra were background corrected as previously described (Ch. 3.6.3). The metalated OEP monolayer (degree of metalation 40%) is now represented by a broad peak, while the Fe L_3-edge of FeHEDMC (degree of metalation 35%) is divided in two features at 708.9 eV and 712.0 eV. Again, the spectra can be interpreted by comparison with other complexes known from the

literature. The already mentioned Fe-phthalocyanine behaves similar to the here regarded porphyrin complex with a simple, broad feature at normal incidence. The double peak shape does not evolve until a film thickness of 0.9 nm.[248] If FeOEP-Cl is dissolved in CH_2Cl_2, the Fe(III) center experiences additional influence from the Cl substituent of the solvent by donation of electron charge into the ion. The coordination situation $CH_2Cl_2 \cdots FeOEP-Cl$ results in a slight decrease in the oxidation state of the former Fe(III) ion.[249] A related case is observed for the FeHEDMC monolayer on Ag(111), when the corresponding NEXAFS spectra are compared. Here, the surface acts as an additional ligand. In contrast to the multilayer results and in contradiction to the involvement of all three former pyrrolic nitrogen atoms in the complexation, the surface affects the metal center in such a strong way that the oxidation state cannot be described as $+\,\mathrm{III}$ anymore.

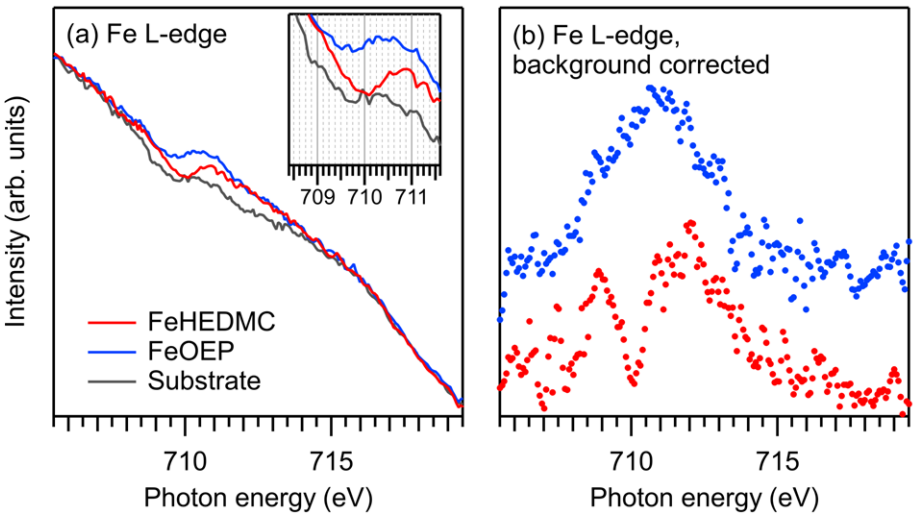

Figure 4.17: Fe L-edge NEXAFS spectra of FeOEP and FeHEDMC monolayers. The metallotetrapyrrole species were prepared by partial metalation with post-deposited Fe. After background-correction of the original data (a), the double peak structure of FeHEDMC becomes obvious (b). The inset in Figure (a) highlights the region of the characteristic features in the raw data. The angle of the incident radiation was 53°.

Since the study of FeHEDMC and FeOEP layers indicates a difference in the electronic state of the metal center, further experimental methods were consulted. Due to the convolution of topography and electronic states in STM measurements, this method is suitable for the characterization of molecules and their electronic properties with spatial resolution. To allow the comparability of characteristic molecular contrasts, the STM measurements were preferably conducted on co-deposition samples. A mixed monolayer of 2HOEP and 3H-HEDMC (50 : 50) was prepared and metalated as stated above. In this case, the amount of deposited Fe was increased to 0.06 ML_{substr}, two times the stoichiometric amount for a monolayer, to achieve a high metalation yield and thus to support locating a high amount of metalated tetrapyrroles in the images. Upon co-deposition, HEDMC and OEP molecules arrange in separate domains, which contain a low number of the corresponding other species (Fig. 4.18). The identification of the respective tetrapyrrole is easily achieved due to the different number of ethyl substituents visible as prominent protrusions for both molecules. Furthermore, the molecules within the HEDMC-rich domains (right) appear rotationally disordered in contrast to the high symmetry

and long-range order of the OEP-rich domains (green). As reported before, the metalation of a macrocycle can be determined by increased contrast in the center of the macrocycle.[109,111,237] The larger white spots on the surface are attributed to three-dimensional Fe(0) clusters as a result of the excess amount.

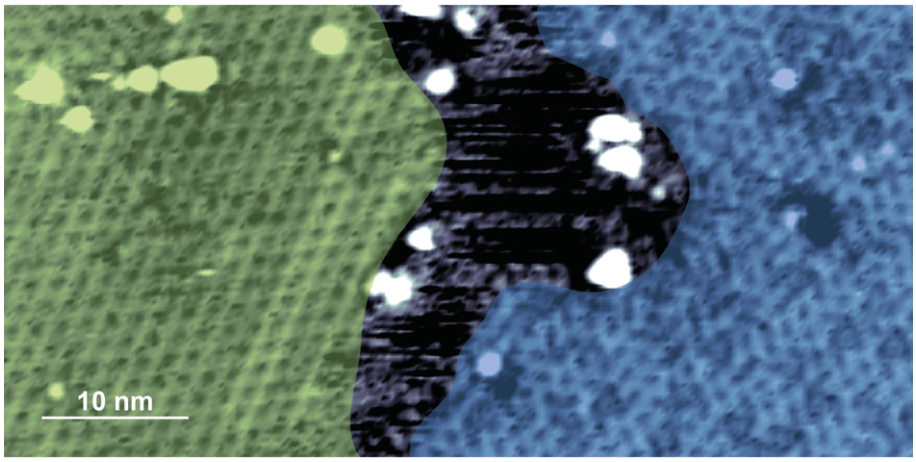

Figure 4.18: Overview STM image of Fe metalated OEP-rich (left, green) and HEDMC-rich (right, blue) domains in a co-deposition experiment. Alongside metalated and unmetalated tetrapyrrole species, three-dimensional Fe clusters are present as bright spots. Tunneling parameters: 1.63 V, 0.08 nA, 100-160 K.

Metalated molecules indeed occur with bright protrusions in the center (Fig. 4.19). To enhance the inspection of the image, corrole and porphyrin molecules are highlighted with dashed frames in different colors. The comparison of molecular contrasts is facilitated by the higher overall rotational symmetry in the OEP-rich phases (Fig. 4.19 (a), (b)) than in the HEDMC-rich domains (Fig. 4.19 (c), (d)). Upon Fe metalation, the total brightness of an FeOEP molecule including its substituents is increased contrary to the unmetalated species. This molecular contrast difference was already reported in the literature for the metalation of tetraphenylporphyrins with Co. Due to the interaction of the metal center with the Ag(111) surface, the corresponding UP spectra of CoTPP show an increased density of states around 0.6 eV below the Fermi edge, which is present in the STM images as increased contrast in a certain range of the bias voltage.[235] The same situation applies for the here observed increased contrast of the ethyl substituents of the FeOEP molecules in the intermixed layer (Fig. 4.19 (a)). The effect is not visible for the intermixed OEP-rich domain at positive polarity (Fig. 4.19 (b)). There, the difference in contrast between the substituents of the FeOEP molecules and those of the OEP molecules is absent. A similar phenomenon was not observed for FeHEDMC, where the ethyl substituents exhibit the same brightness as for unmetalated HEDMC molecules.

A closer inspection of two metalated HEDMC and OEP molecules reveals the appearance of the metal center and the influence of the tunneling polarity. The Fe ion in the center of the porphyrin macrocycle is visible at negative as well as at positive polarity. In contrast, the corrole molecule features a protrusion and a clear dinstinction of the metal center at negative polarity only (Fig. 4.20 (a)), while a dark depression in the center is present at positive polarity (Fig. 4.20 (b)). This observation is far from being coincidental, as it occurs in all images

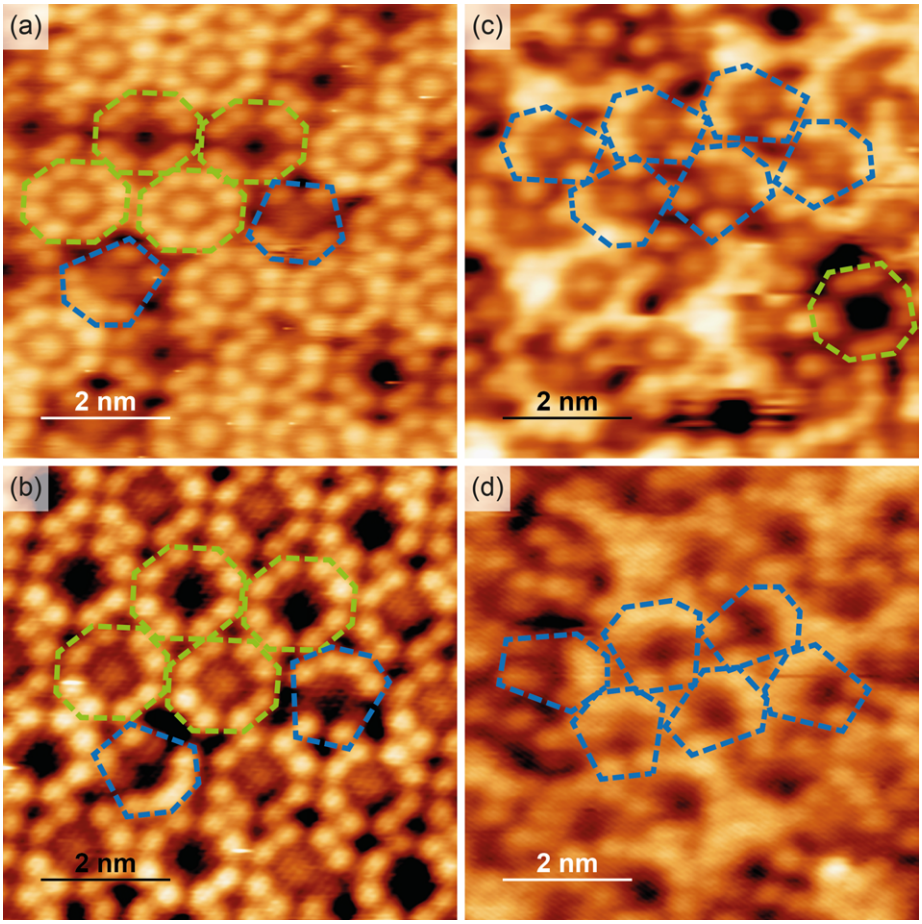

Figure 4.19: Partially Fe metalated (a, b) OEP-rich and (c, d) HEDMC-rich domains. Metalated and unmetalated HEDMC and OEP species are enframed with blue and green dashed lines, respectively. The STM images were recorded at negative and positive polarity with respect to the sample to probe (a, c) occupied and (b, d) unoccupied states. Tunneling parameters: (a) −1.06 V, −0.05 nA, 100-160 K; (b) +1.06 V, +0.10 nA, 100-160 K; (c) −1.49 V, −0.07 nA, 100-160 K; (d) +1.74 V, +0.11 nA, 100-160 K.

(*cf.* Figures 4.19 (a), (c) *vs.* (b), (d)). At this point, it should be repeated that occupied electronic states of the sample are probed at negative polarity of the sample bias voltage, while unoccupied states are probed at positive polarity. The different behavior of the metal centers corroborates the previous findings in the spectroscopic investigations. The appearance of the metal center as well as the influence on the contrast of the ethyl substituents differs for FeHEDMC and FeOEP. Therefore, it can be concluded that the electronic properties of the metal ions in FeHEDMC and FeOEP and thus the interaction of the metallotetrapyrroles with the substrate is significantly different.

Figure 4.21 illustrates the periodic structure of the OEP domains by a superimposed grid. The corrole molecules are integrated in the structural arrangement and occupy the same positions as the porphyrin molecules. Since it is not known whether the adsorbate overlayer is commensurate with the substrate layer, no statement on the adsorption sites occupied by the FeHEDMC and FeOEP molecules is possible. However, it can be excluded that an adsorption site effect is responsible for the contrast difference of the metal center in FeHEDMC at negative and positive polarity due to the presence of this phenomenon in all metalated

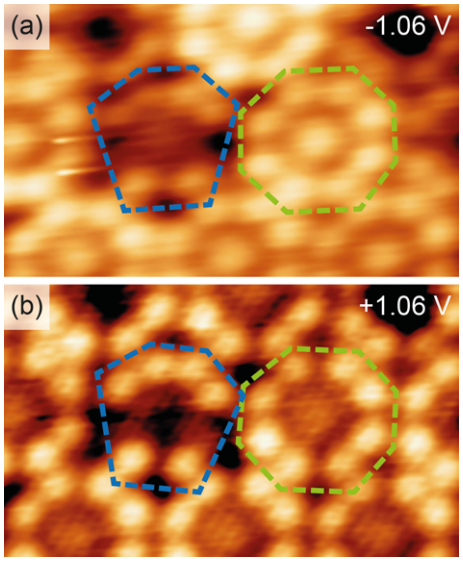

Figure 4.20: Detail STM images of Fe metalated HEDMC (blue) and OEP (green). The distinct difference in the center of FeHEDMC between the STM images at (a) negative polarity (occupied states of the sample) and (b) positive polarity (unoccupied states of the sample) can be explained by considering the density of states observed in UPS measurements. Tunneling parameters: (a) −1.06 V, −0.04 nA, 100-160 K; (b) +1.06 V, +0.10 nA, 100-160 K.

HEDMC macrocycles even in the not so well ordered HEDMC-rich phase. Interestingly, one of the FeHEDMC molecules in Figure 4.21 is rotated by 90° at the recording of the second image. The ability of HEDMC molecules to rotate is the outcome of its slightly smaller size and less intermolecular interaction of the ethyl substituents with the surrounding FeOEP molecules. Such rotations of the OEP molecules cannot be detected due to the symmetry of the molecule.

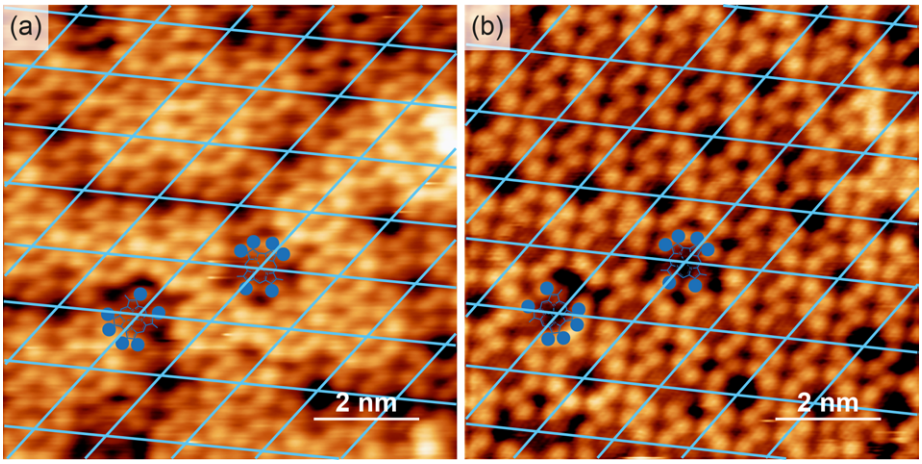

Figure 4.21: Overview STM image of a mixed layer of FeOEP and FeHEDMC. The regularity of adsorption sites is determined by the superimposed grid. Note that the FeHEDMC molecule in the lower left corner is able to rotate by 90° in the time frame of the measurements. Tunneling parameters: (a) −1.06 V, −0.04 nA, 100-160 K; (b) +1.06 V, +0.10 nA, 100-160 K.

To elucidate the contrast mechanisms in STM images of metalated tetrapyrroles, an additional method is needed. Since mainly valence states of the investigated molecules are responsible for the molecular contrast, UPS measurements can provide the required insight.

Monolayers of free-base 3H-HEDMC and 2HOEP as well as the dehydrogenated 2H-HEDMC and the corresponding metallotetrapyrroles were studied (Fig. 4.22). The degree of metalation was determined from the peak integrals in the corresponding N 1s spectra and is 85% and 86% for FeHEDMC and FeOEP, respectively. For comparison, the UP spectra of the clean Ag(111) substrate and with deposited Fe are shown. 3H-HEDMC on Ag(111) (green) gives rise to a prominent signal at a binding energy of 1.7 eV, which is attributed to the highest occupied molecular orbital of the macrocycle and which is also present in the spectra of 2H-HEDMC (orange) and FeHEDMC (red) at 1.4 eV. The small signal close to the FERMI edge in the spectrum of 3H-HEDMC is associated with the surface state of the Ag(111) substrate and result of a coverage below one monolayer. Compared to the FeHEDMC spectrum, FeOEP shows a significant intensity close to the FERMI edge (highlighted in blue). Similar intensity was observed in previous studies on FeTPP adsorbed on Ag(111).[118] To understand the fingerprints of metalloporphyrin molecules, Florian BUCHNER *et al.* calculated the energy levels and examined them with regard to the electron density recorded in STM images.[236] The broad signal of FeTPP close to the FERMI edge is attributed to electronic interaction of the formerly unoccupied d_{xz}/d_{yz} orbitals of the Fe atom with the Ag(111) surface. DFT calculations of the projected partial density of states (PDOS) of unsubstituted Fe-porphine on Ag(111) performed by Jan HERRITSCH reveal a similar contribution of the metal orbitals.[232] The intensity close to the FERMI edge can mainly be attributed to the d_{xz}, d_{yz} and $d_{x^2-y^2}$ orbitals. Therefore, the substituents seem to have no significant influence. The contrast mechanism observed in the here reported experiments can be interpreted considering the probed states in STM images and the literature results. The assumption can be made that the substrate-interaction related intensity of the occupied states in FeOEP visible in the UP spectrum is intersected by the FERMI edge and continues with unoccupied states. Therefore, the metal center is visible both at negative polarity of the tunneling process probing occupied states and at positive polarity probing unoccupied states. In contrast, FeHEDMC most likely does not exhibit enhanced intensity symmetrically distributed around E_F. Therefore, the appearance of the Fe ion in the center of the corrole macrocycle features a bias voltage dependent behavior.

UPS and STM measurements reveal that the differences in the electronic states of FeOEP and FeHEDMC persist in the monolayer, *i.e.*, when the complexes undergo electronic interaction with the Ag(111) surface. XP spectra of monolayer do not permit the determination of the exact formal oxidation state due to the increased interaction with the substrate but the core electronic states of the metal centers in FeOEP and FeHEDMC still show differences in the corresponding XP spectra. Furthermore, the NEXAFS measurements revealed different peak structures.

4.2.2 Metalation of Corrole with Cobalt

In her PhD thesis, Min CHEN performed investigations on the metalation of 3H-HEDMC with Co on Ag(111). To study the organometallic complex without electronic interference by the substrate, a multilayer corrole was metalated by post-deposited Co in an increasing amount. Due to the emerging of a third species in the N 1s region at 398.9 eV, the corresponding XP spectra reveal that the intact 3H-HEDMC is metalated. The parallel occurring decrease of

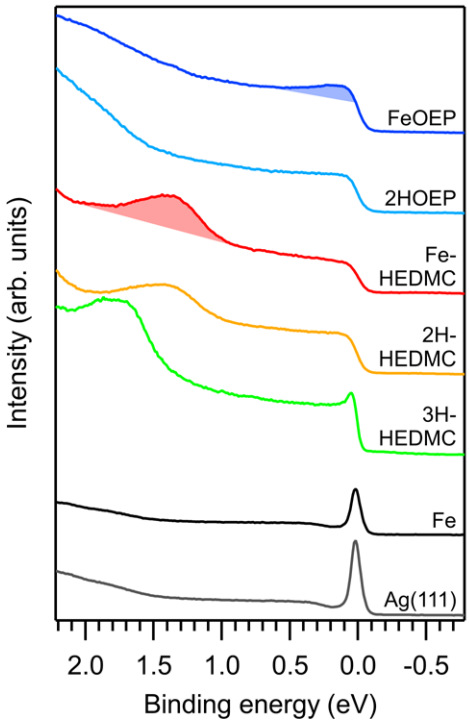

Figure 4.22: Normalized UP spectra of free-base and Fe metalated tetrapyrrole monolayers. The spectra of the clean substrate and of an Fe submonolayer are given for reference. In contrast to the FeHEDMC layer, FeOEP features an enhanced intensity close to the FERMI edge. The intensity at the colored area in the FeOEP spectrum is attributed d-orbital character of the metal center. The colored area in the FeHEDMC originates from the former HOMO of the ligand, but probably contains also some d-orbital character. Photon energy: $h\nu = 21.22\,\text{eV}$. Photon incidence angle: 35°. Electron emission angle: 0° (normal emission).

the unreacted pyrrolic and iminic species at 399.8 eV and 397.7 eV, respectively, proves the participation of all four nitrogen atoms in the complexation reaction. To unveal the oxidation state of the metal center, CHEN analyzed Co 2p XP spectra of multilayers and compared the CoHEDMC results to a CoTPP compound. The Co(II)-porphyrin complex is paramagnetic due to an unpaired electron spin in the Co 3d subshell, which induces multiplet effects in the XP spectra. This multiplet structure is absent in the CoHEDMC experiment leading to the conclusion that the corrole complex is diamagnetic. Consulting other diamagnetic Co(III) complexes in the literature, it was suggested that the metal in CoHEDMC is in its + III oxidation state. As observed in this work for FeHEDMC, the information from the monolayer XPS experiments are not unambiguous with respect to the formal oxidation state due to interactions with the substrate. Further insight was gained by means of UV photoelectron spectroscopy. The valence states at 0.2 eV for CoHEDMC and at 0.6 eV for CoTPP were attributed to the metal centers. Similarities to the valence state of the corrole complex were previously reported for isoelectronic Fe(II) in a FeTPP complex.[118] This observation suggested a + III oxidation state of the Co ion in CoHEDMC. However, CHEN's experiment showed a substantial influence upon interaction with the Ag(111) surface.[34]

To substantiate the investigations, this work contributes experiments probing the occupied and unoccupied electronic states by means of STM and NEXAFS. The success and efficiency of the metalation process was examined in an STM experiment on a partially metalated mono-

layer. Figure 4.23 (a) shows the unmetalated monolayer of 3H-HEDMC generated on a cooled Ag(111) substrate by deposition at a flux of 0.08 nm min^{-1} for 3 min. The low intramolecular resolution allows to identify the molecules as protrusions with a dark center. Another sample was prepared in the same way with a subsequent exposure to Co atoms deposited at a low ion current of 3.7 nA for 10 s, which corresponds to the amount of Co necessary to metalate half of the close-packed monolayer. Additionally, the sample was annealed to 300 K for 3 min to trigger the metalation reaction. The corresponding STM image (Fig. 4.23 (b)) reveals the presence of molecules with dark centers and molecules appearing as bright protrusions, which can be attributed to a successful metalation. Similar observations were made by Yun Bai *et al.* for an intermixed layer of 2HOEP and CoOEP.[237] A low amount of Co did not react and is visible as bright spots with a larger size and contrast indicating a three-dimensional aggregation.

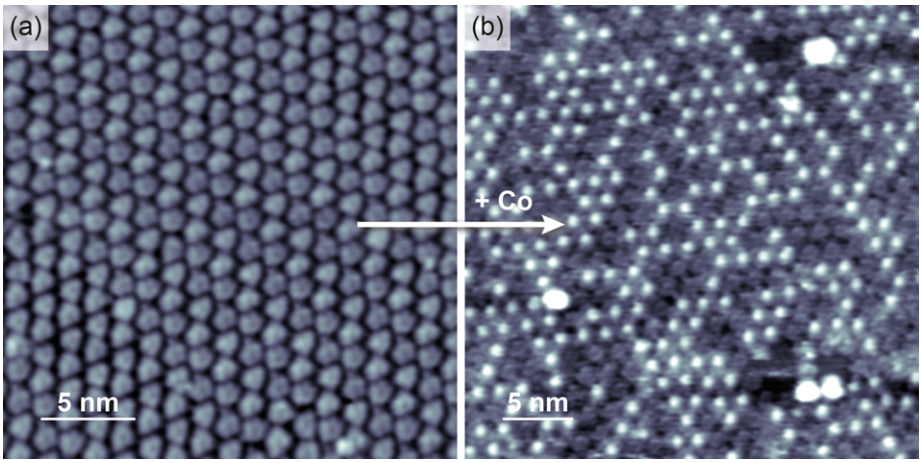

Figure 4.23: Overview STM images of 3H-HEDMC and CoHEDMC on Ag(111). (a) Unmetalated monolayer of 3H-HEDMC. (b) The monolayer was partially metalated by deposition of the corresponding amount of Co. The larger bright features result from Co clusters. Tunneling parameters: (a) −1.86 V, −1.07 nA, 170 K; (b) −1.16 V, −0.78 nA, 160 K.

A comparison of unmetalated 2H-HEDMC and CoHEDMC with submolecular resolution reveals that the new image feature is indeed located in the center of the molecule. 2H-HEDMC instead of 3H-HEDMC was deliberately chosen to further investigate whether the interaction of the free ligand with the substrate results in a different appearance. The measurements revealed that single 2H-HEDMC and 3H-HEDMC molecules are indistinguishable in the STM images. The unmetalated corrole (Fig. 4.24 (a)) shows a depression in the center of the macrocycle, while the same position appears as protrusion in the case of the Co metalated counterpart (Fig. 4.24 (b)).

The investigation of single metalated HEDMC molecules allows only general statements on the metal center, since the thermal stability in the VT-STM measurements were not suitable to permit scanning tunneling spectroscopy, *e.g.*, to study the local density of states by means of $\mathrm{d}I/\mathrm{d}V$ curves. Further insight into the electronic states was therefore achieved by comparing CoHEDMC with the formal Co(II) complex CoOEP. The similar substitution pattern – six ethyl and two methyl moieties *vs.* eight ethyl substituents – provides a comparable chemical environment and simultaneously a proper differentiation of the molecules. A mixed layer of

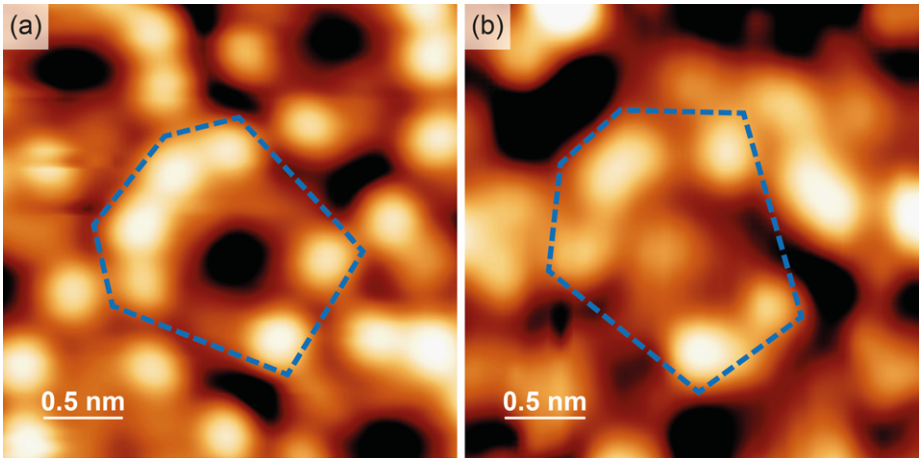

Figure 4.24: STM images of single unmetalated and metalated HEDMC molecules on Ag(111). (a) Unmetalated 2H-HEDMC molecule. Due to thermal drift, the image was distortion corrected. (b) Metalated CoHEDMC molecule. The metal center appears as protrusion. Tunneling parameters: (a) −1.58 V, −1.09 nA, 160 K; (b) −0.94 V, −0.77 nA, 150 K.

CoHEDMC and CoOEP was prepared to study both complexes under the identical tunneling and tip state conditions. Approximately 0.5 ML_{ads} of 3H-HEDMC was deposited onto a cooled Ag(111) crystal. Subsequently the layer was metalated by post-deposition of Co and annealing to 300 K for 3 min. Commercially acquired CoOEP was evaporated onto the sample at a flux of 0.08 nm min^{-1} for 2 min. As visible by the mobile features in Figure 4.25 (a), the total coverage deviates from a close-packed layer. Furthermore, the STM measurement suffered from a strong thermal drift. Nevertheless, an arrangement of adjacent cobalt-corrole highlighted by blue dashed lines and cobalt-porphyrin molecules (green) can be detected. While the metal center of the porphyrin molecules emerges as bright protrusion, the Co ion in the cavity of the corrole macrocycle is less pronounced. The magnification (Fig. 4.25 (b)) shows that also the ethyl groups of both molecules are differently contrasted. As a result of these findings, it can be proposed that the electronic states of the metal centers and their influence on the tetrapyrrole macrocycles are distinctly different as it would be expected according to the formal oxidation states of the metal ions in both complexes in the gas phase.

Since the here presented STM measurements were conducted at negative polarity and thus occupied electronic states were probed, UP spectra can be consulted for an advanced interpretation. In his Master's thesis, Jan Herritsch measured spectra of unmetalated HEDMC and unmetalated as well metalated OEP monolayers and compared those to CoHEDMC from Chen's work.[232] Additionally, he performed DFT calculations on the adsorbate structures and the PDOS of unsubstituted Co-corrole and Co-porphine on Ag(111). In contrast to the unmetalated macrocycles, the UP spectra show increased intensity at 0.6 eV and 1.6 eV for CoOEP monolayers and slightly closer to the Fermi edge intensity at 0.2 eV and 1.2 eV for the corresponding CoHEDMC monolayer. The PDOS of the Co center was projected onto the atomic d-orbitals. The intensity at 1.6 eV can be assigned to the $d_{x^2-y^2}$ states of the cobalt-porphyrin, while the signal at 0.6 eV results from the d_{xz} and d_{yz} states with a small contribution from the d_{z^2} state. A similar distribution was found for the cobalt-corrole, although the d_{z^2} state contributes to both features here. Since a tunneling voltage of −0.86 V

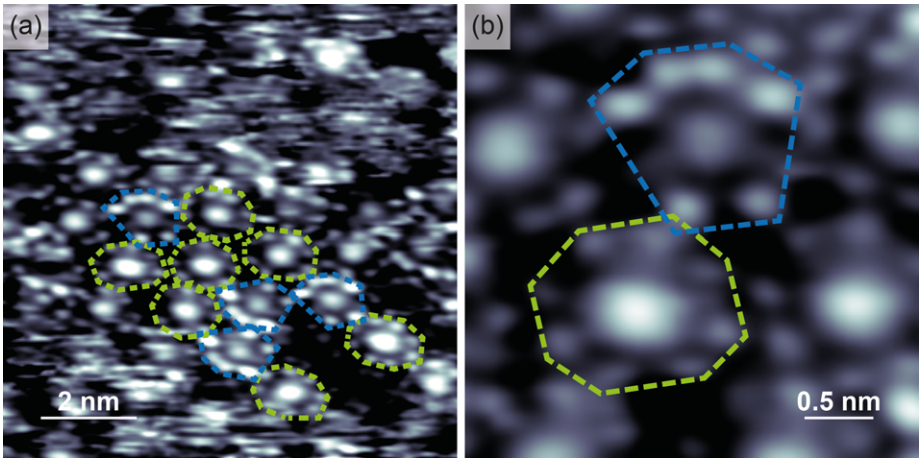

Figure 4.25: Comparison of CoHEDMC and CoOEP in a co-deposition STM experiment. (a) Overview STM image of a mixed layer of CoHEDMC (blue) and CoOEP (green) on Ag(111). The HEDMC was metalated by post-deposition of Co with subsequent annealing to 300 K. (b) Magnification of two adjacent molecules. The metal center of the corrole appears brighter. Due to thermal drift, the image was distortion corrected. Tunneling parameters: −0.86 V, −0.60 nA, 165 K.

was used in the STM measurements shown in Figure 4.25, it can be concluded that the contrast in the center of the macrocycles mostly corresponds to the UPS peaks at lower binding energy. The difference in contrast can be recognized in the UPS comparison. However, the partial charges according to the Bader analysis were calculated to be +0.87 and +0.85 for the metals atoms in Co-porphine and Co-corrole, respectively.

While the previous investigations are mainly focused on the occupied states, NEXAFS spectroscopy was performed to probe unoccupied states of the metal center. HEDMC and CoOEP were prepared as thick multilayers on a Ag foil. The type of the substrate can be neglected in this case, since the thickness of the multilayer provides a decoupling from the substrate. The multilayer of HEDMC was treated with post-deposited Co. The amount of the metal is sufficiently enough to metalate the three top-most layers of the tetrapyrroles. The samples were investigated by means of NEXAFS spectroscopy. The spectra of CoOEP and the CoHEDMC were recorded at an photon incidence angle of 45° (Fig. 4.26). Note that slightly different settings for the slit of the monochromator and different statistics were used. However, these differences can be neglected in the qualitative analysis here. While the Co L_2-edges at higher photon energy appear broad and without a difference, the Co L_3-edges exhibit a characteristic splitting. Both spectra show a small distinguishable resonance directly after the adsorption edge. The following resonance appears as one peak at 781.4 eV in the case of the CoHEDMC multilayer, while the resonance observed for the CoOEP sample is split into two features at 780.6 eV and 781.8 eV. The splitting of the resonance at the Co L_3-edge in the CoOEP spectrum is observed for an angle of incidence of 45° as well as for 90°. Heiko Peisert *et al.* studied various metallophthalocyanines. In their NEXAFS spectra, the splitting effect was as well observed for CoPc.[247] Corresponding to the absent splitting at the Co L_3-edges of CoHEDMC, FePc exhibits a similar structure. Due to the isoelectronicity of Co(III) and Fe(II), it can be expected that the oxidation state of the Co center in CoHEDMC in the bulk phase is + III.

The coverage of a full monolayer of MTPP on Au(111) corresponds to only 0.037 molecules

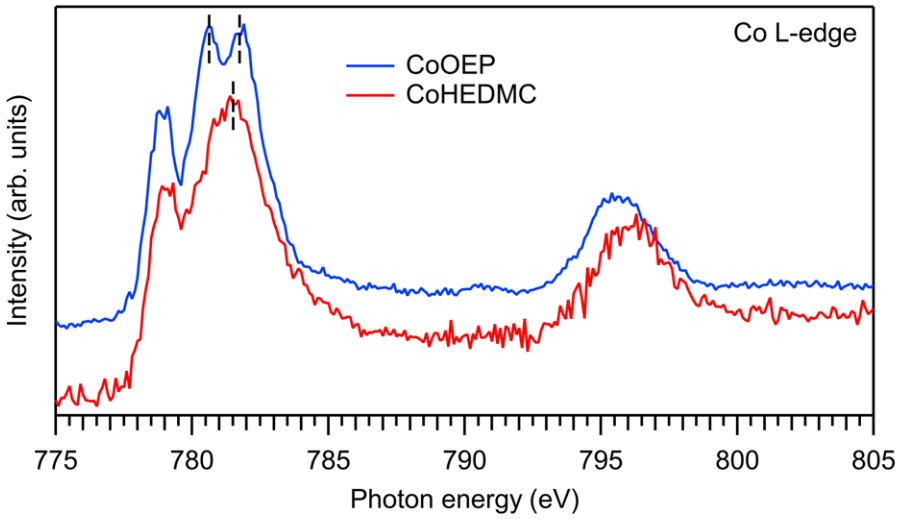

Figure 4.26: Co L-edge NEXAFS spectra of CoOEP and CoHEDMC multilayers on Ag(111). The spectra show a distinct difference in the resonances between 780 eV and 782 eV. Angle of incidence: 45°.

or 0.037 metal centers per surface atom.[109] This situation can be transferred to the here investigated monolayers on Ag(111), since the lattice constants of Au(111) and Ag(111) are very similar. Due to the low amount of metal ions, only very low intensities are observed in the corresponding NEXAFS spectra in the following experiment. To overcome this limitation, the spectral region was measured multiple times and the spectra were averaged. Figure 4.27 shows the background corrected spectra of the Co L_3-edges of a CoOEP and a partially metalated CoHEDMC monolayer. CoOEP features a mostly symmetric resonance at 780 eV. The spectrum of CoHEDMC is dominated by a 2 eV broader peak with a shoulder at 784 eV. Due to the limitation in intensity and the air-instability of Fe(II) complexes, which would serve as isoelectronic objects of comparison, no literature spectra were available for a further interpretation and comparison of the monolayer data.

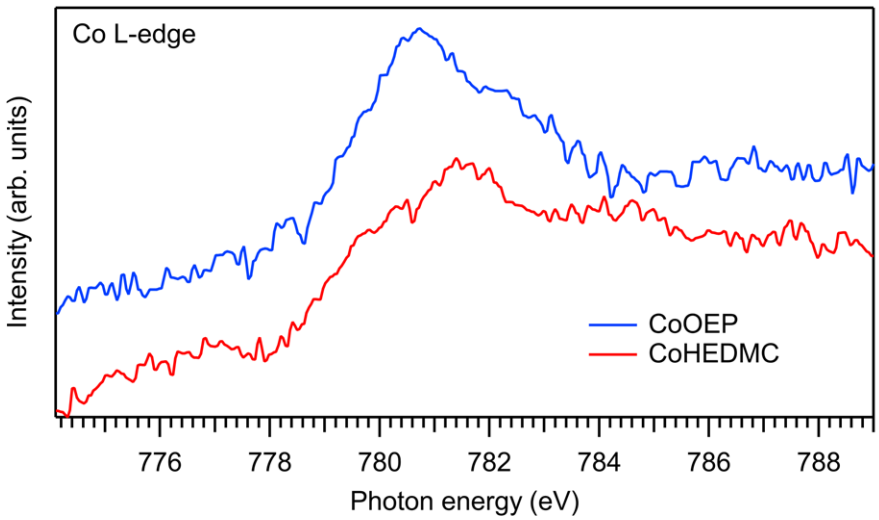

Figure 4.27: Co L-edge NEXAFS spectra of CoOEP and CoHEDMC monolayers on Ag(111). Although the resonance peaks are similar, the feature of CoHEDMC is by 2 eV broader. Angle of incidence: 45°.

To conclude, the measurements revealed in congruence to the study by Min Chen that the Co ion in CoHEDMC most likely possesses a + III oxidation state in the multilayer. Upon direct contact with the surface in the monolayer, the strong interaction with the surface prevents an unambiguous evidence for the character of the oxidation state, although a certain difference between the electronic states of the corresponding metalated corrole and porphyrin remains.

4.2.3 Metalation of Corrole with Nickel

A third d-block metal which was employed to metalate 3H-HEDMC is Ni. The metalation reaction was studied in a deposition series monitored by means of XPS. The preparation of the 3H-HEDMC monolayer was carried out as aforementioned. To avoid any interference with the mono-dehydrogenation of the −NH− groups due to interaction with the surface, the temperature of the Ag(111) substrate was kept at approximately 100 K. Ni was deposited at the lowest stable ion current of 1 nA to avoid unnecessary cluster formation. The amount of Ni was gradually increased in steps of 20 s with subsequent annealing to 180 K for 3 min. The given duration refers to the total deposition time.

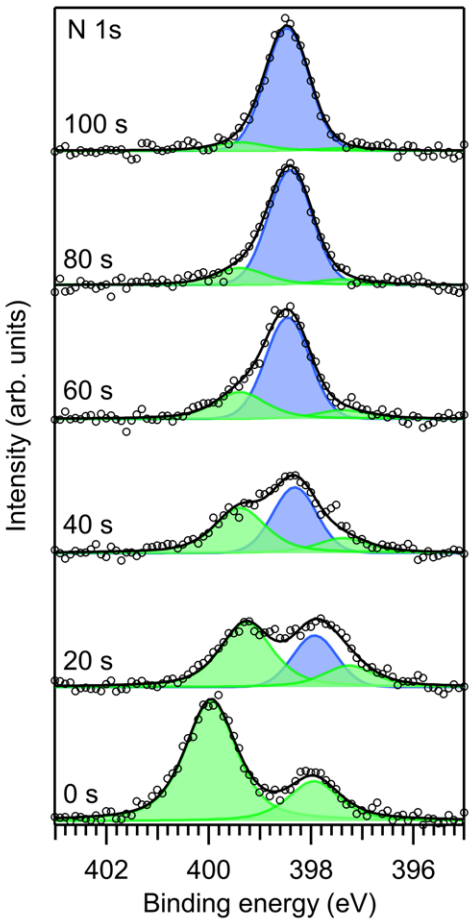

Figure 4.28: N 1s XP spectra of 3H-HEDMC with gradually post-deposited Ni. Ni atoms were deposited for a total time of 0-100 s onto a monolayer 3H-HEDMC on Ag(111). Unreacted −NH− and the −N= species are represented by the green fit integrals. Upon deposition, a third component, −N−Ni− (blue), arises.

In Figure 4.28, the resulting N 1s XP spectra are shown. While the pristine 3H-HEDMC is represented by the pyrrolic and iminic nitrogen species (green) located at 400.0 eV and 397.9 eV in the expected ratio of 3 : 1, the reacted species arises at 397.9 eV (blue) upon deposition of Ni. After a total deposition time of 80 s, the unreacted species are nearly vanished. The change from a doublet in the unmetalated state toward the singlet proves the equivalent binding situation between the metal center and all four nitrogen atoms in the coordination reaction and thus the formation of NiHEDMC as observed before in the reactions with Fe and Co. The shift of the unreacted nitrogen species toward lower binding energy is at least partially caused by a work function change.

To further investigate the electronic state of the central Ni ion, the spectral region of the Ni 2p orbitals was measured for monolayers of NiHEDMC (orange) formed by direct metalation and NiOEP (light blue) for comparison (Fig. 4.29). The monolayer of 3H-HEDMC was exposed to a substoichiometric amount of Ni to avoid an influence of unreacted Ni on the electronic states of the complexes. NiOEP was deposited onto Ag(111) from the commercially available substance. To have the Ni(0) signal as reference, the monolayers of NiHEDMC and NiOEP were additionally treated with an excess amount of Ni shown in red and blue, respectively. The Ni $2p_{3/2}$ signals observed for both organometallic complexes differ from the Ni(0) position. While the signal is located at 855.1 eV for NiHEDMC, the position of the NiOEP peak is at 855.3 eV. Although a difference in the signal positions of the Ni ions can be found, no conclusion can be drawn with respect to the expected formal oxidation state, as the substrate interacts significantly with the metal center.

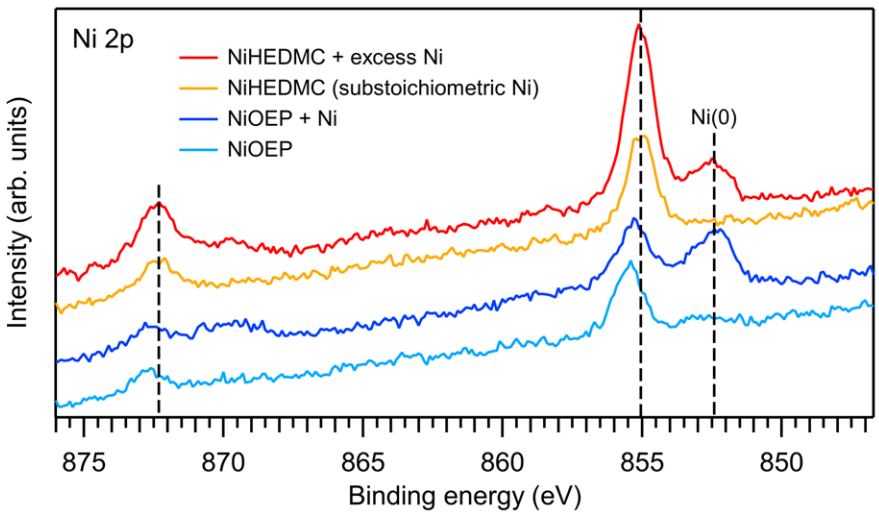

Figure 4.29: Comparison of Ni 2p XP spectra of NiHEDMC and NiOEP monolayers on Ag(111). NiHEDMC was produced by vapor deposition of a substoichiometric amount of Ni onto a monolayer of 3H-HEDMC. NiOEP was commercially acquired. An excess of Ni was deposited for reference.

To gain further insight into the metalation, STM experiments were performed on the metalated monolayer. The monolayer 3H-HEDMC was prepared on Ag(111) as before. Onto this monolayer, Ni was deposited for a total time of 80 s, enough for the metalation of the full monolayer. To ensure a high metalation yield and thus a prevalence of metalated corrole molecules, the substrate was subsequently annealed to 400 K for 3 min. The success of the

metalation was ensured by consulting the corresponding N 1s XP spectra of the investigated sample. In the STM measurement, the NiHEDMC molecules appear laterally ordered. The center of the macrocycles exhibits a dark depression at negative voltages from −0.86 V to −1.54 V (Fig. 4.30). With increasing voltage, the appearance of the molecule changes. While the corrole macrocycle is pronounced at −0.86 V, the ethyl substituents dominate the STM image at −1.54 V. A similar situation applies at positive bias voltages, at which the center of the nickel-corrole complex is as well present as depression (Fig. 4.31). The chemical environment is differently pronounced. The contrast changes at positive polarity resemble those at negative polarity, but the ethyl moieties are more prominent. Furthermore, the position of the methyl groups, which were not observed in aforementioned experiments, presents itself with a slightly increased contrast. It seems that the accentuation of the macrocycle and especially the methyl groups is associated with the Ni metalation. In contrast to the metal center of FeHEDMC, evidence for the metal ion is absent at both polarities. The dark center was observed before by Louis Scudiero for the case of Ni(II)-porphyrins.[234,251]

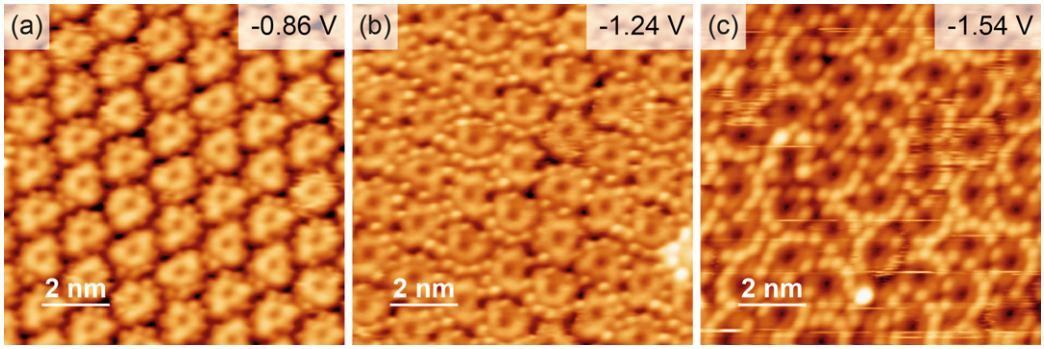

Figure 4.30: STM images of NiHEDMC at different negative polarities. From (a) toward (c), the strong presence of the macrocycle decreases and the ethyl moieties become more prominent. Tunneling parameters: (a) −0.86 V, −0.51 nA, 150 K; (b) −1.24 V, −0.40 nA, 150 K; (c) −1.54 V, −0.32 nA, 150 K.

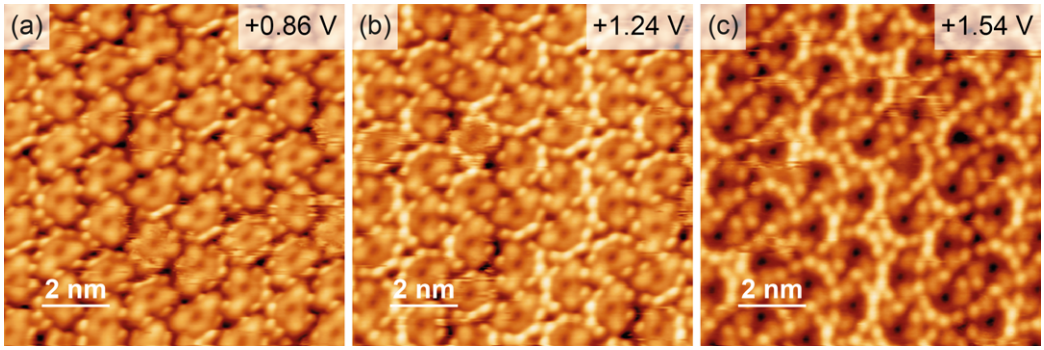

Figure 4.31: STM images of NiHEDMC at different positive polarities. The images resemble those at negative polarity. However, the ethyl substituents are more dominating at all voltages. Tunneling parameters: (a) +0.86 V, +0.39 nA, 150 K; (b) +1.24 V, +0.52 nA, 150 K; (c) +1.54 V, +0.39 nA, 150 K.

For an additional analysis of the occupied valence electronic states, UPS measurements of NiHEDMC and NiOEP monolayers were compared (Fig. 4.32). NiOEP shows increased intensity at 0.7 eV. In the spectrum of NiHEDMC, two features are present at 1.3 eV and 2.0 eV. The lower lying electron density is similar to the intensity observed at 1.7 eV for 3H-HEDMC and suggested to result from the HOMO of the free ligand. To assign the feature

to the elements in the metalorganic complex and to the d-orbitals of the central Ni ion, Jan-Niclas Luy calculated the PDOS of NiHEDMC by means of DFT.[233] Indeed, the intensity at 1.3 eV results from the former HOMO of the organic ligand, which is now shifted to lower binding energies. The projection of the PDOS on the d-orbitals reveals that the peak at 2.0 eV experiences contributions from the d_{xz}, d_{yz} and d_{z^2} orbitals. A higher bias voltage in the STM experiments would probably have provided contrast in the cavity of the macrocycle but this voltage was not achievable, since increasing the voltage led to instabilities in the tunneling condition.

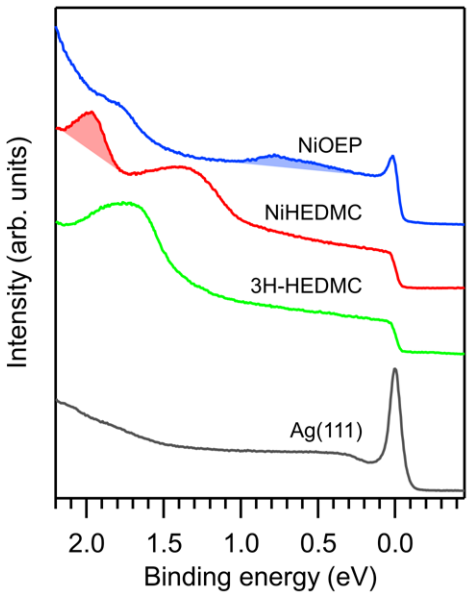

Figure 4.32: UP spectra of free-base and Ni metalated tetrapyrrole layers. NiOEP exhibits an electron density close to the Fermi edge, where no intensity is visible in the NiHEDMC spectrum. The spectrum of the clean substrate is given for reference. The intensity at the colored areas results from the states with d-orbital character of the metal ion. Photon energy: $h\nu = 21.22$ eV. Photon incidence angle: 35°. Electron emission angle: 0° (normal emission).

4.3 Metalation of Tetrapyridylporphyrins with Lead

In the group of Prof. Dr. Nian Lin from the Hong Kong University of Science and Technology, the reaction of 2HTPyP with Pb was studied by means of STM.[252] Upon deposition of Pb onto close-packed domains of 2HTPyP on Au(111), the apparent height of some molecules increases from 2.1 Å to 3.0 Å above the surface (Fig. 4.33). Variation of the amount of deposited Pb reveals a proportionality with the number of bright appearances. Annealing of the sample leads to a gradual decrease of apparent heights toward the lower species. The question arises whether PbTPyP is the product of the metalation reaction, since the images after initial Pb deposition resemble the results of other porphyrin metalations, and how the behavior upon annealing can be explained. Furthermore, the geometry of the possible metalloporphyrin is of interest, since the Pb(II) cation is unlikely to be incorporated directly in the cavity of the macrocycle due to the relatively large ionic radius compared to the ionic radii of the other here studied transition elements in tetrapyrrole metalations. *E.g.*, from CeTPP, it is known that the Ce ion sits above the macrocycle plane, since the metal center is too big for a planar complex.[113] To address the metalation reaction, an XPS heating series was employed.

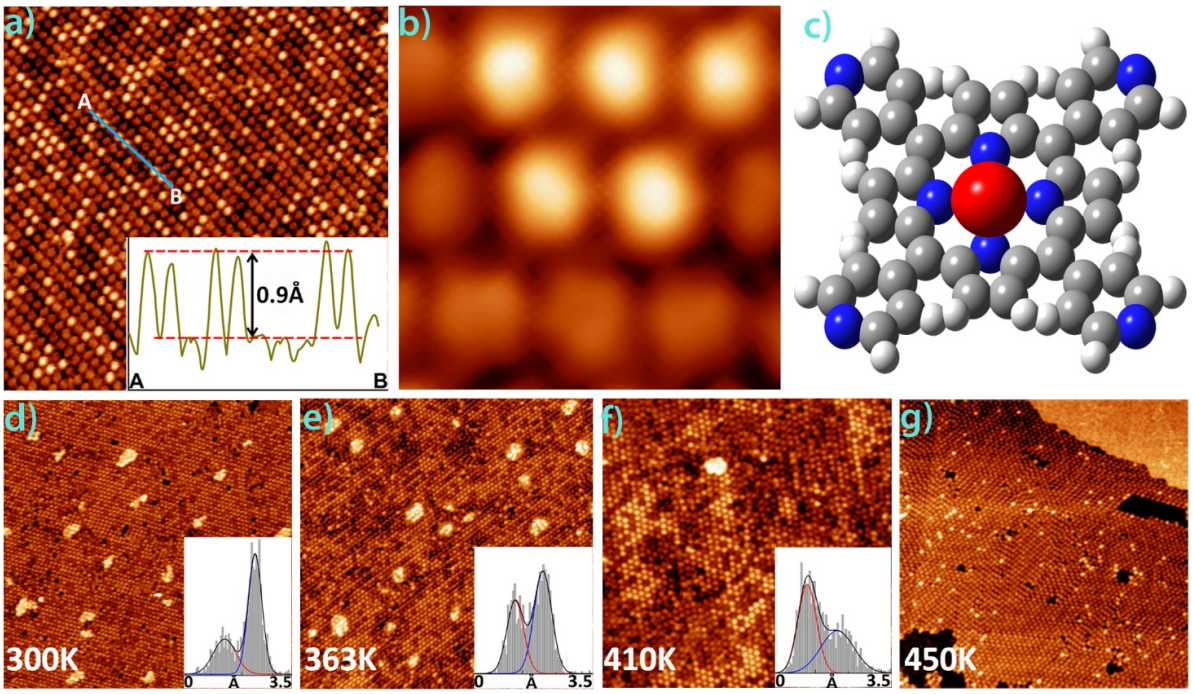

Figure 4.33: STM images of a monolayer 2HTPyP with post-deposited Pb as measured in the group of Prof. Dr. Nian Lin. (a) The overview image shows that some 2HTPyP molecules exhibit a larger apparent height after dosing of Pb. The inset reveals the difference in the height profile of the molecules indicated by the blue line. (b) Close-up image of molecules with an increased apparent height and of unaffected molecules. (c) Structural model of a PbTPyP complex. (d-g) The figures show STM images after annealing to the indicated temperatures. The insets show histograms of the molecular height distributions. Image sizes: (a) $50 \times 50\,\mathrm{nm}^2$; (b) $5 \times 5\,\mathrm{nm}^2$; (d) $100 \times 100\,\mathrm{nm}^2$; (e) $100 \times 100\,\mathrm{nm}^2$; (f) $70 \times 70\,\mathrm{nm}^2$; (g) $100 \times 100\,\mathrm{nm}^2$.[252]

2HTPyP possesses N heteroatoms in the substituents. STM experiments benefit from this periphery due to increased interaction between the molecules. In XPS measurements, the absence of these heteroatoms is advantageous because additional nitrogen species impede the analysis of the nitrogen atoms in the core of the macrocycle. Therefore, 2HTPyP was replaced

by the closely related 2HTPP in the XPS experiments. Monolayers of 2HTPP (0.037 ML_{substr}) were prepared by desorption of previously vapor-deposited multilayers at 520 K. Pb was deposited by evaporation from pellets at 840 K with a flux of 0.11 nm min^{-1} resulting in a Pb coverage of 0.061 ML_{substr}. The sample was gradually annealed in the range of 300-550 K. At each step, the temperature was kept for 3 min. A multilayer Pb(0) on Au(111) was produced for comparison.

The untreated monolayer exhibits the expected pyrrolic and iminic species at 399.8 eV and 398.0 eV with a ratio of 1 : 1 in the N 1s XP spectrum (Fig. 4.34 (a), bottom). As observed before, deposition of the metallic component results in the formation of a third nitrogen species with a binding energy of 398.2 eV at room temperature (Fig. 4.34 (a), second from bottom). Simultaneously, the peak integrals of the former nitrogen species of the unreacted porphyrin are reduced indicating a metalation of the macrocycle under involvement of all four nitrogen atoms in the core. This behavior is consistent with the above discussed metalation of corrole and with the porphyrin metalation known from the literature[2,3,5] and indicates the formation of PbTPP. Unexpectedly, the reacted nitrogen species do not correspond to the amount of deposited Pb (0.061 ML_{substr}, calculated from a comparison of the C 1s peak integrals and the sum of the Pb(II) and Pb(0) integrals), which should allow the metalation of 1.65 monolayers of 2HTPP. Increasing the temperature does not result in further changes of the ratio between unreacted and reacted porphyrin as determined from the N 1s spectra until a temperature of 470 K. The spectra at 520 K and 550 K show a significant change in the position and integral of the peak assigned to the metalated porphyrins. The positions of the unreacted components were held constant during the fitting procedure. The Pb 4f spectra show also a drastic change upon further annealing (Fig. 4.34 (b)). The Pb $4f_{7/2}$ peak of metallic Pb(0) (grey) is present at 136.7 eV. Upon deposition of Pb onto the 2HTPP monolayer, two species can be identified. The peak at the same position as observed for the metallic multilayer can be attributed to Pb(0), while the other component at 138.2 eV indicates a + II oxidation state[253], which would correspond to the formation of a Pb(II)-porphyrin. Unexpectedly, the peak integral of the Pb(II) decreases with increasing temperature in favor of a rise in the integral at the Pb(0) position. This observation corresponds to the change of the reacted component in the N 1s spectra. However, a temperature-independent behavior or at least no reduction of the Pb(II) species attributed to a possibly formed PbTPP would be expected.

To achieve further insight, the spectra were analyzed quantitatively. The ratio between the peak integrals (sum of Pb $4f_{7/2}$ and Pb $4f_{5/2}$) of Pb(II) and Pb(0) changes from 1 : 1.6 upon deposition onto the 2HTPP monolayer to 1 : 7.4 after annealing to 550 K. The largest rise in Pb(0) intensity starts at 410 K. From this temperature on, changes in the reacted N 1s species are observed. A comparison of different elements has to take the atomic subshell photoionization cross sections, 0.024 Mb for N 1s and 0.3330 Mb[219] for Pb 4f, and the transmission function of the spectrometer into account as stated before. At 300 K, the ratio between reacted 2HTPP (integral of the blue colored peak) and Pb(II) is 1 : 1.3. The ratio between reacted 2HTPP and Pb(0) is 1 : 2.1. Although, the ratio between the two components 2HTPP and Pb(II) is slightly lower than expected, the quantitative and qualitative analysis of the room-temperature spectra suggest the instantaneous formation of PbTPP upon deposition

of Pb onto the 2HTPP monolayer. Judging from the temperature-dependent changes in the Pb 4f spectra and considering the out-of-plane position of the oversized metal ion in the organometallic complex, it is proposed that a Pb-up geometry with a shuttlecock shape as reported for SnPc[38,254,255] and PbPc[256] is formed initially. Due to the eletronically decoupled position above the macrocycle, the +II oxidation state is retained. It can be assumed that higher temperatures result in a change of the adsorption geometry forcing the metal ion to move from an up- to a down-position. As observed for various Co(II)-porphyrins[257,258], a substrate interaction induced reduction of the oxidation state would explain the neutral state peaks in the Pb 4f spectra.

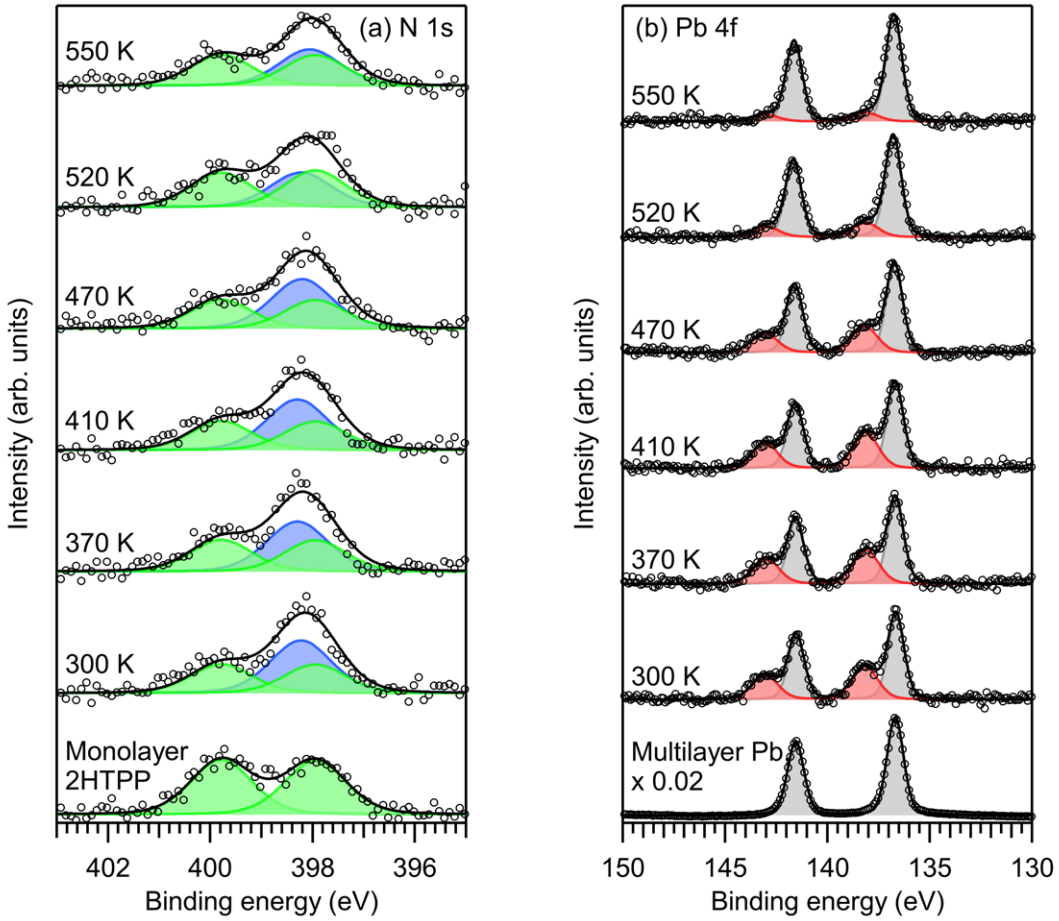

Figure 4.34: XPS temperature series of a 2HTPP monolayer on Au(111) in a range of 300-550 K after deposition of 0.061 ML_{substr} Pb at 300 K. (a) N 1s XP spectra of a pristine 2HTPP monolayer (bottom), after deposition of Pb and after annealing at the indicated temperatures. Green color represents the −NH− and the −N= species of unreacted 2HTPP. Reacted PbTPP is represented by the blue peaks. (b) Pb 4f XP spectra of a pristine multilayer Pb (bottom) shown for comparison and spectra of Pb/2HTPP/Au(111) corresponding to the spectra in (a) after deposition and after annealing. The spectra show the initial composition of Pb(0) (grey) and Pb(II) (red) and the decrease of the Pb(II) components upon annealing.

In contrast to this interpretation of the results concerning the geometry of the metalloporphyrins, preliminary DFT calculations yield a high inversion barrier of >200 kJ mol^{-1}.[259] The Bader charge analysis results in a charge of +1.38 for the Pb ion in the adsorbed state and +0.66 in the gas phase and thus a charge transfer from the metal ion to the surface. These

findings are contradictory to the assumption that the adsorption geometry changes from Pb-up to Pb-down with a simultaneous reduction of the ion by a charge transfer from the surface. Experimental and theoretical examinations on SnPc adsorbed on Ag(111) show a charge transfer similar to these theoretical results.[255,260] The mechanism of the PbTPP formation has therefore to be rectified. An explanation for the initial formation of a Pb-up geometry cannot be found, since a landing of the Pb atoms on the surface and a subsequent diffusion into the organic macrocycle seems to be more likely resulting in a Pb-down geometry. This adsorption geometry is then attributed to the Pb(II) peaks in the corresponding room-temperature XP spectrum. For PbPc, a detachment of the Pb ion upon deposition onto Pt(111) and Ag(111) was observed by N. Papageorgiou *et al.* and J. D. Baran *et al.*, respectively[256,261]. In this light, the shift from Pb(II) to Pb(0) can be interpreted as the Pb ion being detached from the TPP macrocycle. The remaining species in the N 1s formerly attributed to PbTPP, which experiences a change as well, can now be assigned to an on-surface transmetallation raising the question whether a Au atom is extracted from the surface and incorporated into a Au-porphyrin or whether the deprotonated nitrogen atoms bind to the surface. Further evidence could not be achieved at this point. The question and further necessary experiments will later be addressed in the summary (Ch. 7.1).

4.4 Reactive Coupling of Tetraphenylporphyrins on Cu(111)

If the substituents of tetrapyrrole macrocycles are terminated with reactive moieties, the molecules can undergo chemical coupling reactions. While the self-assembly of metalloporphyrins, *e.g.*, nickel-tetraphenylporphyrin[251], on metal substrates is exclusively determined by VAN DER WAALS forces, the brominated counterparts can further strengthen the robustness of the porphyrin layer by covalent linkage of the molecules. Leonhard GRILL *et al.* reported the covalent assembly of Br substituted tetraphenylporphyrins. By varying the substitution pattern of the building blocks, the structure of the nano-architectures can be steered and result in dimers, linear chains or molecular networks.[142] Sergey A. KRASNIKOV *et al.* observed well-ordered assemblies of nickel(II)-5,10,15,20-tetrakis(4-bromophenyl)porphyrin (NiTBrPP) on Au(111) upon deposition. In the structure, the molecules are close-packed with the bromophenyl lobes of adjacent molecules parallel to each other. The structure is stabilized by π–π bonding between the phenyl rings and Br···H–C hydrogen bonds.[262] Upon annealing to 525 K, the C–Br bond is cleaved and the Br 3d species in the corresponding XP spectra disappear. The authors report subsequently formed covalently bound porphyrin networks. In the here presented study, the reactive coupling of NiTBrPP on Cu(111) by means of the ULLMANN reaction will be discussed (Fig. 4.35) including the investigation of an organocopper intermediate.

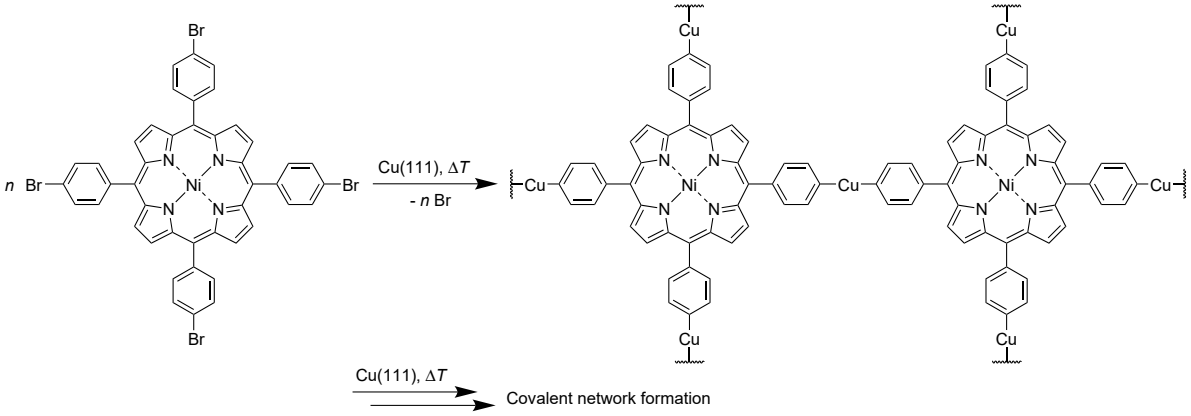

Figure 4.35: Surface-mediated coupling of NiTBrPP on Cu(111) by means of the ULLMANN reaction including an organocopper intermediate at room temperature.

A submonolayer (approximately 0.73 ML_{ads}) NiTBrPP was deposited onto Cu(111) at a flux of 0.08 nm min^{-1}. In contrast to the aforementioned situation on Au(111), the cleavage of the bromine substituents readily happens directly upon adsorption at room temperature due to the strong interaction with the copper substrate. Furthermore, Br does not desorb from Cu(111) until very high temperatures and was only removed by Ar^+ ion sputtering between the experiments. The overview STM image (Fig. 4.36 (a)) shows the presence of large islands with dimensions over 200 nm. The obvious defects in the islands originate from bromine residues. While the defects exhibit fuzzy edges due to the direct contact with the residues, the outer edges of the islands appear mostly smooth. Some dark depressions are visible and will be explained later. A magnification (Fig. 4.36 (b)) reveals the composition of the island. The bright protrusions can be attributed to the porphyrin molecules. The cavities seem to be

filled with either Br residues or Cu adatoms. However, it cannot be excluded that a double-tip is responsible for features in the cavities. The molecules are arranged in a rectangular pattern with a slight deviation from an angle of 90°. By estimation of the size of the porphyrin molecules, the formation of a two-dimensional coordination network between the debrominated NiTBrPP and Cu adatoms is concluded. To illustrate this situation, the corresponding STM image is superimposed with space-filling models. The coordination networks are similar to those observed for 2HTPyP with co-deposited Cu on Au(111).[263]

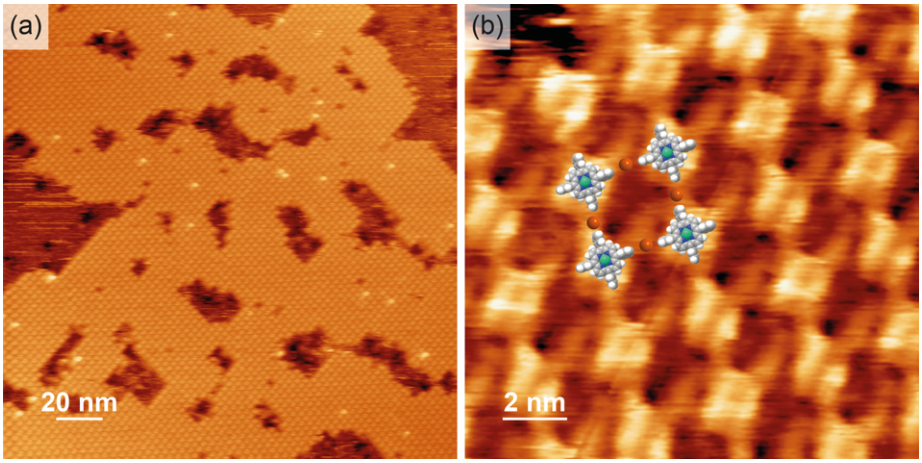

Figure 4.36: STM images with large islands of organocopper intermediates after deposition of NiTBrPP onto Cu(111). (a) The islands expand over more than 200 nm. The bromine atoms are immobilized in the cavities and outside the island. (b) Detail view of the organocopper coordination network with superimposed models. Tunneling parameters: (a) −1.24 V, −0.87 nA, 300 K; (b) −1.23 V, −1.25 nA, 300 K.

To study the behavior of the organocopper intermediate, the sample was annealed to 370 K. As visible in Figure 4.37 (a), the coordination networks disappeared. Instead, depressions in the form of equilateral triangles have formed. Porphyrin molecules are immobilized in the vicinity of those structures, while mobile species are indicated in larger distance to the triangles. The STM measurements were performed at room temperature. A close-up image reveals spot-like protrusions on the edges of the triangle. The origin of the triangular structures can be assigned to assembled bromine residues and were observed before in other studies containing Br atoms dissociated from precursor molecules on Cu(111). Dimas G. de Oteyza *et al.* describe these features as "a concomitant etching of triangular holes [...] lined along their sides by Br atoms".[264] In their study, the triangles are as well oriented only in one direction in registry to the Cu(111) substrate, although the surface lattice would also allow an other distinguishable orientation. Some adsorbed Br atoms were already visible as depressions in the overview image after the room-temperature deposition (Fig. 4.36 (a)). According to Robert G. Jones and M. Kadodwala, Br assembles in a $(\sqrt{3}\times\sqrt{3})$R30° structure at a coverage of 0.33 ML_{ads}.[265] The image resolution of the here reported triangles does not allow further quantitive evaluations. The porphyrin molecules appear bright in their center, where formerly a depression was present. It can be suggested that they exist as surface-stabilized radicalic moieties with a substantially different electronic structure.

Since the STM measurements did not provide evidence for covalent linkage, the substrate was further annealed to 500 K for 1 min. Figure 4.38 (a) presents a meanderingly linked

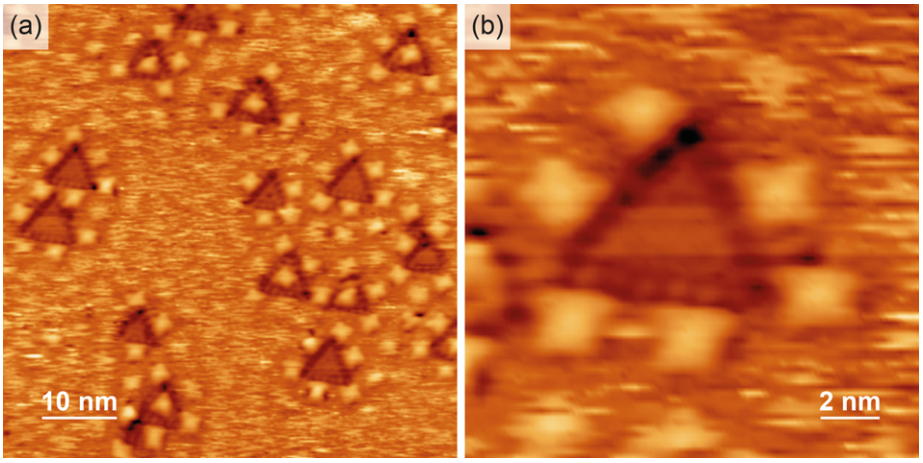

Figure 4.37: Triangular structures of bromine after annealing of NiTBrPP on Cu(111) to 370 K. On the outside, the structures are decorated with immobilized porphyrin molecules. Tunneling parameters: (a) −1.56 V, −0.71 nA, 300 K; (b) −1.56 V, −0.71 nA, 300 K.

network, which obviously consists of interlinked NiTPP macrocycles. Only one small ordered network including six porphyrin molecules can be observed (Fig. 4.38 (b)) in contrast to the findings of Sergey A. Krasnikov *et al.* However, also their results revealed only small well-ordered covalent networks of at most four molecules in a row, while the majority of molecules is linked without long-range order. In the here presented case of NiTBrPP on Cu(111), it can be concluded that the dissolving of the coordination networks upon annealing is the cause for the formation of covalent C–C to result in random orientation.

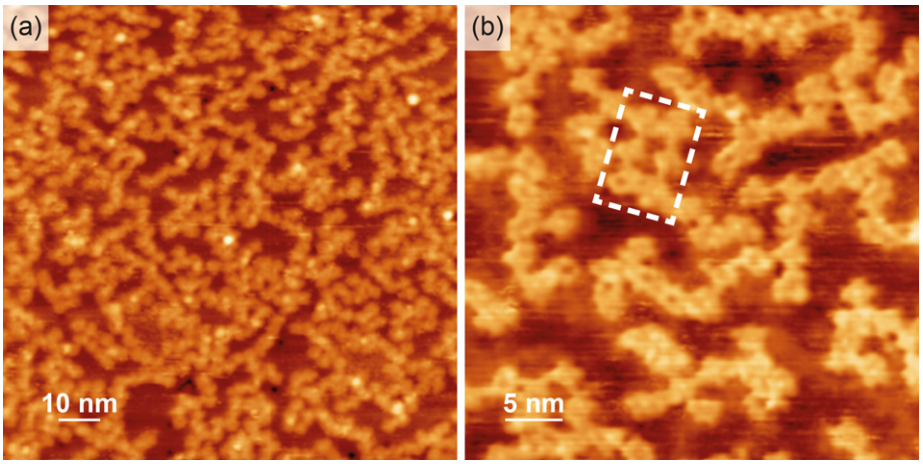

Figure 4.38: Covalently linked NiTPP molecules in disordered networks. (a) The covalently linked molecules form a meandering network without long-range order. (b) Alongside randomly connected molecules, a network formed by six molecules highlighted by the white dashed rectangle emerges. Tunneling parameters: (a) −1.16 V, −0.71 nA, 300 K; (b) −0.67 V, −0.52 nA, 300 K.

5 Aromatic Dicarbonitriles

Carbonitrile functionalization is a convenient possibility to achieve intermolecular interactions of molecules adsorbed on surfaces and thus frequently used in on-surface synthesis. Aromatic molecules terminated with carbonitrile groups were subject to intermolecular cyclization reactions and to self-assembly in large-area or spatially limited structures.

5.1 On-Surface Tetramerization of Dicarbonitriles

This project combines the ideas of on-surface synthesis with insights from metalation reactions of organic macrocycles. Due to the high technological interest in metallophthalocyanines, Mathieu Abel established an on-surface metal-assisted route to synthesize those complexes from small organic ligands.[41,266] 1,2,4,5-Tetracyanobenzene was used as a versatile precursor. Due to the four nitrile moieties, the molecules undergo a cyclization on one side as well as further polymerization of the formed octacyanophthalocyanine complexes involving the remaining nitrile groups on the periphery. By this means, polymeric networks of phthalocyanines can be generated in order to study their promising ferromagnetic or antiferromagnetic properties.[42,267–269]

The focus of the following work is to explore the synthetic route for future studies of larger (aza-)naphthalocyanines, which are thermally unstable under the harsh evaporation conditions of the physical vapor deposition. The simplest precursor of an extended naphthalocyanine subunit will be discussed here. As a dicarbonitrile-functionalized ligand (Fig. 5.1), 1′,1′,4′,4′-tetramethyl-1′,2′,3′,4′-tetrahydroanthracene-6,7-dicarbonitrile (NDN*) is subject to a tetramerization without subsequent network formation. The opposite side of the annulated system is terminated with methyl groups, which will have significant influence on the appearance in the STM images. The abbreviation NDN stands for the unsubstituted 2,3-naphthalenedicarbonitrile, while the asterisk indicates the annulation with 2,2,5,5-tetramethylcyclohexane. At this point, the abbreviation Nc* for the annulated naphthalocyanine is introduced.

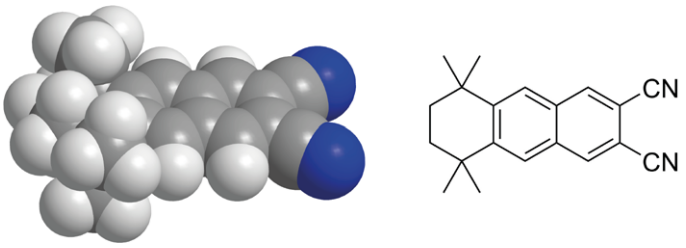

Figure 5.1: Space-filling model and Kekulé structure of the precursor 1′,1′,4′,4′-tetramethyl-1′,2′,3′,4′-tetrahydroanthracene-6,7-dicarbonitrile (NDN*).

5.1.1 Self-Metalation on Cu(111)

Preliminary experiments were performed on NDN* adsorbed on Cu(111). It was expected that upon annealing the dicarbonitrile molecules interact in a surface-mediated reaction with the

metal substrate similar to the self-metalation observed for porphyrins.[270,271]

The relatively high vapor pressure required a preparation deviating from the standard procedures, since the commonly used temperature for the bake-out of the UHV chamber could not be applied. Therefore, the chamber was pumped for approximately 48 h (base pressure $2 \cdot 10^{-9}$ mbar) before the experiment was carried out. Subsequently, the stainless steel crucible was carefully heated to degas the substance. The success of the degassing procedure was checked by monitoring the pressure, which was approximately $2 \cdot 10^{-8}$ mbar during the evaporation. A submonolayer NDN* was deposited onto Cu(111).

Initial STM images show individual molecules. Annealing to 370 K, 450 K and 500 K resulted in an increasing number of molecular clusters. Figure 5.2 reveals the formation of tetramers in a low yield after annealing to 550 K. The experimentally approximated dimension of 2.7 nm resembles the theoretically expected value of 2.7 nm for the corresponding extended Cu-naphthalocyanine (CuNc*).

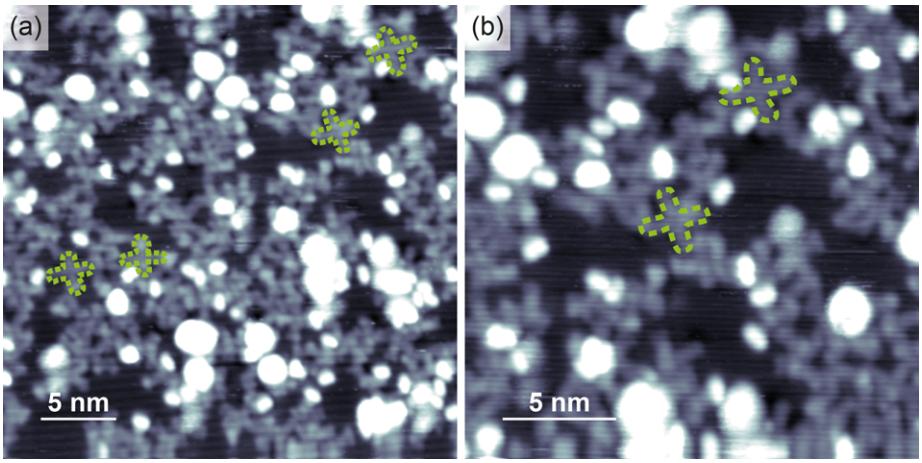

Figure 5.2: STM images of a tetramerization of NDN* on Cu(111) after annealing to 550 K. The green, dashed lines indicate individually recognizable tetramer products alongside a high number of molecules which did not undergo the desired reaction. The bright spots result from three-dimensionally aggregated molecules. Tunneling parameters: (a, b) −1.25 V, −0.14 nA, 300 K.

The low yield of tetrameric products required a variation of the sample environment. It is suggested that the tetramers are formed at surface adatoms and that the precursor exhibits an insufficiently low mobility on Cu(111) due to increased interaction between the terminal nitrile groups and the Cu substrate. Further experiments were conducted on Ag(111) as a less strongly interacting substrate, on which a higher mobility of the dicarbonitrile molecules is expected. The metal-mediated reaction was initiated by means of post-deposited Fe atoms and a subsequent annealing step. A deposition of NDN* onto Ag(111) with exposition to Ni atoms did not result in further, conclusive insights and is therefore omitted here.

5.1.2 Tetramerization Reaction with Iron on Ag(111)

NDN* was deposited onto Ag(111) at a flux of 0.13 nm min^{-1} for a duration of 15 s resulting in a closed monolayer. Subsequently, the organic layer was exposed to Fe atoms. The amount of Fe atoms was chosen in such a way that the stoichiometric ratio between the NDN* molecules and the metal atoms results in 4 : 1. An overview STM image (Fig. 5.3 (a)) shows the

presence of two phases with differently arranged molecules, while the upper right corner of the image contains disordered molecules and clusters probably formed by adsorbed Fe. A closer look (Fig. 5.3 (b)) gives insight into the phases. Phase I consists of molecules aggregated in groups of four, five and six members. The hexamers exist in two different forms, either as a close-packed group or in a cyclic form. Phase II exhibits a long-range order. Especially the structure of phase II appears to be porous, which will be clarified in a further magnification. The structures can be explained by assigning the image contrast to the moieties of the NDN* molecule. While the naphthalene backbone is planar, the sp^2 hybridized carbon atoms in the annulated ring and the methyl substituents result in a protrusion in the STM images.

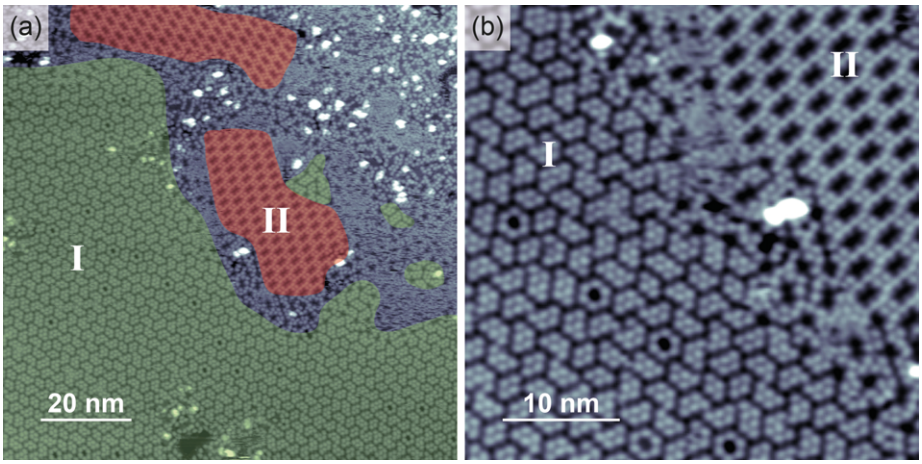

Figure 5.3: STM images of unreacted NDN* domains after deposition of Fe. (a) The overview image shows two phases (green, red) alongside disordered molecules and Fe clusters. (b) The magnification of the overview reveals details of the domains. Phase I (green) contains unreacted tetramers, pentamers and cyclic hexamers, while the molecules in phase II (red) appear to be arranged in porous structures. Tunneling parameters: 1.40 V, 0.10 nA, 165 K.

In Figure 5.4, oval protrusions adjacent to features with a lower contrast are visible. The protrusions can be assigned to the tetramethylcyclohexane ring. By superimposing the image features with space-filling molecular models of NDN*, the orientation of the molecules with a length of approximately 1.2 nm can be determined in phase I and II. Each motif in phase I is formed by the corresponding number of molecules with the nitrile groups on the periphery (Fig. 5.4 (a)). The driving force of the structure formation are the intermolecular dipole-dipole interactions between the nitrile moieties. The same applies for phase II, in which the nitrile groups of each six molecules are pointing toward the cavity (Fig. 5.4 (b)). The domains were also observed for samples consisting only of NDN* on Ag(111). Obviously, the NDN* molecules did not yet react with the Fe atoms to form Fe-naphthalocyanine molecules.

To initiate the reaction of the nitrile groups with the deposited Fe atoms, the substrate was annealed to 450 K. Large ordered islands of reacted tetramers can be observed in the STM images (Fig. 5.5 (a)). In contrast to the previous aggregation of four molecules, the tetramers have reacted in a cyclization, since the experimental size is as expected for FeNc*. The molecules are densely packed and slightly deviating from a square arrangement. The primitive unit cell is defined by the centers of four Fe-naphthalocyanine molecules with a size of $(20.0 \pm 0.2) \times (21.0 \pm 0.2)\,\text{Å}^2$ and an inner angle $(100 \pm 2)°$ (Fig. 5.5 (b)). The area of the unit cell contains one FeNc* molecule and two Fe atoms, one as an ion being part of the

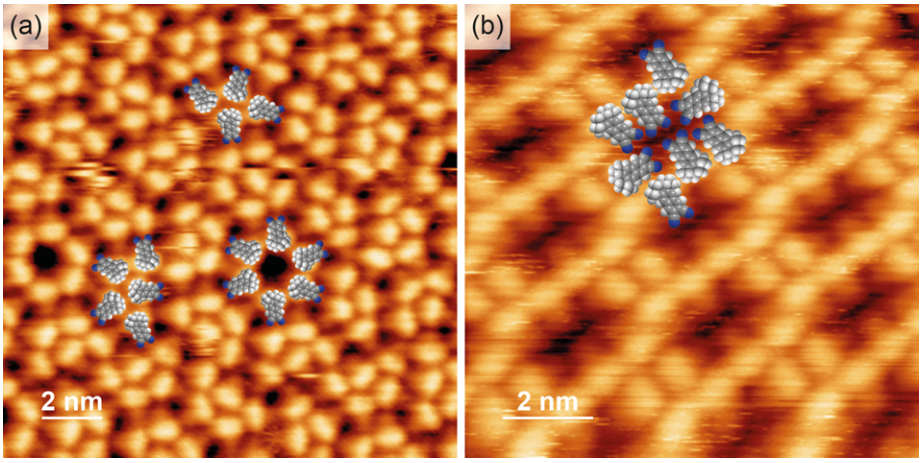

Figure 5.4: Assignment of the features in STM images of NDN* domains. The bright features can be attributed to the protruding alkyl groups. Attractive dipole-dipole interactions occur between the nitrile groups of the molecules. The orientation is visualized by superimposed space-filling models. Nitrogen atoms are colored blue. (a) Phase I consists of unreacted tetramers, pentamers and cyclic hexamers. (b) In phase II, six NDN* molecules are pointing towards each other arranged in rectangular units. Tunneling parameters: (a) 0.81 V, 0.12 nA, 165 K; (b) 1.63 V, 0.08 nA, 165 K.

metallonaphthalocyanines and probably one adatom coordinated by four molecules. Due to the dense packing of the molecules, the matching size and the functional groups on only one side of the precursor molecules, it can be excluded that the observed structures at this annealing temperature are only 2D coordination networks as reported by Shawulienu Kezilebieke *et al.*[268] The presence of the Fe adatoms probably results from an excess amount of deposited Fe in the corresponding local structure.

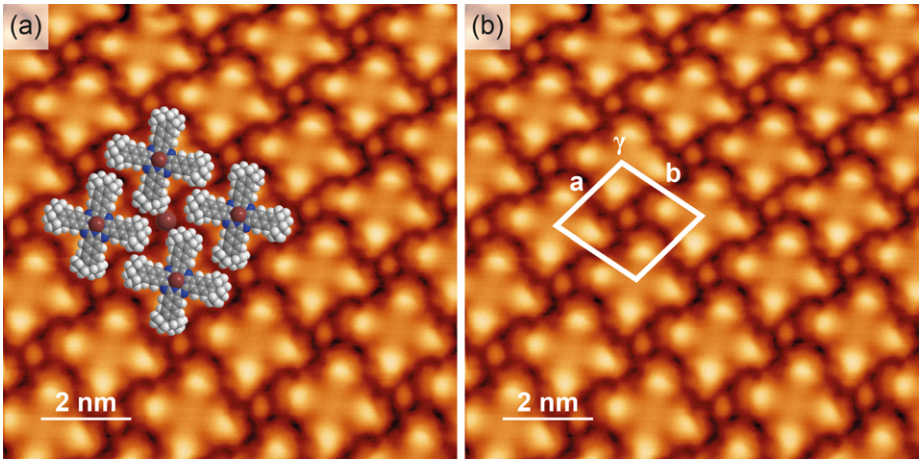

Figure 5.5: Fe-naphthalocyanine molecules, FeNc*, on Ag(111) formed upon annealing of NDN* and Fe on Ag(111) to 450 K. (a) The complexes are illustrated by the superimposed space-filling molecular models. (b) The unit cell contains one FeNc* molecule and an additional Fe adatom, coordinated by four Fe-naphthalocyanine molecules. Unit cell parameters: $(20.0 \pm 0.2) \times (21.0 \pm 0.2)$ Å^2, $(100 \pm 2)°$. Tunneling parameters: 1.85 V, 0.28 nA, 165 K.

By changing the bias voltage, different parts of the reacted tetramers are represented. While the lobes exhibit a high contrast at 1.85 V (Fig. 5.6 (a)), the inner parts of the naphthalocyanine molecules and thus the conjugated systems are more pronounced at 1.28 V (Fig. 5.6 (b)). In both cases, the Fe atom in the center of the macrocycle is hard to detect. By changing to a

blue-yellow color palette and adding contour lines (Fig. 5.6 (c)), the electron density resulting from the metal ion in the cavity of the molecule is exposed. Most likely, the contrast of the Fe center is covered by the protrusions at the four lobes of the macrocycle due to the non-planarity of the cyclohexane ring and the four outstanding methyl groups.

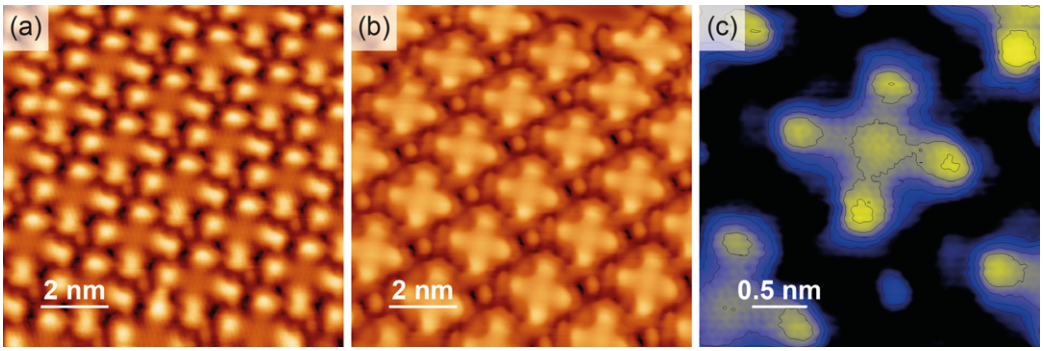

Figure 5.6: Bias voltage dependent constrast in STM images (a, b) of Fe-naphthalocyanines, FeNc*. (c) Contour lines reveal the slight protrusion in the center of the macrocycle. Tunneling parameters: (a) 1.85 V, 0.13 nA, 165 K; (b, c) 1.28 V, 0.28 nA, 165 K.

In the presence of post-deposited Fe atoms, an intramolecular cyclization of the dicarbonitrile precursor NDN* was achieved (Fig. 5.7). The on-surface synthesis results in islands of well-ordered FeNc* molecules.

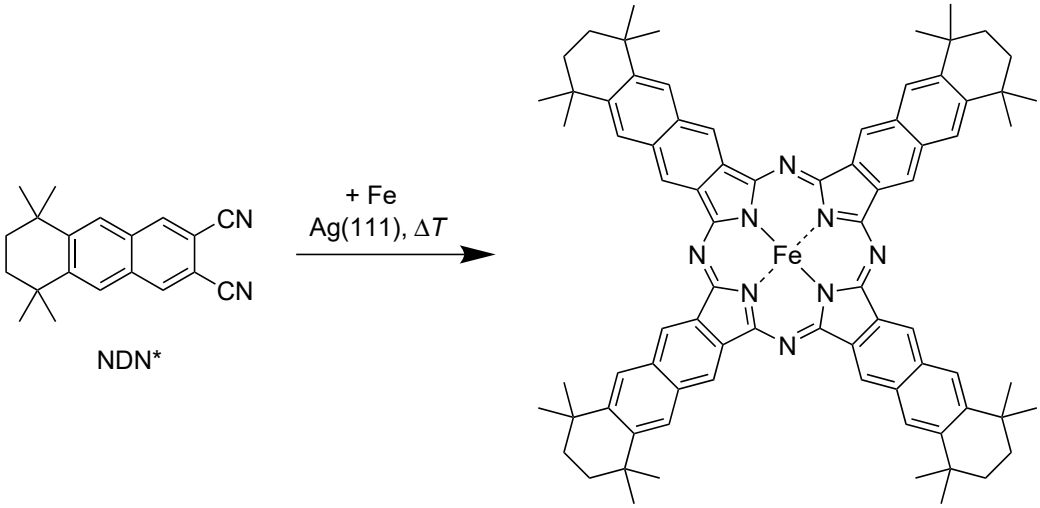

Figure 5.7: On-surface synthesis of Fe-naphthalocyanine from the dicarbonitrile precursor NDN*.

However, an overview STM image reveals also other oligomeric species. While the naphthalocyanine domain exhibits a high symmetry, the other domains are disordered and contain malformed tetramers, pentamers, hexamers and even heptamers. Pristine domains of either tetramers or oligomers are highlighted by green and red transparent areas, respectively, in Figure 5.8 (a). The oligomers show a contrast similar to the FeNc* tetramers despite the lack of symmetry. Since no intramolecular details are distinguishable in the center of the oligomers, it cannot be concluded whether one or more Fe atoms are incorporated, although it is suggested that the oligomers are formed due to metal-mediated reactions of the dicarbonitrile moieties and can thus be identified as reactions products.

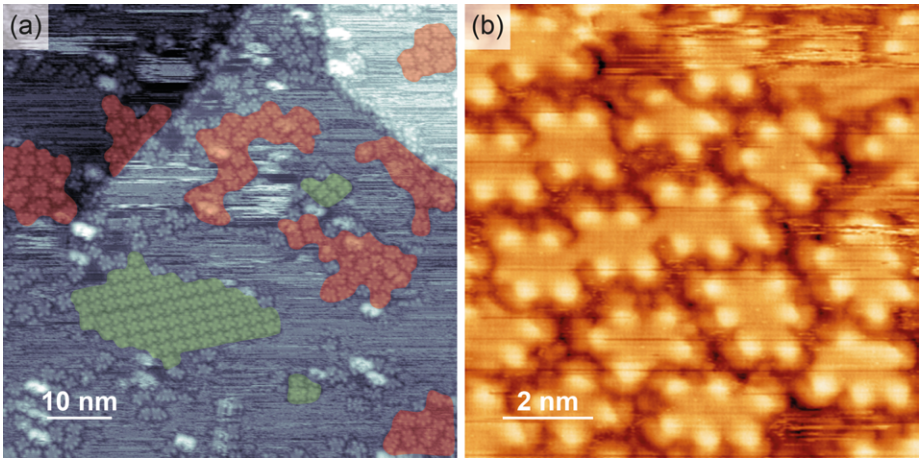

Figure 5.8: STM images with domains of tetramers and oligomers of NDN* on Ag(111) after annealing to 450 K. (a) The image shows domains of tetramers (green) and oligomers (red) of NDN* formed upon annealing. The naphthalocyanine domains stand out through their long-range order. (b) Details of the oligomers. The oligomers exhibit irregular shapes. Inner details are not visible. Tunneling parameters: (a) 0.94 V, 0.23 nA; (b) 1.32 V, 0.33 nA, 165 K.

In a separate project, Katharina Greulich studied the formation of supernaphthalocyanine molecules beyond the tetramers and the formation of linear oligopyrroles.[272] By choosing a cation with a large radius like Gd as template, the linkage of the NDN* molecules can be forced to result in pentamers.

5.2 Self-Assembly of *meta*-Linked Dicarbonitriles on Ag(111)

While the previous section was aimed at generating single macrocycles on the surface, functionalized aromatic molecules can also be used to form large self-assembled structures. The type and porosity depends on various properties. Most obvious is the geometric shape of the molecular building block themselves, *e.g.*, the length of a polyphenylene chain.[104,273] Furthermore, the coverage of the organic compound on a surface as well as the interaction with other building blocks like adsorbed metal atoms can influence the resulting long-range order.

A work which gained huge attraction in the surface science community was the formation of Sierpiński triangles, a kind of fractals, in the 4$^{\text{th}}$ generation from dibromo-substituted building blocks, kinked terphenyl and quaterphenyl molecules, due to self-assembly.[274] Jian Shang *et al.* were the first to observe those complex chemical reactions on a surface, whose result is, furthermore, also esthetically very appealing. Further studies reported the achievement of Sierpiński triangles by using other substituents at otherwise similar building blocks and other interaction types. Dicyano-substituted terphenyl molecules form coordination fractals with Fe or Ni.[275,276]. Dihydroxy-substitution can be used for fractals defined either by hydrogen-bonds or by coordination-bonds with deposited Fe atoms.[277,278] Threefold symmetric, thiol-functionalized aromatic molecules arrange in Sierpiński triangles under covalent thioether linkage. The here presented project is focused on self-assemblies of dicarbonitrile molecules to investigate the general behavior of functionalized molecules, but the comparison with more complex structures demonstrates the significance of chemically simple molecules in the controlled generation of surface structures. The studied molecular building blocks are the dicarbonitriles 1,1′:3′,1″-terphenyl-4,4″-dicarbonitrile (*m*-3PDN) and 1,1′:3′,1″:4″,1‴-quaterphenyl-4,4‴-dicarbonitrile (*m*-4PDN) (Fig. 5.9), which arrange in large-area or spatially limited structures. *m*-3PDN and *m*-4PDN were deposited at a flux of $1\,\mathrm{nm\,min^{-1}}$ and $0.1\,\mathrm{nm\,min^{-1}}$, respectively. To induce different adsorption structures, low submonolayer to monolayer coverages were prepared.

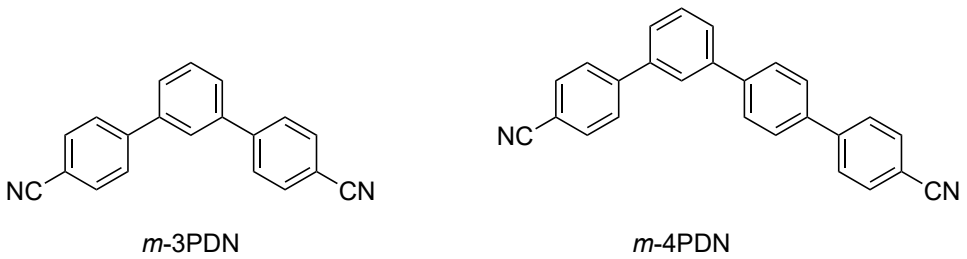

Figure 5.9: Kekulé structures of 1,1′:3′,1″-terphenyl-4,4″-dicarbonitrile and 1,1′:3′,1″:4″,1‴-quaterphenyl-4,4‴-dicarbonitrile.

5.2.1 Adsorbate Structures of *m*-3PDN on Ag(111)

After deposition of approximately one monolayer *m*-3PDN onto Ag(111) held at room temperature, the molecules self-assemble in two different structures. While minor parts of the substrate are covered without long-range order, the highly ordered self-assemblies expand over large areas. Particularly striking is a well-ordered structure which can be described as zipper-

like (Fig. 5.10 (a)). This structure is composed of double rows of *m*-3PDN molecules. The unit cell is rectangular with a dimension of $(12.7 \pm 0.1) \times (17.2 \pm 0.1)\,\text{Å}^2$ (Fig. 5.10 (b)). Since the unit cell contains two molecules, the molecular density within this zipper-like structure yields $0.92\,\text{nm}^{-2}$. The double rows interact by hydrogen bonds between the hydrogen atoms attached to the phenyl rings in the inner 120° angle of a molecule with the lone pairs of a nitrile moiety in the adjacent row. While this interaction ensures the stability within a double row, the next double row is only loosely connected by VAN DER WAALS forces. This difference in the interconnection results in defects visible in Figure 5.10 (a). These defects arise either in shifts between the zipper-like features or in lines between double rows. Since these lines appear blurred, it can be concluded that they contain mobile molecules possibly upright standing.

On the same sample, areas with paired molecules were detected. These dimers appear in two enantiomeric forms as illustrated by the space-filling molecular models superimposed onto the STM image in Figure 5.10 (c). The lattice parameters of the unit cell of this dimer containing structure are $(19.9 \pm 0.1) \times (27.9 \pm 0.1)\,\text{Å}^2$ with an angle of $(130 \pm 2)°$. With four molecules in the unit cell, a molecular density of $0.94\,\text{nm}^{-2}$ emerges. The dimers are therefore slightly denser packed. The driving force in the formation of the dimer structure are again intermolecular hydrogen bonds. While the molecules in the zipper-like structure are rotated by 120° and the nitrile groups point toward the inner angle of the neighboring molecule, the molecules of a dimer are rotated by 180° and the molecular wings are parallel to each other.

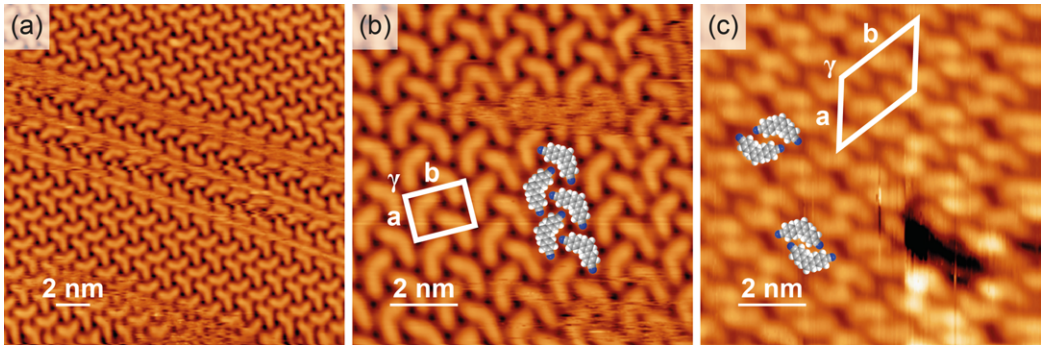

Figure 5.10: Self-assembled adsorption structures of *m*-3PDN on Ag(111). (a) Zipper-like structure with defect lines. (b) Detail of the zipper-like structure with superimposed unit cell containing two molecules ($(12.7 \pm 0.1) \times (17.2 \pm 0.1)\,\text{Å}^2$, $(90 \pm 1)°$) and space-filling molecular models. (c) The molecules are paired and appear in two enantiomers. The unit cell contains four molecules ($(19.9 \pm 0.1) \times (27.9 \pm 0.1)\,\text{Å}^2$, $(130 \pm 2)°$). Tunneling parameters: (a) −1.16 V, −0.60 nA, 300 K; (b) −1.16 V, −0.63 nA, 300 K; (c) 1.96 V, 0.53 nA, 300 K.

Liangliang CAI *et al.* investigated *m*-3PDN on Cu(111) at different coverages. At a low coverage of $(0.21 \pm 0.20)\,\text{ML}_{\text{ads}}$, they achieved metal-organic coordination networks in the form of SIERPIŃSKI triangles. With increasing coverage the intermolecular bonds are more and more determined by hydrogen bonds. The zipper-like structure was as well observed at close-packed layers ($(0.98 \pm 0.20)\,\text{ML}_{\text{ads}}$). The authors conclude that the loss of intermolecular interaction energy between the strong Cu−N coordination bonds and the relatively weak CH···N hydrogen bonds is compensated by an increased molecular adsorption energy at higher coverages.[279]

5.2.2 Orientations of *m*-4PDN and the Influence on Structure Formations

The structures of *m*-4PDN are determined by the prochirality of the molecules resulting in chiral objects once adsorbed onto a surface in contrast to the achiral *m*-3PDN. The following study shows that *m*-4PDN appears both in enantiomerically pure and mixed domains. At a closed packed layer, the adsorption structure of *m*-4PDN resembles the dimer arrangement of *m*-3PDN apart from being enantiopure. As visible in Figure 5.11 (a), the close-packed arrangement covers wide areas. The unit cell is $(15.1 \pm 0.1) \times (36.7 \pm 0.2)\,\text{Å}^2$, $(90 \pm 1)°$ (Fig. 5.11 (b)). With four molecules in the unit cell, the molecular density yields $1.39\,\text{nm}^{-2}$. Reducing the coverage leads to more complex assemblies.

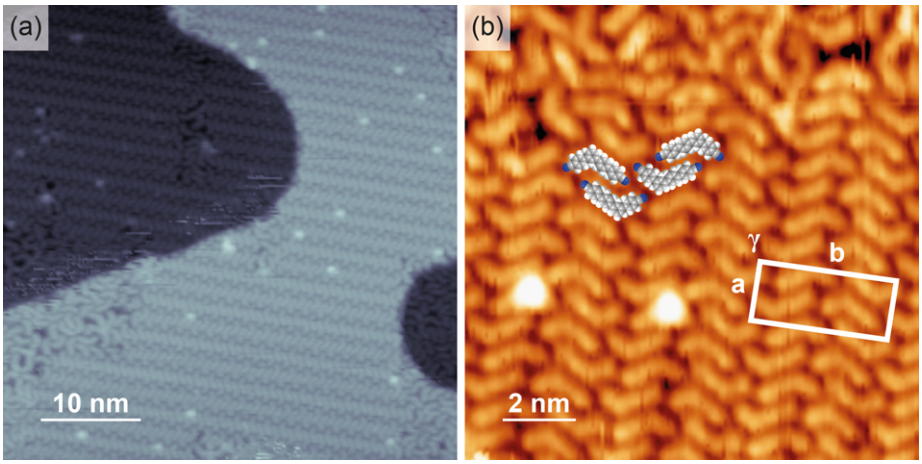

Figure 5.11: STM images of the close-packed adsorption structure of *m*-4PDN. (a) The ordered structure covers large areas. (b) A closer look reveals the presence of both enantiomers as visualized by the superimposed molecular models. The unit cell is $(15.1 \pm 0.1) \times (36.7 \pm 0.2)\,\text{Å}^2$, $(90 \pm 1)°$. Tunneling parameters: (a) $-1.24\,\text{V}$, $-0.90\,\text{nA}$, $170\,\text{K}$; (b) $-1.24\,\text{V}$, $-0.69\,\text{nA}$, $170\,\text{K}$.

Upon deposition of *m*-4PDN onto Ag(111) in a low submonolayer coverage, two different structures were observed. By means of XPS, the total coverage was determined to yield $0.1\,\text{ML}_{\text{ads}}$. The local coverage in the STM images is higher, since the molecules self-assemble in islands alongside uncovered areas as reported for other chemical compounds. The widespread island of *m*-4PDN molecules in Figure 5.12 (a) shows large, hexagonally arranged voids. The cavities are surrounded by six nodes. The unit cell expands over $(42.6 \pm 0.2) \times (42.1 \pm 0.2)\,\text{Å}^2$. The inner angle of the rhombic unit cell is $(118 \pm 2)°$. A magnification of the STM images reveals that the nodes contain three molecules (Fig. 5.12 (b)). Thus, the unit cell contains six molecules and the molecular density is $0.38\,\text{nm}^{-2}$. The local coverage is almost one fourth of the close-packed layer of *m*-4PDN with a molecular density of $1.39\,\text{nm}^{-2}$. The porous structure resembles the Kagome lattice or trihexagonal tiling (vertex configuration: $(3.6)^2$) as indicated by the superimposed ideal lattice. A closer look reveals that the molecular structure deviates from the ideal case, since the molecular nodes, which coincide with the triangles, exhibit a lower symmetry. The only possible symmetry operation for the molecular nodes in the *m*-4PDN (wallpaper group in Hermann-Mauguin notation: *p*6) structure are rotations, while the ideal Kagome lattice (wallpaper group: *p*6*m*) possesses also mirror planes. The reason for this deviation is the chiral character of the objects. As seen before, the nodes are stabilized by hydrogen bonds between neighboring molecules. While the nitrile moiety terminating the

long wing of the molecular backbone points toward the inner angle of the adjacent molecule, the short end interacts with the next node.

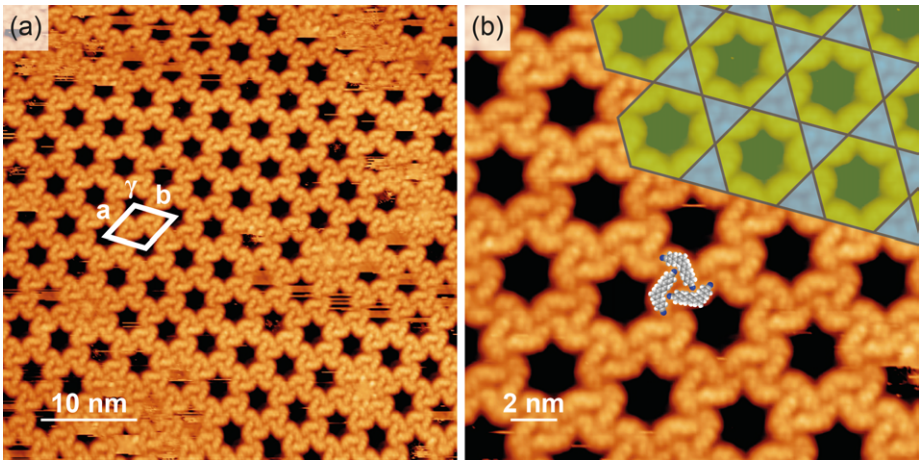

Figure 5.12: Kagome-like adsorption structure of *m*-4PDN revealed by STM. (a) The regular structure covers a large area and exhibits a unit cell of $(42.6 \pm 0.2) \times (42.1 \pm 0.2)$ Å^2, $(118 \pm 2)°$. (b) Each node consist of three counterclockwise arranged molecules. Six nodes surround a void. For comparison, the ideal Kagome structure is superimposed. Tunneling parameters: 1.79 V, 0.54 nA, 170 K.

Figure 5.13 (a) presents a highly ordered, linear structure beside molecules without short- or long-range order. The structure contains two types of features. The kinked objects aligned in double rows were observed before and can be assigned to flat lying *m*-4PDN molecules. In this case, the molecules of one row point with their shorter end toward the inner 120° angle of the molecules, while the molecules of the opposite are oriented with their long wing toward their neighbors. Due to this alignment, the double row exhibits a zigzagged and a straight side. Between the zipper-like features, linear objects are visible with every third being shorter and kinked in the center. Matthias Marschall *et al.* reported upright standing 1,1′:4′,1″-terphenyl-3,3″-dicarbonitrile molecules on Cu(111) and Co-induced reorientation on Ag(111) after subsequent deposition of Co atoms.[280] In both systems, the upright standing molecules were achieved at high coverages, while the molecules are adsorbed coplanarly to the substrate at low coverages. By means of overlaid molecular models, the detailed STM image of *m*-4PDN on Ag(111) (Fig. 5.13 (b)) reveals that the linear features can be assigned to upright standing molecules. By comparison with an STM image of the clean substrate, the high-symmetry directions were determined. The superimposed arrows in Figure 5.13 indicating the close-packed directions of the Ag(111) surface show that the upright standing molecules are exactly aligned. It can be suggested that every third molecule is tilted to achieve an exact matching of the only one atom wide molecular structures with the substrate lattice. Furthermore, the molecular backbone of this molecule is bent resulting in a shorter length. The superimposed space-filling model exhibits a dihedral angle of 20° between the first and the second as well as between the third and the fourth phenyl ring. At these positions, the backbone of the model was bent by 15° to correspond to the experimental situation. Crystal structures of the linear 1,1′:4′,1″:4″,1‴-quaterphenyl-4,4‴-dicarbonitrile obtained by X-ray structure analysis and the DFT optimized geometry of 1,1′:4′,1″-terphenyl-3,3″-dicarbonitrile on Cu(111) show likewise tilted phenyl rings with dihedral angles in the same order of magnitude.[280,281] Although the

total coverage in the here presented experiment is by far lower than in the literature studies, the conclusion of upright standing molecules can be drawn. Probably due to the lateral confinement of the zipper-like rows, the molecules in between are forced into this orientation. The intermolecular forces are determined by π–π stacking achieving a stable packing of the upright standing molecules.

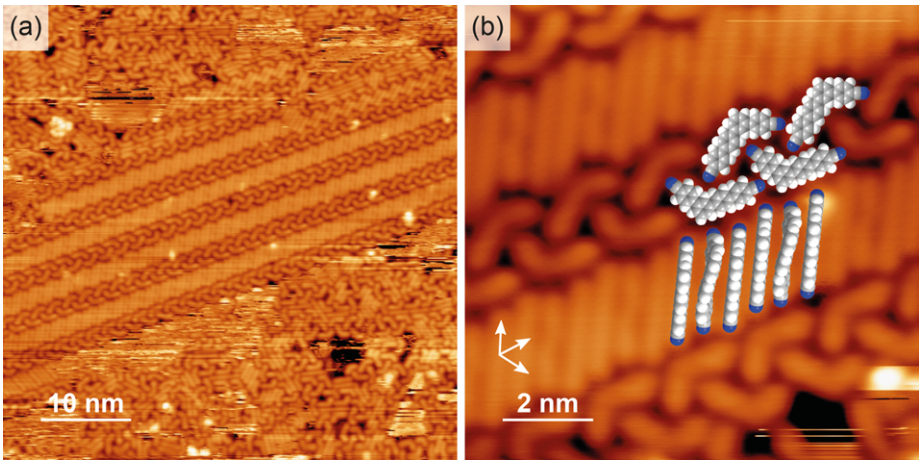

Figure 5.13: Upright standing and flat lying *m*-4PDN on Ag(111). (a) Beside only short-range ordered molecules, some *m*-4PDN molecules assemble in long double rows with linear features in between. (b) The linear features result from upright standing molecules and are aligned along the close-packed directions of the substrate surface. Every third molecule appears broader and shorter due to tilted phenyl rings and a slightly bent backbone. Tunneling parameters: (a) 1.68 V, 0.29 nA, 170 K; (b) 1.68 V, 0.31 nA, 170 K.

In Figure 5.14 (a), assembled *m*-4PDN molecules in an area with a lower local coverage are reproduced. The blurry areas most likely contain mobile molecules, whereas some molecules are immobilized at the step edges. Starting from these assemblies, zipper-like structures of molecules are formed expanding over more than 200 nm. Similar to the aforementioned structure, upright standing molecules were found between the double rows. The linear features appear in two directions. The rotation by 60° indicates the alignment with the high-symmetry directions of the Ag(111) surface. Since no upright standing molecules are present outside the double rows, the upright orientation seems to exist only in the lateral confinement.

The Kagome-like structure consists of only one enantiomer in the above presented area. The opposite enantiomer was found in identically constructed arrangements. A domain containing nodes of both enantiomers is shown in Figure 5.14 (b). The nodes correspond to the building blocks of the Kagome-like structure and are composed of rotationally arranged molecules. Due to the enantiomerism, the nodes are oriented clockwise and counterclockwise as illustrated by the arrows. Between the *m*-4PDN molecules, very narrow lines with a lower contrast can be detected. These features do not result from molecules but from the substrate and were also found in other experiments on Ag(111) with totally different organic molecules.

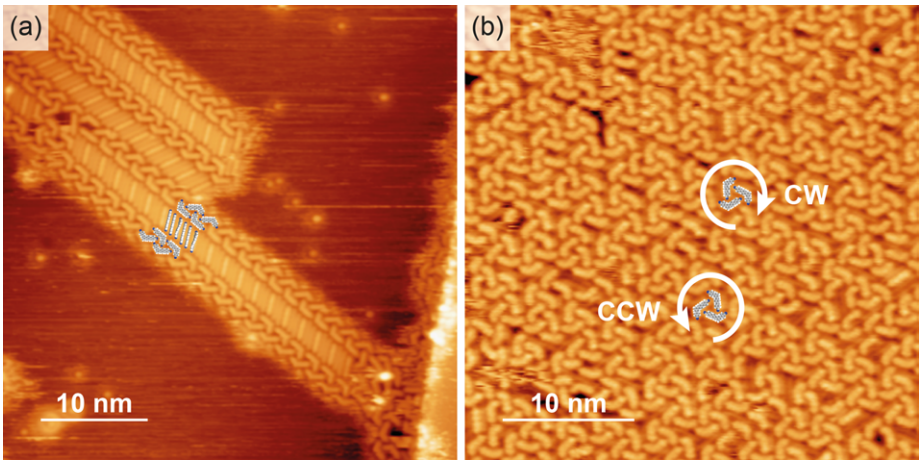

Figure 5.14: STM images with a comparison of different adsorption structures of *m*-4PDN. (a) Starting from molecules immobilized at a step edge, double rows surrounding upright standing molecules are formed. (b) Triangularly arranged molecules occur in both enantiomeric forms forming clockwise and counterclockwise nodes. Tunneling parameters: (a) −1.58 V, −0.76 nA, 170 K; (b) 1.68 V, 0.21 nA, 170 K.

6 On-Surface Synthesis of Heptacene and Its Interaction with Metal Surfaces

In the case of heptacene, the intending reason was the prospect of synthesizing a molecule which is accessible only under very restricting conditions.[I] As mentioned in the introductory part, polyacenes are highly reactive and the history of their synthesis is marked by several throwbacks. The aim of this work was to use a surface-assisted approach to generate heptacene from the α-diketone precursor 7,16-dihydro-7,16-ethanoheptacene-19,20-dione (Fig. 6.1), which was already used as reactant in a photochemical route[69], and to use the interaction with the Ag(111) substrate for the stabilization of the molecule. DEH contains an α-diketone bridge at the 7,16-position functioning as a protecting group. The intention of the reaction study was to cleave the diketone bridge by means of thermal didecarbonylation under the release of carbon monoxide. This study includes an experimental part and calculations. The calculations were not part of the present work and were not performed by the author, but are summarized here to complete the project and substantiate its results.

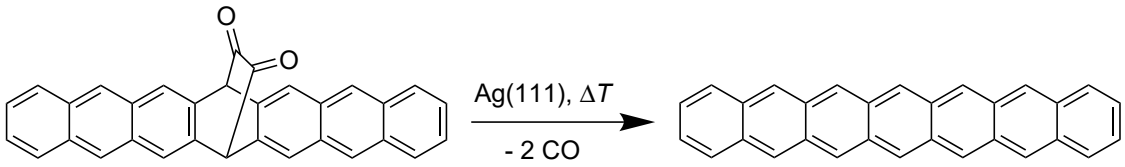

Figure 6.1: Surface-assisted formation of heptacene from the bridged α-diketone precursor DEH on Ag(111) by thermal activation.

The precursor was contributed by Ralf Einholz and Holger Bettinger. Prior to deposition, the substance was subject to standard degassing procedures as aforementioned. The deposition was done in different coverages. Coverages of one monolayer or above – for the heating series – were produced for the spectroscopic measurements. Concerning the STM experiments, the challenging circumstance of a high mobility of the precursor had to be overcome. VT-STM experiments were therefore performed at coverages close to a monolayer with a dense packing of the molecules. LT-STM experiments, on the other hand, required low submonolayer coverages to improve the imaging quality by tip pulsing on the bare substrate. Deposition was executed at a flux of 0.08-0.13 nm min^{-1}, while the substrate was held at RT.

6.1 Triggering and Monitoring a Didecarbonylation Reaction

On-surface synthesis often involves thermal activation of molecules by annealing of the substrate with the adsorbed precursor. DEH was deposited onto Ag(111) with an inital coverage of 2 ML$_{ads}$ and gradually annealed in a temperature range of 360-700 K with an increment of 20 K. The heating series was studied by means of XPS to monitor the ongoing reaction. Figure

[I] The results of this project were published in: M. Zugermeier, M. Gruber, M. Schmid, B. P. Klein, L. Ruppenthal, P. Müller, R. Einholz, W. Hieringer, R. Berndt, H. F. Bettinger, J. M. Gottfried, *Nanoscale* **2017**, *9*, 12461–12469, DOI 10.1039/c7nr04157h .

6.2 shows that a transition takes place at 420 K indicated by a shift of the C 1s peak toward lower binding energies, a reduction of the peak integral, and a difference in the peak form. Furthermore, the O 1s signal significally changes at this temperature witnessing the absence of a formerly present oxygen species. A residual oxygen species still remains and vanishes completely at 620 K.

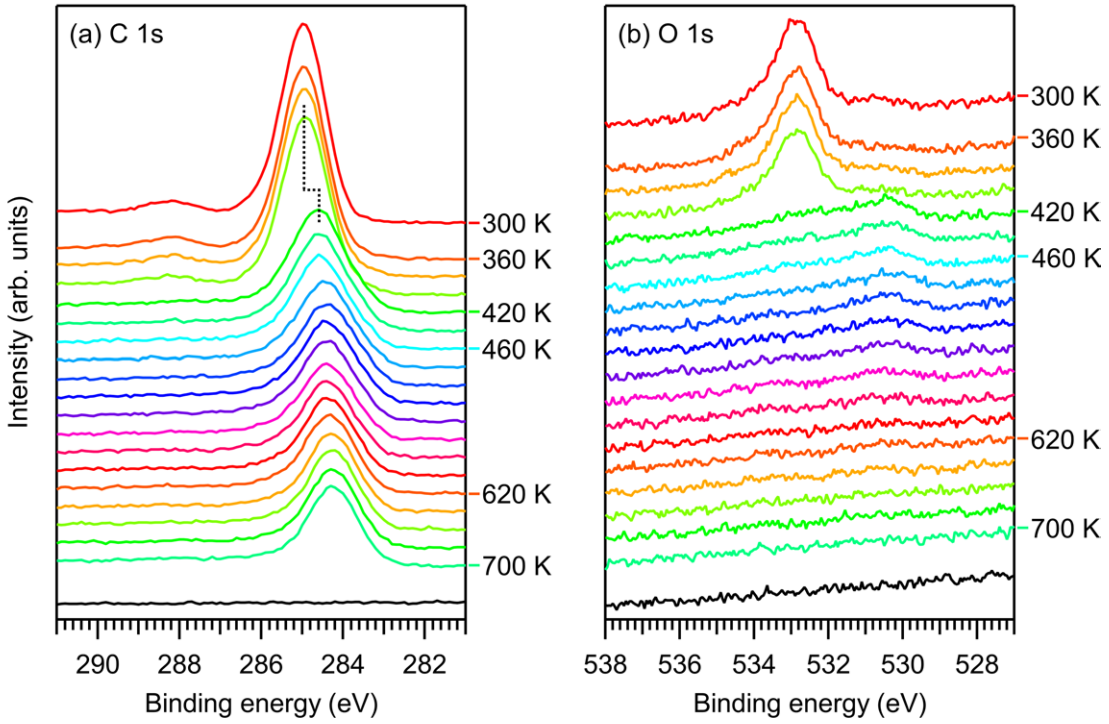

Figure 6.2: XPS temperature series of a DEH layer (initial coverage 2 ML_{ads}) on Ag(111). The (a) C 1s and (b) O 1s spectra were recorded at RT and in a temperature range of 360-700 K with an increment of 20 K. The transition from the precursor, DEH, to heptacene can be seen in the shift of the aromatic carbon peak by 0.4 eV and the absence of the carbonyl oxygen at 420 K. At 620 K, the residual O 1s signal attributed to physisorbed oxygen completely disappears. The spectra of the clean substrate (black) are provided for comparison. The visible energy range was reduced for a better representation of the relevant features.

For a detailed analysis, XPS measurements at three relevant temperatures were selected and the corresponding spectra were fitted. To ensure a sufficiently high transition yield, an annealing temperature of 460 K, slightly above the transition temperature, was chosen for the analysis and the later following STM experiments. The expected stoichiometry of the carbon species in DEH ($C_{32}H_{18}O_2$) is 14 : 1 : 1 representing the aromatic, aliphatic and carbonyl carbon atoms. Corresponding to this ratio, the spectral features in the C 1s region (Fig. 6.3 (a)) were fitted. The binding energies were determined to be 285.0 eV (aromatic), 286.1 eV (aliphatic) and 288.2 eV (carbonyl) at 300 K, and agree with literature values from K. Sieg-bahn *et al.*[283] The annealing induces a reduction of the C 1s integral by half corresponding to the desorption of the second layer, and a loss of two carbonyl species due to the conversion of the molecule. In the O 1s spectral region, two signals are to be identified (Fig. 6.3 (b)). The major signal situated at 532.9 eV can be attributed to the carbonyl oxygen, as it features the same behavior as the corresponding carbonyl carbon at 420 K. The carbon to carbonyl oxygen ratio at 300 K can be calculated with Equation 3.22 considering the individual trans-

mission function for the XPS analyzer (equations 3.23 and 3.24 for $E_{\text{pass}} = 30\,\text{eV}$) and the atomic subshell photoionization cross sections of 0.013 Mb for C 1s and 0.040 Mb for O 1s valid for the photon energy of the Al K_α X-ray line (here 1486.6 eV).[219] Since the experimentally determined ratio of 18.6 : 1 is close to the expected value of 16 : 1, the adsorbed molecules can be considered as intact. The absence of the carbonyl oxygen species as well as the carbonyl and aliphatic carbon species at 420 K reveals the didecarbonylation reaction and thus the conversion of the precursor into heptacene on the surface. Upon further annealing to 620 K, the aromatic carbon undergoes a shift by 0.2 eV attributed to a work function change resulting from a further, partial reduction of the coverage to 0.8 ML_{ads}.[284–286] In the O 1s region, the residual oxygen species formerly present at 530.6 eV is not detectable anymore. The binding energy and the desorption temperature match chemisorbed molecular oxygen on Ag(111) as reported by Bukhtiyarov and Campbell.[287,288] The chemisorbed oxygen most likely results from an impurity already in the deposited compound, but emerges to be insignificant in the study.

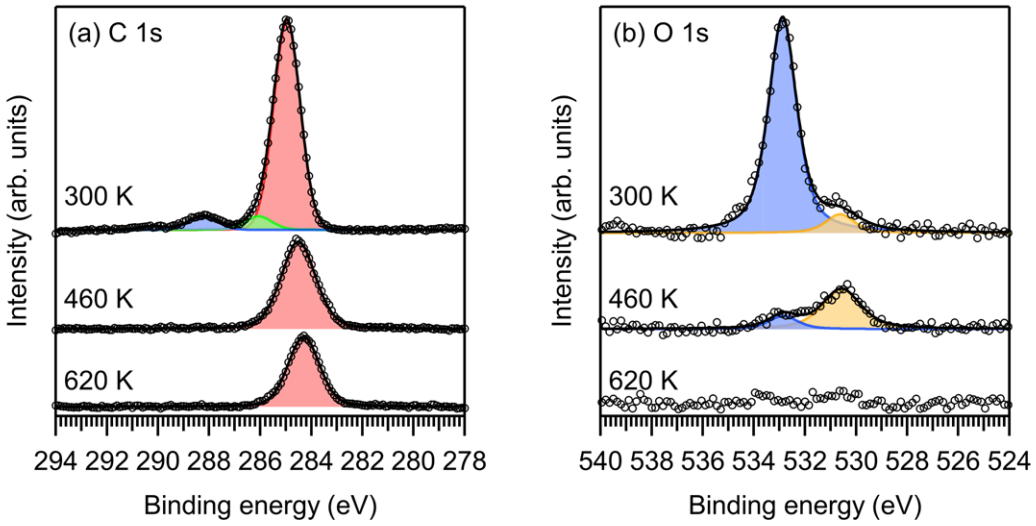

Figure 6.3: Selected XP spectra of a DEH layer (initial coverage 2 ML_{ads}) on Ag(111) at RT and after annealing at 460 K and 620 K. The peak colors in the (a) C 1s and (b) O 1s spectra represent aromatic carbon (red), aliphatic carbon (green) and carbonyl carbon/oxygen (blue). The sample contains an impurity caused by chemisorbed oxygen (orange), which amounts to 10% of the carbonyl oxygen signal and disappears at 620 K.

6.2 Highly Mobile Precursor and Reaction Products in STM Images

To determine the orientation of the molecules on the Ag(111) substrate and to ensure the intactness of the precursor upon adsorption and of the heptacene after conversion, the molecules were investigated by means of STM. During the experiments, the precursor molecules showed a high mobility on the surface and thus hindered the imaging. Due to the sp^3 hybridization at the positions 7 and 16, the molecular backbone is bent by 53.5° (angle 126.5° between the molecular wings) in the gas phase as determined by DFT calculations. Although the angle should be higher for the absorbed structure on the surface, the backbone is substantially bent and thus permits only a low overlapping of the molecular orbitals with the surface resulting in

the observed high mobility. Therefore, VT-STM measurements were performed on coverages close to one complete monolayer and at around 150 K. Precursor molecules are predominantly oriented along the high-symmetry directions of the surface lattice. Some molecules are aggregated and second layers are visible as it can be seen in the bright areas in Figure 6.4 (a). The diketone bridge appears as protrusion in the center of the molecule (Fig. 6.4 (b)). Upon annealing to 460 K, the molecules converted into heptacene are immobilized either at the step edges in RT measurements or on regular terrace sites at liquid nitrogen cooling. Due to the uniform contrast of the objects, the adsorption structure of heptacene should be flat. However, the molecules exhibit a slightly brighter appearance at their ends, which will be more prominent in the following LT experiments. As reported above, the transition from the precursor to heptacene takes place at 420 K. Nevertheless, unreacted DEH molecules are still present in the corresponding images and can be identified by the protrusions in the center.

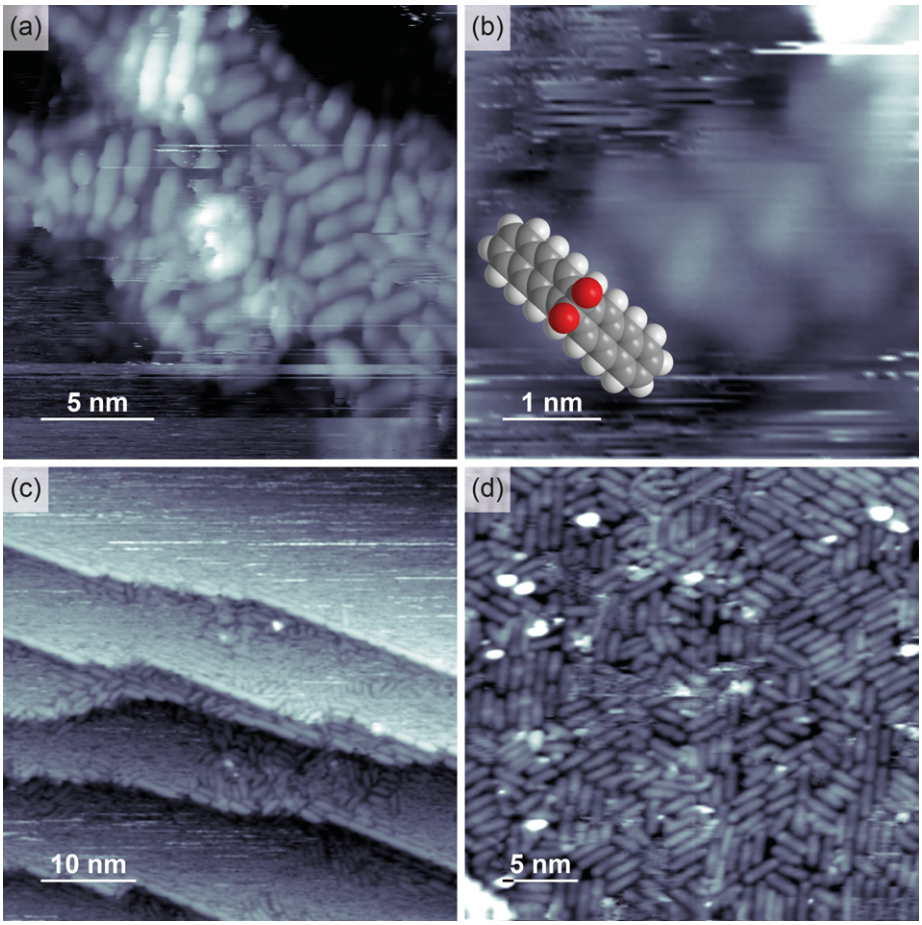

Figure 6.4: VT-STM images of (a, b) DEH after room-temperature adsorption onto Ag(111) with a superimposed molecular model in (b) and (c, d) of heptacene molecules after annealing to 460 K. Except for image (c), all measurements were performed at 150 K. Images (c, d) show the immobilization of heptacene molecules at the step edges in a room-temperature measurement and on the plain surface at low temperatures, respectively. Tunneling parameters: (a) 1.24 V, 0.25 nA; (b) 1.24 V, 0.26 nA; (c) −1.49 V, −0.15 nA; (d) −1.54 V, −0.14 nA.

For further insight, the experiments were repeated using the LT-STM setup in Kiel in a collaboration with Richard Berndt and Manuel Gruber. Preliminary attempts revealed that monolayer coverages led to a modification of the STM tip by strong accumulation of

molecules at the apex and thus prevented the recording of clear images. By considerable reduction of the deposition time, the coverage was sufficiently low to allow indentations and voltage pulsing on areas of the bare substrate for tip conditioning.

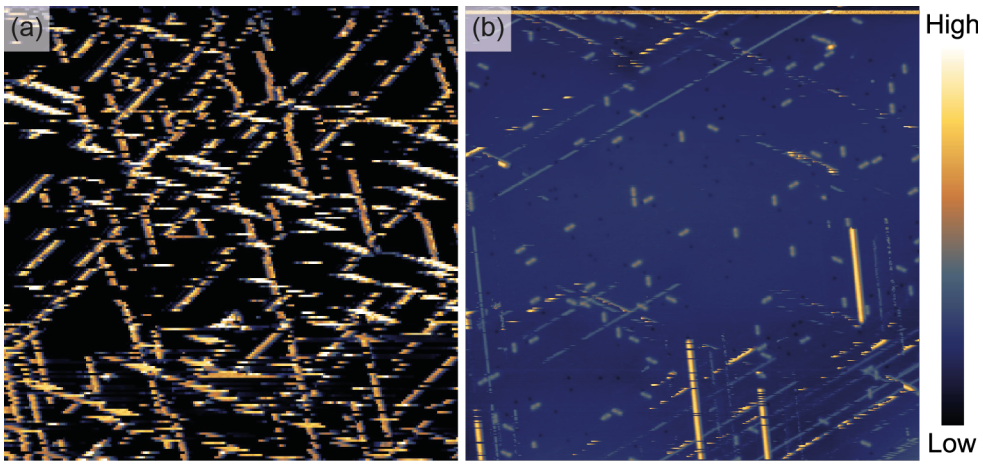

Figure 6.5: LT-STM images of (a) DEH after deposition onto Ag(111) at 300 K and (b) after annealing to 460 K. The stripe-like features are attributed to one-dimensional diffusion traces of (residual) DEH molecules. The heptacene molecules formed upon thermal didecarbonylation are immobile at 4 K. Image sizes: (a) $40 \times 40\,\mathrm{nm}^2$; (b) $100 \times 100\,\mathrm{nm}^2$. Tunneling parameters: (a) 0.4 V, 2 pA; (b) 1.3 V, 2 pA.

Upon adsorption of the precursor, strip-like features appear (Fig. 6.5 (a)). It seems that the DEH molecules exhibit an exceptional mobility already at 4 K. The diffusion barrier is, however, not overcome thermally but by influence of the tip. Matthias Böhringer *et al.* discovered that anthracene molecules on Ag(110) interact with the tip during the scanning process and thus influence the image formation.[289] The attractive force of the tip is higher than the activation barrier for the hopping between neighboring adsorption sites, and the molecules move during every line scan appearing as 1D diffusion traces in the STM image. If the image resolution and the scan speed is appropriate, individual molecules are recorded multiple times and it can be differentiated between cross-channel and in-channel jumps. The tip-induced motions can be recognized in Figure 6.5 (a) for the untreated sample and in Figure 6.5 (b) for residual DEH molecules after annealing to 460 K. Here, the fuzziness of the 1D diffusion traces in the first image is a result of a high scan speed in a large imaging area and of a limited control over the tip condition in turn caused by the low possibilities of tip preparations due to tip-molecule interaction. Figure 6.5 (b) includes individual, immobile heptacene molecules and traces of DEH. Furthermore, dark spots appear, which can be attributed to adsorbed CO molecules originating from residual CO gas in the UHV chamber due to the annealing process.[290] CO desorbs from Ag(111) in the monolayer only above 52 K.[291] By counting, the ratio between unreacted and reacted molecules was determined. 29 mobile and 93 immobile molecules can be detected in the frame of $100 \times 100\,\mathrm{nm}^2$. The determined high percentage of residual precursor molecules (24%), however, only represents an upper limit, since the tip-induced motion of the molecules does not necessarily end at the edges of the represented image and could therefore be attributed to a larger area. Another restriction must be made by the identification of the mobile species, since brighter and darker features are present. A closer look reveals that some bright features reappear darker and offset to the right side. It can

be concluded that a multiple-tip is the reason for this phenomenon, which is absent for the heptacene molecules due to their lower adsorption geometry. Therefore, the counting of the features must be revaluated and leads to an upper limit of 14% (15 mobile features) taking into account only the diffusion traces with an apparent height of 360 nm.

As stated above, the individual molecules and the diffusion traces are oriented along the high-symmetry directions of the substrate ($[\bar{1}01]$, $[\bar{1}10]$, $[01\bar{1}]$). The heptacene molecules are immobilized and appear slightly darker in the center of the molecule (Fig. 6.6 (a)). The diffusion trace of DEH is distinctly segmented (Fig. 6.6 (b)) due to the hopping from one adsorption site to the next. The 1D lattice constant of the periodic segmentation of 2.9 Å is in good agreement with the interatomic Ag – Ag distance (2.89 Å) along the high-symmetry directions of the surface. The width of the mobile feature is 1.18 nm. Considering the spatial expansion in the VT-STM image (Fig. 6.4), DEH most likely diffuses parallel to its long side. The heptacene molecules are spread over 2.26 nm in length and 0.59 nm in width (expected values: 2.027 nm and 0.607 nm). Slight deviations in the size of horizontally and vertically aligned molecules can be attributed to scan speed artifacts.

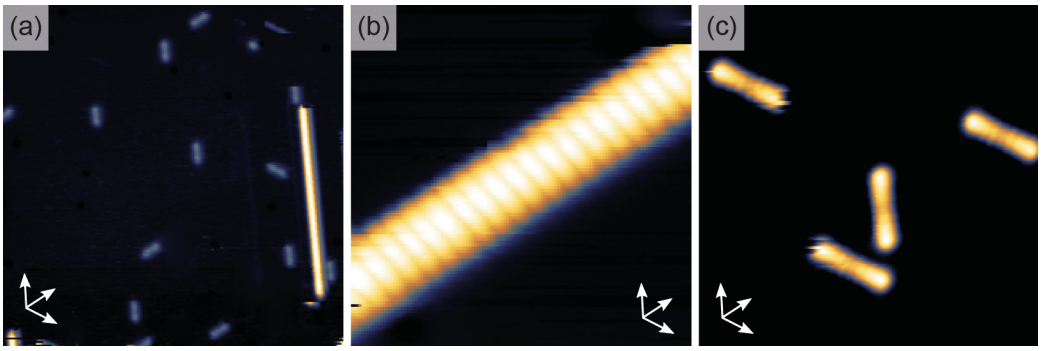

Figure 6.6: (a) LT-STM images of heptacene molecules and diffusion traces from residual DEH after annealing to 460 K. Magnified views of (b) a diffusion trace and (c) individual heptacene molecules. The heptacene molecules and diffusion traces of DEH align along the high-symmetry directions of the substrate ($[\bar{1}01]$, $[\bar{1}10]$, $[01\bar{1}]$), which are indicated by the arrows. Image sizes: (a) $40 \times 40\,\mathrm{nm}^2$; (b) $4.7 \times 4.7\,\mathrm{nm}^2$; (c) $9.5 \times 9.5\,\mathrm{nm}^2$. Tunneling parameters: (a) 1.3 V, 2 pA; (b) 1.5 V, 10 pA; (c) −1.1 V, 10 pA. All images were taken at 4 K.

Figure 6.7 shows bias-dependent changes in the electronic structure of heptacene molecules. However, the bright appearance of the wings or the dark protrusion in the center of the molecule are predominant at all bias voltages and only a little bit more prominent at positive polarity (Fig. 6.7 (d) *vs.* 6.7 (f)). The close vicinity of the heptacene to two adsorbed CO molecules was chosen to evaluate the mobility of the molecules. In contrast to the very high mobility of the precursor molecules, the didecarbonylated heptacene diffuses exceedingly slowly over the surface in the timescale of the STM experiment (304 min). The interaction with the substrate is much higher due to the flat adsorption structure. Nevertheless, the adsorption structure seems not to be totally flat and the depression gives a hint for a pronounced interaction of the center of the molecule with the surface.

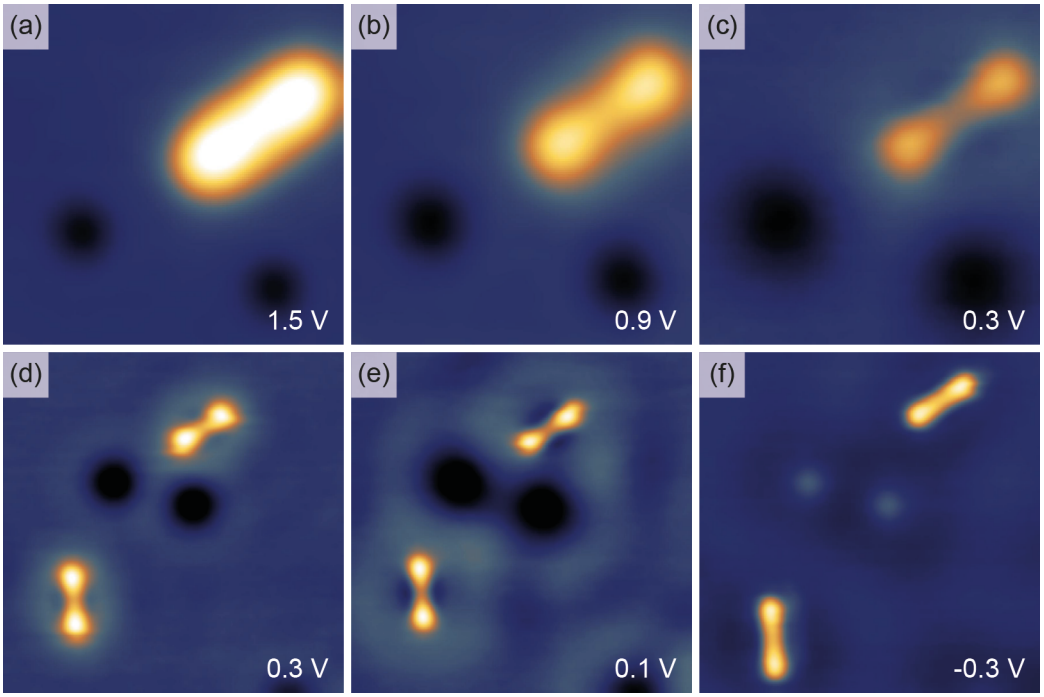

Figure 6.7: Individual heptacene molecules on Ag(111) at varied bias voltages after annealing to 460 K. Low bias voltage at positive as well as negative polarity reveals the dumbbell shape of the molecules. The dark spots indicate the presence of adsorbed CO molecules from residual gas in the UHV chamber due to the annealing process. Images sizes: (a-c) $4.5 \times 4.5\,\mathrm{nm}^2$; (d-f) $11 \times 11\,\mathrm{nm}^2$. All images were recorded with a tunneling current of 2 pA and at a temperature of 4 K. Color scale: (a-c) 5 to 140 pm, (d-f) adjusted independently.

6.3 Unoccupied States of Heptacene Molecules on Ag(111)

Additional insight into the conversion of DEH and the orientation of the molecules on the Ag(111) surface is gained by means of NEXAFS spectroscopy. A sample with an inital coverage of $1\,\mathrm{ML}_{\mathrm{ads}}$ was investigated prior to and after annealing (Fig. 6.8) using incident radiation in an angular range of 90° (s-polarized light, perpendicular to the surface) to 25° (p-polarized light, grazing incidence) to study the X-ray dichroism. Comparison of the untreated sample (Fig. 6.8 (a)) and after annealing to 460 K (Fig. 6.8 (b)) yields a decent change of the π^*-peaks subsequent to the carbon K-edge (284-285.5 eV) due to the transition into heptacene. In consideration of the STM images, heptacene should adsorb almost flat and with the π-system facing to the surface. It is therefore expected that the π^*-resonance is largest for a grazing (25° incidence angle) and zero for a normal incidence (90° incidence angle). Indeed, the π^*-intensity decreases with increasing angle of incidence and *vice versa* for the σ^*-region (Fig. 6.8 (b)). However, the spectra still show a substantial, residual intensity of a π^*-peak at 90°. The same applies for the precursor (Fig. 6.8 (a)). Here, the remaining intensity is inherent to the bent structure of its molecular backbone. To quantify the angular orientation of the molecular π-system on the surface or in other words the angle α between the surface normal and the transition vector $\vec{T}$, the π^*-intensities at 284.5 eV were analyzed and plotted against the angle of incidence ε (Fig. 6.8 (c)). The data points were fitted with Equation 3.19 considering a factor b for the normalization of the curves. The experimentally determined value of 17.2° for the precursor deviates from the expected value of 26.75°. The deviation can be explained

by the deformation of the precursor molecule caused by the interaction with the surface in contrast to the undisturbed gas phase structure. The angle 18.7° for heptacene on Ag(111) is surprisingly high and contradictory to the previous results, since a value close to 0° would have been expected for a flat adsorption structure. As the STM results show in the characteristic contrasts at the center and at the ends of the molecules, the converted molecules interact with the substrate surface. It can therefore be concluded that also the π-system is affected and different for the adsorbed heptacene in contrast to the situation in the gas phase. If a substantial interaction at the center of the molecule is assumed, the hybridization of the carbon atoms at the positions 7 and 16 would differ from the sp^2-case resulting in a rehybridization of the molecular orbitals with the substrate. The system partially gets a sp^3-character. The adsorption induced rehybridization was already reported by C. Mainka *et al.* for chemisorbed planar aromatic molecules, pyromellitic dianhydride and benzene, on Pt(111).[292] Due to the out-of-plane deformation, excitation into π*-orbitals has become allowed at 90° incidence angle. Therefore, the angular dependent analysis leads only apparently to a non-zero adsorption angle but does not provide real geometrical information on the orientation of the molecular plane on the surface. The evaluation gives, however, an important hint on the molecule-substrate interaction, which will be quantified in the following theoretical approach.

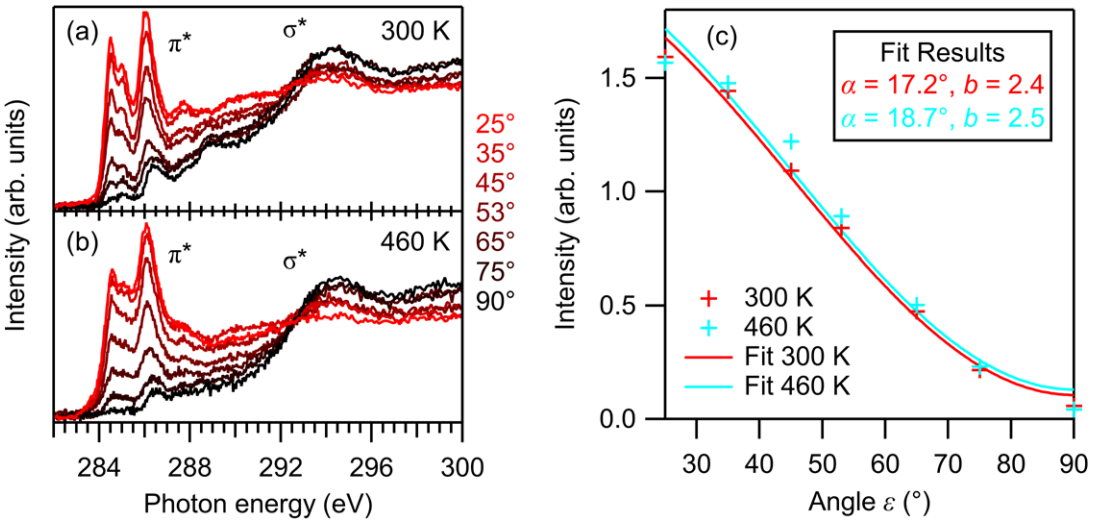

Figure 6.8: Carbon K-edge NEXAFS spectra of (a) DEH (1 ML_{ads}) after deposition onto Ag(111) at RT and (b) after transition into heptacene by annealing at 460 K. The spectra were recorded in dependence on the angle ε of the incident radiation. (c) The analysis of the π*-peak intensities as a function of the incidence angle reveals an apparent angle of 17.2° between the surface normal and the normal of the molecular π-system for DEH and 18.7° for heptacene. The degree of polarization at the HE-SGM beamline is $P = 0.91$. The parameter b was introduced as a normalization factor for the curve fitting.

6.4 Surface-Assisted Stabilization of Heptacene Molecules

The periodic DFT calculations were performed by Wolfgang Hieringer. See Ref. [282] for details on the calculations, used programs and methods.

As indicated by the contrast variations in the STM images and by the rehybridization

concluded from the NEXAFS measurements, a substantial interaction of heptacene with the substrate Ag(111) is expected going along with a deformation of the molecule. The adsorption geometry in its minimum-energy configuration was therefore calculated by means of DFT as shown in Figure 6.9. A deformation of the molecular backbone is obvious already from the side view (Fig. 6.9 (a)). To quantify the deformation, two planes (red and blue) were defined by three different numbers of outer-most carbon atoms (Fig. 6.9 (b)). Including the outermost 10 atoms on each side (corresponding to naphthalene units at the ends of the molecule), the angle between the planes is 3.5°. The same applies for the outermost 14 atoms. If only the outermost 6 atoms are enclosed in the planes, the angle is, however, reduced to 2.8°. Therefore, the molecule is not only closer to the surface at the central ring but also deformed at the ends of the chain, and appears to be mustache-shaped (upside down) by the interaction-induced deformation. The adsorption site of heptacene on Ag(111) is between two rows of Ag atoms of the (111) lattice (Fig. 6.9 (c)). The slightly closer distance of the two central carbon atoms to the plane through the Ag atoms is 2.67 Å for the atop-C and 2.74 Å for the bridge-C, while the four terminal carbon atoms exhibit a larger distance of 2.95 Å and 2.94 Å for the atop-C and 2.94 Å and 2.93 Å for the hollow-C. Small changes in the C−C bond lengths of the peripheral atoms were identified.

The interaction with the metal substrate can be quantified by a Bader charge analysis resulting in a total charge transfer of −0.6 e from the substrate to the heptacene molecule. The charge density difference plots (Fig. 6.9 (d), (e)) show an increased electron density in the center of the molecule, specifically at the outer carbon atoms.

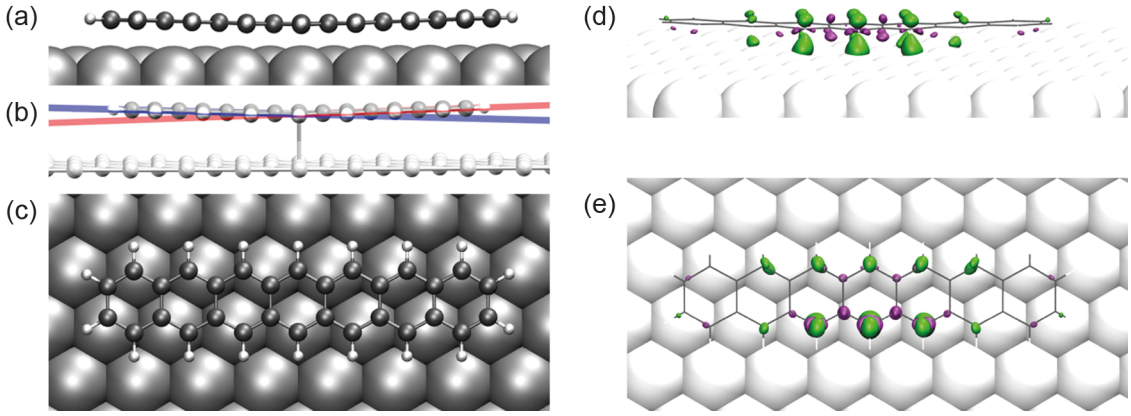

Figure 6.9: (a-c) Optimized geometry of heptacene on Ag(111) from the DFT calculations; (a) side view, (b) side view with emphasis on the deviation from planarity as described by the angle (3.5°) between two planes that are defined by the 10 outermost carbon atoms on each side of the molecule, and (c) top view. (d, e) Skew and top views of the calculated charge density difference upon adsorption; green and magenta represent increased and decreased electron density, respectively, with respect to the isolated molecule and slab; the isodensity values of the contours shown are ±0.015 eÅ^{-3}.[282] (Reproduced by permission of The Royal Society of Chemistry.)

As mentioned in the introduction and illustrated in a simplified way by the presence of only one Clar sextet, acenes lose their benzenoid character with increasing molecular length accompanied by a reduced stability, unless the conjugation of the π-system is interrupted, *e.g.* by a diketone bridge in the precursor. The high reactivity can lead to the formation of a dimer. While Mondal and Bettinger prevented the dimerization of heptacene by using a

solid or inert gas matrix, the surface acts as a two-dimensionally confined matrix in the here presented case. The heptacene molecules are stabilized due to the central interaction with the substrate. This interaction appears as a depression in the STM image (Fig. 6.10 (a)). The correlation of the interaction with this feature was verified by a DFT simulation exhibiting the same contrast change (Fig. 6.10 (b)). The charge transfer from the surface and thus a partially negatively charged molecular center results in the formation of a second CLAR sextet and the presence of two anthracene-like wings (Fig. 6.10 (c)). Michael BENDIKOV *et al.* already predicted theoretically the presence of open-shell diradical singlet ground states for oligoacenes larger than hexacene.[56] The change from a closed-shell to an open-shell state and thus the loss of a π-bond is thermodynamically favored for [n]acenes with $n > 6$, which can be explained in the same fashion as for the here observed case, namely the formation of an additional π-sextet and 1,4-interaction of the central ring for an increased stability of the system.[54] This size-dependency is the reason that no indications of an increased interaction were found for hexacene.[86] Furthermore, heptacene is a better electron donor and acceptor than hexacene due to the smaller HOMO-LUMO gap represented also in the reduction potentials of substituted derivates.[65]

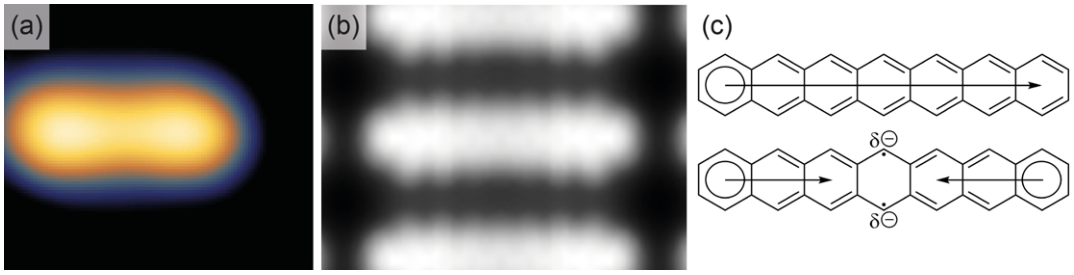

Figure 6.10: Comparison of dumbbell shaped features of a heptacene molecule in (a) an experimental LT-STM image on Ag(111) ($2.7 \times 2.3\,\mathrm{nm}^2$, +1.7 V, 2 pA, 4 K) and (b) a DFT-calculated STM image (+1.7 V, 2 pA). (c) CLAR structures with the corresponding π-sextets of a neutral heptacene and a heptacene which is partially negatively charged due to the interaction with the substrate. As a result of the interaction, the central ring is saturated leading to the formation of two separate anthracene-like units and thus the dumbbell shape in STM images.

6.5 Heptacene on a Cu(111) Surface

As reported by Meng-Chao Lu *et al.*, pentacene exhibits a similar monolayer growth with an almost flat-lying adsorption structure on all substrates of the 11$^{\text{th}}$ group in the periodic table.[293] In the multilayer, a tilted orientation of pentacene was found on Ag(111) and Cu(111). On Au(111), evidences for intermolecular rehybridization suggest a π-stacked growth, while other studies also show a tilt angle of 31°.[82] The results of heptacene on Ag(111) prove a considerable increase in the surface-molecule interaction for larger oligoacenes, wherefore the influence of an even more reactive surface like Cu(111) was also subject to investigations.

Unambiguous conclusions from the XPS measurements could not be drawn due to the presence of the Cu L_2VV (548 eV) and Cu L_3VV (568 eV) Auger transitions in the relevant O 1s spectral region for the photon energy of the used Al K_α radiation. Therefore, only the phenomena observed in STM experiments will be discussed here.

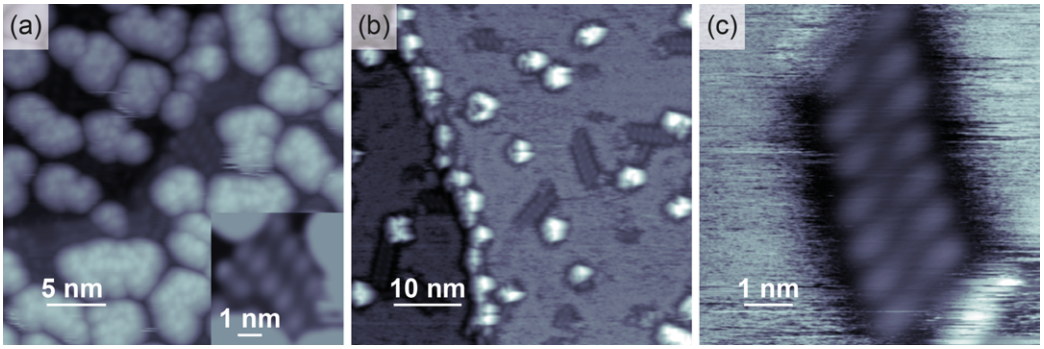

Figure 6.11: VT-STM images of (a) a multilayer deposition of DEH onto Cu(111) at room temperature and (b, c) of a second experiment with a reduced coverage. Image (a) show that the molecules in the first layer are individually resolved and immobilized, visible also in the inset, while other molecules are aggregated. In a reduced coverage, the aggregation is less pronounced and the DEH molecules appear in stacks. Tunneling parameters: (a) 1.20 V, 0.10 nA; (b) 3.21 V, 0.19 nA; (c) 3.21 V, 0.17 nA. The measurements were performed at 150 K.

Upon room-temperature adsorption of DEH onto Cu(111), three-dimensional aggregates are visible parallel to individual molecules in the first layer (Fig. 6.11 (a) and inset). Since the same deposition parameters as for the experiments on Ag(111) were used, it can be concluded that the sticking probability of DEH on Cu(111) is higher than on Ag(111) leading to a coverage larger than one monolayer. After reducing the amount of deposited molecules in a second experiment, the number of aggregates is decreased and DEH molecules are visible arranged in stacks of up to 10 molecules (Fig. 6.11 (b)) The blurry areas most likely result from highly mobile species in a second layer, since these areas appear brighter than the recognizable molecules. The stacked molecules exhibit a depression in the center and are shifted laterally (Fig. 6.11 (c)). If the sample is annealed to 460 K to trigger the didecarbonylation reaction, individual heptacene molecules are immobilized at the step edges of the substrate (Fig. 6.12 (a)). At a measurement temperature of 150 K, mobile features are still visible. Extensive increasing of the tunneling voltage to values higher than 5 V immediately results in the immobilization of molecules in the affected area (Fig. 6.12 (b), (c)). Due to the high voltages, the C–H bonds are cleaved leading to an increased interaction with the Cu(111) surface. The DEH molecules in Figure 6.11 (c) are, however, immobilized by a strong Cu–O interaction of the diketone bridge

pointing downward suggested by the appearance of the molecular shape with wide features and bright contrast at the ends different than observed before.

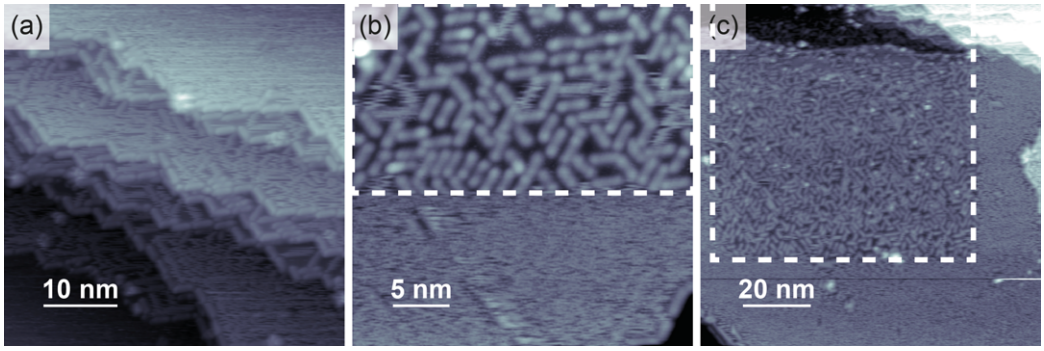

Figure 6.12: VT-STM images of (a) heptacene on Cu(111) after annealing of DEH to 460 K and (b, c) of tip-induced reactions of heptacene on Cu(111). The dashed lines mark the areas in which the high bias voltage was applied. Tunneling parameters: (a) 2.02 V, 0.03 nA; (b) 3.11 V, 0.05 nA; (c) 3.02 V, 0.08 nA. The measurements were performed at 150 K.

7 Summary

The results of this thesis illustrate the diverse approaches emerging from the field of surface chemistry. The investigations comprise reactive aromatic molecules adsorbed on coinage metal surfaces (Cu(111), Ag(111), Au(111)). The interaction with the metal substrate as well as coordination reactions with post-deposited d-block (Fe, Co, Ni) and main group metals (Pb) were part of the studies. The main experimental focus of this work was the microscopic evidence of reaction products and structural formations in coordination or covalent networks characterized by means of STM. The experiments were carried out at ambient temperatures for the examination of close-packed monolayers or on cooled samples at 150 K to optimize a stable imaging of the STM. Low-temperature measurements at 4 K were essential in the study of single molecules. The choice of the employed spectroscopic techniques had aimed at the study of occupied and unoccupied electronic states of core and valence orbitals. Spectroscopy was performed as photoemission (XPS, UPS) and photoabsorption processes (NEXAFS). The corresponding experiments were conducted with a laboratory UHV apparatus and at a synchrotron radiation facility.

The molecules of investigation stand out due to their aromatic character. Functional moieties or inherent heteroatoms provide a reactive behavior of the chemical compounds even on inert surfaces. The majority of studied molecules arise from the family of tetrapyrroles. Porphyrins have been investigated concerning their coordination reaction, either in the form of a metalation of the cavity in the macrocycle or as coordination of metal adatoms due to a cleavage of bromine substituents with a subsequent C−C bond formation. The structurally similar but chemically different corrole has been studied in metalation reactions and in respect to the dehydrogenation of the inner nitrogen heteroatoms occurring already below room temperature due to an interaction with the metal substrate. Extended phthalocyanines, annulated naphthalocyanines, were synthesized from a dicarbonitrile precursor in a cyclization reaction with post-deposited metal atoms. The self-assembly of nitrile terminated oligophenylenes has been discussed in dependence on the coverage and the nature of the intermolecular forces. In the competing field of the on-surface synthesis of linearly annulated aromatic molecules, a hitherto challenging synthesis of heptacene, which lacks stability due to a decreased benzenoid character, was accomplished *via* a surface-stabilized route. Together with collaboration partners in the field of theoretical chemistry, further insight was achieved concerning the adsorption geometry of the investigated molecules as well as their electronic properties and the charge transfer between the organic or organometallic compounds and the metal substrates.

Although all experimental projects possess their own character and individual questions, the conducted experiments can be subdivided into three topics, namely organic macrocycles and their coordination chemistry, the role of reactive functionalization of aromatic molecules in tetramerization reactions and self-assembled structures, and the on-surface synthesis of highly reactive molecules from suitable precursors. The following will summarize the results which were achieved in each field.

7.1 Organic Macrocycles and their Coordination Chemistry on Surfaces

As presented in the introduction, porphine and corrole are closely related parent macrocycles in the family of tetrapyrroles. Due to the absence of a bridging methine group in the corrole macrocycle, the chemical environment in the cavity of the organic molecules is distinctly different. Although both macrocycles act as tetradentate organic ligands in the coordination of metal atoms providing a square planar geometry, the coordination mechanism is different due to the tribasic acid character of the corrole molecule. While the metal ion in a metalloporphine macrocycle exhibits a $+\,\mathrm{II}$ oxidation state as it was suggested in solution chemistry works and in fundamental considerations, the corrole macrocycle stabilizes an oxidation state of $+\,\mathrm{III}$. Additionally to the chemical environment, the smaller ion diameter of high-valent metal cations matches with the tighter cavity in the corrole molecule. Since the knowledge of the electronic properties of the central metal ions, which serve as an accessible coordination site, would be beneficial for future applications in heterogeneous catalysis, the fundamental question has arisen whether the oxidation states of the metal centers in metallocorroles are different from the oxidation states in metalloporphyrins even in the adsorbed state.

The metalation of porphyrins was already addressed in previous works. Additionally, first spectroscopic results on the on-surface metalation of corrole existed in the group of Prof. Dr. J. Michael Gottfried. These findings have been intensified and extended to further metals with another d-orbital configuration in this work, *i.a.*, by employing complementary experimental methods. Since the contrast in STM experiments is a convolution of the sample topography and electronic states of the sample and the tip, qualitative conclusions on the local electronic properties including the molecular or atomic orbitals can be drawn. Depending on the deposited metals, the STM images exhibit different features in the contrast of the metal ion. While the Co ion in CoHEDMC can easily be detected at moderate tunneling conditions, the Fe and Ni ions in the corresponding metallocorroles are subject to an obvious bias voltage dependency. CoHEDMC was compared to adjacent CoOEP molecules in a co-deposition experiment and a different contrast of the Co ions was detected. Due to the number of ethyl substituents, the hexaethyldimethylcorrole and octaethylporphyrin molecules can be detected in a facile way. The choice of the porphyrin compound proved to be suitable for the comparison. The central Ni ions in NiHEDMC were not detectable under the employed conditions. However, an influence on the appearance of the macrocycle was observed in the images of NiHEDMC. The visibility of the coordinated metal ion in FeHEDMC is connected to the polarity of the bias voltage. While the Fe ion is visible in the case of negative voltages, the same feature is absent, when the polarity is changed. Co-deposited FeOEP molecules do not show this dependency. The STM measurements were interpreted by means of UPS experiments probing the occupied valence states. In those experiments, the observed phenomena were verified. In the case of FeOEP, the image features of the metal ion visible at both polarities were attributed to intensity intersected by the Fermi edge, whereas FeHEDMC shows no enhanced intensity close to the Fermi edge. The UV photoelectron spectrum of FeHEDMC exhibits a broad peak above 1.0 eV, which is similar to the feature in the 2H-HEDMC spectrum

but probably contains contributions from metal d-orbitals. For NiHEDMC in contrast to NiOEP, the intensity resulting from the Ni d-orbitals is located at higher binding energies and was therefore not visible in the conducted STM experiments. The contrast mechanism of CoHEDMC and CoOEP was explained by an energy difference in the occupied states of 0.4 eV. The comparison of STM and UPS results showed that the imaging contrast and thus the electronic properties are different for metalated porphyrins and corroles in adsorbed monolayers.

XP spectra of the metalated monolayers are not unambiguous with regard to the oxidation state of the metal center. The M 2p spectra exhibit only a slightly shifted position of the corresponding corrole peaks in contrast to the porphyrin peaks and can therefore not explain the electronic state of the metal ions in the macrocycles. Nevertheless, XPS measurements of the metal orbitals in the organic multilayers after the metalation with Co and Fe suggest the presence of metal ions in the oxidation state + III in the metalated complex of HEDMC and an oxidation state of + II for the corresponding M(II)OEP complex. For all studied systems, the N 1s spectra show a participation of all four nitrogen atoms including their dehydrogenation and thus prove the tetradentate character of the corrole macrocycle. According to these spectra, the metalation can be declared as successful. The unoccupied states of the metallotetrapyrroles were probed by means of NEXAFS. FeHEDMC and FeOEP multilayers differ in the Fe L_3-edge. While the resonance peak of FeOEP shows a characteristic splitting, this feature is absent in the case of FeHEDMC. By comparison with literature experiments, conclusions on the oxidation states could be drawn. The double peak structure observed for FeOEP multilayers was also reported for FePc. The broad resonance of FeHEDMC resembles Fe(III)TPP-Cl and Mn(II)Pc with an isoelectronic metal center. The oxidation state of the Fe ion in the corrole complex is therefore suggested to be + III in adsorbed multilayers. Monolayers of FeHEDMC and FeOEP likewise show different resonances in the NEXAFS spectra. In analogy to those experiments, NEXAFS measurements of CoHEDMC and CoOEP revealed the presence of Co(III) and Co(II) ions in metalated corrole and porphyrin multilayers, respectively. In the case of metalated porphyrin and corrole molecules adsorbed on Ag(111) in a monolayer coverage, the metal ion in the cavity of macrocycle is influenced by the surface. The substrate acts as an additional ligand effecting the oxidation state of the ion by charge transfer. The former + III oxidation state in the multilayer can therefore not be detected in the monolayer experiment. STM, UPS and NEXAFS measurements though suggest that electronic differences due to the nature of the corrole macrocycle and the chemical environment of the coordinated metal ions remain.

While porphyrins show no enhanced surface reactivity on coinage metal surfaces at room temperature, the related corrole molecules reactively interact with the Ag(111) substrate already from 240 K on. In an XPS series with annealing steps at increasing temperatures, the behavior of the N 1s species was studied. As aforementioned, the corrole macrocycle possesses three protonated, pyrrolic nitrogen atoms and one iminic nitrogen. The ratio of these species was found in the corresponding spectrum of a 3H-HEDMC monolayer at 180 K. Upon annealing, the ratio is shifted to a 1 : 1 situation at slightly lower binding energies. The transformation is completed at room temperature. The newly derived ratio indicates the co-

existence of two species in an equal amount. This finding led to the conclusion that one pyrrolic nitrogen atom is subject to a surface-assisted dehydrogenation. The difference to the more inert porphyrins can be explained by the higher acidity for the first deprotonation step of corroles. The acidic hydrogen in ring D deviates from the corresponding pyrrole plane and points toward the surface upon adsorption on Ag(111). The hydrogen consequently interacts strongly with the surface and is detached already far below room temperature. This fact has to be respected, when corrole molecules are investigated in monolayers on metal surfaces. The shift of the peaks in the N 1s spectrum assigned to the 2H-HEDMC reaction product and absent in the corresponding C 1s region, and the reduced peak separation, suggest a charge transfer from the surface located at the N atoms. Although previous studies reported a homolysis of the N−H bond, no evidence for a radicalic character was found in the here presented spectra.

Additionally to the reactive interaction of 3H-HEDMC with the Ag(111) substrate, the formation of superstructures was observed upon reaching room temperature. The ethyl substituents of hexaethyldimethylcorrole dominate the STM images. Due to the proximity of four ethyl groups on one side and two groups on the other side of the molecules, the orientation of the macrocycle can directly be concluded from STM images with submolecular resolution. The azimuthal orientation of the molecules determined by the position of the ethyl moieties of 3H-HEDMC at 150 K exhibits two preferred but yet statistically distributed orientations within a diagonal row. In contrast, highly regular arrangements occur in close-packed domains of 2H-HEDMC at 300 K. Within a row of molecules, 2H-HEDMC shows the orientational sequence $\downarrow$, $\uparrow$, $\rightarrow$, $\leftarrow$. The sequence reappears in the adjacent row but is shifted. The resulting superstructure shows chiral double-S motifs, which consist of the protruding ethyl groups of four 2H-HEDMC molecules. The molecular density is higher in the low-temperature phase of 3H-HEDMC than in the double-S phase of 2H-HEDMC. The increased intermolecular distances result from an altered alignment of the flexible ethyl substituents in order to maximize the VAN DER WAALS forces between neighboring molecules. The large 2H-HEDMC should therefore be more stable than the 3H-HEDMC at lower temperatures. The dehydrocyclization of HEDMC was observed above 500 K. The molecules appear planarized in the corresponding STM images and the protrusions of the ethyl moieties are vanished in favor of laterally expanded edges of the molecules. Furthermore, some molecules seem to be interconnected.

To provide complementary information to an STM investigation on the metalation of porphyrins with Pb, a heating series of a sample containing 2HTPP and Pb on Au(111) was conducted. The reaction was monitored by means of XPS. The N 1s spectra show the expected metalation feature upon deposition of Pb onto the 2HTPP monolayer. The Pb $4f_{7/2}$ and Pb $4f_{5/2}$ signals, respectively, at higher binding energy were attributed to a Pb(II) species by regarding literature results. A comparison with the reacted nitrogen species reveals a slight deviation from the expected ratio but suggests the formation of Pb(II)TPP. Increasing temperatures do not change the general composition of the N 1s region except for a shift of the reacted species above 520 K. In contrast, the Pb 4f spectra are subject to a distinct transformation due to the thermal treatment. The species assigned to the formation of Pb(II)TPP decreases in favor of the peak at the Pb(0) position. Two approaches to explain these findings

have been presented. The first idea is that the adsorption geometry allows a Pb-up and a Pb-down position and that the Pb-up is present as Pb(II) due to a decoupling from the substrate. Annealing would then induce a transformation to the Pb-down geometry and a reduction of the metal ion. However, this suggestion is in contradiction to DFT calculations, which show a charge transfer in the opposite direction. Alternatively, the Pb ion is detached from the macrocycle upon annealing and the reacted nitrogen species at higher temperatures result from an interaction of the macrocycle with Au atoms from the substrate. The performed experiments are not capable of revealing the exact mechanism. Further information could be achieved by employing TPD. In this experiment, the desorbed species, *e.g.*, AuTPP, would be determined by means of mass spectrometry. The formation of Au-porphyrins from the free-base ligands on Au(111) were not reported before, but could be the result of a transmetalation. In the light of new insights, the changes in the N 1s spectral region could be explained. Preliminary TPD experiments should be performed on the commercially available PbPc on Au(111) to ensure the presence of metalated macrocycles. Additionally, multilayer experiments could be regarded to discover whether the metalation process in the multilayer is decoupled from the substrate or whether it resembles the situation of 2HPc on a barrier layer of NiPc on Cu(111), where an exchange between the layers was observed.[294]

The reactive coupling of macrocycles has been discussed on NiTBrPP, whose phenylene substituents are terminated with bromine atoms in the *para*-position. Upon deposition on Cu(111), the C–Br bonds are dissociated and the macrocycles are arranged in a rectangular coordination network, in which Cu adatoms are coordinated by the phenyl groups of two adjacent porphyrins. The organocopper compound represents a reaction intermediate. A subsequent C–C coupling by means of the Ullmann reaction is expected to occur at elevated temperatures. The formation of ordered covalent networks in sizes of more than six molecules was not observed, since the coordination networks were already dissolved upon annealing to 370 K. The resulting NiTPP molecules are, however, covalently linked albeit in a disordered, meandering network. The adsorbed bromine atoms emerge in a triangular form, which was observed in other experiments containing bromine residues on Cu(111) as reported in the literature.

7.2 Functional Groups in On-Surface Synthesis and Self-Assemblies

Related to the tetrapyrrole macrocycles, annulated naphthalocyanines were synthesized by on-surface reaction of a dicarbonitrile precursor (NDN*) with post-deposited Fe atoms on Ag(111). Initially, the formation of self-assembled short-range and long-range ordered domains of NDN* were observed. The domains are stabilized by intermolecular dipole-dipole interactions between the nitrile groups. The observed motifs contain four to six molecules, of which some are arranged around cavities in the domains. Upon annealing to 450 K, the nitrile moieties of adjacent molecules react with each other resulting in a tetramerization and the formation of metallonaphthalocyanines. Beside those FeNc* molecules, oligomers were observed. The suggestion was made that the oligomers likewise result from a metal-mediated reaction, but the submolecular resolution of the STM images cannot prove the incorporation of metal atoms

in the oligomeric macrocycle. The formation of FeNc* occurs readily on Ag(111). A reaction with surface adatoms in the style of a self-metalation on Cu(111) yielded only small amounts of tetrameric products. The on-surface tetramerization proves to be a suitable pathway for the investigation of extended phthalocyanines. While the employed precursor was a relatively stable model system, the formation of even larger as well as chemically and thermally unstable molecules could be performed on the same route. The project contributes to the attempts in surface science of enabling the investigation of complex systems with interesting electronic properties.

The self-assembly of nitrile terminated oligophenylenes provides insight into the interaction of molecules on surfaces with special regard to the functional groups. *m*-3PDN arranges in zipper-like and dimer structures on Ag(111). A similar domain was observed in the case of *m*-4PDN on the same substrate. The interaction of the nitrile moieties with the phenyl unit in the center of the kinked oligophenylene chain can be ascribed to CH···N hydrogen bonds. These bonds stabilize the arrangements of molecules in a row or in the dimers, whereas only weak VAN DER WAALS forces are expected between molecules placed back-to-back.

A systematic introduction of prochiral molecules can be beneficial for achieving more complex structures. Domains of *m*-4PDN show an enantiomeric separation. Similar to the previously described interaction between adjacent molecules due to hydrogen bonds, a prominent adsorption structure of *m*-4PDN exhibits threefold nodes which are arranged in a Kagome-like superstructure. The porosity of this structure could by applicable in the systematic functionalization of surfaces. Upright standing molecules were observed in lateral confinements. The molecules appear stacked and are stabilized by π–π-interactions. The appearance of the superstructures can be steered depending on the coverage of the molecules on the surface. While self-assemblies of these dicarbonitrile molecules have been discussed regarding their intermolecular electrostatic attraction due to hydrogen bonds and VAN DER WAALS forces, literature studies reported the utilization of those dicarbonitrile functionalized molecules in the formation of SIERPIŃSKI triangles. A corresponding literature work shows the formation of the fractals at low coverages on Cu(111). The nodes of the fractals consist of coordination bonds to Cu adatoms. At a coverage close to the monolayer, the dicarbonitrile oligophenylenes are assembled by hydrogen bonds as it was observed in this work.

7.3 On-Surface Synthesis of Highly Reactive Molecules

The synthesis of heptacene was highly controversial for more than 60 years, until the formation of the pure compound was finally achieved. The high reactivity of heptacene toward oxygen and the occurrence of photodimerization products required inert solid or gaseous matrices. This work contributes a novel synthetic pathway. Based on the α-diketone reactant DEH, the assistance and stabilization by the Ag(111) surface was used to achieve the formation of heptacene. In this process, the Ag(111) surface replaces the matrices. Furthermore, the interaction with metal surfaces has been discussed. Adsorbed DEH was gradually annealed and the transition was monitored by means of XPS. The aliphatic and carbonyl carbon species disappeared above 460 K in the C 1s spectra, while the aromatic species remains. Together with

the absence of the previously observed carbonyl oxygen in the corresponding O 1s spectra, this finding proves the cleavage of the diketone bridge. While charring was observed in literature works for the decarbonylation of diketone precursors at higher temperatures, the Ag(111) catalyzes the didecarbonylation reaction of DEH resulting in heptacene and allows milder conditions without evidence for side reactions. To gain insight into the appearance of the molecules, the precursor molecules and the heptacene products were investigated in VT- and LT-STM experiments. Due to its backbone, the DEH molecule appeared highly mobile on the surface. By constricting the molecules into a close-packed monolayer, the shape of the adsorbed precursor was revealed. The aromatic wings point toward the surface and the α-diketone bridge can be observed as a protrusion. In LT-STM images of a submonolayer, the DEH molecules are subject to tip-induced one-dimensional diffusion. Upon annealing to the transition temperature, the resulting heptacene molecules are immobilized on the surface. As well as the precursor, the molecules are oriented along the high-symmetry directions of the surface. STM images at 4 K show the heptacene molecules as elongated objects. Depending on the bias voltage, the molecules exhibit a slightly dumbbell shaped feature. The depression in the center of the heptacene molecules suggests a strong interaction with the Ag(111) surface. The orientation of the precursor and the reaction product was additionally studied by means of NEXAFS spectroscopy. The evaluation of the π^*-resonances at the carbon K-edge at varied incidence angles of the X-ray radiation yields angles of 17.2° and 18.7° between the surface normal and the normal of the molecular π-system for DEH and heptacene, respectively. While the derived value is close to the expected orientation of the π-system of DEH on the surface, the apparent non-zero adsorption angle of heptacene was explained by a rehybridization of the molecular orbitals with the substrate due to the adsorbate-substrate interaction at the center of the heptacene backbone. Periodic DFT calculations revealed the deformation of the adsorbed heptacene molecule and a charge transfer of −0.6 e from the substrate. The combination of the experimental and theoretical methods proves the formation of heptacene on a surface-assisted route. STM, XPS and DFT reveal the substantial interaction between the long, unsubstituted acene and the metal substrate. The results are in congruence with the concept of Clar's aromatic π-sextets. Large acenes suffer from the loss of benzenoid character with increasing length of the linearly annulated system illustrated by the presence of only one Clar sextet. The interaction of heptacene with the surface interrupts the conjugation of the π-system and results in a stabilization of the heptacene molecule.

A Bibliography

[1] J. M. Gottfried, H. Marbach, *Z. Phys. Chem.* **2009**, *223*, 53–74, DOI 10.1524.zpch.2009.6024.

[2] J. M. Gottfried, *Surf. Sci. Rep.* **2015**, *70*, 259–379, DOI 10.1016/j.surfrep.2015.04.001.

[3] H. Marbach, *Acc. Chem. Res.* **2015**, *48*, 2649–2658, DOI 10.1021/acs.accounts.5b00243.

[4] W. Auwärter, D. Écija, F. Klappenberger, J. V. Barth, *Nat. Chem.* **2015**, *7*, 105–120, DOI 10.1038/nchem.2159.

[5] K. Diller, A. C. Papageorgiou, F. Klappenberger, F. Allegretti, J. V. Barth, W. Auwärter, *Chem. Soc. Rev.* **2016**, *45*, 1629–1656, DOI 10.1039/c5cs00207a.

[6] *Physics of Organic Semiconductors*, (Ed.: W. Brütting), Wiley-VCH Verlag, **2005**.

[7] N. Koch, *ChemPhysChem* **2007**, *8*, 1438–1455, DOI 10.1002/cphc.200700177.

[8] I. G. Hill, A. Rajagopal, A. Kahn, Y. Hu, *Appl. Phys. Lett.* **1998**, *73*, 662–664, DOI 10.1063/1.121940.

[9] A. Kahn, N. Koch, W. Gao, *J. Polym. Sci. Part B: Polym. Phys.* **2003**, *41*, 2529–2548, DOI 10.1002/polb.10642.

[10] F. Amy, C. Chan, A. Kahn, *Org. Electron.* **2005**, *6*, 85–91, DOI 10.1016/j.orgel.2005.03.003.

[11] C. Barraud, P. Seneor, R. Mattana, S. Fusil, K. Bouzehouane, C. Deranlot, P. Graziosi, L. Hueso, I. Bergenti, V. Dediu, F. Petroff, A. Fert, *Nat. Phys.* **2010**, *6*, 615–620, DOI 10.1038/nphys1688.

[12] H. Ma, H.-L. Yip, F. Huang, A. K.-Y. Jen, *Adv. Funct. Mater.* **2010**, *20*, 1371–1388, DOI 10.1002/adfm.200902236.

[13] *The Molecule-Metal Interface*, (Eds.: N. Koch, N. Ueno, A. T. S. Wee), Wiley-VCH Verlag, **2013**.

[14] R. Berndt, J. Kröger, N. Néel, G. Schull, *Phys. Chem. Chem. Phys.* **2010**, *12*, 1022–1032, DOI 10.1039/b908672m.

[15] I. Aviv-Harel, Z. Gross, *Chem. Eur. J.* **2009**, *15*, 8382–8394, DOI 10.1002/chem.200900920.

[16] M. Chen, H. Zhou, B. P. Klein, M. Zugermeier, C. K. Krug, H.-J. Drescher, M. Gorgoi, M. Schmid, J. M. Gottfried, *Phys. Chem. Chem. Phys.* **2016**, *18*, 30643–30651, DOI 10.1039/c6cp05894a.

[17] K. M. Smith in *Porphyrins and Metalloporphyrins*, (Ed.: K. M. Smith), Elsevier Scientific Publishing Company, **1975**, Chapter General Features of the Structure and Chemistry of Porphyrin Compounds, pp. 3–28.

[18] M. Toganoh, T. Yamamoto, T. Hihara, H. Akimaru, H. Furuta, *Org. Biomol. Chem.* **2012**, *10*, 4367–4374, DOI 10.1039/c2ob25351h.

[19] M. Bröring, *Angew. Chem.* **2011**, *50*, 2484–2486, DOI 10.1002/ange.201007442; *Angew. Chem. Int. Ed.* **2011**, *50*, 2436–2438, DOI 10.1002/anie.201007442.

[20] F. Sondheimer, R. Wolovsky, Y. Amiel, *J. Am. Chem. Soc.* **1962**, *84*, 274–284, DOI 10.1021/ja00861a030.

[21] E. Vogel, *Angew. Chem.* **2011**, *123*, 4366–4375, DOI 10.1002/ange.201101347; *Angew. Chem. Int. Ed.* **2011**, *50*, 4278–4287, DOI 10.1002/anie.201101347.

[22] J. I. Wu, I. Fernández, P. von Ragué Schleyer, *J. Am. Chem. Soc.* **2013**, *135*, 315–321, DOI 10.1021/ja309434t.

[23] M. Kielmann, C. Prior, M. O. Senge, *New J. Chem.* **2018**, DOI 10.1039/c7nj04679k.

[24] D. T. Gryko, *Eur. J. Org. Chem.* **2002**, *2002*, 1735–1743, DOI 10.1002/1099-0690(200206)2002:11<1735::aid-ejoc1735>3.0.co;2-k.

[25] A. W. Johnson, I. T. Kay, *J. Chem. Soc.* **1965**, 1620–1629, DOI 10.1039/jr9650001620.

[26] S. Licoccia, E. Morgante, R. Paolesse, F. Polizio, M. O. Senge, E. Tondello, T. Boschi, *Inorg. Chem.* **1997**, *36*, 1564–1570, DOI 10.1021/ic960334i.

[27] M. Bröring, M. Cordes, S. Köhler, *Z. Anorg. Allg. Chem.* **2008**, DOI 10.1002/zaac.200700332.

[28] A. Haber, I. Angel, A. Mahammed, Z. Gross, *J. Diabetes Complicat.* **2013**, *27*, 316–321, DOI 10.1016/j.jdiacomp.2013.02.005.

[29] I. Aviv, Z. Gross, *Chem. Commun.* **2007**, 1987–1999, DOI 10.1039/B618482K.

[30] Z. Zhang, H.-H. Wang, H.-J. Yu, Y.-Z. Xiong, H.-T. Zhang, L.-N. Ji, H.-Y. Liu, *Dalton Trans.* **2017**, *46*, 9481–9490, DOI 10.1039/c7dt00992e.

[31] L.-L. Wang, H. Wang, F. Cheng, Z.-H. Liang, C. Liu, Y. Li, W.-Q. Wang, S.-H. Peng, X. Wang, X. Ying, L.-N. Ji, H.-Y. Liu, *J. Phys. Chem. C* **2017**, DOI 10.1021/acs.jpcc.7b00168.

[32] I. Aviv, Z. Gross, *Chem. Eur. J.* **2008**, *14*, 3995–4005, DOI 10.1002/chem.200701885.

[33] A. Mahammed, Z. Gross, *Angew. Chem.* **2006**, *118*, 6694–6697, DOI 10.1002/ange.200601399; *Angew. Chem. Int. Ed.* **2006**, *45*, 6544–6547, DOI 10.1002/anie.200601399.

[34] M. Chen, PhD thesis, Philipps-Universität Marburg, **2016**.

[35] M. B. Liebold, PhD thesis, Philipps-Universität Marburg, **2016**.

[36] H. Choi, G.-H. Lee, K. S. Kim, S. K. Hahn, *ACS Appl. Mater. Interfaces* **2018**, *10*, 2338–2346, DOI 10.1021/acsami.7b16595.

[37] P. Liljeroth, J. Repp, G. Meyer, *Science* **2007**, *317*, 1203–1206, DOI 10.1126/science.1144366.

[38] Y. Wang, J. Kröger, R. Berndt, W. A. Hofer, *J. Am. Chem. Soc.* **2009**, *131*, 3639–3643, DOI 10.1021/ja807876c.

[39] Y. He, J. Kröger, Y. Wang, *ChemPhysChem* **2017**, *18*, 429–450, DOI 10.1002/cphc.201600979.

[40] M. Lackinger, M. Hietschold, *Surf. Sci. Lett.* **2002**, *520*, L619–L624, DOI 10.1016/S0039-6028(02)02269-0.

[41] E. Nardi, M. Koudia, S. Kezilebieke, J.-P. Bucher, M. Abel in *On-Surface Synthesis*, (Ed.: A. Gourdon), Springer International Publishing, **2016**, Chapter On-Surface Synthesis of Phthalocyanine Compounds, pp. 115–129.

[42] M. Koudia, M. Abel, *Chem. Commun.* **2014**, *50*, 8565–8567, DOI 10.1039/c4cc02792b.

[43] H. F. Bettinger, C. Tönshoff, *Chem. Rec.* **2014**, *15*, 364–369, DOI 10.1002/tcr.201402068.

[44] C. Tönshoff, H. F. Bettinger in *Polyarenes I. Topics in Current Chemistry, Vol. 349*, (Eds.: J. S. Siegel, Y.-T. Wu), Springer Berlin Heidelberg, Berlin, Heidelberg, **2014**, Chapter Beyond Pentacenes: Synthesis and Properties of Higher Acenes, pp. 1–30, DOI 10.1007/128_2013_437.

[45] J. E. Anthony, *Angew. Chem.* **2008**, *120*, 460–492, DOI 10.1002/ange.200604045; *Angew. Chem. Int. Ed.* **2008**, *47*, 452–483, DOI 10.1002/anie.200604045.

[46] F. Ortmann, K. S. Radke, A. Günther, D. Kasemann, K. Leo, G. Cuniberti, *Adv. Funct. Mater.* **2015**, *25*, 1933–1954, DOI 10.1002/adfm.201402334.

[47] C. Wang, H. Dong, W. Hu, Y. Liu, D. Zhu, *Chem. Rev.* **2012**, *112*, 2208–2267, DOI 10.1021/cr100380z.

[48] M. Watanabe, Y. J. Chang, S.-W. Liu, T.-H. Chao, K. Goto, M. M. Islam, C.-H. Yuan, Y.-T. Tao, T. Shinmyozu, T. J. Chow, *Nat. Chem.* **2012**, *4*, 574–578, DOI 10.1038/nchem.1381.

[49] M. Winkler, K. N. Houk, *J. Am. Chem. Soc.* **2007**, *129*, 1805–1815, DOI 10.1021/ja067087u.

[50] B. D. Lindner, J. U. Engelhart, O. Tverskoy, A. L. Appleton, F. Rominger, A. Peters, H.-J. Himmel, U. H. F. Bunz, *Angew. Chem.* **2011**, *123*, 8747–8750, DOI 10.1002/ange.201103676; *Angew. Chem. Int. Ed.* **2011**, *50*, 8588–8591, DOI 10.1002/anie.201103676.

[51] J. E. Anthony, *Chem. Rev.* **2006**, *106*, 5028–5048, DOI 10.1021/cr050966z.

[52] C. Tönshoff, H. F. Bettinger, *Chem. Eur. J.* **2012**, *18*, 1789–1799, DOI 10.1002/chem.201101036.

[53] E. Clar, *The Aromatic Sextet*, 2nd ed., John Wiley & Sons, London, New York, Sydney, Toronto, **1972**.

[54] M. Solà, *Front. Chem.* **2013**, *1*, 22, DOI 10.3389/fchem.2013.00022.

[55] C. H. Suresh, S. R. Gadre, *J. Org. Chem.* **1999**, *64*, 2505–2512, DOI 10.1021/jo990050q.

[56] M. Bendikov, H. M. Duong, K. Starkey, K. N. Houk, E. A. Carter, F. Wudl, *J. Am. Chem. Soc.* **2004**, *126*, 7416–7417, DOI 10.1021/ja048919w.

[57] E. Clar, *Ber. dtsch. Chem. Ges. A/B* **1939**, *72*, 1817–1821, DOI 10.1002/cber.19390721002.

[58] E. Clar, *Nachr. Chem. Tech.* **1962**, *10*, 264–264, DOI 10.1002/nadc.19620101703.

[59] E. Clar, *Ber. dtsch. Chem. Ges. A/B* **1942**, *75*, 1330–1338, DOI 10.1002/cber.19420751114.

[60] C. Marschalk, *Bull. Soc. Chim. Fr.* **1943**, *10*, 511–512.

[61] E. Clar, C. Marschalk, *Bull. Soc. Chim. Fr.* **1950**, 444–452.

[62] W. J. Bailey, C.-W. Liao, *J. Am. Chem. Soc.* **1955**, *77*, 992–993, DOI 10.1021/ja01609a055.

[63] B. Boggiano, E. Clar, *J. Chem. Soc.* **1957**, 2681–2689, DOI 10.1039/jr9570002681.

[64] T. Fang, PhD thesis, University of California, Los Angeles, **1986**.

[65] M. M. Payne, S. R. Parkin, J. E. Anthony, *J. Am. Chem. Soc.* **2005**, *127*, 8028–8029, DOI 10.1021/ja051798v.

[66] H. F. Bettinger, R. Mondal, D. C. Neckers, *Chem. Commun.* **2007**, 5209–5211, DOI 10.1039/b713059g.

[67] R. Mondal, C. Tönshoff, D. Khon, D. C. Neckers, H. F. Bettinger, *J. Am. Chem. Soc.* **2009**, *131*, 14281–14289, DOI 10.1021/ja901841c.

[68] J. Strating, B. Zwanenburg, A. Wagenaar, A. Udding, *Tetrahedron Lett.* **1969**, *10*, 125–128, DOI 10.1016/s0040-4039(01)87489-x.

[69] R. Mondal, B. K. Shah, D. C. Neckers, *J. Am. Chem. Soc.* **2006**, *128*, 9612–9613, DOI 10.1021/ja063823i.

[70] R. Mondal, PhD thesis, Bowling Green State University, **2007**.

[71] R. Mondal, A. N. Okhrimenko, B. K. Shah, D. C. Neckers, *J. Phys. Chem. B* **2008**, *112*, 11–15, DOI 10.1021/jp076738l.

[72] R. Einholz, H. F. Bettinger, *Angew. Chem.* **2013**, *125*, 10000–10003, DOI 10.1002/ange.201209722; *Angew. Chem. Int. Ed.* **2013**, *52*, 9818–9820, DOI 10.1002/anie.201209722.

[73] C. Tönshoff, H. F. Bettinger, *Angew. Chem.* **2010**, *122*, 4219–4222, DOI 10.1002/ange.200906355; *Angew. Chem. Int. Ed.* **2010**, *49*, 4125–4128, DOI 10.1002/anie.200906355.

[74] H. F. Bettinger, *Pure Appl. Chem.* **2010**, *82*, 905–915, DOI 10.1351/pac-con-09-10-29.

[75] S. S. Zade, M. Bendikov, *Angew. Chem.* **2010**, *122*, 4104–4107, DOI 10.1002/ange.200906002; *Angew. Chem. Int. Ed.* **2010**, *49*, 4012–4015, DOI 10.1002/anie.200906002.

[76] R. Dorel, A. M. Echavarren, *Eur. J. Org. Chem.* **2017**, *2017*, 14–24, DOI 10.1002/ejoc.201601129.

[77] R. Einholz, T. Fang, R. Berger, P. Grüninger, A. Früh, T. Chassé, R. F. Fink, H. F. Bettinger, *J. Am. Chem. Soc.* **2017**, *139*, 4435–4442, DOI 10.1021/jacs.6b13212.

[78] P. G. Schroeder, C. B. France, J. B. Park, B. A. Parkinson, *J. Appl. Phys.* **2002**, *91*, 3010–3014, DOI 10.1063/1.1445286.

[79] S. Lukas, G. Witte, C. Wöll, *Phys. Rev. Lett.* **2002**, *88*, 028301, DOI 10.1103/PhysRevLett.88.028301.

[80] M. Pedio, B. Doyle, N. Mahne, A. Giglia, F. Borgatti, S. Nannarone, S. K. M. Henze, R. Temirov, F. S. Tautz, L. Casalis, R. Hudej, M. F. Danisman, B. Nickel, *Appl. Surf. Sci.* **2007**, *254*, 103–107, DOI 10.1016/j.apsusc.2007.07.125.

[81] D. Käfer, G. Witte, *Chem. Phys. Lett.* **2007**, *442*, 376–383, DOI 10.1016/j.cplett.2007.06.006.

[82] D. Käfer, L. Ruppel, G. Witte, *Phys. Rev. B* **2007**, *75*, DOI 10.1103/physrevb.75.085309.

[83] D. Käfer, C. Wöll, G. Witte, *Appl. Phys. A* **2009**, *95*, 273–284, DOI 10.1007/s00339-008-5011-3.

[84] J. M. Morbec, P. Kratzer, *J. Chem. Phys.* **2017**, *146*, 034702, DOI 10.1063/1.4973839.

[85] J. Krüger, N. Pavliček, J. M. Alonso, D. Pérez, E. Guitián, T. Lehmann, G. Cuniberti, A. Gourdon, G. Meyer, L. Gross, F. Moresco, D. Peña, *ACS Nano* **2016**, *10*, 4538–4542, DOI 10.1021/acsnano.6b00505.

[86] J. Krüger, F. Eisenhut, J. M. Alonso, T. Lehmann, E. Guitián, D. Pérez, D. Skidin, F. Gamaleja, D. A. Ryndyk, C. Joachim, D. Peña, F. Moresco, G. Cuniberti, *Chem. Commun.* **2017**, *53*, 1583–1586, DOI 10.1039/c6cc09327b.

[87] J. Krüger, F. García, F. Eisenhut, D. Skidin, J. M. Alonso, E. Guitián, D. Pérez, G. Cuniberti, F. Moresco, D. Peña, *Angew. Chem.* **2017**, *129*, 12107–12110, DOI 10.1002/ange.201706156; *Angew. Chem. Int. Ed.* **2017**, *56*, 11945–11948, DOI 10.1002/anie.201706156.

[88] J. Krüger, F. Eisenhut, T. Lehmann, J. M. Alonso, J. Meyer, D. Skidin, R. Ohmann, D. A. Ryndyk, D. Pérez, E. Guitián, D. Peña, F. Moresco, G. Cuniberti, *J. Phys. Chem. C* **2017**, *121*, 20353–20358, DOI 10.1021/acs.jpcc.7b06131.

[89] R. Zuzak, R. Dorel, M. Krawiec, B. Such, M. Kolmer, M. Szymonski, A. M. Echavarren, S. Godlewski, *ACS Nano* **2017**, *11*, 9321–9329, DOI 10.1021/acsnano.7b04728.

[90] C. Rogers, C. Chen, Z. Pedramrazi, A. A. Omrani, H.-Z. Tsai, H. S. Jung, S. Lin, M. F. Crommie, F. R. Fischer, *Angew. Chem.* **2015**, *127*, 15358–15361, DOI 10.1002/ange.201507104; *Angew. Chem. Int. Ed.* **2015**, *54*, 15143–15146, DOI 10.1002/anie.201507104.

[91] J. I. Urgel, H. Hayashi, M. Di Giovannantonio, C. A. Pignedoli, S. Mishra, O. Deniz, M. Yamashita, T. Dienel, P. Ruffieux, H. Yamada, R. Fasel, *J. Am. Chem. Soc.* **2017**, *139*, 11658–11661, DOI 10.1021/jacs.7b05192.

[92] I. Langmuir, *Chem. Rev.* **1933**, *13*, 147–191, DOI 10.1021/cr60045a001.

[93] C. B. Duke, *P. Natl. Acad. Sci. USA* **2003**, *100*, 3858–3864, DOI 10.1073/pnas.0730358100.

[94] A. Werner, *Z. Anorg. Allg. Chem.* **1893**, *3*, 267–330, DOI 10.1002/zaac.18930030136.

[95] J. M. Gottfried, PhD thesis, Freie Universität Berlin, **2003**.

[96] J. V. Barth, *Annu. Rev. Phys. Chem.* **2007**, *58*, 375–407, DOI 10.1146/annurev.physchem.56.092503.141259.

[97] J. V. Barth, *Surf. Sci.* **2009**, *603*, 1533–1541, DOI 10.1016/j.susc.2008.09.049.

[98] S. Stepanow, N. Lin, J. V. Barth, *J. Phys.: Condens. Matter* **2008**, *20*, 184002, DOI 10.1088/0953-8984/20/18/184002.

[99] G. Ertl, *Angew. Chem.* **2008**, *120*, 3578–3590, DOI 10.1002/ange.200800480; *Angew. Chem. Int. Ed.* **2008**, *47*, 3524–3535, DOI 10.1002/anie.200800480.

[100] *Organic Electronics*, (Ed.: C. Wöll), Wiley-VCH Verlag, **2009**.

[101] W. R. Browne, B. L. Feringa, *Nat. Nanotechnol.* **2006**, *1*, 25–35, DOI 10.1038/nnano.2006.45.

[102] H. Brune, *Surf. Sci. Rep.* **1998**, *31*, 125–229, DOI 10.1016/s0167-5729(99)80001-6.

[103] S. Clair, S. Pons, S. Fabris, S. Baroni, H. Brune, K. Kern, J. V. Barth, *J. Phys. Chem. B* **2006**, *110*, 5627–5632, DOI 10.1021/jp057239s.

[104] U. Schlickum, R. Decker, F. Klappenberger, G. Zoppellaro, S. Klyatskaya, M. Ruben, I. Silanes, A. Arnau, K. Kern, H. Brune, J. V. Barth, *Nano Lett.* **2007**, *7*, 3813–3817, DOI 10.1021/nl072466m.

[105] S. Stepanow, N. Lin, D. Payer, U. Schlickum, F. Klappenberger, G. Zoppellaro, M. Ruben, H. Brune, J. V. Barth, K. Kern, *Angew. Chem.* **2007**, *119*, 724–727, DOI 10.1002/ange.200603644; *Angew. Chem. Int. Ed.* **2007**, *46*, 710–713, DOI 10.1002/anie.200603644.

[106] F. Klappenberger, A. Weber-Bargioni, W. Auwärter, M. Marschall, A. Schiffrin, J. V. Barth, *J. Chem. Phys.* **2008**, *129*, 214702, DOI 10.1063/1.3021291.

[107] J. M. Gottfried, Habilitation thesis, Friedrich-Alexander-Universität Erlangen-Nürnberg, **2009**.

[108] J. W. Buchler in *Porphyrins and Metalloporphyrins*, (Ed.: K. M. Smith), Elsevier Scientific Publishing Company, **1975**, Chapter Static Coordination Chemistry of Metalloporphyrins, pp. 157–232.

[109] F. Buchner, V. Schwald, K. Comanici, H.-P. Steinrück, H. Marbach, *ChemPhysChem* **2007**, *8*, 241–243, DOI 10.1002/cphc.200600698.

[110] J. M. Gottfried, K. Flechtner, A. Kretschmann, T. Lukasczyk, H.-P. Steinrück, *J. Am. Chem. Soc.* **2006**, *128*, 5644–5645, DOI 10.1021/ja0610333.

[111] T. E. Shubina, H. Marbach, K. Flechtner, A. Kretschmann, N. Jux, F. Buchner, H.-P. Steinrück, T. Clark, J. M. Gottfried, *J. Am. Chem. Soc.* **2007**, *129*, 9476–9483, DOI 10.1021/ja072360t.

[112] M. Chen, X. Feng, L. Zhang, H. Ju, Q. Xu, J. Zhu, J. M. Gottfried, K. Ibrahim, H. Qian, J. Wang, *J. Phys. Chem. C* **2010**, *114*, 9908–9916, DOI 10.1021/jp102031m.

[113] A. Weber-Bargioni, J. Reichert, A. P. Seitsonen, W. Auwärter, A. Schiffrin, J. Barth, *J. Phys. Chem. C* **2008**, *112*, 3453–3455, DOI 10.1021/jp076961i.

[114] G. Ricciardi, A. Rosa, E. J. Baerends, S. A. J. van Gisbergen, *J. Am. Chem. Soc.* **2002**, *124*, 12319–12334.

[115] D. Écija, W. Auwärter, S. Vijayaraghavan, K. Seufert, F. Bischoff, K. Tashiro, J. V. Barth, *Angew. Chem.* **2011**, *123*, 3958–3963, DOI 10.1002/ange.201007370; *Angew. Chem. Int. Ed.* **2011**, *50*, 3872–3877, DOI 10.1002/anie.201007370.

[116] J. Mielke, F. Hanke, M. V. Peters, S. Hecht, M. Persson, L. Grill, *J. Am. Chem. Soc.* **2015**, *137*, 1844–1849, DOI 10.1021/ja510528x.

[117] K. Flechtner, A. Kretschmann, H.-P. Steinrück, J. M. Gottfried, *J. Am. Chem. Soc.* **2007**, *129*, 12110–12111, DOI 10.1021/ja0756725.

[118] W. Hieringer, K. Flechtner, A. Kretschmann, K. Seufert, W. Auwärter, J. V. Barth, A. Görling, H.-P. Steinrück, J. M. Gottfried, *J. Am. Chem. Soc.* **2011**, *133*, 6206–6222, DOI 10.1021/ja1093502.

[119] Y. Bai, F. Buchner, M. T. Wendahl, I. Kellner, A. Bayer, H.-P. Steinrück, H. Marbach, J. M. Gottfried, *J. Phys. Chem. C* **2008**, *112*, 6087–6092, DOI 10.1021/jp711122w.

[120] F. Buchner, K. Flechtner, Y. Bai, E. Zillner, I. Kellner, H.-P. Steinrück, H. Marbach, J. M. Gottfried, *J. Phys. Chem. C* **2008**, *112*, 15458–15465, DOI 10.1021/jp8052955.

[121] L. Bogani, W. Wernsdorfer, *Nat. Mater.* **2008**, *7*, 179–186, DOI 10.1038/nmat2133.

[122] Z. Huang, Y. Zhang, Y. He, H. Song, C. Yin, K. Wu, *Chem. Soc. Rev.* **2017**, *46*, 1955–1976, DOI 10.1039/c6cs00891g.

[123] I. Hong, N. Li, Y.-J. Zhang, H. Wang, H.-J. Song, M.-L. Bai, X. Zhou, J.-L. Li, G.-C. Gu, X. Zhang, M. Chen, J. M. Gottfried, D. Wang, J.-T. Lü, L.-M. Peng, S.-M. Hou, R. Berndt, K. Wu, Y.-F. Wang, *Chem. Commun.* **2016**, *52*, DOI 10.1039/c6cc03359h.

[124] R. P. Feynman, *Eng. Sci.* **1960**, *23*, 22–36.

[125] Intel Corporation, https://www.intel.com/content/www/us/en/history/museum-story-of-intel-4004.html, **27.07.2017**.

[126] Intel Corporation, https://www.intel.com/content/www/us/en/products/processors/core/i7-processors/i7-7920hq.html, **27.07.2017**.

[127] J. Méndez, M. F. López, J. A. Martín-Gago, *Chem. Soc. Rev.* **2011**, *40*, 4578, DOI 10.1039/c0cs00161a.

[128] R. Lindner, A. Kühnle, *ChemPhysChem* **2015**, *16*, 1582–1592, DOI 10.1002/cphc.201500161.

[129] J. Björk, *J. Phys.: Condens. Matter* **2016**, *28*, 083002, DOI 10.1088/0953-8984/28/8/083002.

[130] P. A. Held, H. Fuchs, A. Studer, *Chem. Eur. J.* **2017**, *23*, 5874–5892, DOI 10.1002/chem.201604047.

[131] G. Binnig, H. Rohrer, *Rev. Mod. Phys.* **1987**, *59*, 615–625, DOI 10.1103/revmodphys.59.615.

[132] G. Binnig, C. F. Quate, C. Gerber, *Phys. Rev. Lett.* **1986**, *56*, 930–933, DOI 10.1103/PhysRevLett.56.930.

[133] F. J. Giessibl, *Science* **1995**, *267*, 68–71, DOI 10.1126/science.267.5194.68.

[134] F. J. Gießibl, DE19633546C2, **2000**.

[135] F. J. Giessibl, *Rev. Mod. Phys.* **2003**, *75*, 949–983, DOI 10.1103/revmodphys.75.949.

[136] M. Lackinger, *Chem. Commun.* **2017**, *53*, 7872–7885, DOI 10.1039/c7cc03402d.

[137] F. Ullmann, *Justus Liebigs Ann. Chem.* **1904**, *332*, 38–81, DOI 10.1002/jlac.19043320104.

[138] S.-W. Hla, L. Bartels, G. Meyer, K.-H. Rieder, *Phys. Rev. Lett.* **2000**, *85*, 2777, DOI 10.1103/physrevlett.85.2777.

[139] X.-L. Zhou, M. E. Castro, J. M. White, *Surf. Sci.* **1990**, *238*, 215–225, DOI 10.1016/0039-6028(90)90079-n.

[140] P. S. Weiss, M. M. Kamna, T. M. Graham, S. J. Stranick, *Langmuir* **1998**, *14*, 1284–1289, DOI 10.1021/la970736i.

[141] M. Xi, B. E. Bent, *Surf. Sci.* **1992**, *278*, 19–32, DOI 10.1016/0039-6028(92)90580-y.

[142] L. Grill, M. Dyer, L. Lafferentz, M. Persson, M. V. Peters, S. Hecht, *Nat. Nanotechnol.* **2007**, *2*, 687–691, DOI 10.1038/nnano.2007.346.

[143] L. Lafferentz, V. Eberhardt, C. Dri, C. Africh, G. Comelli, F. Esch, S. Hecht, L. Grill, *Nat. Chem.* **2012**, *4*, 215–220, DOI 10.1038/nchem.1242.

[144] R. Gutzler, H. Walch, G. Eder, S. Kloft, W. M. Heckl, M. Lackinger, *Chem. Commun.* **2009**, 4456–4458, DOI 10.1039/b906836h.

[145] M. O. Blunt, J. C. Russell, N. R. Champness, P. H. Beton, *Chem. Commun.* **2010**, *46*, 7157–7159, DOI 10.1039/c0cc01810d.

[146] Q. Fan, C. Wang, Y. Han, J. Zhu, W. Hieringer, J. Kuttner, G. Hilt, J. M. Gottfried, *Angew. Chem.* **2013**, *125*, 4766–4770, DOI 10.1002/ange.201300610; *Angew. Chem. Int. Ed.* **2013**, *52*, 4668–4672, DOI 10.1002/anie.201300610.

[147] Q. Fan, J. M. Gottfried, J. Zhu, *Acc. Chem. Res.* **2015**, *48*, 2484–2494, DOI 10.1021/acs.accounts.5b00168.

[148] Q. Fan, T. Wang, J. Dai, J. Kuttner, G. Hilt, J. M. Gottfried, J. Zhu, *ACS Nano* **2017**, *11*, 5070–5079, DOI 10.1021/acsnano.7b01870.

[149] Q. Fan, J. Dai, T. Wang, J. Kuttner, G. Hilt, J. M. Gottfried, J. Zhu, *ACS Nano* **2016**, *10*, 3747–3754, DOI 10.1021/acsnano.6b00366.

[150] Q. Sun, L. Cai, Y. Ding, H. Ma, C. Yuan, W. Xu, *Phys. Chem. Chem. Phys.* **2016**, *18*, 2730–2735, DOI 10.1039/c5cp06459g.

[151] Q. Sun, L. Cai, H. Ma, C. Yuan, W. Xu, *Chem. Commun.* **2016**, *52*, 6009–6012, DOI 10.1039/c6cc01059h.

[152] Q. Sun, L. Cai, H. Ma, C. Yuan, W. Xu, *ACS Nano* **2016**, *10*, 7023–7030, DOI 10.1021/acsnano.6b03048.

[153] L. E. Dinca, C. Fu, J. M. MacLeod, J. Lipton-Duffin, J. L. Brusso, C. E. Szakacs, D. Ma, D. F. Perepichka, F. Rosei, *ACS Nano* **2013**, *7*, 1652–1657, DOI 10.1021/nn305572s.

[154] Y.-Q. Zhang, N. Kepčija, M. Kleinschrodt, K. Diller, S. Fischer, A. C. Papageorgiou, F. Allegretti, J. Björk, S. Klyatskaya, F. Klappenberger, M. Ruben, J. V. Barth, *Nat. Commun.* **2012**, *3*, 1286, DOI 10.1038/ncomms2291.

[155] Q. Shen, H.-Y. Gao, H. Fuchs, *Nano Today* **2017**, *13*, 77–96, DOI 10.1016/j.nantod.2017.02.007.

[156] J. Cai, P. Ruffieux, R. Jaafar, M. Bieri, T. Braun, S. Blankenburg, M. Muoth, A. P. Seitsonen, M. Saleh, X. Feng, K. Müllen, R. Fasel, *Nature* **2010**, *466*, 470–473, DOI 10.1038/nature09211.

[157] B. Schuler, S. Fatayer, F. Mohn, N. Moll, N. Pavliček, G. Meyer, D. Peña, L. Gross, *Nat. Chem.* **2016**, *8*, 220–224, DOI 10.1038/nchem.2438.

[158] L. Gross, F. Mohn, N. Moll, B. Schuler, A. Criado, E. Guitián, D. Peña, A. Gourdon, G. Meyer, *Science* **2012**, *337*, 1326–1329, DOI 10.1126/science.1225621.

[159] S. Weigelt, C. Busse, C. Bombis, M. M. Knudsen, K. V. Gothelf, T. Strunskus, C. Wöll, M. Dahlbom, B. Hammer, E. Lægsgaard, F. Besenbacher, T. R. Linderoth, *Angew. Chem.* **2007**, *119*, 9387–9390, DOI 10.1002/ange.200702859; *Angew. Chem. Int. Ed.* **2007**, *46*, 9227–9230, DOI 10.1002/anie.200702859.

[160] M. Abel, S. Clair, O. Ourdjini, M. Mossoyan, L. Porte, *J. Am. Chem. Soc.* **2011**, *133*, 1203–1205, DOI 10.1021/ja108628r.

[161] E. J. Abbott, F. A. Firestone, *Mech. Eng.* **1933**, *55*, 569–572.

[162] J. B. P. Williamson in Proceedings of the Institution of Mechanical Engineers, Conference Proceedings, *Vol. 182*, SAGE Publications Sage UK: London, England, **1967**, pp. 21–30, DOI 10.1243/pime_conf_1967_182_300_02.

[163] F. Hund, *Z. Phys.* **1927**, *43*, 805–826, DOI 10.1007/bf01397249.

[164] R. Young, J. Ward, F. Scire, *Rev. Sci. Instrum.* **1972**, *43*, 999–1011, DOI 10.1063/1.1685846.

[165] I. Giaever, *Rev. Mod. Phys.* **1974**, *46*, 245–250, DOI 10.1103/revmodphys.46.245.

[166] G. Binnig, H. Rohrer, C. Gerber, E. Weibel, *Appl. Phys. Lett.* **1982**, *40*, 178–180, DOI 10.1063/1.92999.

[167] G. Binnig, H. Rohrer, C. Gerber, E. Weibel, *Phys. Rev. Lett.* **1982**, *49*, 57–61, DOI 10.1103/physrevlett.49.57.

[168] G. Binnig, H. Rohrer, *Helv. Phys. Acta* **1982**, *55*, 726–735, DOI 10.1016/0039-6028(85)90120-7.

[169] D. M. Eigler, E. K. Schweizer, *Nature* **1990**, *344*, 524–526, DOI 10.1038/344524a0.

[170] *Nat. Nanotechnol.* **2010**, *5*, 237, DOI 10.1038/nnano.2010.80.

[171] G. J. Leggett in *Surface Analysis - The Principal Techniques*, (Eds.: J. C. Vickerman, I. S. Gilmore), John Wiley & Sons, **2009**, Chapter Scanning Probe Microscopy, pp. 479–562.

[172] G. Wedler, H.-J. Freund, *Lehrbuch der Physikalischen Chemie*, 6th ed., Wiley-VCH Verlag, **2012**.

[173] J. Tersoff, D. R. Hamann, *Phys. Rev. B* **1985**, *31*, 805–813, DOI 10.1103/physrevb.31.805.

[174] M. Schunack, PhD thesis, University of Aarhus, **2002**.

[175] E. K. Vestergaard, PhD thesis, University of Aarhus, **2004**.

[176] SPECS Surface Nano Analysis GmbH, SPM Aarhus Series - Product Brochure, tech. rep., **2015**.

[177] E. Lægsgaard, F. Besenbacher, K. Mortensen, I. Stensgaard, *J. Microsc.* **1988**, *152*, 663–669, DOI 10.1111/j.1365-2818.1988.tb01435.x.

[178] Interdisciplinary Nanoscience Center Aarhus, http://inano.au.dk/research/research-platforms/nanoanalysis/scanning-tunnelling-microscopy/, **10.10.2017**.

[179] B. D. Ratner, D. G. Castner in *Surface Analysis - The Principal Techniques*, (Eds.: J. C. Vickerman, I. S. Gilmore), John Wiley & Sons, **2009**, Chapter Electron Spectroscopy for Chemical Analysis, pp. 47–112.

[180] H. Hertz, *Ann. Physik* **1887**, *267*, 983–1000, DOI 10.1002/andp.18872670827.

[181] W. Hallwachs, *Ann. Physik* **1888**, *269*, 301–312, DOI 10.1002/andp.18882690206.

[182] A. Einstein, *Ann. Physik* **1905**, *322*, 132–148, DOI 10.1002/andp.19053220607.

[183] T. Koopmans, *Physica* **1934**, *1*, 104–113, DOI 10.1016/s0031-8914(34)90011-2.

[184] M. P. Seah, W. A. Dench, *Surf. Interface Anal.* **1979**, *1*, 2–11, DOI 10.1002/sia.740010103.

[185] M. P. Seah, *Surf. Interface Anal.* **2012**, *44*, 497–503, DOI 10.1002/sia.4816.

[186] P. Bouguer, *Essai d'optique sur la gradation de la lumière*, Claude Jombert Paris, **1729**.

[187] Beer, *Ann. Physik* **1852**, *162*, 78–88, DOI 10.1002/andp.18521620505.

[188] L. Meitner, *Z. Phys.* **1922**, *9*, 131–144, DOI 10.1007/BF01326962.

[189] F. R. Elder, A. M. Gurewitsch, R. V. Langmuir, H. C. Pollock, *Phys. Rev.* **1947**, *71*, 829–830, DOI 10.1103/physrev.71.829.5.

[190] Helmholtz-Zentrum Berlin für Materialien und Energie GmbH, https://www.helmholtz-berlin.de/quellen/bessy/elektronenspeicherring/wie-funktioniert-bessy_en.html, **21.12.2017**.

[191] A. Nefedov, C. Wöll in *Surface Science Techniques*, (Eds.: G. Bracco, D. Holst), Springer-Verlag, Heidelberg, **2013**, Chapter Advanced Applications of NEXAFS Spectroscopy for Functionalized Surfaces, pp. 277–303, DOI 10.1007/978-3-642-34243-1_10.

[192] J. L. Wiza, *Nucl. Instrum. Methods* **1979**, *162*, 587–601, DOI 10.1016/0029-554x(79)90734-1.

[193] K. Weiss, S. Gebert, M. Wühn, H. Wadepohl, C. Wöll, *J. Vac. Sci. Technol. A* **1998**, *16*, 1017–1022, DOI 10.1116/1.581225.

[194] J. Stöhr, *NEXAFS Spectroscopy*, Corr. 2nd printing, Springer-Verlag Berlin Heidelberg, **1996**.

[195] T. Breuer, M. Klues, G. Witte, *J. Electron. Spectrosc. Relat. Phenom.* **2015**, *204*, 102–115, DOI 10.1016/j.elspec.2015.07.011.

[196] J. Schweppe, R. D. Deslattes, T. Mooney, C. J. Powell, *J. Electron. Spectrosc. Relat. Phenom.* **1994**, *67*, 463–478, DOI 10.1016/0368-2048(93)02059-u.

[197] J. A. Bearden, *Rev. Mod. Phys.* **1967**, *39*, 78–124, DOI 10.1103/revmodphys.39.78.

[198] S. Duhm, A. Gerlach, I. Salzmann, B. Bröker, R. L. Johnson, F. Schreiber, N. Koch, *Org. Electron.* **2008**, *9*, 111–118, DOI 10.1016/j.orgel.2007.10.004.

[199] C. Wöll, S. Chiang, R. J. Wilson, P. H. Lippel, *Phys. Rev. B* **1989**, *39*, 7988–7991, DOI 10.1103/PhysRevB.39.7988.

[200] J. V. Barth, H. Brune, G. Ertl, *Phys. Rev. B* **1990**, *42*, 9307–9318, DOI 10.1103/physrevb.42.9307.

[201] N. Takeuchi, C. T. Chan, K. M. Ho, *Phys. Rev. B* **1991**, *43*, 13899–13906, DOI 10.1103/PhysRevB.43.13899.

[202] F. Hanke, J. Björk, *Phys. Rev. B* **2013**, *87*, 235422, DOI 10.1103/PhysRevB.87.235422.

[203] K. Hermann, Surface Explorer, version 2, based on BALSAC, **2010**, http://surfexp.fhi-berlin.mpg.de.

[204] J. T. Yates, Jr., *Experimental Innovations in Surface Science*, 2nd ed., Springer International Publishing, **2015**, DOI 10.1007/978-3-319-17668-0.

[205] L. A. Kibler, Preparation and Characterization of Noble Metal Single Crystal Electrode Surfaces, International Society of Electrochemistry, **2003**, https://www.uni-ulm.de/fileadmin/website_uni_ulm/nawi.inst.080/mitarbeiter/Kibler/KiblerSingleCrystals2003.pdf.

[206] U. Harten, A. M. Lahee, J. P. Toennies, C. Wöll, *Phys. Rev. Lett.* **1985**, *54*, 2619–2622, DOI 10.1103/PhysRevLett.54.2619.

[207] M. Knudsen, *Ann. Physik* **1909**, *333*, 75–130, DOI 10.1002/andp.19093330106.

[208] M. Knudsen, *Ann. Physik* **1909**, *333*, 999–1016, DOI 10.1002/andp.19093330505.

[209] M. Knudsen, *Ann. Physik* **1909**, *334*, 179–193, DOI 10.1002/andp.19093340614.

[210] A. Freedman, P. L. Kebabian, Z. Li, W. A. Robinson, J. C. Wormhoudt, *Meas. Sci. Technol.* **2008**, *19*, 125102, DOI 10.1088/0957-0233/19/12/125102.

[211] J. R. Kuttner, PhD thesis, Philipps-Universität Marburg, **2016**.

[212] Focus GmbH, Technical reference drawing EFM 4, http://www.focus-gmbh.com/resources/UHV-Instruments/e-beam-evaporation/efm4-drwg.pdf, **27.09.2017**.

[213] M. Henzler, W. Göpel, *Oberflächenphysik des Festkörpers*, B. G. Teubner Stuttgart, **1994**.

[214] I. Ekvall, E. Wahlström, D. Claesson, H. Olin, E. Olsson, *Meas. Sci. Technol.* **1999**, *10*, 11–18, DOI 10.1088/0957-0233/10/1/006.

[215] I. Horcas, R. Fernández, J. M. Gómez-Rodríguez, J. Colchero, J. Gómez-Herrero, A. M. Baro, *Rev. Sci. Instrum.* **2007**, *78*, 013705, DOI 10.1063/1.2432410.

[216] D. Nečas, P. Klapetek, *Cent. Eur. J. Phys.* **2012**, *10*, 181–188, DOI 10.2478/s11534-011-0096-2.

[217] M. Schmid, H.-P. Steinrück, J. M. Gottfried, *Surf. Interface Anal.* **2014**, *46*, 505–511, DOI 10.1002/sia.5521.

[218] M. Schmid, XPST – X-ray Photoelectron Spectroscopy Tools, unpublished version, http://www.igorexchange.com/project/XPStools.

[219] J. Yeh, I. Lindau, *At. Data Nucl. Data Tables* **1985**, *32*, 1–155, DOI 10.1016/0092-640X(85)90016-6.

[220] S. Reiß, H. Krumm, A. Niklewski, V. Staemmler, C. Wöll, *J. Chem. Phys.* **2002**, *116*, 7704–7713, DOI 10.1063/1.1460855.

[221] S. Reiß, PhD thesis, Ruhr-Universität Bochum, **2001**.

[222] Y. Bai, PhD thesis, Friedrich-Alexander-Universität Erlangen-Nürnberg, **2010**.

[223] F. Buchner, J. Xiao, E. Zillner, M. Chen, M. Röckert, S. D. M. Stark, H.-P. Steinrück, J. M. Gottfried, H. Marbach, *J. Phys. Chem. C* **2011**, *115*, 24172–24177, DOI 10.1021/jp206675u.

[224] G. D. Santo, C. Castellarin-Cudia, M. Fanetti, B. Taleatu, P. Borghetti, L. Sangaletti, L. Floreano, E. Magnano, F. Bondino, A. Goldoni, *J. Phys. Chem. C* **2011**, *115*, 4155–4162, DOI 10.1021/jp111151n.

[225] P. Borghetti, G. D. Santo, C. Castellarin-Cudia, M. Fanetti, L. Sangaletti, E. Magnano, F. Bondino, A. Goldoni, *J. Chem. Phys.* **2013**, *138*, 144702, DOI 10.1063/1.4798934.

[226] D. H. Karweik, N. Winograd, *Inorg. Chem.* **1976**, *15*, 2336–2342, DOI 10.1021/ic50164a003.

[227] P. Schweyen, K. Brandhorst, R. Wicht, B. Wolfram, M. Bröring, *Angew. Chem.* **2015**, *127*, 8331–8334, DOI 10.1002/ange.201503624; *Angew. Chem. Int. Ed.* **2015**, *54*, 8213–8216, DOI 10.1002/anie.201503624.

[228] A. Mahammed, J. J. Weaver, H. B. Gray, M. Abdelas, Z. Gross, *Tetrahedron Lett.* **2003**, *44*, 2077–2079, DOI 10.1016/s0040-4039(03)00174-6.

[229] Z. Gross, N. Galili, L. Simkhovich, I. Saltsman, M. Botoshansky, D. Bläser, R. Boese, I. Goldberg, *Org. Lett.* **1999**, *1*, 599–602, DOI 10.1021/ol990739h.

[230] M. Röckert, M. Franke, Q. Tariq, D. Lungerich, N. Jux, M. Stark, A. Kaftan, S. Ditze, H. Marbach, M. Laurin, J. Libuda, H.-P. Steinrück, O. Lytken, *J. Phys. Chem. C* **2014**, *118*, 26729–26736, DOI 10.1021/jp507303h.

[231] S. Tebi, M. Paszkiewicz, H. Aldahhak, F. Allegretti, S. Gonglach, M. Haas, M. Waser, P. S. Deimel, P. C. Aguilar, Y.-Q. Zhang, A. C. Papageorgiou, D. A. Duncan, J. V. Barth, W. G. Schmidt, R. Koch, U. Gerstmann, E. Rauls, F. Klappenberger, W. Schöfberger, S. Müllegger, *ACS Nano* **2017**, DOI 10.1021/acsnano.7b00766.

[232] J. Herritsch, Master's thesis, Philipps-Universität Marburg, **2018**.

[233] J.-N. Luy, Master's thesis, Philipps-Universität Marburg, **2017**.

[234] L. Scudiero, D. E. Barlow, K. W. Hipps, *J. Phys. Chem. B* **2002**, *106*, 996–1003, DOI 10.1021/jp012436m.

[235] K. Comanici, F. Buchner, K. Flechtner, T. Lukasczyk, J. M. Gottfried, H.-P. Steinrück, H. Marbach, *Langmuir* **2008**, *24*, 1897–1901, DOI 10.1021/la703263e.

[236] F. Buchner, K.-G. Warnick, T. Wölfle, A. Görling, H.-P. Steinrück, W. Hieringer, H. Marbach, *J. Phys. Chem. C* **2009**, *113*, 16450–16457, DOI 10.1021/jp904680c.

[237] Y. Bai, F. Buchner, I. Kellner, M. Schmid, F. Vollnhals, H.-P. Steinrück, H. Marbach, J. M. Gottfried, *New J. Phys.* **2009**, *11*, 125004, DOI 10.1088/1367-2630/11/12/125004.

[238] B. W. Heinrich, G. Ahmadi, V. L. Müller, L. Braun, J. I. Pascual, K. J. Franke, *Nano Lett.* **2013**, *13*, 4840–4843, DOI 10.1021/nl402575c.

[239] C. G. Williams, M. Wang, D. Skomski, C. D. Tempas, L. L. Kesmodel, S. L. Tait, *Surf. Sci.* **2016**, *653*, 130–137, DOI 10.1016/j.susc.2016.06.013.

[240] D. van Vörden, M. Lange, M. Schmuck, J. Schaffert, M. C. Cottin, C. A. Bobisch, R. Möller, *J. Chem. Phys.* **2013**, *138*, 211102, DOI 10.1063/1.4810879.

[241] B. Cirera, N. Giménez-Agulló, J. Björk, F. Martínez-Peña, A. Martin-Jimenez, J. Rodriguez-Fernandez, A. M. Pizarro, R. Otero, J. M. Gallego, P. Ballester, J. R. Galan-Mascaros, D. Ecija, *Nat. Commun.* **2016**, *7*, 11002, DOI 10.1038/ncomms11002.

[242] B. M. Weckhuysen, R. A. Schoonheydt, *Catal. Today* **1999**, *51*, 223–232, DOI 10.1016/s0920-5861(99)00047-4.

[243] J. J. H. B. Sattler, J. Ruiz-Martinez, E. Santillan-Jimenez, B. M. Weckhuysen, *Chem. Rev.* **2014**, *114*, 10613–10653, DOI 10.1021/cr5002436.

[244] M. Schmid, M. Zugermeier, J. Herritsch, B. P. Klein, C. K. Krug, L. Ruppenthal, P. Müller, M. Kothe, P. Schweyen, M. Bröring, J. M. Gottfried, *J. Phys. Chem. C* **2018**, *122*, 10392–10399, DOI 10.1021/acs.jpcc.8b00067.

[245] M. Schmid, J. Zirzlmeier, H.-P. Steinrück, J. M. Gottfried, *J. Phys. Chem. C* **2011**, *115*, 17028–17035, DOI 10.1021/jp204524s.

[246] A. Dees, N. Jux, O. Tröppner, K. Dürr, R. Lippert, M. Schmid, B. Küstner, S. Schlücker, H.-P. Steinrück, J. M. Gottfried, I. Ivanović-Burmazović, *Inorg. Chem.* **2015**, *54*, 6862–6872, DOI 10.1021/acs.inorgchem.5b00770.

[247] H. Peisert, J. Uihlein, F. Petraki, T. Chassé, *J. Electron. Spectrosc. Relat. Phenom.* **2015**, *204*, 49–60, DOI 10.1016/j.elspec.2015.01.005.

[248] F. Petraki, H. Peisert, U. Aygul, F. Latteyer, J. Uihlein, A. Vollmer, T. Chassé, *J. Phys. Chem. C* **2012**, *116*, 11110–11116, DOI 10.1021/jp302233e.

[249] J. Xiao, R. Golnak, K. Atak, M. Pflüger, M. Pohl, E. Suljoti, B. Winter, E. F. Aziz, *J. Phys. Chem. B* **2014**, *118*, 9371–9377, DOI 10.1021/jp5023339.

[250] F. Petraki, H. Peisert, F. Latteyer, U. Aygül, A. Vollmer, T. Chassé, *J. Phys. Chem. C* **2011**, *115*, 21334–21340, DOI 10.1021/jp207568q.

[251] L. Scudiero, D. E. Barlow, K. W. Hipps, *J. Phys. Chem. B* **2000**, *104*, 11899–11905, DOI 10.1021/jp002292w.

[252] N. Lin, Unpublished data, **2016**.

[253] K. S. Kim, T. J. O'Leary, N. Winograd, *Anal. Chem.* **1973**, *45*, 2214–2218, DOI 10.1021/ac60335a009.

[254] C. Stadler, S. Hansen, F. Pollinger, C. Kumpf, E. Umbach, T.-L. Lee, J. Zegenhagen, *Phys. Rev. B* **2006**, *74*, 035404, DOI 10.1103/physrevb.74.035404.

[255] J. D. Baran, J. A. Larsson, *J. Phys. Chem. C* **2012**, *116*, 9487–9497, DOI 10.1021/jp210771d.

[256] J. D. Baran, J. A. Larsson, R. A. J. Woolley, Y. Cong, P. J. Moriarty, A. A. Cafolla, K. Schulte, V. R. Dhanak, *Phys. Rev. B* **2010**, *81*, 075413, DOI 10.1103/physrevb.81.075413.

[257] T. Lukasczyk, K. Flechtner, L. R. Merte, N. Jux, F. Maier, J. M. Gottfried, H.-P. Steinrück, *J. Phys. Chem. C* **2007**, *111*, 3090–3098, DOI 10.1021/jp0652345.

[258] Y. Bai, M. Sekita, M. Schmid, T. Bischof, H.-P. Steinrück, J. M. Gottfried, *Phys. Chem. Chem. Phys.* **2010**, *12*, 4336–4344, DOI 10.1039/b924974p.

[259] J.-N. Luy, R. Tonner, Unpublished data, **2017**.

[260] C. Stadler, S. Hansen, I. Kröger, C. Kumpf, E. Umbach, *Nat. Phys.* **2009**, *5*, DOI 10.1038/nphys1176.

[261] N. Papageorgiou, J. C. Mossoyan, M. Mossoyan-Deneux, G. Terzian, E. Janin, M. Göthelid, L. Giovanelli, J. M. Layet, G. Le Lay, *Appl. Surf. Sci.* **2000**, *162-163*, 178–183, DOI 10.1016/s0169-4332(00)00189-6.

[262] S. A. Krasnikov, C. M. Doyle, N. N. Sergeeva, A. B. Preobrajenski, N. A. Vinogradov, Y. N. Sergeeva, A. A. Zakharov, M. O. Senge, A. A. Cafolla, *Nano Res.* **2011**, *4*, 376–384, DOI 10.1007/s12274-010-0092-7.

[263] Y. Li, J. Xiao, T. E. Shubina, M. Chen, Z. Shi, M. Schmid, H.-P. Steinrück, J. M. Gottfried, N. Lin, *J. Am. Chem. Soc.* **2012**, *134*, 6401–6408, DOI 10.1021/ja300593w.

[264] D. G. de Oteyza, A. García-Lekue, M. Vilas-Varela, N. Merino-Díez, E. Carbonell-Sanromà, M. Corso, G. Vasseur, C. Rogero, E. Guitián, J. I. Pascual, J. E. Ortega, Y. Wakayama, D. Peña, *ACS Nano* **2016**, *10*, 9000–9008, DOI 10.1021/acsnano.6b05269.

[265] R. G. Jones, M. Kadodwala, *Surf. Sci.* **1997**, *370*, L219–L225, DOI 10.1016/s0039-6028(96)01298-8.

[266] E. Nardi, L. Chen, S. Clair, M. Koudia, L. Giovanelli, X. Feng, K. Müllen, M. Abel, *J. Phys. Chem. C* **2014**, *118*, 27549–27553, DOI 10.1021/jp508990s.

[267] S. Kezilebieke, A. Amokrane, M. Boero, S. Clair, M. Abel, J.-P. Bucher, *Nano Res.* **2014**, *7*, 888–897, DOI 10.1007/s12274-014-0450-y.

[268] S. Kezilebieke, A. Amokrane, M. Abel, J.-P. Bucher, *J. Phys. Chem. Lett.* **2014**, *5*, 3175–3182, DOI 10.1021/jz5015696.

[269] J. Zhou, Q. Sun, *J. Am. Chem. Soc.* **2011**, *133*, 15113–15119, DOI 10.1021/ja204990j.

[270] K. Diller, F. Klappenberger, M. Marschall, K. Hermann, A. Nefedov, C. Wöll, J. V. Barth, *J. Chem. Phys.* **2012**, *136*, 014705, DOI 10.1063/1.3674165.

[271] J. Xiao, S. Ditze, M. Chen, F. Buchner, M. Stark, M. Drost, H.-P. Steinrück, J. M. Gottfried, H. Marbach, *J. Phys. Chem. C* **2012**, DOI 10.1021/jp301757h.

[272] K. Greulich, Master's thesis, Philipps-Universität Marburg, **2018**.

[273] U. Schlickum, R. Decker, F. Klappenberger, G. Zoppellaro, S. Klyatskaya, W. Auwärter, S. Neppl, K. Kern, H. Brune, M. Ruben, J. V. Barth, *J. Am. Chem. Soc.* **2008**, *130*, 11778–11782, DOI 10.1021/ja8028119.

[274] J. Shang, Y. Wang, M. Chen, J. Dai, X. Zhou, J. Kuttner, G. Hilt, X. Shao, J. M. Gottfried, K. Wu, *Nat. Chem.* **2015**, *7*, DOI 10.1038/nchem.2211.

[275] N. Li, X. Zhang, G.-C. Gu, H. Wang, D. Nieckarz, P. Szabelski, Y. He, Y. Wang, J.-T. Lü, H. Tang, L.-M. Peng, S.-M. Hou, K. Wu, Y.-F. Wang, *Chin. Chem. Lett.* **2015**, *26*, 1198–1202, DOI 10.1016/j.cclet.2015.08.006.

[276] Q. Sun, L. Cai, H. Ma, C. Yuan, W. Xu, *Chem. Commun.* **2015**, *51*, 14164–14166, DOI 10.1039/c5cc05554g.

[277] X. Zhang, N. Li, G.-C. Gu, H. Wang, D. Nieckarz, P. Szabelski, Y. He, Y. Wang, C. Xie, Z.-Y. Shen, J.-T. Lü, H. Tang, L.-M. Peng, S.-M. Hou, K. Wu, Y.-F. Wang, *ACS Nano* **2015**, *9*, 11909–11915, DOI 10.1021/acsnano.5b04427.

[278] X. Zhang, N. Li, L. Liu, G. Gu, C. Li, H. Tang, L. Peng, S. Hou, Y. Wang, *Chem. Commun.* **2016**, *52*, 10578–10581, DOI 10.1039/c6cc04879j.

[279] L. Cai, Q. Sun, M. Bao, H. Ma, C. Yuan, W. Xu, *ACS Nano* **2017**, *11*, 3727–3732, DOI 10.1021/acsnano.6b08374.

[280] M. Marschall, J. Reichert, K. Diller, S. Klyatskaya, M. Ruben, A. Nefedov, C. Wöll, L. N. Kantorovich, F. Klappenberger, J. V. Barth, *J. Phys. Chem. C* **2014**, *118*, 2622–2633, DOI 10.1021/jp4118584.

[281] F. Klappenberger, D. Kühne, M. Marschall, S. Neppl, W. Krenner, A. Nefedov, T. Strunskus, K. Fink, C. Wöll, S. Klyatskaya, O. Fuhr, M. Ruben, J. V. Barth, *Adv. Funct. Mater.* **2011**, *21*, 1631–1642, DOI 10.1002/adfm.201001940.

[282] M. Zugermeier, M. Gruber, M. Schmid, B. P. Klein, L. Ruppenthal, P. Müller, R. Einholz, W. Hieringer, R. Berndt, H. F. Bettinger, J. M. Gottfried, *Nanoscale* **2017**, *9*, 12461–12469, DOI 10.1039/c7nr04157h.

[283] U. Gelius, P. F. Hedén, J. Hedman, B. J. Lindberg, R. Manne, R. Nordberg, C. Nordling, K. Siegbahn, *Phys. Scr.* **1970**, *2*, 70–80, DOI 10.1088/0031-8949/2/1-2/014.

[284] C. Baldacchini, C. Mariani, M. G. Betti, *J. Chem. Phys.* **2006**, *124*, 154702, DOI 10.1063/1.2187486.

[285] N. Koch, A. Kahn, J. Ghijsen, J.-J. Pireaux, J. Schwartz, R. L. Johnson, A. Elschner, *Appl. Phys. Lett.* **2003**, *82*, 70–72, DOI 10.1063/1.1532102.

[286] T. Suzuki, M. Kurahashi, X. Ju, Y. Yamauchi, *Appl. Phys. Lett.* **2003**, *83*, 4342–4344, DOI 10.1063/1.1630161.

[287] V. I. Bukhtiyarov, V. V. Kaichev, I. P. Prosvirin, *J. Chem. Phys.* **1999**, *111*, 2169–2175, DOI 10.1063/1.479488.

[288] C. T. Campbell, *Surf. Sci.* **1985**, *157*, 43–60, DOI 10.1016/0039-6028(85)90634-x.

[289] M. Böhringer, W.-D. Schneider, R. Berndt, *Surf. Sci.* **1998**, *408*, 72–85, DOI 10.1016/s0039-6028(98)00151-4.

[290] M. Kulawik, H.-P. Rust, N. Nilius, M. Heyde, H.-J. Freund, *Phys. Rev. B* **2005**, *71*, 153405, DOI 10.1103/physrevb.71.153405.

[291] W. Hansen, M. Bertolo, K. Jacobi, *Surf. Sci.* **1991**, *253*, 1–12, DOI 10.1016/0039-6028(91)90576-e.

[292] C. Mainka, P. S. Bagus, A. Schertel, T. Strunskus, M. Grunze, C. Wöll, *Surf. Sci.* **1995**, *341*, L1055–L1060, DOI 10.1016/0039-6028(95)00795-4.

[293] M.-C. Lu, R.-B. Wang, A. Yang, S. Duhm, *J. Phys.: Condens. Matter* **2016**, *28*, 094005, DOI 10.1088/0953-8984/28/9/094005.

[294] M. Chen, M. Röckert, J. Xiao, H.-J. Drescher, H.-P. Steinrück, O. Lytken, J. M. Gottfried, *J. Phys. Chem. C* **2014**, *118*, 8501–8507.

B List of Figures

C List of Tables

Danksagungen

Ganz besonders danke ich meinem Doktorvater, Prof. Dr. J. Michael Gottfried, für die Möglichkeit unter seiner Betreuung meine Doktorarbeit schreiben und sehr spannende Forschungsprojekte bearbeiten zu können. Durch ihn habe ich ein unglaublich faszinierendes Fachgebiet, die Oberflächenchemie, kennengelernt und helfen dürfen, die wissenschaftlichen Erkenntnisse auszubauen. Es war mir außerdem eine große Ehre, als einer der beiden ersten Doktoranden an einer neuen UHV-Apparatur, dem kombinierten Aufbau für STM und XPS, arbeiten zu können und deren kontinuierliche Erweiterung voranzutreiben. Danken möchte ich ihm auch dafür, im Rahmen meiner Doktorarbeit internationale Fachkonferenzen besuchen und mich an Kooperationen beteiligen zu dürfen.

Ich danke Prof. Dr. Gerhard Hilt für die Übernahme des Zweitgutachtens zu meiner Doktorarbeit sowie für die Bereitstellung von zwei hier untersuchten Substanzen. Prof. Dr. Jörg Sundermeyer danke ich ebenfalls für die Bereitstellung einer Ausgangssubstanz sowie dafür, als weiteres Mitglied in meiner Prüfungskommission bereitzustehen.

Für die finanzielle Unterstützung durch die Übernahme der Kosten für Synchrotron-Messzeiten, Forschungsmittel und meine Stelle als wissenschaftlicher Mitarbeiter danke ich dem Sonderforschungsbereich 1083.

Dem Team des Kellerlabors, Benedikt Klein, Claudio Krug und Qitang Fan, danke ich für die unterhaltsame Zeit, die gemeinsamen Stunden im Labor und die hervorrangende gegenseitige Unterstützung. Martin Schmid möchte ich besonders für die Diskussionen über wissenschaftliche Fragestellungen, die Tipps zur Durchführung von Experimenten sowie die Zusammenarbeit danken. Marco Hill gebührt Dank für die Hilfe bei technischen Problemen und die schnelle Beschaffung von Materialien. Min Chen danke ich für die gemeinsame Erarbeitung des Umgangs mit der damals neu angeschafften UHV-Apparatur. Allen Mitgliedern der Arbeitsgruppe von Prof. Dr. J. Michael Gottfried danke ich für die tolle Zeit in Marburg, am Synchrotron in Berlin und bei diversen Sommerfesten und Ausflügen.

Unseren Kooperationspartnern Prof. Dr. Richard Berndt und Dr. Manuel Gruber danke ich für die Möglichkeit, das gemeinsame Forschungsprojekt um Messungen am LT-STM in Kiel erweitern zu können. Des Weiteren gilt mein Dank PD Dr. Ralf Tonner, Jan-Niclas Luy und PD Dr. Wolfgang Hieringer für die Betrachtung der wissenschaftlichen Fragestellungen aus Sicht der theoretischen Chemie.

Der Feinmechanischen Werkstatt und der Werkstatt für Elektronik und Informationstechnik danke ich für die Unterstützung bei der Umsetzung verschiedenster Projekte und der teilweise auch sehr kurzfristigen Bearbeitung von dringend benötigten Bauteilen.

Im Rahmen dieser Doktorarbeit habe ich zahlreiche Studenten im Praktikum und bei ihren Abschlussarbeiten betreut. Für ihre Unterstützung bei den Laborarbeiten danke ich den Vertiefungsstudenten Vivane Heddinga, Sebastian Kranz, Falk Niefind, Stefan Spannenberger, Viola Krein, Konstantin Gaul, Fabian Pieck, Simon Werner, Matthias Oebbeke, Jan Wiemer und Zacharenia Eirini Kostaki (in chronologischer Reihenfolge). Auch das Schulpraktikum von Romy-Maria Hossfeld war für mich sehr interessant und abwechs-

lungsreich. Meinen Bachelorstudenten Dennis Gruber, Janek Bernzen und Lukas Heuplick sowie den Masterstudenten Claudio Krug, Jan Herritsch und Falk Niefind danke ich für die Mithilfe bei den gemeinsamen Forschungsprojekten und die unterhaltsame Laborarbeit.

Meinen Eltern gebührt ein sehr umfassender Dank, den man in ein paar Zeilen gar nicht wiedergeben kann. Ich danke ihnen nicht nur dafür, dass sie mich sehr liebevoll in meinem Leben begleiten, sondern auch dafür, dass sie mich im Speziellen während meiner Doktorarbeit und dem vorhergehenden Studium stets ermutigt und unterstützt haben. Meiner Schwester danke ich besonders für die kurzweiligen Erholungspausen während der teils doch recht anstrengenden Messzeiten am Synchrotron BESSY II in Berlin.

Von Herzen möchte ich meiner Freundin Jessika Stiefken dafür danken, dass sie für mich da ist und mich immer wieder in die Welt des Segelns entführt. Als gute Abwechslung von den geistigen Tätigkeiten haben wir gemeinsam in den letzten Jahren viele tolle Momente auf und am Wasser erlebt, sei es mit einer Valk in Friesland oder mit dem Flying Junior auf diversen Regatten.

Curriculum Vitae

Die Seiten 137-138 (Curriculum Vitae) enthalten persönliche Daten. Sie sind deshalb nicht Bestandteil der Online-Veröffentlichung.

Scientific Contributions

During the studies for this thesis and beforehand, the following journal articles were published and several conference contributions were given. Some contributions originate from projects which are independent from this thesis.

Publications

1. M. Sachs, M. Gellert, M. Chen, H.-J. Drescher, S. R. Kachel, H. Zhou, M. Zugermeier, M. Gorgoi, B. Roling, J. M. Gottfried, *"LiNi0.5Mn1.5O4 High-Voltage Cathode Coated with Li4Ti5O12: A Hard X-ray Photoelectron Spectroscopy (HAXPES) Study"*, *Phys. Chem. Chem. Phys.* **2015**, *17*, 31790–31800.

2. M. Chen, H. Zhou, B. P. Klein, M. Zugermeier, C. K. Krug, H.-J. Drescher, M. Gorgoi, M. Schmid, J. M. Gottfried, *"Formation of an Interphase Layer During Deposition of Cobalt onto Tetraphenylporphyrin: A Hard X-Ray Photoelectron Spectroscopy (HAXPES) Study"*, *Phys. Chem. Chem. Phys.* **2016**, 18, 30643–30651.

3. B. Wagner, N. Dehnhardt, M. Schmid, B. P. Klein, L. Ruppenthal, P. Müller, M. Zugermeier, J. M. Gottfried, S. Lippert, M.-U. Halbich, A. Rahimi-Iman, J. Heine, *"Color Change Effect in an Organic-Inorganic Hybrid Material Based on a Porphyrin Diacid"*, *J. Phys. Chem. C* **2016**, 120, 28363–28373.

4. M. Zugermeier, M. Gruber, M. Schmid, B. P. Klein, L. Ruppenthal, P. Müller, R. Einholz, W. Hieringer, R. Berndt, H. F. Bettinger, J. M. Gottfried, *"On-Surface Synthesis of Heptacene and its Interaction with a Metal Surface"*, *Nanoscale* **2017**, 9, 12461–12469.

5. M. Schmid, M. Zugermeier, J. Herritsch, B. P. Klein, C. Krug, L. Ruppenthal, P. Müller, M. Kothe, P. Schweyen, M. Bröring, J. M. Gottfried, *"On-Surface Synthesis and Characterization of an Iron Corrole"*, *J. Phys. Chem. C* **2018**, *122*, 10392–10399.

6. M. Zugermeier, M. Chen, J. Herritsch, F. Niefind, J.-N. Luy, P. Rosenow, R. Tonner, P. Schweyen, M. Bröring, M. Schmid, J. M. Gottfried, *"Structure and Surface Reactivity of an Adsorbed Free-Base Corrole"*, in preparation.

7. Q. Fan, K. Greulich, M. Zugermeier, J.-N. Luy, R. Tonner, J. Sundermeyer, J. M. Gottfried, *"Template-Controlled Synthesis of Lanthanide Superphthalocyanine and Its Open-Chain Counterpart"*, in preparation.

Conferences

1. M. Zugermeier, M. Chen, H.-J. Drescher, J. M. Gottfried, *"Growth of Semiconducting Organic Crystals by Physical Vapor Deposition onto Thin Liquid Films"*, 112$^{\text{th}}$ General Assembly of the German Bunsen Society for Physical Chemistry (DBG), Karlsruhe, May 9$^{\text{th}}$-11$^{\text{th}}$, 2013. (Poster)

2. M. Zugermeier, M. Chen, H.-J. Drescher, H. Zhou, B. Klein, C. Krug, M. Gorgoi, J. M. Gottfried, *"Reactive Cobalt/Porphyrin Interfaces Probed with Hard X-ray Photoelectron Spectroscopy (HAXPES)"*, Materialforschungstag Mittelhessen, Gießen, June 26$^{\text{th}}$, 2014. (Poster)

3. M. Zugermeier, M. Chen, H.-J. Drescher, H. Zhou, B. Klein, C. Krug, J. M. Gottfried, *"Reactive Cobalt/Porphyrin Interfaces Probed with Hard X-ray Photoelectron Spectroscopy (HAXPES)"*, International Summer School on Semiconductor Interfaces - Methods and Model Systems, San Sebastian (Spain), July 27$^{\text{th}}$-31$^{\text{st}}$, 2014. (Poster)

4. M. Zugermeier, M. Chen, M. Schmid, J. M. Gottfried, *"Reactive Coupling and Self-Assembly of Tetraphenylporphyrins on Cu(111)"*, 79$^{\text{th}}$ Annual Meeting and Spring Meeting of the German Physical Society (DPG), Berlin, March 15$^{\text{th}}$-20$^{\text{th}}$, 2015. (Poster)

5. M. Zugermeier, J. Bernzen, V. Krein, C. Krug, J. Kuttner, M. Schmid, G. Hilt, J. M. Gottfried, *"Functional Organic Molecules on Surfaces Studied with Scanning Tunneling Microscopy"*, Materialforschungstag Mittelhessen, Marburg, Juli 09$^{\text{th}}$, 2015. (Poster)

6. M. Zugermeier, N. Bock, M. Chen, F. Niefind, J. Herritsch, L. Ruppenthal, M. Schmid, P. Schweyen, M. Bröring, J. M. Gottfried, *"Oxidation State Tuning in Ligand-Metal Surface Reaction: Formation of M(III)-Corroles on Ag(111)"*, 80$^{\text{th}}$ Annual Meeting and Spring Meeting of the German Physical Society (DPG), Regensburg, March 06$^{\text{th}}$-11$^{\text{th}}$, 2016. (Talk)

7. M. Zugermeier, N. Bock, M. Chen, F. Niefind, J. Herritsch, L. Ruppenthal, M. Schmid, P. Schweyen, M. Bröring, J. M. Gottfried, *"Metalation Reactions of Corroles at Metal-Organic Interfaces"*, ICII-2016 International Conference on Internal Interfaces, Marburg, May 31$^{\text{st}}$ - June 3$^{\text{rd}}$, 2016. (Poster)

8. M. Zugermeier, M. Chen, H.-J. Drescher, B. P. Klein, C. K. Krug, F. Niefind, M. Schmid, H. Zhou, J. M. Gottfried, *"From Metal-Organic Interfaces Towards More Complex Interphase Systems"*, CRC 1083 - Winter School, January 17$^{\text{th}}$-18$^{\text{th}}$, 2017. (Talk, and organizer)

9. M. Zugermeier, M. Chen, L. Heuplick, M. Liebold, N. Bock, F. Niefind, L. Ruppenthal, M. Schmid, P. Schweyen, M. Bröring, J. Sundermeyer, J. M. Gottfried, *"On-Surface Synthesis of Naphthalocyanine and Corrole Complexes"*, Spring Meeting of the German Physical Society (DPG), Dresden, March 19$^{\text{th}}$-24$^{\text{th}}$, 2017. (Poster)

10. M. Zugermeier, M. Chen, H.-J. Drescher, L. Heuplick, B. P. Klein, C. K. Krug, M. Liebold, F. Niefind, L. Ruppenthal, M. Schmid, P. Schweyen, H. Zhou, M. Bröring, J. Sundermeyer, J. M. Gottfried, *"Synthesis, Metalation and Structures of Tetrapyrroles at Interfaces"*, 116$^{\text{th}}$ General Assembly of the German Bunsen Society for Physical Chemistry (DBG), Kaiserslautern, May 25$^{\text{th}}$-27$^{\text{th}}$, 2017. (Poster)

11. M. Zugermeier, M. Chen, L. Heuplick, M. Liebold, N. Bock, F. Niefind, L. Ruppenthal, M. Schmid, P. Schweyen, M. Bröring, J. Sundermeyer, J. M. Gottfried, *"On-Surface Synthesis of Naphthalocyanine and Corrole Complexes"*, Materialforschungstag Mittelhessen, Gießen, June 28$^{\text{th}}$, 2017. (Poster)

12. M. Zugermeier, M. Gruber, M. Schmid, B. P. Klein, L. Ruppenthal, P. Müller, R. Einholz, W. Hieringer, R. Berndt, H. F. Bettinger, J. M. Gottfried, *"On-Surface Synthesis of Heptacene and its Interaction with a Metal Surface"*, Spring Meeting of the German Physical Society (DPG) and Meeting of the Condensed Matter Section of the European Physical Society (EPS), Berlin, March 11$^{\text{th}}$-16$^{\text{th}}$, 2018. (Talk)